Annual reports on
NMR Spectroscopy

Volume 62

ANNUAL REPORTS ON

NMR SPECTROSCOPY

This page intentionally left blank

ANNUAL REPORTS ON

NMR SPECTROSCOPY

Edited by

G. A. WEBB

Royal Society of Chemistry, Burlington House, London, England

VOLUME 62

ELSEVIER

Amsterdam • Boston • Heidelberg • London • New York
Oxford • Paris • San Diego • San Francisco • Singapore
Sydney • Tokyo

Academic Press is an Imprint of Elsevier

Academic Press is an imprint of Elsevier
84 Theobald's Road, London WC1X 8RR, UK
Radarweg 29, PO Box 211, 1000 AE Amsterdam, The Netherlands
Linacre House, Jordan Hill, Oxford OX2 8DP, UK
30 Corporate Drive, Suite 400, Burlington, MA 01803, USA
525 B Street, Suite 1900, San Diego, CA 92101-4495, USA

First edition 2007

ISBN: 978-0-12-373919-3
ISSN: 0066-4103

For information on all Academic Press publications
visit our website at books.elsevier.com

Printed and bound in the United Kingdom

07 08 09 10 11 10 9 8 7 6 5 4 3 2 1

List of Contributors

Michael Bühl, *Max-Planck Institut für Kohlenforschung, 45470 Mülheim, Germany*

Julio C. Facelli, *Center for High Performance Computing and Departments of Chemistry and Biomedical Informatics, University of Utah, Salt Lake City, UT 84112-0190, USA*

Peter F. Flynn, *Department of Chemistry, University of Utah, Salt Lake City, UT 84112-0850, USA*

Paul A. Keifer, *Varian NMR Instruments, 3120 Hansen Way D-298, Palo Alto, CA 94304-1030, USA*

Anita M. Orendt, *Center for High Performance Computing and Department of Chemistry, University of Utah, Salt Lake City, UT 84112-0190, USA*

Tatyana Polenova, *Departments of Chemistry and Biochemistry, University of Delaware, Newark, DE 19716, USA*

Dieter Rehder, *Department Chemie, Universität Hamburg, D-20146 Hamburg, Germany*

Alana K. Simorellis, *Department of Chemistry, University of Utah, Salt Lake City, UT 84112-0850, USA*

Wade D. Van Horn, *Department of Chemistry, University of Utah, Salt Lake City, UT 84112-0850, USA*

This page intentionally left blank

Preface

As is customary in this series of reports on NMR Spectroscopy, Volume 62 consists of accounts of research activities in a number of diverse scientific areas. The first to be reviewed is 'Flow Techniques in NMR Spectroscopy' by P.A. Keifer; this is followed by a report from D. Rehder, T. Polenova and M. Bühl on 'Vanadium-51 NMR'; next comes a review of 'Solid State Effects on NMR Chemical Shifts' by A.M. Orendt and J.C. Facelli; finally 'NMR Studies of Encapsulated Macromolecules' are covered by P.F. Flynn, A.K. Simorellis and W.D. Van Horn.

It is my pleasure to thank all of these reporters for their very informative and lucid contributions.

Royal Society of Chemistry
Burlington House
Piccadilly
London, UK

G.A. WEBB
February 2007

This page intentionally left blank

Contents

NMR Studies of Encapsulated Macromolecules
P.F. FLYNN A.K. SIMORELLIS AND W.D. VAN HORN

Flow techniques in NMR spectroscopy

P.A. KEIFER[1,2]

[1]*University of Nebraska Medical Center, Eppley Institute, 986805 Nebraska Medical Center, Omaha, NE 68198-6805, USA*
[2]*Current address: Varian Inc., NMR Instruments, 3120 Hansen Way D-298, Palo Alto, CA 94304-1030, USA*

ANNUAL REPORTS ON NMR SPECTROSCOPY
VOLUME 62 ISSN 0066 4103
DOI 10.1016/S0066-4103(07)62001-8

Flow techniques have been used in NMR for over 50 years, and there has been a lot of growth and interest in the field over the last decade. Most of that growth has focused on LC-NMR type techniques, but it has also led to the development of other flow-NMR methods, each of which is suited to different applications. Some of these methods use different kinds of chromatography, whereas others use different plumbing schemes. All of these variations will be discussed here, with particular emphasis being given to the techniques of Flow-Injection-Analysis NMR (FIA-NMR), Direct-Injection NMR (DI-NMR), Solid-Phase-Extraction NMR (SPE-NMR), and loop collection. By understanding how and why each flow-NMR method was developed, a user can more easily select the best tool for any given application.

1. INTRODUCTION

"Flow NMR" is a broad term that encompasses a variety of techniques, and these techniques have been used for a wide range of applications. To help define the scope of this chapter, the definition used here is that a "flow-NMR technique" is any NMR technique in which the sample is flowing through a tube into the NMR probe at some time during the measurement process. More specifically, the sample may – or may not – actually be flowing at the precise moment that the NMR signal is acquired.

Flow-NMR techniques have been around for decades, and the field really blossomed starting in the mid-1990s. This was due in part to hardware developments that happened then, which allowed flow-NMR techniques to finally become more feasible. We will explore here how flow-NMR techniques got started, what hardware developments took place, and what variations on the technique were developed. We will look at some representative applications and explore the problems and limitations of flow NMR methods.

The early development of essentially all flow-NMR techniques was based upon the development of liquid chromatography NMR (LC-NMR). The other flow-NMR techniques then evolved from LC-NMR. As a result, although this article will not focus upon LC-NMR itself (as LC-NMR has already been the subject of many

other reviews[1–3]), it will cover LC-NMR enough to provide a background for understanding all the other flow-NMR techniques. The three main categories of flow-NMR techniques that will be discussed in detail are Direct Injection NMR (DI-NMR),[4] Flow Injection Analysis NMR (FIA-NMR),[5] and Solid-Phase-Extraction NMR (SPE-NMR),[6] along with all of their variants.

2. THE START OF FLOW NMR AND THE EVOLUTION OF LC-NMR

2.1. The first flow-NMR experiments

The first reported use of a flow-NMR technique was in 1951, when the ^{1}H spectrum of water (doped with $FeCl_3$) was recorded as it flowed through the NMR probe.[7] The intensity of the water signal was found to be proportional to the flow rate, and the effects of T_1 and T_2 on the signal were evaluated. Over the next two decades there were a number of other investigations that acquired NMR data on flowing liquids, all of which used the "flow" aspects to either measure, study, or reduce the effects of either T_1 or T_2 in a given sample, by measuring either ^{1}H or ^{13}C spectra.[8–17] Typically, the goal of these research projects was to either improve the signal-to-noise of the resulting spectra (by apparently "shortening" T_1 via sample flow),[11,18] or to use NMR to measure aspects of the flow itself.[10,16] As a part of these investigations, NMR "flow probes" – probes capable of acquiring data on liquids flowing through a tube located in the NMR magnet – were designed and used.[15,19]

2.1.1. *Stopped-flow NMR, rapid-injection NMR, continuous-flow NMR, and flow NMR*

The next technique to come into common use was actually a group of related techniques which were variously called "stopped-flow NMR",[20–30] "rapid-injection NMR",[31–35] "continuous-flow" NMR,[36,37] or just "flow NMR".[24,38,39] Their use started in the 1970s[20–22] and continues to this day.[35,40] In all of these techniques, the goal is to acquire NMR data on unstable or rapidly reacting samples. The limitation in doing this with ordinary tube-based NMR (in which the sample under investigation is placed in a precision glass tube that is then lowered into the probe in the magnet) is that the time between "creating" the sample and actually acquiring the NMR data is too long to allow transient species to be observed. (That is, the time required to transport the sample into the transceiver coil of the NMR probe is too long.) The strategy of these alternative methods is to instead create the transient species of interest at the site of the NMR measurement, rather than on the lab bench, so as to eliminate the transport time. Some of the first groups (among many) to do this were Sykes *et al.*,[21,23,41,42] Moore *et al.*,[22,43–46] Fyfe *et al.*,[24,47–51] and Cocivera *et al.*;[38,52–55] they did this by mixing the two reactive species at the site of the NMR probe. There are two general ways to accomplish this. First, as shown in Fig. 1A, one can inject a liquid through a tube (where this tube runs through the magnet bore)

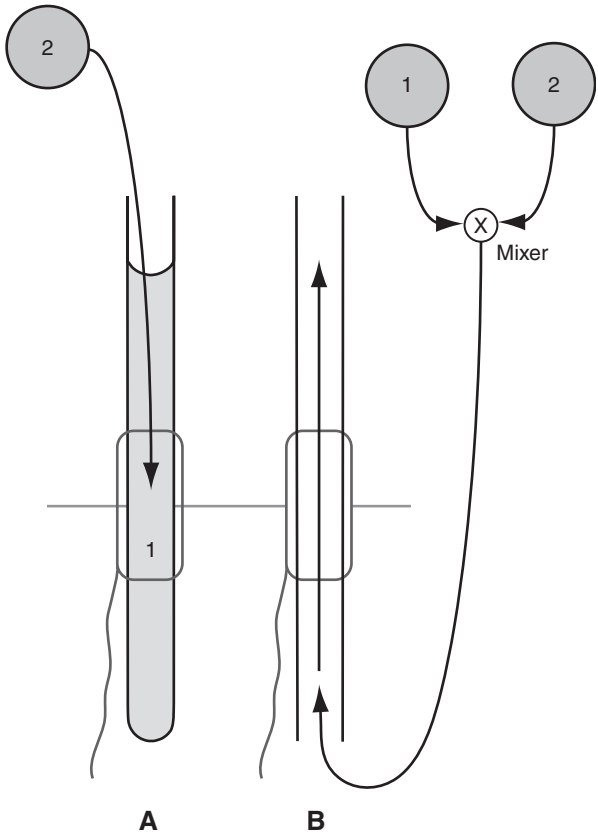

Fig. 1. Representations of the two different fluidic methods used to perform rapid-injection-NMR type experiments. One method (A; on the left) is to place reactant 1 in a tube in the magnet, and then inject reactant 2 into 1 via tubing that is ultimately connected to a syringe located outside the magnet. The other method (B; on the right) is to flow reactants 1 and 2 into a mixer located outside the magnet (upper right) and then flow the resulting mixture (through tubing) into the NMR rf coil. The "active" (detected) volume of the probe is generated by the rf coil, which itself is represented by the black "wire" outline. The thin horizontal line shows the midpoint of the rf coils, which are located in the center of the magnet.

into a different liquid that is in a standard (non-flow; traditional precision-glass) sample tube located in the NMR probe.[30,56] (Hence, this setup does not use an "NMR flow probe".) The second setup, shown in Fig. 1B, uses two (flow) tubes that each contain a separate flowing liquid, which are then joined together to form a single outlet tube.[57] The two reactive liquids mix together and – while they are reacting – flow through one single tube into the NMR transceiver coil. Both of these setups can be used to study kinetics, however, each setup has its own unique advantages and disadvantages. In the first setup (Fig. 1A), even though one can control the time between mixing (injection) and analysis, there is only one single

discreet mixing step – so the sample may continue to change with time (during the measurement). In contrast, in the second setup (Fig. 1B), one controls the time between mixing and analysis by instead varying either the flow rate or the length of the combined (single-tube) tubing. The mixing step in this second setup is normally continuous (because the two streams of liquid normally flow continuously), which is an advantage when one needs to signal average the NMR data for a longer time than the lifetime of the transient species. (Because the NMR transceiver coil is continuously being replenished with a fresh mixture, one could signal average almost indefinitely.) Yet a different advantage of the first setup is that the reacted sample can be better maintained at a very low temperature, which can be critical when studying unstable products.[35]

2.1.2. *The start of LC-NMR*

The first published paper in which the outlet of an HPLC system was linked to an NMR probe appeared in 1978.[58] This led several other groups to begin to investigate the uses, advantages, and limitations of LC-NMR, including Dorn *et al.*,[59–63] Bayer and Albert *et al.*,[64–67] Buddrus *et al.*,[68–70] and Wilkins *et al.*[71] among others. This eventually led to hundreds of publications on LC-NMR starting in the early 1980s, and research in the field continues to this day. There are many published reviews of LC-NMR, and the reader is directed toward those sources for more a complete treatment of the technique.[1–3]

In hindsight, one might call LC-NMR a natural development, considering all the other non-chromatographic flow-NMR work that had became "routine" in the 1970s (as discussed above). As an evolutionary change from before, however, LC-NMR now required one to use an NMR probe that was dedicated solely to the observation of a sample flowing through tubing from another source. This led to many investigations that attempted to optimize the design of the flow-NMR probe – a probe specifically designed to acquire NMR data on a sample introduced to the magnet bore and probe via capillary tubing. (This sample-delivery style was in sharp contrast to the traditional delivery method of "pipette the sample into a precision-glass NMR tube, and use an air cushion to drop this tube into the transceiver coil located in the NMR probe".)

2.2. Flow NMR probes

The criteria for designing a good flow-NMR probe (or LC-NMR probe) were initially threefold. First, the inlet port had to be attached to capillary tubing so that it could connect to the HPLC column/system. Second, the probe's "filling factor" had to be optimized to produce the best sensitivity possible on a "chromatographic peak" (liquid) sample. Third, no bubbles could be in the NMR flow cell, otherwise the NMR lineshape would be degraded by magnetic-susceptibility inhomogeneities. These criteria were typically met by using a flow cell within the NMR probe like the one shown in Fig. 2A. The outlet line exits from the top of the flow cell, and the inlet line enters from the bottom, both so as to naturally eliminate bubbles. The

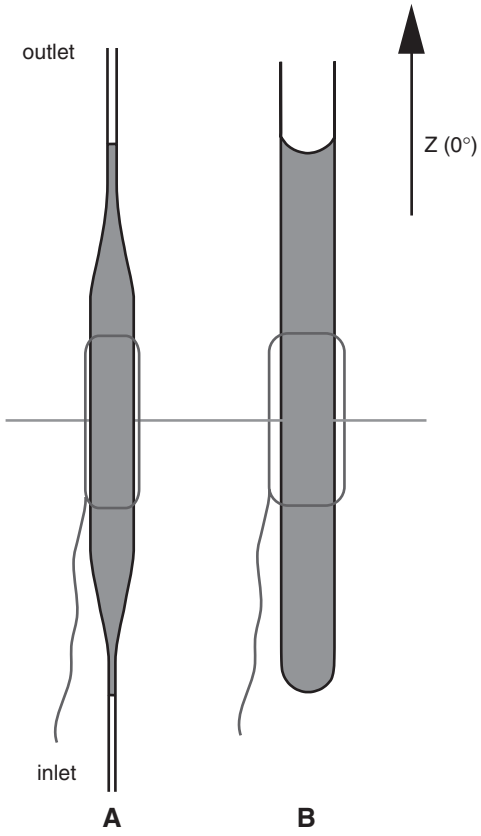

Fig. 2. Representations of the rf coil and sample-tube geometries for both an NMR flow cell (A; on the left) and a traditional 5 mm NMR sample tube (B; on the right). NMR flow cells typically have the inlet at the bottom and the outlet at the top, so that any air bubbles that happen to get into the flow cell are easily eliminated out the top whenever the fluid is in motion. Note the gradually widening connections where the capillary tubings join into the flow cell (A), which helps the incoming fluid displace the contents of the flow cell, rather than just mix with it – or (worse yet) to simply "jet" in. The length of the rf coil along the Z axis (represented by the black "wire" outline) is approximately the same in both cases; however, the diameters of the rf coils used for most NMR flow cells is less than that used for 5 mm tubes (as is shown). The horizontal line shows the midpoint of the rf coils (along the Z axis) which should be coincident with the center of the magnetic field.

sensitivity limitations of NMR caused users to increase the volume of the flow cell; making it larger than is typically used for other chromatographic detectors (hence the expanded diameter of the tubing at the location of the transceiver coil). This led to concerns about chromatographic band broadening, which had two effects. First, it forced the NMR detector to be placed last (most downstream) whenever multiple detectors were used in series. Second, it encouraged the NMR flow cells to be designed so that the incoming solvent would "sweep" the contents of the flow cell to

the exit port, and not simply "jet in". ("Jetting in" causes excessive sample dilution, which will reduce the NMR signal.)

Even as late as the 1980s and early 1990s, the NMR probes used for LC-NMR still had to be custom made,[72,73] but by the mid-1990s, flow-NMR probes became commercially available and were soon considered to be standard items. This led even more research groups into investigating the utility of LC-NMR. Most of this work focused on either solving specific scientific problems,[74,75] exploring various kinds of chromatography,[1,76] or studying the physics of chromatography itself.[77] As will be discussed below, however, research was also done on the development of new fundamental methodological tools for LC-NMR – tools such as different kinds of fluid flow and different kinds of solvent suppression.

2.3. Variations in fluid flow: "on-flow" versus "stopped-flow" LC-NMR

Liquid chromatography alone (without NMR) is always performed "on-flow"; that is, the solvent stream always flows during the analysis, and never stops. A good chromatographer would always avoid stopping the flow during a chromatographic run, because that could lead to chromatographic band broadening – and the primary concern of chromatographers is usually to achieve the best possible chromatographic resolution. Practitioners of LC-NMR, however, usually struggle with NMR signal-to-noise limitations more than with chromatographic resolution. The NMR signal-to-noise can be improved by signal averaging, however, this usually requires the flow to be stopped – often for substantial periods of time. The outcome of all this is that, although modern LC-NMR can be run in an entirely "on-flow" mode, a more common practice is to stop the solvent flow (when needed) in such a way that chromatographic peaks of interest can be stopped in the NMR probe for as long as is needed to allow the NMR spectrometer to signal average that chromatographic-peak's NMR spectrum to an acceptable signal-to-noise. This process is called "stopped-flow" LC-NMR. In practice, chromatographic peaks are often stopped in the NMR probe as long as overnight (or more) for signal averaging. Usually the LC-NMR operator does not detect much measurable degradation of the chromatographic resolution by stopping the flow, but this greatly depends on the volume of chromatographic peak as compared with the volume of the flow cell, and by how much the operator is overlooking the problem. Chromatographic broadening is often overlooked in part due to the ability of NMR spectroscopy to "resolve" compounds that are still chromatographically overlapped. It may also be overlooked due to the tendency of an LC-NMR operator to often focus on the NMR resolution more than the chromatographic resolution. It certainly is influenced by the fact that the NMR flow cells – which normally have capacities of 10–150 μL – can sometimes serve as large-volume "solvent mixers" from a chromatographic viewpoint. This is particularly true if the chromatographic peak's solvent volume is much smaller than the volume of the NMR flow cell, in which case incoming peaks can be significantly diluted and "chromatographically broadened" as they flow into the NMR flow cell. But overall, in summary, on-flow and stopped-flow LC-NMR techniques both are

freely used techniques,[78] and there is no hesitation in LC-NMR to stop the chromatographic peaks in the NMR probe for long periods of time. It is also quite common to use both techniques on a given sample for different purposes – normally using on-flow-LC-NMR to first survey the mixture, followed by stopped-flow LC-NMR (often in combination with 2D-NMR) to examine certain chromatographic peaks in more detail – as was done by Ikeda and coworkers.[79]

2.3.1. *Sample recovery*

LC-NMR, like analytical LC, usually does not involve recovering the compounds separated during the analysis. (Preparative LC does, by definition, but analytical LC usually does not.) In part this is because the NMR flow cell itself usually significantly degrades chromatographic resolution and causes dilution. Some investigators do, however, chose to recover chromatographically separated peaks after LC-NMR. (LC-NMR is technically "non-destructive".) One way to do this is to blow the sample solution out of the outlet of the probe with nitrogen gas.[80] This is easier to do when using certain alternative plumbing schemes (discussed below).

2.4. Developments in solvent suppression

LC-NMR usually acquires ^{1}H NMR spectra. If mobile-phase solvents that contain protons are used, the resulting solvent signals usually need to be suppressed to obtain a quality NMR spectrum. The problem of how to best suppress these signals has been an issue since the early days of LC-NMR.[81]

2.4.1. *Presaturation and binomial sequences*

Early investigators suppressed solvent NMR signals by using either presaturation[81] or binomial sequences such as 1331[67,72] or 11.[82,83] Spin-echo-difference spectra of isotope-labeled samples have also been used to "suppress" (avoid) solvent signals.[84] Through the early 1990s, a presaturation/first-increment NOESY sequence was commonly used. (Presat-NOESY suppresses solvent resonances better than does presaturation alone, although the resulting spectrum is less quantatively accurate.) Prior to the invention of SLP pulses,[85] however, presaturation required a separate rf channel in the spectrometer for each NMR signal that needed to be suppressed, which made it difficult to suppress multiple resonances within a spectrum. In addition, because of their long "dead" time, presaturation sequences are poorly suited to on-flow techniques. (No data can be collected during the long 1–2 sec presaturation-irradiation period, and so half of the sample is uselessly flowing to waste during that half of the experimental time.)

2.4.2. *WET*

A significant advance was made in 1995 when the WET solvent-suppression method was created (Fig. 3).[86] The advantages of WET were numerous. The signal

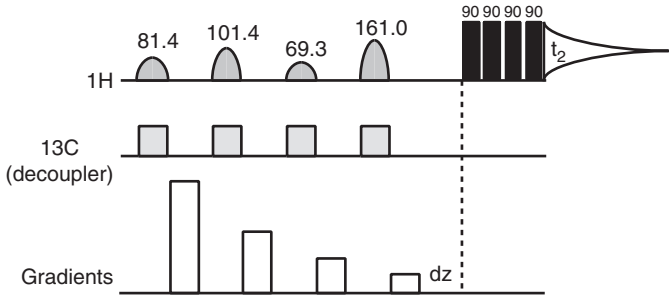

Fig. 3. The NMR pulse sequence used for WET solvent suppression. The tip angles of each of the four CHESS pulses is indicated in the figure above each shaped pulse. These pulses can be SLP (phase-ramped) pulses to suppress off-resonance signals, and can be convoluted so as to suppress multiple signals as needed. The ^{13}C decoupling pulses remove the ^{13}C-satellites of the suppressed signals. The spatially selective composite read pulse, shown in this figure as four 90° pulses (having phases of X, Y, $-X$, and $-Y$, respectively), is actually delivered as a single pulse with a smoothly changing phase. The "dz" delay is empirically optimized so as to minimize the residual solvent signal (as the spins relax back along the Z axis).

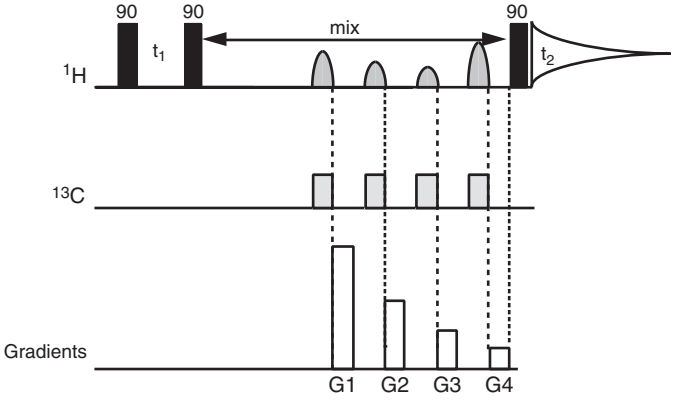

Fig. 4. The NMR pulse sequence used for NOESY with WET solvent suppression. The WET sequence is incorporated into the end of the mix delay.

suppression was fast so that it worked equally well for both on-flow and stopped-flow samples. (Presaturation was an equilibrium method that did not work as well on flowing samples, and it was slower in its recycle rate.) WET could also suppress multiple solvent lines with only a single rf channel by using SLP pulses.[85] WET also suppressed the ^{13}C satellites, and allowed one to view (unsuppressed) resonances that were under these ^{13}C satellites. WET was a robust and forgiving technique that required no fiddling or optimization (unlike WATERGATE). WET was more frequency selective than many techniques, and generated minimal bleaching. And WET had also been incorporated into all standard 2D-NMR sequences (Fig. 4).[86] This made WET the preferred solvent suppression method for LC-NMR. It has

also led to WET being used to acquire NMR data on samples dissolved in fully non-deuterated solvents.[4,87] Additionally, WET is now often used for water suppression in conventional tube-based biomolecular NMR spectroscopy.[88,89]

2.4.3. *Other solvent-suppression methods*

More recently a variety of other solvent-suppression techniques for LC-NMR have been developed, although none of them yet seem to be widely accepted. Some examples include FLIPSY,[90] excitation sculpting,[91,92] and pulsed field gradient (PFG) double quantum methods.[93]

The key point of this section has been to document that the solvent-suppression developments that occurred because of LC-NMR now allowed researchers to routinely acquire acceptable-quality ^{1}H NMR spectra on samples dissolved in fully non-deuterated solvents and solvent mixtures. (In other words, because of WET, solvent suppression was now no longer limited simply to samples dissolved in H_2O, but could be done on samples that contained organic solvents.) This point led to the development of other flow techniques, as discussed below.

2.5. Variations in the chromatography

To most people, the term "LC-NMR" generally means that a reversed-phase chromatographic separation is being used. Other forms of chromatography were investigated, however, soon after LC-NMR was first developed. At a minimum, the following variations were described by at least the indicated dates: gel-permeation chromatography-NMR (GPC-NMR) by 1981,[60] gas chromatography-NMR (GC-NMR) by 1981,[94] supercritical-fluid chromatography-NMR (SFC-NMR) by 1988,[95] capillary electrophoresis-NMR (CE-NMR) by 1994,[96,97] capillary LC-NMR (CapLC-NMR) by 1996,[98–100] capillary electrochromatography-NMR (CEC-NMR) by 1998,[101] and size-exclusion chromatography-NMR (SEC-NMR) by 1998.[102] For more detailed descriptions of the development of these techniques, the reader is directed to other dedicated reviews.[1,76]

Generally, these various forms of chromatography involve simply changing the chromatographic equipment. Sometimes, however, that change influences other aspects of the whole system. For example, although normal-phase chromatography is simple to mechanically implement, the normal-phase solvents that would typically be used (i.e., alkanes) produce complex ^{1}H spectra full of coupled resonances, which obliterate large (critical) portions of the ^{1}H spectral width and whose suppression is difficult. (Solvents like CCl_4[58] and $CHCl_3$,[103] which either have no ^{1}H signal or are NMR "singlets", produce cleaner NMR spectra in normal-phase LC-NMR and SEC-NMR.) Likewise, in SFC-NMR, although the higher pressures used put higher demands on the pressure limitations of the NMR flow cell, the corresponding use of CO_2 as a solvent nicely eliminates solvent-background signals.[104] In CE-NMR and CEC-NMR, the probes need to be able to handle high voltages,[101] which could otherwise perturb the NMR spectra.

2.6. Hyphenation/hypernation

Another set of developments that is critical to understanding this field is the whole area of hyphenated techniques. Hyphenation (or multiple hyphenation which is also known as "hypernation"[105]) involves adding on other analytical techniques, almost as if they were "building blocks". Fig. 5B shows a block diagram for LC-NMR, as compared with a simple HPLC system (Fig. 5A). By adding a UV detector (or diode array detector) inline, one can get the more useful (and typical) LC-UV-NMR configuration shown in Fig. 5C. Here the UV signal can be used to trigger NMR events – "stop on a peak", "time-slice through a peak", "don't stop", etc. By adding even more building blocks, such as a refractive-index detector and a mass spectrometer, one can construct a LC-UV-RI-NMR-MS system as shown in Fig. 5D. Any common HPLC detector (like radiochemical detectors or evaporative light scattering detectors or various kinds of mass spectrometry) can be hyphenated to the system. Output signals from these detectors are then routinely interfaced to the NMR to serve as trigger signals.

LC-NMR-MS, which was first described in 1995,[106] is an extremely powerful analytical tool. There are already many dozens of papers describing its use.[1] An application of the combination "LC-MS/MS-NMR-CD" was described in 2003.[107] Interestingly, even "LC-NMR-MS with (semi-)offline FTIR" was once described (in 1999).[108] All of this points to how useful it can be to incorporate ("hyphenate") different additional building blocks. DI-NMR and FIA-NMR (discussed below) were created in part by using that same concept, but now by removing building blocks from LC-NMR, instead of just adding them.

2.7. Various NMR experiments: different nuclei and pulse sequences

NMR is known for being flexible: a researcher can use any one of hundreds of known pulse sequences for extracting information out of a sample, or study different kinds of nuclei. LC-NMR shares that same flexibility. Most LC-NMR studies acquire only one-dimensional ^{1}H spectra (usually by using stop-flow methods). Other nuclei have been directly detected in LC-NMR, such as ^{13}C[36,37] and ^{19}F,[63,109] and a 1986 paper even described the direct detection of both ^{29}Si and ^{13}C data in the same recycled-flow-NMR study.[110] (It is interesting to note that a 1993 paper claimed to be the first to perform ^{19}F-detected LC-NMR,[111] whereas it had already been published before in at least 1984[63] and 1988.[109]) The low sensitivity of direct-detection ^{13}C-observe flow NMR can be greatly improved by using dynamic nuclear polarization (DNP).[112,113] Indirect-detection experiments are also commonly used in flow NMR; $^{1}H\{^{13}C\}$ is the most common,[84,114] but $^{1}H\{^{29}Si\}$ detection has also been reported.[115]

Two-dimensional techniques of all types are commonly used in flow NMR – when the sensitivity is high enough. For example, various two-dimensional J-resolved, homonuclear, and heteronuclear ($^{1}H\{^{13}C\}$) correlation experiments, and 1D-NMR at multiple temperatures, were used to analyze blood plasma in a 1995 study.[114]

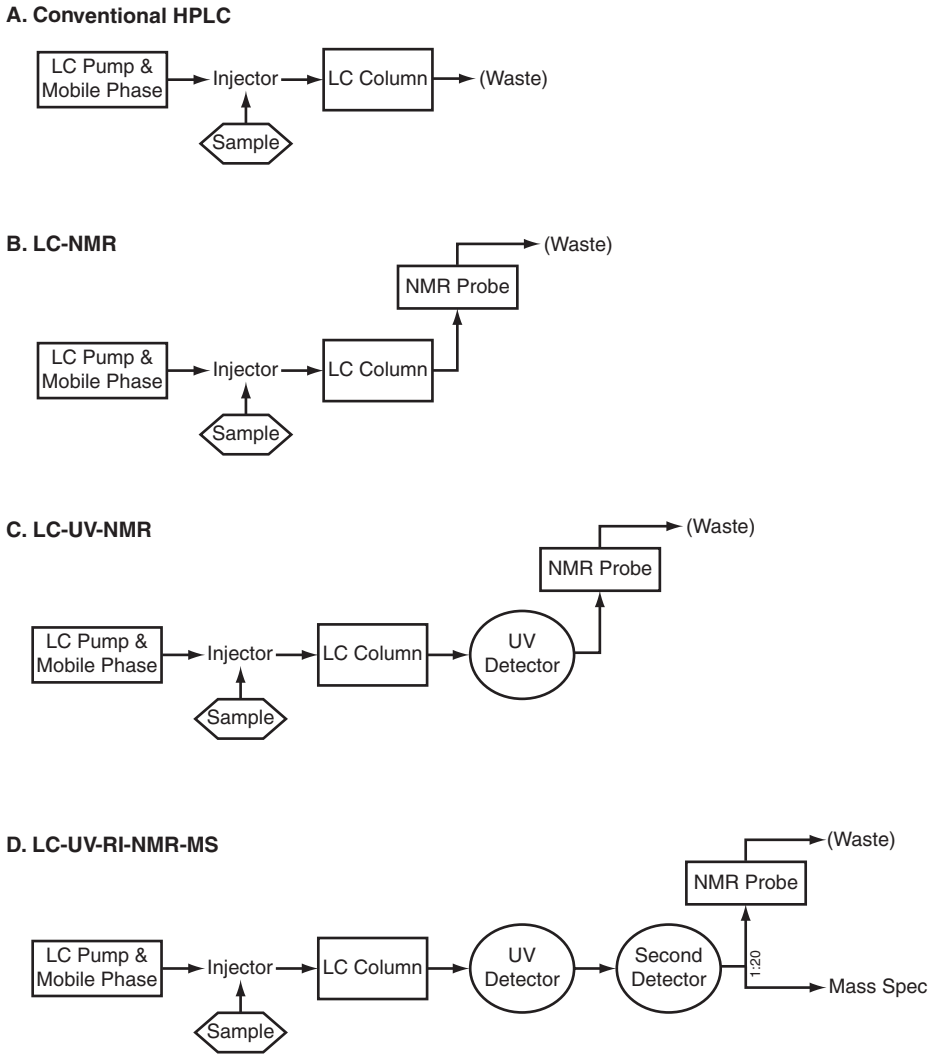

Fig. 5. Examples of increasing amounts of hyphenation/hypernation. Part A (top) is a block diagram of conventional HPLC. By adding an inline NMR probe to this, one generates an LC-NMR system (B). By further adding a UV detector of some sort, one generates the most common configuration: an LC-UV-NMR system (C), which is commonly referred to simply as an ''LC-NMR''. The most complete, expensive, and powerful configuration further adds both a mass spectrometer and an additional detector of some sort, such as a refractive index (RI) or evaporative light scattering (ELS) detector (D; bottom). In this figure, the ''second detector'' would be the RI detector. The effluent from the two detectors (in series) is then split and sent in uneven proportions to the MS and the NMR, often in 1 : 10–50 ratios. Overall, this illustrates how different analytical techniques can be built up by hyphenating different building blocks.

It would be particularly exciting if diffusion-ordered spectroscopy (DOSY) were ever combined with LC-NMR, but this has not yet been reported. It is interesting to note that EPR was used as a (non-contact) flow-EPR detector as early as 1983[116] – for the analysis of flowing coal.

3. NON-CHROMATOGRAPHIC FLOW NMR

In the previous section we saw how "building blocks" can be added to LC-NMR to make ever more sophisticated (and complex) analytical tools. In this section we will do something equally useful, but in a different way – we will simplify the systems by removing building blocks. This has created two new types of non-chromatographic flow NMR: FIA-NMR and DI-NMR. These methods can then be altered further by the addition of any of the building blocks (or modules, or variations) described in the previous section.

As high-resolution NMR spectroscopy becomes more automated, there is a growing need to move the samples to be analyzed in and out of the NMR probe faster and more reliably. For decades, mechanical robots have been used to move the traditional precision glass samples tubes in and out of the magnet under automation,[117] but users want even more speed and reliability, and preferably reduced cost as well.

3.1. Flow injection analysis NMR (FIA-NMR): columnless LC-NMR

One way to think about LC-NMR is to view it as simply a sample-changer for an NMR spectrometer. In LC-NMR you start with a mixture and let the LC step separate the compounds before they are passed into the NMR flow cell. Alternatively, if you want to analyze the samples intact (without separation), you can do the same thing, but without the chromatography column. If you remove the chromatography column and keep everything else intact (i.e., the pump, injector, mobile phase, [connective tubing] and probe, and maybe even the optional UV detector), a sample placed in the injector can be swept by the "mobile" phase into the NMR probe. Just like in stopped-flow LC-NMR, you can stop this plug of injected sample in the NMR probe. The pump can be triggered off (which stops the mobile phase, and hence the sample transport) either with a signal from the optional UV detector (just like in LC-NMR; where the pump is stopped after a calibrated delay once the UV detector registers a peak maximum) or by simply calibrating the delay time (from the injector port to the probe) as a function of the rate of solvent flow. Once the delay times are properly calibrated, the maximum concentration of the injected sample plug can be stopped reproducibly inside the NMR flow cell.

This concept was initially called "columnless LC-NMR", and later called "Flow Injection Analysis NMR" (FIA-NMR), and was first demonstrated in 1997 by Keifer and coworkers.[3,118–120] (Although a brief report on FIA-NMR published in 1987 has since been found.[121]) A typical delay time (from the injector port to the

probe) is only 10–20 sec, and this appeared to be a fast and easy way to automate the movement of samples in and out of an NMR probe – especially when one considers how many commercially available devices there are for loading injector ports (sample loops) into an HPLC system and automating the injection process. A diagram of the hardware is shown in Fig. 6B, which graphically illustrates how

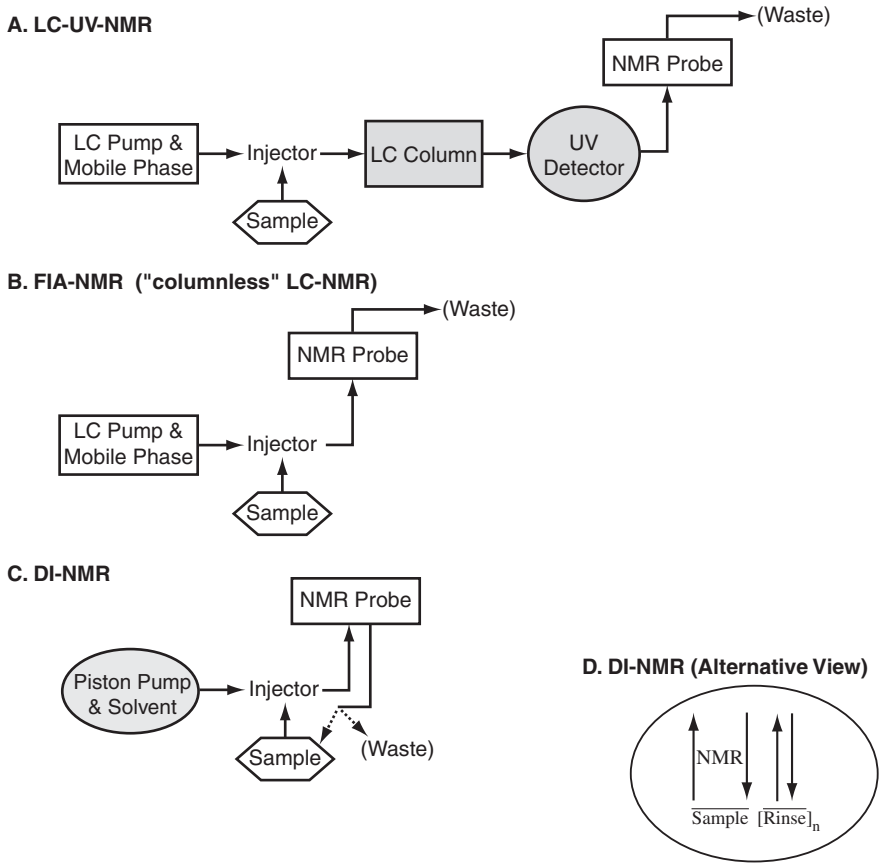

Fig. 6. Block diagrams of LC-NMR (A; top), FIA-NMR (B; middle), and DI-NMR (C; bottom), showing the progressive simplification of the fluidics of the systems. The hardware used for FIA-NMR (B) is very much like that used for LC-NMR (A), but with the removal of the LC-column and usually the UV detector (both shown in gray in A). In DI-NMR (C), although the block diagram makes it look like it is just a simplified version of FIA-NMR (which it is in concept), the hardware actually used – and the fluidics involved – are very different, as is described in the text. Part D is an alternative way to illustrate how the fluidics of DI-NMR are different from those of LC-NMR: in DI-NMR, the sample fluid is pushed into the NMR flow cell for the NMR measurement, then normally withdrawn the way it came in – then one or more rinse cycles repeat this in/out process. If the diameter of the NMR flow cell is the same as the attached capillary tubing, however, all solvents involved instead usually follow a unidirectional path through the NMR probe, more like in FIA-NMR.

the hardware used for FIA-NMR is a simplified version of the hardware used to perform LC-NMR.

A more detailed (complete) description of FIA-NMR was published in 2003.[5] FIA-NMR was shown to be especially useful for repetitive analyses. Sample volumes of 20–200 μL were injected, and the reproducibility of the analysis was shown to be quite good. (The relative standard deviation of the peak integrals was 1.38% for 15 duplicate injections; it was 0.38% for 15 repetitions of the same static sample left in the probe.) This study did not attempt to determine minimum-detectable sample sizes, but did show that 20 μg sample-injection sizes were easily detected in 1-min acquisitions. Data were acquired using a mobile phase of CH_3CN-D_2O (50 : 50) to transport the samples into the probe. WET solvent suppression[86] was used, which allowed non-deuterated acetonitrile to be used. This data,[5] as well as other more rigorous testing,[4] has shown that the "mobile phases" do not need to be deuterated when WET is used, although some users of capillary systems argue that the cost is minimal in those cases and the improved spectra justify the cost.

One goal for FIA-NMR was the ability to perform analyses rapidly (high throughput). There are three requirements that need to be taken into account to accomplish this. First, you need to be able to move the samples from the injector port into the NMR probe quickly. Second, you need good sensitivity from the NMR probe to allow the total NMR acquisition time to be short. And third, you need to be able to remove the sample from the probe quickly, and ideally rinse out all traces of the sample quickly (before the next sample is introduced).

This FIA-NMR system,[5,118,119] and others like it,[105,122,123] easily meet the second requirement by being able to detect 20 μg (injected) sample quantities.[5] One study, however, suggested that up to 140–840 μg of injected material might be needed more routinely, or in less favorable cases.[105] In contrast, when a capillary NMR flow probe (1–5 μL detection volume) is used for FIA-NMR instead of a "standard" flow probe (typically a 60 μL detection volume), the detection limits can be reduced significantly (easily to the range of 10 μg).[124]

The quality with which FIA-NMR meets the first requirement (moving the sample from the injector port into the NMR probe quickly) depends on the variables of the solvent flow.[5] For pumping speeds of 4.0 mL/min, the sample can be mechanically moved into the probe in 6–8 sec (depending on the length of the capillary transfer line); however, it then can take *ca.* 2 min for the NMR signal to fully stabilize, and even then the NMR peak heights are typically less reproducible. In contrast, for pumping speeds of 0.25 mL/min, the mechanical transfer takes much longer (*ca.* 1.5 min), and an additional stabilization time of *ca.* 1.5 min is needed (hence *ca.* 3 min total from injection to the start of acquisition), but the peak heights are then the most reproducible. Data from intermediate flow rates verify these trends: that the fastest flow rates (4.0 mL/min) allow you to start acquiring NMR data faster (even though the stabilization time is then the longest, the reduced pumping time more than makes up for that delay), but the slowest flow rates provide the most reproducible (quantitative) NMR data. If quantification is not needed, one could start the NMR acquisition earlier, but it still requires

1–2 min to transfer and stabilize the sample. This is still a big advantage over mechanical tube-based sample changers, however, which typically change samples slower than this, and they require additional time to then lock and shim the sample – activities which take no additional time in FIA-NMR (which is a big advantage).[5] We have noted that the time needed to stabilize an injected-plug sample in FIA-NMR appears to be longer than the stabilization time needed for an LC-NMR sample – this is presumably because an LC-NMR sample has a Gaussian distribution of concentration at the trailing and leading edges of the sample plug, whereas an injected plug sample has a more discontinuous interface with the mobile phase.

The third requirement (you need to remove the sample from the probe quickly) is the most variable parameter in FIA-NMR. It depends in part on how much carryover from sample-to-sample can be tolerated. (Note that the carryover in a mechanical tube-based sample changer is absolutely 0%.) To achieve $<0.1\%$ carryover, we found it took 0.5 min at a flow rate of 4.0 mL/min (2 mL total solvent consumed), and 4.0 min at 0.25 mL/min (1 mL total solvent consumed). Although flushout is faster at 4.0 mL/min, flushing at 0.25 mL/min uses less solvent (which may be more important if a deuterated mobile phase is used – to avoid NMR solvent suppression).[5]

There are a few other reports on the use of "flow injection NMR",[125–127] all of which have occurred since the original report in 1997.[118] These applications, however, use what is described here more properly as DI-NMR (see below).

3.2. Direct injection NMR (DI-NMR)

One could say that DI-NMR(Fig. 6C) is conceptually just a simplified version of FIA-NMR (Fig. 6B); however, in practice the two systems are mechanically very different. In DI-NMR, the pump is simplified, and the mobile phase is removed (as are all optional detectors), to give the simplest possible flow-NMR system. DI-NMR injects the sample directly into the NMR flow probe, and the whole injection process is then driven by automation. (You could essentially say that the NMR flow probe is just a sample loop for the injector port of an automated injector.) There is no mobile phase – just the solvent the sample is dissolved in – although an additional batch of solvent is used to either rinse the NMR flow probe (flow cell) and transfer lines, or to hydraulically push the sample into the flow cell, or (typically) both.

The first demonstrations of DI-NMR were published starting in 1997 by Keifer and coworkers,[3,118–120] where the technique was compared – and contrasted with – FIA-NMR. This was followed by a full description and evaluation of the technique in 2000.[4] The original impetus to develop DI-NMR was the desire to do automated NMR faster and better. Experience with LC-NMR and FIA-NMR had shown us that flow NMR had several potential speed and simplicity advantages over traditional tube-based automation. First, in flow NMR, no additional time was needed to lock or shim each sample (assuming the solvent composition was kept constant). Second, deuterated solvents were not required, both because of WET solvent suppression, and because there was no real reason to bother locking the sample (due to

Scout-Scan[4] frequency registration). And third, more samples were being either stored or synthesized in microtiter plates, and automated liquid handlers could inject aliquots from those microtiter plates into standard injector ports. This also eliminated the breakage of glass sample tubes.

The original application that pushed the development of DI-NMR was the analysis of combinatorial-chemistry libraries. (In part because the author was involved in combinatorial chemistry at the time, due to his prior development of HR-MAS for the NMR analysis of resin-bound samples.[128]) Combinatorial chemistry provided an ideal justification (and proving ground) for DI-NMR because you often had thousands of samples in a library, all dissolved in similar concentrations, normally in a common (uniform) solvent, all stored in microtiter plates – all of which needed a simple ^{1}H-NMR spectrum to either help confirm a probably known structure or to verify purity. You wanted the spectrum fast, at a low cost, and you wanted to repeat the same NMR experiment thousands of time in a row with minimal human intervention. DI-NMR was designed to do just that.

The seminal DI-NMR paper[4] analyzed combinatorial-chemistry samples stored in (septum covered) 96-well microtiter plates, all dissolved in either DMSO-d_6 or DMSO-h_6, at a concentration of either 25 or 2.5 mM. The volume of injected sample solution was 350 μL. A Gilson 215 liquids handler was interfaced to the NMR spectrometer, and, under NMR control, one sample was withdrawn from a well in the microtiter plate and injected, via an injector port and a transfer line, into the NMR flow cell (in the probe in the magnet) using the syringe pump on the Gilson 215. The Gilson then triggered the NMR to acquire an NMR spectrum (a 32-scan 1-min acquisition in this case). When the NMR acquisition was complete, the NMR sent a signal back to the liquids handler, which withdrew the sample (with assist from a synchronized source of air backpressure) and returned it to the original well of the microtiter plate (or another location of the user's choice). The syringe pump then was used to rinse the NMR flow cell by a similar "out-and-back" motion with an aliquot of clean solvent.

The original paper also shows that the data acquired on samples dissolved in DMSO-h_6 can be almost as good as the data acquired on the samples dissolved in DMSO-d_6 (the reader can judge; see Fig. 7). It also shows a number of ways to display and analyze the NMR data acquired on a library of compounds stored in a 96-well plate (one way is shown in Fig. 8). There is also a discussion of the various possible ways to get quality-control information for the fluidic injection process, by using either the Scout-Scan data or signals from an internal standard (Fig. 9).[4]

DI-NMR differs from both LC-NMR and FIA-NMR in that the flow cell is empty of solvent when the sample is injected. This allows the DI-NMR user to acquire the highest possible sensitivity on the sample and also allows the sample to be recovered in an unaltered (undiluted) state. This does, however, require the DI-NMR user to inject at least a certain minimum sample volume in order to acquire an acceptable NMR spectrum. (This minimum sample volume is *ca.* 150 μL for standard "60-microliter observe volume" flow cells, but it can be as low as 2 μL for a "0.5-microliter observe volume capillary flow cell"[129] discussed below.) If this minimum volume (which depends on the volume of the flow cell) is not met, the

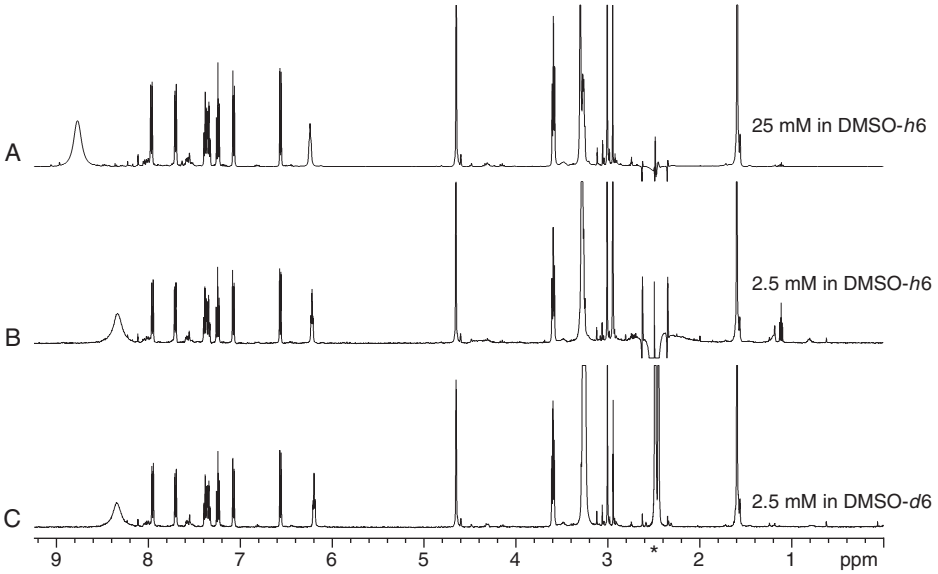

Fig. 7. This figure shows that data acquired on samples dissolved in DMSO-h_6 have the potential to be almost as good as the data acquired on the samples dissolved in DMSO-d_6. Shown are 32-scan (1 min) ^{1}H NMR spectra acquired on a compound dissolved in 25 mM DMSO-h_6 (top; A), 2.5 mM DMSO-h_6 (middle; B), and 2.5 mM DMSO-d_6 (bottom; C). The spectra acquired on samples dissolved in DMSO-h_6 (A and B) were acquired with WET solvent suppression of both the DMSO central resonance and its ^{13}C satellites, and processed with a single-frequency DSP notch filter. The chemical shift of these resonances (2.5 ppm) is marked with a "*" in the chemical shift scale. Other than a 10-fold reduced vertical scale for A, all data acquisition, processing, and display parameters were identical for these three spectra.

flow cell will contain air, which will ruin the NMR lineshape (and because there is no solvent mixing in DI-NMR, the volume difference cannot be made up with a "push" solvent). This different fluid behavior of DI-NMR as compared with FIA-NMR influences many performance aspects of the analysis, such as carryover, detection efficiency, recovery efficiency, and speed. The biggest disadvantage of DI-NMR (which is addressed by FIA-NMR) is the possibility that the tubing in the system could become clogged with particulate matter if unfiltered samples are injected.

3.2.1. *Applications of DI-NMR*

After the original description of DI-NMR (and the commercialization of the technique by both Varian and Bruker as VAST and BEST, respectively), there followed numerous papers that used DI-NMR as a tool. Most of these applications fall into one of three general categories, all of which utilize repetitive analyses. (One-dimensional ^{1}H spectra were always acquired unless noted otherwise below.) The first category (described above) is the analysis of libraries of relatively pure

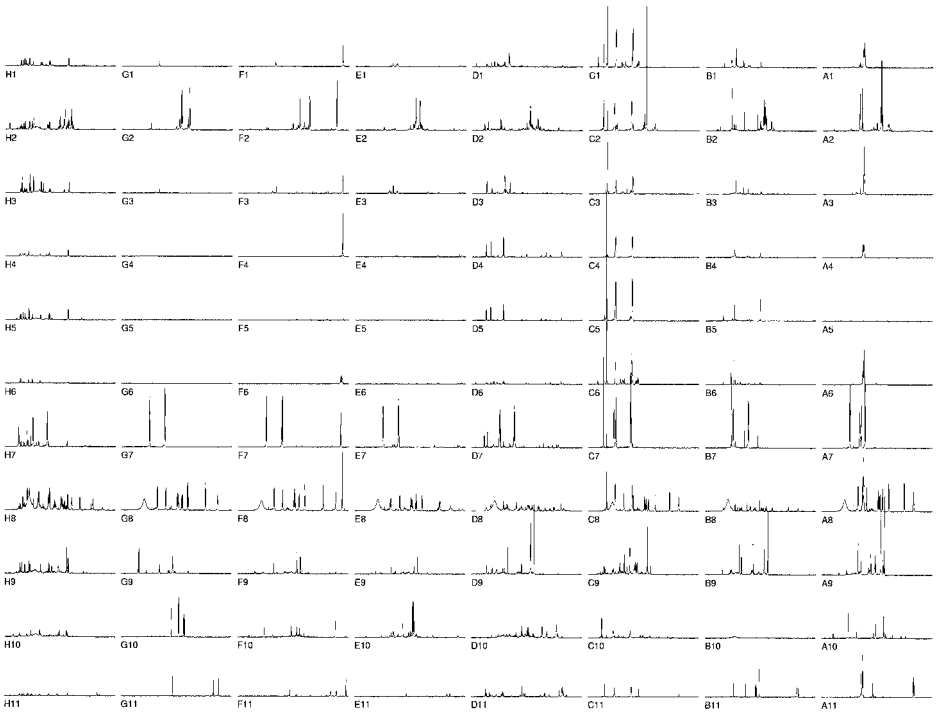

Fig. 8. One way (out of several) to present DI-NMR data – specifically data that were acquired on a library of compounds stored in a 96-well plate. Here, the spectra are presented with the same graphical layout as the compounds are stored in the plate. This allows the user to easily see relationships along rows or columns, which is a particularly useful ability when analyzing combinatorial libraries (as opposed to random libraries). These data were acquired by using DI-NMR on samples dissolved (2.5 mM) in DMSO-h_6, and show the 5.8–9 ppm region. All data acquisition and processing parameters were identical for each spectrum.

(normally organic) compounds. The second category is the analysis of biofluids (urine, plasma, etc.) – an application that ultimately leads to the analysis of samples for clinical diagnoses. The third category is the study of biomolecules; most commonly to use $^{1}H\{^{15}N\}$ HSQC to analyze combinations of ligands and ^{15}N-labeled receptors (proteins) to either study binding properties or to screen ligands for binding affinities. Some of the heaviest users of DI-NMR are located in private industry (typically the pharmaceutical industry) and so the resulting data are often not published much; hence the publication record for DI-NMR is not necessarily an accurate measure of its popularity.

Spraul *et al.*[130] used DI-NMR to screen rat urine. Gmeiner *et al.*[131] used DI-NMR to study ligand binding to a biomolecule. Hamper *et al.*[132] used DI-NMR to analyze a combinatorial-chemistry library. Additional demonstrations of the utility of DI-NMR to analyze libraries were published by Combs *et al.*,[133] Lewis *et al.*,[134]

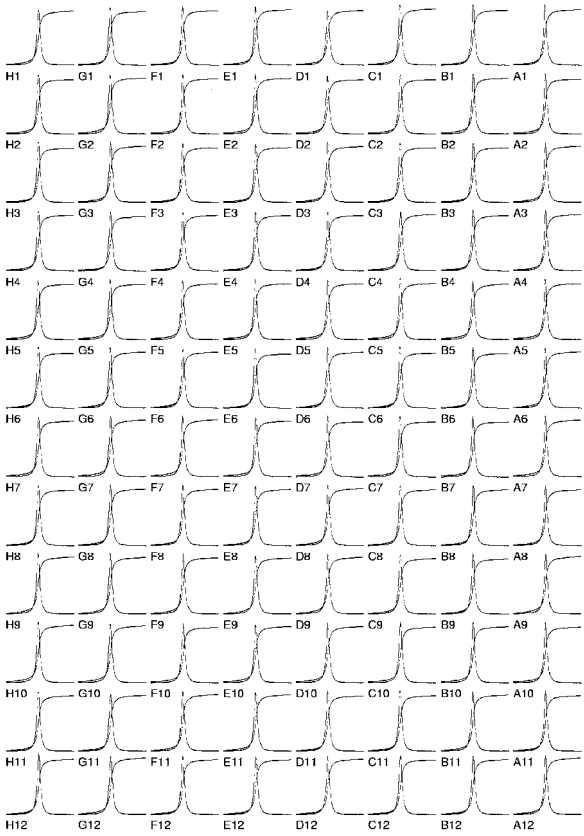

Fig. 9. In flow NMR, it is advantageous to have some way to monitor the success (or "quality") of each sample injection. One way to obtain this kind of quality-control information in DI-NMR is to monitor either the lineshape, or the integral, or both, of an internal standard. This figure shows one way to display both the lineshape and the integral of an internal standard contained in each injected sample of an 8×12 matrix of samples (in a 96-well plate). This kind of information can be displayed either graphically (shown) or numerically (not shown). It is very practical to use the NMR spectral lineshape as a measure of the "quality of injection" in flow NMR (more so than in tube-based NMR), because any type of bubble in the active region of the flow cell (or an under-filled flow cell) will easily be detected by its degraded lineshape.

Eldridge *et al.* (for a natural product library),[135] Kalelkar *et al.*,[136] Leo *et al.*,[137] Kautz *et al.*,[129] and Pierens *et al.* (natural product library).[138] Additional publications on the use of DI-NMR for the analysis of biomolecules and the screening of binding were published by Stockman *et al.*,[127,139] Ross *et al.*,[140] and Tisne *et al.*[126]

Additional demonstrations of the use of DI-NMR to study biofluids have been published by Robertson *et al.*[141] and Potts *et al.*[142] (all on urine), although several companies, like Liposcience (www.Liposcience.com), are using DI-NMR to commercially analyze biofluids (often plasma). DI-NMR has also been recently used to analyze olive oils,[143] various other food oils,[144] and beer.[125] The summary of all of this work is that DI-NMR has proven to be useful as an NMR automatic sample changer in a wide variety of applications.

3.3. Comparisons

FIA-NMR and DI-NMR have both proven to be useful, but they have different strengths and weakness; both as compared with each other, and as compared with other flow-NMR techniques like LC-NMR. For example, LC-NMR is appropriate whenever chromatographic separations are needed, but it tends to be time consuming. DI-NMR is appropriate if maximum sensitivity is required, or if the sample needs to be recovered, or if there is a sufficient sample volume, and if the sample contains no sediment. FIA-NMR is more appropriate if carryover needs to minimized faster, or if the sample does not need to be recovered intact, and if a wider range of smaller sample volumes must be analyzed. Clearly, each technique has its own set of advantages and disadvantages, and all three techniques are useful for different applications.

4. NEW TECHNOLOGIES TO FACILITATE FLOW NMR

Starting with LC-NMR, FIA-NMR, and DI-NMR as the three seminal techniques, researchers have since developed variations upon these methods. These variations are all being covered in this (different) section because they all required the development of some type of new hardware. The hardware developments fall into one of two groups: variations in the plumbing scheme or variations in the flow probe.

4.1. Plumbing variations: loop collectors

A typical HPLC detector is a real-time device: the data are generated instantaneously (on-the-fly) as the mobile phase flows through the detector cell. Likewise, in LC-NMR, the NMR detector can also operate in real time – but only if the analysis is performed in an on-flow mode. If the LC-NMR analysis is performed in a stopped-flow mode, however, the data is not generated on-the-fly (NMR data is only acquired when the LC pump is idle, and the LC pump only runs when the NMR spectrometer is idle). This ''non-real-time'' nature of stopped-flow LC-NMR has been further expanded upon by the development of loop collectors.

Loop collectors allow LC-NMR to be run in a more time- and equipment-efficient manner. They allow the user to separate the LC and NMR functions in both time and space. In a loop collector, the HPLC performs the chromatographic

separation, and analyzes the separation with a typical LC detector, but instead of sending the used effluent to waste (or perhaps to an open air fraction collector), selected portions of the effluent (downstream from the detector) are trapped and stored in sections of in-line capillary tubing (''loops'') by using a coordinated system of valves. At a later time, these valves can be triggered in a way that causes the mobile phase to flush (and push) the contents of a given loop into an NMR flow cell (usually by backflushing); then the valves can trigger again (diverting the mobile phase elsewhere) so that the loop's contents remain in the NMR probe. The HPLC pump can then be shut off, which allows the fraction that came from the loop collector to remain in the NMR probe indefinitely if desired.

The loops can be designed to store aliquots of any desired size. (Although the inside diameter of the tubing is typically fixed, the tubing can be cut to any length to achieve the desired volume.) The loop-collector system can also be designed to contain any number of loops – by using multi-port rotary valves. The loops and valves are located downstream from the LC detector, so that the LC-detector signal can be used as a trigger to activate the valves. Once the user has calibrated the lag time between the LC-detector and the loop-collector valves (which is flow-rate dependent), the system can be programmed to automatically trap multiple chromatographic peaks in the loops, all under computer control (based upon the LC-detector's signal output).

A loop collector is essentially a fraction collector, although unlike typical fraction collectors, the fractions are trapped in a pressurized loop, in a dark and anaerobic environment. The plumbing is configured so that each loop's contents can be pumped into the NMR flow cell (using the LC pump) at any user-controllable time (in ideally any order; after the chromatographic separation is finished). This means that when the loop-collector technique is used, the LC separation and the NMR analysis are always separated temporally. Spatially they may or may not be separate (the operator can set it up either way). A typical loop collector is designed so that the loops can either be integrated spatially into the LC-NMR system (Fig. 10A), or they can be removed as a unit (as a ''cartridge'' of loops) and moved to another

Fig. 10. Block diagrams of the LC-NMR variations that use loop collectors or solid-phase-extraction (SPE) cartridges. Part A (top) shows an integrated LC-Loop Collector-NMR system. The Loop Collector (valve ''c'') is plumbed in with multiple computer-controlled valves (valves ''a'' and ''d'') that can control the flow paths of the fluid, sending it either into any of the various loops, directly to the NMR flow cell, or to waste. Additionally, this valving system is designed to let the user flush the contents of any loop to either the NMR flow cell or to waste. (For simplicity, this figure shows only four loops; typically a system will have more loops and the volume of each loop can be customized.) Parts B1 and B2 (middle) together show the offline use of a loop-collector cartridge. The loop cartridge is first filled by using an offline LC system (B1; no NMR is involved in this step) and then the loop cartridge (typically valve ''c'' alone) is moved to a flow NMR system (B2), where its contents are analyzed one loop at a time. Part C shows how SPE cartridges can be added to a loop-collector style system; this requires some additional fluid pumping capability and some additional valves (valve ''b'' in the figure).

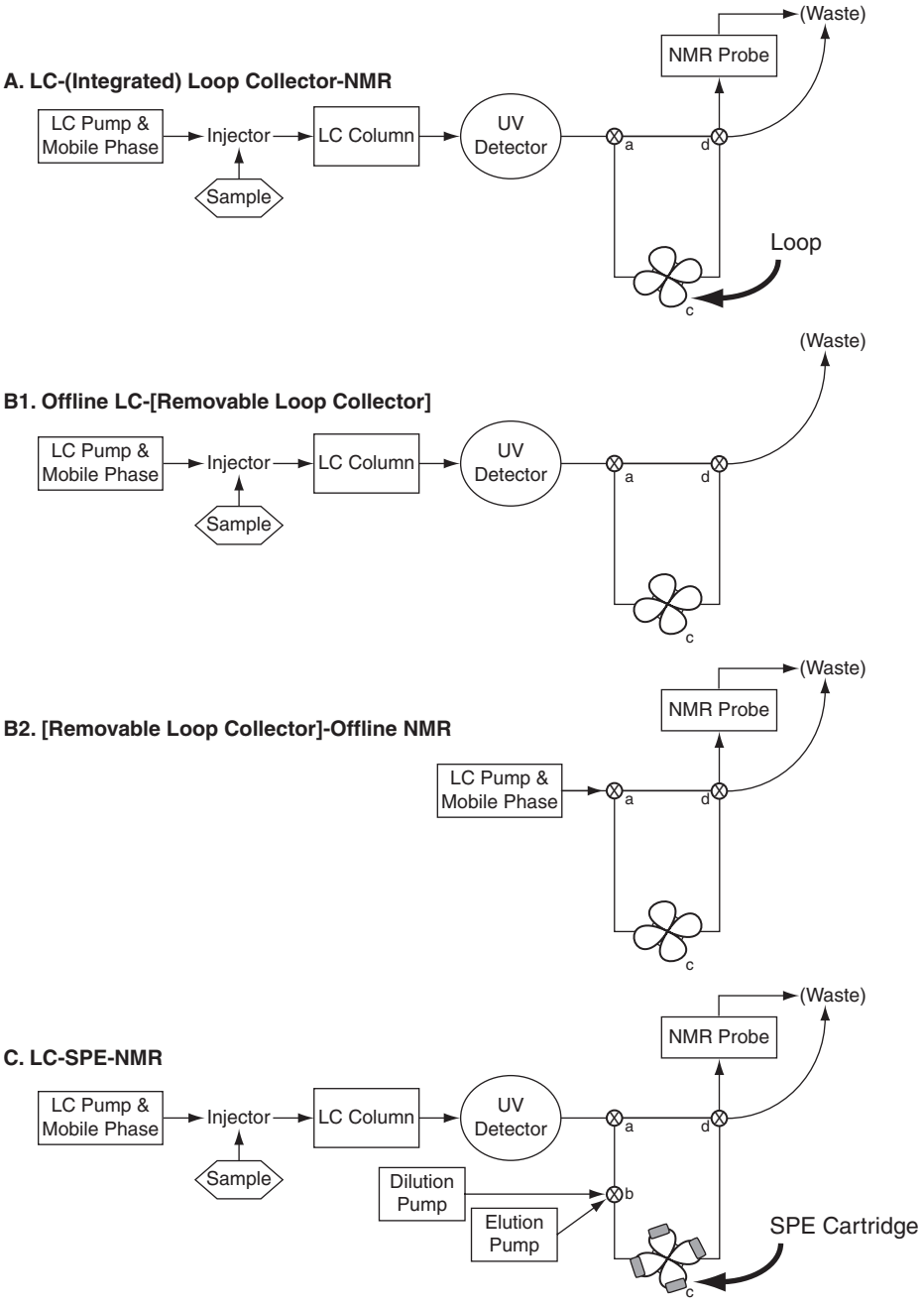
A. LC-(Integrated) Loop Collector-NMR
LC Pump & Mobile Phase
Injector
Sample
LC Column
UV Detector
NMR Probe
(Waste)
a
d
c
Loop
B1. Offline LC-[Removable Loop Collector]
LC Pump & Mobile Phase
Injector
Sample
LC Column
UV Detector
(Waste)
a
d
c
B2. [Removable Loop Collector]-Offline NMR
LC Pump & Mobile Phase
NMR Probe
(Waste)
a
d
c
C. LC-SPE-NMR
LC Pump & Mobile Phase
Injector
Sample
LC Column
UV Detector
NMR Probe
(Waste)
a
d
Dilution Pump
Elution Pump
b
c
SPE Cartridge

remote valve setup if desired. This allows the user to fill the loops at one time or place on a HPLC system (Fig. 10B1), and then disconnect the loop cartridge and move it to the loop-analysis (NMR) system, (which consists of just an LC pump, the valves, the loop cartridge, and the NMR probe; Fig. 10B2), where the loops can be subsequently analyzed by NMR.

Loop collectors are particularly useful when the NMR analyses will take a long time. They allow the user to analyze the contents of each loop at their leisure, and under complete user control, with no fear of diffusion or broadening of the chromatographic peaks. Loop-collector LC-NMR does not replace on-flow LC-NMR, but it is a useful alternative.[145] Loop collectors are discussed here because, if you ignore the chromatographic loop-filling step (Fig. 10B1), which can happen at any time or place (just like any HPLC sample cleanup) the ''NMR analysis of the contents of a loop'' shown in Fig. 10B2 is a form of ''non-chromatographic flow-NMR spectroscopy''. The analysis of the loop's contents can be thought of as being almost the same thing as FIA-NMR. Fig. 10B2 differs from FIA-NMR only in the replacement of an injector port with one loop (as is used in FIA-NMR) with a more complex valving system attached to a cluster of loops (as is used in loop analysis).

The disadvantage of loop-collector LC-NMR is that, if the solvent composition of any loop is significantly different from that of the mobile phase (the solvent coming from the pump that pushes the loop's contents into the NMR probe), you will need to address the magnetic-susceptibility mismatches between the two solvent mixtures – or else your NMR lineshapes will be broad and unshimmable. This can be done in one of three ways. First, you can make the loop volume either much bigger, or much smaller, than the volume of the NMR flow cell. (If the loop's volume is much bigger than the NMR flow cell, then the solvent in the loop will displace the mobile phase from the NMR flow cell. Conversely, if the loop volume is much smaller than the NMR flow cell, then the sample in the loop will ultimately mix with the mobile phase in the NMR flow cell.) Second, you can program the HPLC pump to successively produce mobile phases that match the solvent composition of each loop as it is pumped in. (This is harder than it sounds, because the composition of the mobile phase at the outlet of the LC column is never rigorously known.) Third, you can find a way to remove the solvent in the loop from the solute being analyzed. This third concept is what drove the development of the SPE technique – which is described in the next section.

4.2. Plumbing variations: SPE-NMR (column trapping)

Solid-Phase-Extraction-LC-NMR (SPE-LC-NMR, or SPE-NMR for short; also known as ''column trapping'' or ''peak trapping''), can be thought of as a loop-collector system where each loop is essentially replaced by a SPE cartridge. The analyte is trapped on the SPE cartridge as it elutes from the main HPLC column, and then eluted later, under control of the user. In practice, trapping on the SPE cartridge is often ensured by adding water to the mobile phase post LC-column (making it a weaker eluting solvent; assuming reversed-phase HPLC; see Fig. 10C

for placement). The analyte is then eluted from the SPE cartridge in a separate step by using a stronger solvent. Sometimes this eluting solvent is even deuterated (using CD_3CN or CD_3OD), so as to minimize the need to use solvent-suppression sequences during the NMR data collection and to produce cleaner NMR spectra.

The hardware for SPE-NMR (Fig. 10C) starts with a loop-collector-style setup (Fig. 10A) and add a few pieces. First, each loop in the loop-collector cartridge has an SPE cartridge spliced into the middle of the loop's tubing. Second, a makeup pump is normally added – to add water to the mobile phase (post LC-column). Third, the system may be plumbed so that a separate pump is used to pump the (stronger; possibly deuterated) solvent that elutes the analytes from the SPE cartridges. In any case, the solvent that finally ends up in the NMR probe must always have a uniform magnetic susceptibility (typically by being well mixed), or else the NMR lineshapes will be degraded (broad) – and this is often hard to accomplish when one elutes the effectively ''unrinsed'' SPE cartridges. The advantage of the method, however, is that the analyte normally reaches the NMR flow cell as a more concentrated ''plug'' (especially for broad chromatographic peaks), which produces better NMR spectra in considerably less time.

The idea of SPE-NMR was first demonstrated by Griffiths and Horton,[6] and then Brinkman,[146] in 1998. Since 2001, there have been numerous reports on the use of SPE-NMR.[80,147–157] Some users have pointed out that multiple (repeated) injections can be trapped on a given SPE cartridge before the analyte is eluted; the resulting concentration of analyte is useful for low-concentration analytes and for acquiring heteronuclear NMR spectra.[148,151] Other users have recovered samples from the NMR probe (at the end of the analysis) by blowing it out with gas.[80] It has also been shown that SPE-NMR provides the biggest benefits for chromatographic peaks with long retention times (which are broadest).[153]

One major advantage of SPE-NMR is that it allows the chromatographic step to be performed separately from the NMR analysis – much like in loop-collector LC-NMR.[153] If you take the liberty of regarding a loop-collector loop or an SPE cartridge as simply a sample ''storage container'' (like an NMR sample tube), one could then consider the resulting elution step of SPE-NMR as just another form of ''non-chromatographic flow NMR'' (especially if the SPE cartridges are loaded up at another time, and on another LC system).

4.3. Probes: flow probe optimization

To achieve the maximum NMR signal-to-noise when using an NMR flow cell (Fig. 2A), it is necessary to have the incoming fluid actually displace the fluid previously located in the active volume, rather then simply mix with it. This happens naturally inside straight capillary tubing, but NMR flow cells were initially larger-volume cavities connected to capillary tubing.[19,61,71,72,78,158] (The larger-volume flow cells were needed to improve the signal-to-noise of the NMR spectra.) There has always been a lot of concern about how to design the flow cell so that the incoming solvent smoothly displaces the existing solvent.[158] This is usually

accomplished by having the capillary tubing connect to the active volume of the flow cell (the detected region) via gradually widening connections (Fig. 2A)[159] – which causes the total volume of the flow cell to often be twice as big as the active volume. (Hence a standard 60 μL active-volume flow cell has a total volume of ~120 μL.) There is also a need for the flow cell to naturally flush out any air bubbles, which happens by placing the inlet on the bottom and the outlet on the top. A modern flow probe is also expected to have optimal ^{1}H lineshape, sensitivity, radiofrequency (RF) homogeneity, and heat transfer characteristics, especially when it is used for NMR sequences like HSQC, which contain numerous pulses and heteronuclear decoupling.[160]

In addition, to obtain the optimum NMR signal-to-noise on an analyte within a chromatographic peak, the volume of the NMR flow cell must be matched to the liquid volume of the chromatographic peak. If the volume of the NMR flow cell is vastly smaller or vastly larger than the volume of the chromatographic peak, you will analyze either just a fraction of the peak or dilute the peak, respectively. Optimization is complicated by the fact that the volume of a chromatographic peak is greatly influenced by its retention time (the more a peak is chromatographically retained, the larger its elution volume will be), as well as by the size of the chromatography column being used.

A "standard" NMR flow cell – designed for LC-NMR with 4.6 mm diameter chromatography columns and for most DI-NMR and FIA-NMR applications – has an active volume that is normally ~60 μL (120 μL total volume). Flow cells that are designed for DI-NMR applications that acquire $^{1}H\{^{15}N\}$-HSQC spectra normally have larger (*ca.* 120 μL) active volumes.[160] Flow cells that are designed for CapLC-NMR (which uses capillary chromatography columns) have smaller active volumes, ranging from 30 μL down to as small as 5 nL.[96,98,100,101,161,162]

4.4. Probes: capillary flow probes

The development of the smallest-volume NMR flow cells has led to the development of new methodologies for building NMR probes. Although it is easy to simply run the capillary tube through an NMR probe and build an RF coil around it, it is much harder to also obtain good sensitivity and especially good NMR resolution and lineshape. Much of the work on the smallest rf coils and smallest flow cells has been done by the extended group at Magnetic Resonance Microsensors (MRM; now part of Protasis) and Sweedler and coworkers at the University of Illinois.[96,163–170] They have shown how to produce the smallest capillary microcoils (as solenoids wrapped around the capillary tubing; see Fig. 11B), and how to deal with the magnetic-susceptibility-mismatch problems generated by the resulting coils, tubing, and probe.

Much of the initial applications development on microcoil probes was done on custom-made prototype probes.[96,99,163,168,171] More recently a line of capillary NMR probes has become commercially available from Protasis/MRM (www.protasis.com). These probes are now called CapNMR probes or CapLC microflow probes and

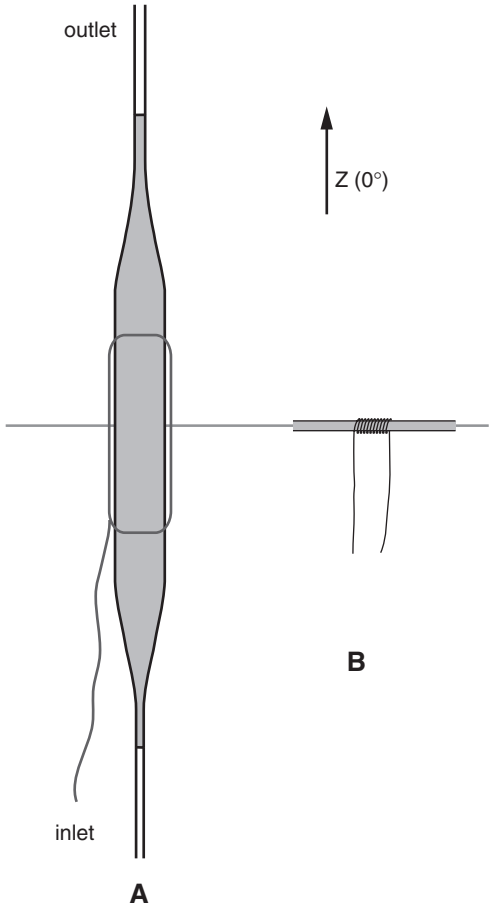

Fig. 11. Graphical illustrations of the size and orientation of an MRM microcoil (B; on the right)) as compared with a conventional flow probe (A; on the left). The relative sizes are drawn approximately to scale (a 0.9 mm ID capillary is shown here). Note that solenoidal coils, which microcoils typically use, need to have their axis in the XY plane; as compared with Helmholtz coils (left), which have their axis aligned along the Z axis.

have flow-cell volumes of typically 1.5, 5, or 10 μL (although other sizes are available). They have been used for a wide variety of small-volume flow applications. The original impetus for designing these probes was to provide NMR detection for capillary-chromatography techniques,[172] such as CapLC-NMR,[152,168,173–176] CE-NMR,[96,166,177] capillary isotachophoresis NMR (cITP-NMR),[178–184] and CEC-NMR.[101,185–188] The advantages reported are a gain in sensitivity, and the ability to use entirely deuterated solvents (hence no NMR solvent suppression is needed), but users have also reported that peak trapping in the NMR flow cell can be unreliable.[176] There are multiple nice reviews of these capillary techniques hyphenated to NMR.[76,159,162,189]

Initially, capillary flow probes were loaded manually (with the user using a syringe to load the sample into the probe).[164,165,171,190–195] More recently, CapNMR probes have been combined with Gilson or other automated liquid handlers to create microscale automated DI-NMR.[129,170,196] (Protasis/MRM now sells commercially available systems optimized for this application; sample volumes are typically 1–10 μL.[197]) Eldridge and coworkers used a syringe pump to load 3 μL samples dissolved in CD_3OD.[135,198] (The use of a syringe pump to help load the flow cell has been referred to as "manual-assisted" – in contrast to a fully manual loading of the flow cell.[170]) Geierstanger and coworkers injected 5 μL samples from 384-well plates into a 400 MHz CapNMR probe under full automation, and acquired 1D and 2D COSY data.[196] Most of their samples were run in DMSO-d_6, but some spectra were acquired on samples dissolved in DMSO-h_6 using WET suppression of both the DMSO and the water resonances. Kautz and coworkers used a Varian DI-NMR system (VAST) and a Protasis sample loader to automatically inject 2 μL samples (in DMSO-d_6) from a 96-well microtiter plate into a 0.5 μL home-built NMR flow cell.[129] By using a semi-continuous train of sample plugs separated by immiscible carrier fluid (discussed below), they nicely demonstrated that it is possible to use automated high-throughput NMR to analyze very small injected volumes; however, a system to perform this has not yet been commercialized.

As a nice complement to the microscale DI-NMR work, Bailey and Marshall[124] demonstrated microscale FIA-NMR by using a CapNMR flow probe and an HTS PAL autosampler to automatically acquire NMR data on 2 μL samples dissolved in CD_3CN located in a 96-well microtiter plate. To explore the limitations of the technique, Lacey *et al.*[168] performed microscale FIA-NMR to understand how injected sample plugs of differing solvent compositions can affect NMR spectral resolution.

Microcoil probes are also proving useful in biomolecular NMR. The short RF pulse widths typical of these small coils provide very wideband excitation (with minimal sample heating). Edison and coworkers used an NMR probe with a 15 μL flow cell to acquire triple-resonance data on proteins dissolved in H_2O.[199] Peti and coworkers[193] later also took advantage of the short pulse widths to run an experiment on a protein in a new way.

Other groups have also been involved in designing capillary NMR flow probes. Albert and coworkers [99,101] have certainly been very active in this area.

4.5. Probes: multiplex probes

Once it was proven that microcoil NMR flow probes with capillary flow cells were a viable product, efforts were made to use them in a parallel fashion to enhance the throughput of the NMR analysis. This is done by placing multiple rf coils within one NMR probe, to produce what is sometimes called a "multiplex probe" (or the technique can be called "multiplex NMR"). Most of this work has been done by the Raftery group at Purdue University[200–206] and the Sweedler group at the University of Illinois,[169,207–210] both starting in 1999. The initial investigations used samples in

sealed glass tubes,[200] but flow-through cells were implemented soon thereafter.[201,207] The literature describes several different approaches to constructing the hardware, as well as different approaches to acquiring the NMR data,[211] but the overall unifying concept is similar in all cases. The unifying concept is to ideally acquire data for the multiple samples simultaneously; or to at least move the second sample into place while you are acquiring data on the first sample. The record currently appears to belong to Webb and coworkers, who used a probe with eight identical solenoidal microcoils (and a Varian NMR spectrometer with four receivers and switches) to acquire NMR spectra from eight different chemical solutions in the time normally required for one.[212] In addition to simply increasing NMR throughput, there are other more unique applications of multiplex NMR – to implement novel solvent-suppression methods, to facilitate electrophoretic techniques,[180,181] and to follow reaction kinetics – and the reader can find details on all of these applications elsewhere.[213] The concept of multiplex NMR offers a lot of potential for high-throughput NMR, and the initial data is tantalizing, but as yet no product using these concepts has been made commercially available.

4.6. Probes: cold probes/cryoprobes

It has been known for some time that if the electronics of the NMR probe are cooled down, the signal-to-noise of the resulting NMR spectra increase severalfold.[214] The first implementations of this (for solution-state samples), which cooled the NMR probe down to 25 K to gain *ca.* fourfold increases in sensitivity, were done with conventional tube-based probes (not flow probes).[30,215] Recently, flow probes that are cryogenic have also now become available and (as expected) are proving useful for their increased sensitivity.[216] Exarchou and coworkers[148] used a cryogenic flow probe to study natural products, while Spraul and coworkers[217] used a cryogenic flow probe to study acetominophen metabolites. Spraul and coworkers also interfaced a cryogenic flow probe with an SPE system, which they compared with loop-collection with a non-cryogenic flow probe.[218] In general, a cryogenic probe will typically be able to acquire NMR data faster, so – because most flow-NMR techniques either struggle with NMR sensitivity or are being used in a high-throughput analysis technique – the author expects many flow-probe users to soon use cryogenic probes. Flow-cell contamination can be a problem in flow NMR (see below), so these probes will probably need to have flow cells that can be replaced while the cold probe remains in the magnet. (This capability is commercially available.)

To summarize this section, many developments have been made lately that make flow NMR more flexible and more useful. Flow probes have been refined to have better fluidics, better temperature control, a much wider range of sample-cell sizes, and substantially better sensitivity. New capillary separation techniques can now be supported, and mutiplex NMR allows solution-state NMR to be truly parallel for the first time. All of these developments will make flow NMR more popular, to more people, for more applications.

5. VARIATIONS OF THE FLOW TECHNIQUES/FLUIDICS

Even though FIA-NMR is a relatively new technique (first published in 1997[118]), the field of FIA itself is much older, larger, and well established. The first FIA applications were published in the mid 1970s;[219] the field has blossomed since then and is now documented in numerous books[220–223] and on its own dedicated web site (www.flowinjection.com; also www.globalfia.com). FIA also overlaps heavily with continuous-flow analysis (CFA) methods.[224] (Note: the terminology used in this paper has been guided heavily by the broad field of FIA, which has caused some of the "FIA-NMR" techniques cited here to be "re-described" with these more widely accepted definitions and terminology.)

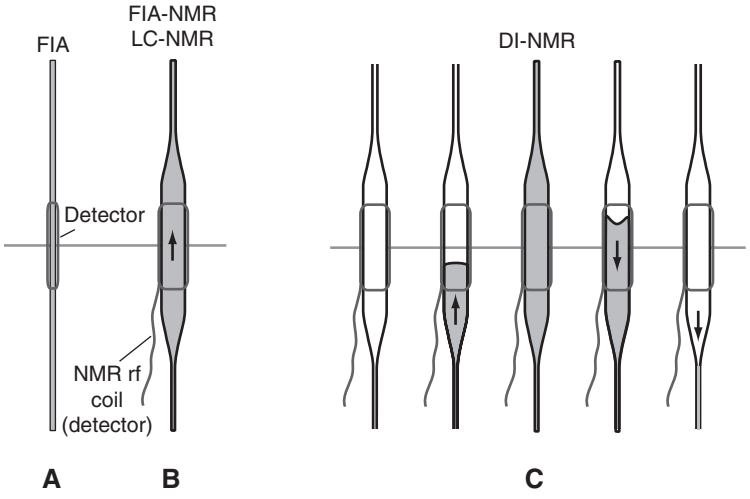

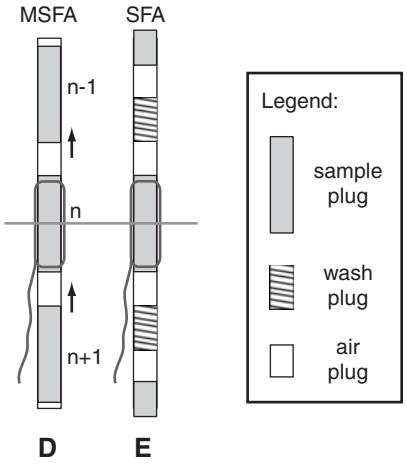

FIA is normally performed within an intact stream of liquid within capillary tubing (Fig. 12A). The fluidics of FIA-NMR and LC-NMR are similar (to FIA alone) with regard to the flow cell, except the flow cell (detector) is now an enlarged cavity connected to the capillary tubing (Fig. 12B). In all three cases, however, the stream of liquid is continuous and fills the entire tubing and detector cavity. This is in contrast to DI-NMR, which empties the flow cell of liquid (filling it with air) between each sample (Fig. 12C). DI-NMR pushes the sample solution into an empty flow cell to eliminate dilution so as to obtain maximum sensitivity, but one drawback is that the user must inject enough solution volume to fill both the inlet tubing and the entire flow cell (to obtain good NMR lineshapes)[4] – hence DI-NMR has a minimum sample volume. DI-NMR also suffers from sample-to-sample carryover from sample solution that clings to the walls of the tubing, which can be reduced by wash cycles, but never completely eliminated. FIA-NMR does not have a minimum sample volume (just a limit of detection), but sample dilution does occur.[5] Sample-to-sample carryover in FIA-NMR is under user control; the user can pump mobile phase for as long as is needed to sufficiently remove sample solution that clings to the walls of the tubing.

In an ideal world, one would like to eliminate all of these potential limitations – no minimum sample size, no dilution, and no sample-to-sample carryover – while retaining the advantages of flow NMR (speed, ease of automation). One way carryover was initially reduced (for non-NMR applications) was by introducing "segmentation" – usually in the form of air bubbles, but also as immiscible liquids or solids – between discrete plugs of each sample (Fig. 12D), an idea that was first introduced in 1966[225] and remains in widespread use today.[137,226–229] This

Fig. 12. A comparison of the fluidics of various flow-NMR methods. Part A illustrates FIA alone: there is an intact stream of liquid, flowing uni-directionally within capillary tubing, which runs through a (non-NMR) detector of some sort. Part B illustrates FIA-NMR and LC-NMR: these are similar to FIA alone (A) except the flow cell has been enlarged to compensate for the sensitivity limitations of NMR. Both techniques use unidirectional fluid flow. (The arrows indicate the presence and direction of fluid flow.) Part C illustrates DI-NMR: here the flow cell starts off empty, is pumped full of fluid, the NMR data is acquired when the fluid flow comes to a halt, then the cell is emptied, and the process is repeated. In DI-NMR, the flow is usually bi-directional; the sample is withdrawn from the bottom (which is the most efficient way to both recover the sample, and reduce sample carryover whenever the flow cell is an enlarged cavity). The in-and-out cycle is often repeated with clean rinse solvent to clean the cell between samples. Part D illustrates Mono-Segmented Flow Analysis (MSFA), which uses air bubble separators (or plugs of inert and immiscible solvent) between plugs of the samples being analyzed. Part E is another Segmented Flow Analysis (SFA) technique in which plugs of wash solvent are used to clean the detector region between samples. The plugs of wash solvent are separated from the sample plugs by air-bubble separators. The fluid flow paths for MSFA and SFA are uni-directional, and the fluid streams typically start and stop (at least for NMR detection). Note the sample indicators ($n-1$, n, $n+1$), which indicate the stepwise progression of the samples through the detector in a linear serial fashion. These latter techniques, D and E, are suitable for straight capillary tubing systems, but do not work in systems where the detector uses an "expanded" flow cell. The limitations of using the MSFA and SFA techniques for NMR are discussed in the text.

method, often called ''segmented'' or ''segmental'' flow, ''air-segmentation'' flow, ''mono-segmented'' flow, or ''air-sandwiched'' flow (Fig. 12D),[230,231] is well known to have some disadvantages, such as unstable flow rates, and an inability to instantly ''start'' or ''stop'' the liquid flow – both caused by the compressability of the air bubbles.[220] The air segments also do not always eliminate sample-to-sample carryover caused by ''sticky'' solvents that leave a film that adheres to the walls of the capillary tubing.[230] Air bubbles (or immiscible liquids) are an even bigger problem in NMR-detected applications, because a physically inhomogeneous bubble (or interface) of any size in the NMR detector cell will ruin the NMR lineshapes (due to the magnetic-susceptibility discontinuities). (Air-segmented methods have been tried in some DI-NMR applications starting in the late 1990s, and they do indeed suffer from these problems. They are still sometimes being used, but the author is unaware of any published articles that document any of these efforts.) Air-segmented methods, including the more complicated version shown in Fig. 12E, have been more successfully applied to FIA-NMR and in capillary tubing methods (without an ''expanded'' flow cell), as discussed below.

To achieve maximum NMR sensitivity, the sample solution needs to simply fill the NMR detector coil. To achieve the best NMR lineshape (which also directly affects NMR signal-to-noise), NMR techniques also need to have the same liquid (or at least a liquid of the sample's magnetic susceptibility) fill the entire flow cell, and maybe even fill portions of the inlet and outlet tubing as well. This ''extra'' liquid, however, does not contribute directly to the signal-to-noise of the NMR spectrum. Behnia and Webb[232] addressed these issues in a capillary tubing system by placing the entire plug of sample within the detector coil (to maximize signal-to-noise) and recovering decent lineshape by bracketing the sample plug with materials other than air. They showed that the narrowness of the NMR lineshape was directly controlled by how close the match was in magnetic susceptibility between the sample plug and the bracketing materials. (They used a single, mostly D_2O, sample, and bracketed it with either air bubbles, Teflon plugs, or plugs of Fluorinert [FC-43; a mixture of ^{12}C perfluorobutylamines]. They determined a minimum sample volume for their tubing/coil system to be 400 nL.) This method addressed the minimum-sample-size limitation by bracketing a minimum-sized sample plug between plugs of an immiscible liquid that has the proper magnetic susceptibility. Later, Sweedler and coworkers used this technique to study a sample cleaved from a single solid-phase-synthesis resin bead (using a sample size of 2.5 μL injected into a 800 nL detector cell).[171]

Most recently, Kautz and coworkers[129] automated this concept, and applied it to a string of samples, and used it to analyze the contents of a 96-well microtiter plate. They injected 2 μL sized sample plugs into a flow cell with an active volume of 0.5 μL located in 50 μm-i.d. capillary tubing. (The fluid flowed through only capillary tubing; no ''expanded'' flow cell was used.) The 2 μL sample plugs (in DMSO-d_6) were bracketed by plugs of immiscible FC-43 and alternated with plugs of clean (wash) solvent. (Similar to Fig. 12E, but with plugs of FC-43 instead of air.) The inside of the capillary tubing was silanized, and the FC-43 was viscous enough to form a film on the tubing wall, both of which helped to minimize sample-to-sample

carryover as the train of sample plugs was pushed through the capillary tubing. Their "segmented flow analysis" (SFA-NMR) method addresses the potential limitations listed above: they use a minimum volume of liquid, there is minimal dilution, and there is a minimum of sample-to-sample carryover. Note that this technique can only be used in a capillary flow cell detector. It will be interesting to see how far this technique can be pushed.

6. APPLICATIONS

There are far more applications of flow NMR techniques than can be comprehensively listed here. It is useful, however, to get a flavor of the wide range of applications for which people have used flow NMR. For clarity, the applications listed below have been partially separated into methods that used chromatography, and those that did not, although there is often overlap.

6.1. Detection of other (non-hydrogen) nuclei

LC-NMR-type methods normally detect ^{1}H nuclei. Other nuclei, however, have also been directly observed. ^{13}C nuclei were detected in non-chromatographic flow NMR by 1984,[36] and ^{13}C-detected LC-NMR was done in 1994 by using DNP.[112] ^{19}F was detected by at least 1993,[111] and ^{29}Si nuclei were detected by 2006.[115]

6.2. Drug metabolism

LC-NMR is commonly used to measure drug metabolites, especially in biofluids. Some early examples include the analysis of urine to study metabolites of ibuprofin,[74] antipyrine,[75] and flurbiprofen,[111] all in 1993. Human and rat urine and bile were analyzed for paracetamol metabolites in 1994.[233]

6.3. Drug impurities

Numerous drug companies use LC-NMR (and LC-NMR-MS) to analyze impurities in drug formulations.[234,235] These impurities are sometimes decomposition products that form during storage, but regardless of their source, they need to be analyzed and quantified prior to FDA approval.

6.4. Metabonomics

The fields of metabonomics and metabolomics have emerged as ways to study disease states by analyzing biofluids. LC-NMR plays a role in this field,[236,237] as do

non-chromatographic flow-NMR techniques (like DI-NMR).[141,142] When a microcoil flow probe is used, one can even now analyze fluids from single kinds of tissues (''tissue-targeted metabonomics'').[238] There are also now companies that have used DI-NMR to analyze biofluids (such as plasma, serum, and urine) for clinical diagnostics.[239] For example, Liposcience (at www.liposcience.com) now has an FDA-approved clinical analyzer called ''Numera'' that uses DI-NMR for the high-throughput analysis of clinical plasma samples for cholesterol and lipids.[240]

6.5. The study of unstable compounds

One very nice application for LC-NMR is in the analysis of mixtures of compounds that are unstable when isolated or when exposed to air or light. (Once injected onto the column, the compounds encounter minimal light or oxygen, and they can be analyzed rapidly after separation.) This lets researchers study compounds that undergo rapid mutarotation or functional-group migration. A number of publications of this application started to appear in the mid 1990s.[241–244]

6.6. Natural products

LC-NMR has been used extensively for the analysis of mixtures of natural products.[145,245] The use of a chiral column to perform the separation (of plant extracts) has extended its utility.[246] Its utility has been increased even farther through the use of LC-SPE-NMR to concentrate isolated compounds[247] and microcoils (in both LC-NMR and DI-NMR mode) to minimize the sample quantities used.[194,195,198,248–251]

6.7. Polymers

LC-NMR and GPC-NMR are both useful tools for polymer analysis.[102,252,253] The mobile phases used for polymer analyses often differ from those used for other reversed-phase LC-NMR applications, and may even consist of single solvents like acetonitrile and chloroform. For some polymers, an additional requirement for the design of the flow probe is that it must allow all of the fluidics of the entire GPC-NMR system to be maintained at high temperatures ($>100^{\circ}C$).[254]

6.8. Combinatorial chemistry

The analysis of combinatorial chemistry libraries was the original impetus for developing DI-NMR, specifically to achieve speed and resolution.[4] This has since become a regular application of the technique.[132,133,136] LC-NMR has been proposed as a tool for analyzing combinatorial-chemistry libraries,[255] although the concept is not widely embraced, probably in large part to throughput limitations.

6.9. Organic chemistry

It has often been proposed that DI-NMR (or even FIA-NMR) could be used in an open-access environment as a way to either speed up or simplify walk-up automation for NMR. There are some issues with making it robust and routine (like finding one solvent that never precipitates any compounds injected), but some groups are investigating its utility for this purpose.[137]

6.10. Environmental chemistry

Related to natural-products work is the use of LC-NMR to look at environmental samples.[184] It can be used to look either at the naturally occurring materials themselves,[256] or to look at man-made compounds like herbicides, either in their natural form or to study how they undergo degradation.[257]

6.11. Biomolecular NMR

Flow-NMR techniques have been used to look at protein dynamics, both by analyzing a flowing stream in a microcoil probe[57] (or in a capillary multiplex probe[209]) and by analyzing a rapid-injection sample in a cold probe.[30] Flow techniques have also been used to screen for ligand binding,[127,258] and in one case flow aided in part by recycling the ^{15}N-labeled protein.[259]

6.12. Perfusion

In a totally separate application (one that is not related to any other techniques described here), a form of flow NMR is used to look at cell cultures. In this case the cells being studied are fixed within the NMR probe, while an oxygenated nutrient solution flows through the sample to keep it alive and viable. For example, Jardetzky *et al.* used this in 1982 to acquire ^{31}P data on live mammalian cells,[260] and Sahm and coworkers used it in 1992 to acquire ^{31}P data on bacterial cultures.[261]

6.13. MR imaging

Another unique application is the use of MR imaging to study LC separations.[262] The goal was to design better chromatography. This did not include LC-NMR, but did perform a type of NMR analysis on a flowing sample. (There are indeed many other applications of the use of MR imaging to study flow, especially the flow of biological fluids like blood, but that field is far removed from the scope of this article.)

7. PROBLEMS AND CHALLENGES

As with any analytical technique, flow NMR has some limitations, problems, and challenges. These limitations tend to be very different from those encountered during conventional tube-based NMR, so it is nice to have flow as an alternative technique.

7.1. Carryover

One of the bigger issues encountered during flow NMR is sample-to-sample carryover. This carryover can arise from residue in the injector port, from cracks within capillary-tube fittings that are either not zero-dead volume or are poorly assembled, from material that adheres to the tubing (either on the surface or diffused under the surface layer), or from cavity flow cells that take time to be totally flushed out. (The author has noticed that methanol can absorb into some PEEK tubing and can take many hours to diffuse out.) In DI-NMR, carryover can come from the previous sample; in LC-NMR it can come from a large leading peak that contaminates a small trailing peak (either by poor flushing, overloaded columns, or by improper surface chemistry on the column). In DI-NMR, carryover can be reduced by using more washes or by using less viscous solvents (those that do not stick to the tubing as much). In FIA-NMR, carryover can be reduced by pumping more mobile phase between each sample. In LC-NMR, carryover can be influenced by many aspects of the whole setup.

7.2. Clogging

Clogging, as a mechanical blockage of the capillary tubing or a frit, can occur in any of the flow techniques. The blockage impedes flow, and results in increased backpressure. Clogging may occur because the samples are not filtered prior to injection, or it can occur if a sample precipitates out of solution (usually due to solubility issues encountered when the solvent composition gets changed). It is exacerbated as the inside diameter of the tubing decreases, so clogging is a bigger problem for capillary techniques.

In LC-NMR, the use of an easily replaced guard column will control most clogging issues. In FIA-NMR, a small filter can be placed in-line just after the injector, and this can probably eliminate most clogging. In DI-NMR, it is hard to add a filter anywhere, so clogging issues are more likely to arise. (The author does not find clogging to be a major issue, however, and has run thousands of DI-NMR samples successively without clogging.) Geierstanger *et al.* addressed clogging during DI-NMR on a CapNMR probe by placing a 2 μm filter at the inlet of the NMR probe, and sometimes on the injector valve.[196] Additionally, they injected a wash solvent (non-deuterated acetone/chloroform/DMSO vol./% of 40/20/40) every 25 samples and also cleaned the probe with 3% hydrogen peroxide in H_2O (at 45°C for 12 h) every month.[196] Similarly (also for DI-NMR), Bailey and Marshall[124] tried to

prevent clogging by placing a 10 μm frit just upstream from the NMR flow cell, and then backflushing it after every NMR acquisition.

7.3. Dirty flow cells

The author has more commonly observed what you could call "dirty flow cells". After many repetitive injections (especially in DI-NMR), the proton lineshape slowly degrades with time until the probe is washed well. This is especially problematic if a sample solution is left in the flow cell and not properly washed out (or worse yet – left to dry out). Aggressive cleaning of the flow cell (with solvents) can restore the lineshape to its previous level. The author ascribes the degraded lineshape to contamination in the flow cell, and believes that it is an inevitable fate of a flow probe – given enough time and use.

Aside from a regular program of washing the flow cell occasionally with aggressive solvents (discussed above), the next best solution appears to be an interchangeable flow cell (IFC) within the NMR probe that lets the user replace the flow cell whenever it gets unacceptably dirty.[3] These IFC NMR probes have been commercially available since 1999; the interchangeability feature usually generates only a small reduction in NMR performance. This capability has now been extended to cold probes, where the interchangeable (removable) flow cell facilitates making the cryogenic probes readily available for flow NMR.

7.4. Precipitating samples

One of the bigger concerns for flow-NMR users is to make sure they avoid any conditions that might cause samples to precipitate out of solution. The most common way this could happen would be if the dissolved sample sees a change in solvent – if it was dissolved in one solvent for injection, but it was injected into a mobile phase in which it was less soluble. A precipitating sample could contribute to clogging, dirty flow cells, and maybe even carryover; all of which will eventually make a system unusable. All samples injected onto a flow-NMR system should be filtered, or at least very clean, but this alone is insufficient to stop a sample from precipitating within the system. Only user awareness can help.

7.5. Bubbles

In all of these flow techniques, bubbles can be a constant and troublesome problem to the inexperienced user, but with proper technique and training (and hardware design), they can be eliminated. In LC-NMR, bubbles can arise from mixing solvents, which then outgas (especially as they leave the high pressure of the chromatography column and enter the relatively low-pressure environment of the NMR flow cell). Outgassing – and hence bubbles – can be eliminated in LC-NMR and FIA-NMR by using standard solvent-degassing techniques (such as sparging with helium). Bubbles in DI-NMR more commonly arise from poor calibration of

injection volumes or from pulling liquid too rapidly with a syringe pump (which can induce bubbles via cavitation). In all modern flow probes that have their outlet at the top of the flow cell (Fig. 2A), any bubbles that do form tend to be self-clearing. Note well, however, that all bubbles that get in the flow cell during acquisition can distort the NMR lineshape enough to render the data unusable, and the user needs to take corrective action. (The bubble's formation needs to be eliminated at the source, and users should not rely upon self-clearing flow cells to solve the problem.) Again, as with all of the problems above, bubbles tend not to plague conscientious experienced users.

7.6. Magnetic-susceptibility mismatches

All high-resolution NMR techniques require the NMR coil, its surroundings, and the sample to have a uniform magnetic susceptibility.[263,264] If this is not satisfied, all of the lineshapes in the NMR spectra will be degraded. This is true in flow NMR as well. The most common manifestation of this problem in flow NMR occurs when solvents that have different magnetic susceptibilities (e.g., almost any two solvents) are incompletely mixed. Solvents are "mixed" regularly in gradient LC-NMR, and in FIA-NMR when the injected sample is dissolved in a solvent other than the mobile phase, or in LC-SPE-NMR and DI-NMR when the "wash" or "push" solvents are different than the sample solvent. What matters most though is how well they are mixed, and how close the region of incomplete mixing is to the NMR receiver coil.

So, in essence, linebroadenings caused by magnetic-susceptibility mismatches are a constant problem in all types of flow NMR. They are an issue with LC-NMR gradient methods, where they require shallow solvent gradients (or else the NMR lines become too broad). They also make it hard to have well-shimmed spectra when the gradient method runs from composition extremes like 100%A : 0%B to 0%A : 100%B – because the two extremes of solvent composition will normally have different optimal shim conditions. Magnetic-susceptibility-mismatch linebroadenings are also a problem whenever a liquid sample has an interface with either a wash solvent or an air plug (as in LC-SPE-NMR, FIA-NMR, or DI-NMR). If the interface gets anywhere close to the NMR coil during acquisition, the NMR lines can be broadened (beyond recognition in the worse cases; especially with air bubbles). This issue gets more complicated (and more prevalent) than expected in certain situations: for example, air bubbles in a transfer line (perhaps used as sample separators) are compressible and their volume is also temperature sensitive – which makes it very difficult to accurately place liquid/sample plugs in the sample coil without any encroachment from any air plug. Likewise, any solvent can cling to the walls of the capillary tubing, and not be well washed (or even well mixed) with a different solvent that displaces it during flow; this phenomenon can easily generate linebroadenings, especially if dissimilar "wash solvents" are used, or if concentrated samples are used. (The magnetic susceptibility of a solution changes as the solute concentration changes. Likewise, note that deuterated and "protio"

versions of the same solvent [i.e., D_2O versus H_2O] exhibit different magnetic susceptibilities. For example, intermixing D_2O samples with H_2O washes can induce magnetic-susceptibility-mismatch linebroadenings if sufficient care is not taken in setting up the experimental parameters.) Sweedler *et al.* even proposed attempting to ''re-match'' the solvent composition, after the chromatographic separation, but prior to entry into the NMR flow cell, to reduce potential linebroadening.[265]

7.7. Reproducibility

Reproducibility is important in all analyses, so it is important to note that a flow interface can unfortunately add a measure of variability to the NMR measurement process. DI-NMR and FIA-NMR have both proven to be reproducible, and there are easy ways to verify that,[4,5] but when various types of chromatography are added to the interface, more variables are created that need to be controlled. HPLC columns can vary in their separation performance over time, and the LC separation itself can be dependent on numerous variables such as column temperature, column ''solvent and hydration'' equilibration, and the amount of deuteration of the mobile phase. CE-NMR uses an electric current that can generate significant increases in temperature that can cause instabilities and variations in the analysis. Sweedler and coworkers have documented that thermal changes as high as 65C are possible, and they have discussed the potential solutions to the problem.[266] Electrophoretic currents during CE-NMR can also distort NMR lineshapes and peak heights, so Webb and coworkers developed a post-processing method to partially restore the lineshape.[177]

7.8. Quantification; standards

Many analyses, especially those that are repetitive, need accurate quantification of the analytes. Over the years there have been many investigations into better ways to do accurate quantification, with internal standards usually being the method of choice. More recently within NMR, the ERETIC method has been evaluated,[267,268] which injects into the NMR spectrum an electronically generated NMR signal that can be used as a reference point for quantification. Also referred to as a Virtual Signal, this method was recently used in a flow-NMR study where other kinds of internal and external standards were rendered impractical.[269] While there are still ongoing debates about the utility and the potential sources of error in the ERETIC method, it is likely to remain as a useful technique in the NMR toolbox.

When compared with tube-based NMR methods, flow NMR possesses some additional potential modes of failure, due to the fluidics involved. There is always the risk that the flowing sample either did not get to the NMR flow cell, or did not entirely fill it (which could degrade peak area, or lineshapes, or both). This could be due to a blockage in the tubing, or to a leak, or to any one of many other potential failures of the ''hydraulic'' aspects of the system. Because of this additional risk, it is

useful in flow NMR to also have some "standard signal" in the NMR spectrum to allow the operator to verify that at least the fluidics behaved properly (for troubleshooting, in cases where the expected NMR signal is not observed). In DI-NMR, the lineshape, peak amplitude, and integral of an internal standard have all been used to verify the integrity of each analysis (Fig. 9).[4] Likewise, it has also been proposed that one can monitor the Scout Scan signal[86] as a way to verify the fluidics. Kautz and coworkers[129] went a bit farther when performing SFA-NMR (segmented flow) to run DI-NMR on a 96-well library when they used plugs of a wash/autodetection solution that contained 1% TMSP (60 mM) in DMSO-d_6. This allowed them to monitor an internal standard that was located between the samples, rather than within the samples.

All of these issues illustrate that flow NMR does have some unique problems and challenges, just like any analytical technique. But it also illustrates that many of these issues have been addressed.

8. CONCLUSIONS

Flow NMR methods have come a long way since their inception – as evidenced by the fact that many varieties of flow-NMR systems are now commercially available. These various products are clearly well suited to solving certain types of scientific problems. Flow techniques are not, however, what one might call a "fully mature and widely accepted technology", as evidenced by the fact that they are not installed in every NMR lab. This lack of a "saturated install base" may be due in part to either fundamental limitations of the concept, or to some (mechanical-like) problems that remain to be solved, or it may be due to the current cost and complexity of the resulting hyphenated systems. Some of it, however, is likely due to the sheer newness of the flow methods and the fact that many researchers can still get "good enough answers" with the conventional ways of performing (tube-based) NMR.

ACKNOWLEDGMENTS

I would like to thank my fellow flow-NMR coworkers from both of my tenures at Varian, including Steve Smallcombe, Steve Patt, Chris Kellogg, Ron Haner, Karen Salomon, and Daina Avizonis. I would also like to thank Varian NMR Instruments for making all of this work possible. Lastly, I am indebted to both the University of Nebraska Medical Center and Varian Inc. for providing the resources that facilitated this manuscript.

REFERENCES

1. K. Albert, *On-Line LC-NMR and Related Techniques*, Wiley, West Sussex, England, 2002.
2. H. C. Dorn, in: *Encyclopedia of Nuclear Magnetic Resonance*, D. M. Grant and R. K. Harris, eds., Wiley, West Sussex, England, 1996, p. 2026.

3. P. A. Keifer, in: *Progress in Drug Research*, E. Jucker ed., Vol. 55, Birkhauser Verlag, Basel, 2000, p. 137.
4. P. A. Keifer, S. H. Smallcombe, E. H. Williams, K. E. Salomon, G. Mendez, J. L. Belletire and C. D. Moore, *J. Comb. Chem.*, 2000, **2**, 151.
5. P. A. Keifer, *Magn. Reson. Chem.*, 2003, **41**, 509.
6. L. Griffiths and R. Horton, *Magn. Reson. Chem.*, 1998, **36**, 104.
7. G. Suryan, *Proc. Indian Acad. Sci. Sect. A*, 1951, **33**, 107.
8. A. L. Bloom and J. N. Shoolery, *Phys. Rev.*, 1953, **90**, 358.
9. A. M. J. Mitchell and G. Phillips, *Br. J. Appl. Phys.*, 1956, **7**, 67.
10. J. R. Singer, *Science*, 1959, **130**, 1652.
11. S. Forsen and A. Rupprecht, *J. Chem. Phys.*, 1960, **33**, 1888.
12. L. R. Hirschel and L. F. Libelo, *J. Appl. Phys.*, 1961, **32**, 1404.
13. L. R. Hirschel and L. F. Libelo, *J. Appl. Phys.*, 1962, **33**, 1895.
14. A. I. Zhernovoi and G. D. Latyshev, *N.M.R. in a Flowing Liquid*, Consultants Bureau, New York, NY, 1965.
15. A. B. Rukhin, O. V. Pavlov and V. V. Ekaterinin, *Izv. Akad. Nauk Kaz. SSR Ser. Fiz. Mat.*, 1966, **4**, 69.
16. O. V. Pavlov, *Vestn. Akad. Nauk Kaz. SSR*, 1969, **25**, 22.
17. O. C. Morse and J. R. Singer, *Science*, 1970, **170**, 440.
18. D. A. Laude Jr., R. W. K. Lee and C. L. Wilkins, *J. Magn. Reson.*, 1984, **60**, 453.
19. M. C. McIvor, *J. Phys. E Sci. Instrum.*, 1969, **2**, 292.
20. J. L. Sudmeier and J. J. Pesek, *Inorg. Chem.*, 1971, **10**, 860.
21. J. Grimaldi, J. Baldo, C. McMurray and B. D. Sykes, *J. Am. Chem. Soc.*, 1972, **94**, 7641.
22. D. A. Couch, O. W. Howarth and P. Moore, *J. Phys. E Sci. Instrum.*, 1975, **8**, 831.
23. J. J. Grimaldi and B. D. Sykes, *J. Am. Chem. Soc.*, 1975, **97**, 273.
24. C. A. Fyfe, W. E. Sanford and C. S. Yannoni, *J. Am. Chem. Soc.*, 1976, **98**, 7101.
25. R. O. Kuehne, T. Schaffhauser, A. Wokaun and R. R. Ernst, *J. Magn. Reson.*, 1979, **35**, 39.
26. C. Frieden, S. D. Hoeltzli and I. J. Ropson, *Protein Sci.*, 1993, **2**, 2007.
27. S. D. Hoeltzli, I. J. Ropson and C. Frieden, in: *Techniques in Protein Chemistry V [Pap. Symp. Protein Soc.], 7th*, J. W. Crabb ed., Academic Press, San Diego, CA, 1994, p. 455.
28. S. D. Hoeltzli and C. Frieden, *Proc. Natl. Acad. Sci. USA*, 1995, **92**, 9318.
29. S. D. Hoeltzli and C. Frieden, *Biochemistry*, 1996, **35**, 16843.
30. S. D. Hoeltzli and C. Frieden, *Biochemistry*, 1998, **37**, 387.
31. J. F. McGarrity, J. Prodolliet and T. Smyth, *Org. Magn. Reson.*, 1981, **17**, 59.
32. J. F. McGarrity and J. W. Prodolliet, *Tetrahedron Lett.*, 1982, **23**, 417.
33. J. F. McGarrity and J. Prodolliet, *J. Org. Chem.*, 1984, **49**, 4465.
34. J. F. McGarrity, C. A. Ogle, Z. Brich and H. R. Loosli, *J. Am. Chem. Soc.*, 1985, **107**, 1810.
35. S. H. Bertz, C. M. Carlin, D. A. Deadwyler, M. D. Murphy, C. A. Ogle and P. H. Seagle, *J. Am. Chem. Soc.*, 2002, **124**, 13650.
36. E. Bayer and K. Albert, *J. Chromatogr.*, 1984, **312**, 91.
37. K. Albert, G. Kruppa, K. P. Zeller, E. Bayer and F. Hartmann, *Z. Naturforsch. C Biosci.*, 1984, **39C**, 859.
38. M. Cocivera and K. W. Woo, *Tetrahedron Lett.*, 1976, **36**, 3109.
39. D. W. Jones and T. F. Child, *Adv. Magn. Reson.*, 1976, **8**, 123.
40. R. Barbieri, P. J. Hore, C. Luchinat and R. Pierattelli, *J. Biomol. NMR*, 2002, **23**, 303.
41. J. J. Grimaldi and B. D. Sykes, *J. Biol. Chem.*, 1975, **250**, 1618.
42. B. D. Sykes and J. J. Grimaldi, *Methods Enzymol.*, 1978, **49**, 295.
43. A. J. Brown, D. A. Couch, O. W. Howarth and P. Moore, *J. Magn. Reson.*, 1976, **21**, 503.
44. A. J. Brown, O. W. Howarth and P. Moore, *J. Am. Chem. Soc.*, 1978, **100**, 713.
45. A. E. Merbach, P. Moore, O. W. Howarth and C. H. McAteer, *Inorg. Chim. Acta*, 1980, **39**, 129.
46. P. Moore, *Pure Appl. Chem.*, 1985, **57**, 347.
47. C. A. Fyfe, M. Cocivera and S. W. H. Damji, *J. Chem. Soc. Chem. Commun.*, 1973, 743.
48. C. A. Fyfe, M. Cocivera, S. W. H. Damji, T. A. Hostetter, D. Sproat and J. O'Brien, *J. Magn. Reson.*, 1976, **23**, 377.

49. C. A. Fyfe, A. Koll, S. W. H. Damji, C. D. Malkiewich and P. A. Forte, *J. Chem. Soc.*, 1977, 335.
50. C. A. Fyfe and L. Van Veen Jr., *J. Am. Chem. Soc.*, 1977, **99**, 3366.
51. C. A. Fyfe, M. Cocivera and S. W. H. Damji, *Acc. Chem. Res.*, 1978, **11**, 277.
52. M. Cocivera, K. W. Woo and P. Livant, *Can. J. Chem.*, 1978, **56**, 473.
53. L. K. Tan and M. Cocivera, *Can. J. Chem.*, 1982, **60**, 772.
54. M. Cocivera and A. Effio, *J. Am. Chem. Soc.*, 1976, **98**, 7371.
55. M. Cocivera and A. Effio, *J. Chem. Soc. Chem. Commun.*, 1976, **11**, 393.
56. D. B. Green, J. Lane and R. M. Wing, *Appl. Spectrosc.*, 1987, **41**, 847.
57. M. Kakuta, D. A. Jayawickrama, A. M. Wolters, A. Manz and J. V. Sweedler, *Anal. Chem.*, 2003, **75**, 956.
58. N. Watanabe and E. Niki, *Proc. Jpn. Acad. Ser. B*, 1978, **54**, 194.
59. J. F. Haw, T. E. Glass, D. W. Hausler, E. Motell and H. C. Dorn, *Anal. Chem.*, 1980, **52**, 1135.
60. J. F. Haw, T. E. Glass and H. C. Dorn, *Anal. Chem.*, 1981, **53**, 2332.
61. J. F. Haw, T. E. Glass and H. C. Dorn, *Anal. Chem.*, 1981, **53**, 2327.
62. J. F. Haw, T. E. Glass and H. C. Dorn, *J. Magn. Reson.*, 1982, **49**, 22.
63. H. C. Dorn, *Anal. Chem.*, 1984, **56**, 747A.
64. E. Bayer, K. Albert, M. Nieder, E. Grom and T. Keller, *J. Chromatogr.*, 1979, **186**, 497.
65. E. Bayer, K. Albert, M. Nieder, E. Grom and Z. An, *Fresenius J. Anal. Chem.*, 1980, **304**, 111.
66. E. Bayer, K. Albert, M. Nieder, E. Grom, G. Wolff and M. Rindlisbacher, *Anal. Chem.*, 1982, **54**, 1747.
67. K. Albert, M. Nieder, E. Bayer and M. Spraul, *J. Chromatogr.*, 1985, **346**, 17.
68. J. Buddrus and H. Herzog, *Org. Magn. Reson.*, 1980, **13**, 153.
69. J. Buddrus, H. Herzog and J. W. Cooper, *J. Magn. Reson.*, 1981, **42**, 453.
70. J. Buddrus and H. Herzog, *Anal. Chem.*, 1983, **55**, 1611.
71. D. A. Laude Jr. and C. L. Wilkins, *Anal. Chem.*, 1984, **56**, 2471.
72. K. Albert, M. Kunst, E. Bayer, M. Spraul and W. Bermel, *J. Chromatogr.*, 1989, **463**, 355.
73. H. Barjat, G. A. Morris, M. J. Newman and A. G. Swanson, *J. Magn. Reson. A*, 1996, **119**, 115.
74. M. Spraul, M. Hofmann, P. Dvortsak, J. K. Nicholson and I. D. Wilson, *Anal. Chem.*, 1993, **65**, 327.
75. I. D. Wilson, J. K. Nicholson, M. Hofmann, M. Spraul and J. C. Lindon, *J. Chromatogr. B Biomed. Sci. Appl.*, 1993, **617**, 324.
76. D. A. Jayawickrama and J. V. Sweedler, *J. Chromatogr. A*, 2003, **1000**, 819.
77. M. Pursch, S. Strohschein, H. Haendel and K. Albert, *Anal. Chem.*, 1996, **68**, 386.
78. K. Albert and E. Bayer, *Trends Anal. Chem.*, 1988, **7**, 288.
79. T. Murai, H. Iwabuchi and T. Ikeda, *J. Mass Spectrom. Soc. Jpn.*, 2004, **52**, 277.
80. M. Godejohann, L. H. Tseng, U. Braumann, J. Fuchser and M. Spraul, *J. Chromatogr. A*, 2004, **1058**, 191.
81. J. Buddrus and H. Herzog, *Anal. Chem.*, 1983, **55**, 1611.
82. D. A. Laude Jr., R. W. K. Lee and C. L. Wilkins, *Anal. Chem.*, 1985, **57**, 1464.
83. D. A. Laude Jr. and C. L. Wilkins, *Anal. Chem.*, 1987, **59**, 546.
84. K. Albert, J. L. Sudmeier, M. S. Anwer and W. W. Bachovchin, *Magn. Reson. Med.*, 1989, **11**, 309.
85. S. L. Patt, *J. Magn. Reson.*, 1992, **96**, 94.
86. S. H. Smallcombe, S. L. Patt and P. A. Keifer, *J. Magn. Reson. A*, 1995, **117**, 295.
87. T. R. Hoye, B. M. Eklov, T. D. Ryba, M. Voloshin and L. J. Yao, *Org. Lett.*, 2004, **6**, 953.
88. X. Liang, J. A. Parkinson, M. Weishaeupl, R. O. Gould, S. J. Paisey, H. -S. Park, T. M. Hunter, C. A. Blindauer, S. Parsons and P. J. Sadler, *J. Am. Chem. Soc.*, 2002, **124**, 9105.
89. J. C. McNulty, D. A. Thompson, K. A. Bolin, J. Wilken, G. S. Barsh and G. L. Millhauser, *Biochemistry*, 2001, **40**, 15520.
90. D. Neuhaus, I. M. Ismail and C. W. Chung, *J. Magn. Reson. A*, 1996, **118**, 256.
91. T. Parella, P. Adell, F. Sanchez-Ferrando and A. Virgili, *Magn. Reson. Chem.*, 1998, **36**, 245.
92. C. Dalvit, G. Shapiro, J. M. Bohlen and T. Parella, *Magn. Reson. Chem.*, 1999, **37**, 7.
93. C. Dalvit and J. M. Bohlen, *Annu. Rep. NMR Spectrosc.*, 1999, **37**, 203.
94. J. Buddrus and H. Herzog, *Org. Magn. Reson.*, 1981, **15(2)**, 211.

95. L. A. Allen, T. E. Glass and H. C. Dorn, *Anal. Chem.*, 1988, **60**, 390.
96. N. Wu, T. L. Peck, A. G. Webb, R. L. Magin and J. V. Sweedler, *J. Am. Chem. Soc.*, 1994, **116**, 7929.
97. K. Albert, *Angew. Chem. Int. Ed. Engl.*, 1995, **34**, 641.
98. K. Albert, G. Schlotterbeck, L. H. Tseng and U. Braumann, *J. Chromatogr. A*, 1996, **750**, 303.
99. B. Behnke, G. Schlotterbeck, U. Tallarek, S. Strohschein, L. H. Tseng, T. Keller, K. Albert and E. Bayer, *Anal. Chem.*, 1996, **68**, 1110.
100. G. Schlotterbeck, L. H. Tseng, H. Haendel, U. Braumann and K. Albert, *Anal. Chem.*, 1997, **69**, 1421.
101. K. Pusecker, J. Schewitz, P. Gfroerer, L. H. Tseng, K. Albert and E. Bayer, *Anal. Chem.*, 1998, **70**, 3280.
102. K. Ute, R. Niimi, S. Y. Hongo and K. Hatada, *Polym. J.*, 1998, **30**, 439.
103. H. Pasch and W. Hiller, *Macromolecules*, 1996, **29**, 6556.
104. K. Albert, U. Braumann, L. H. Tseng, G. Nicholson, E. Bayer, M. Spraul, M. Hofmann, C. Dowle and M. Chippendale, *Anal. Chem.*, 1994, **66**, 3042.
105. E. Lenz, S. Taylor, C. Collins, I. D. Wilson, D. Louden and A. Handley, *J. Pharm. Biomed. Anal.*, 2002, **27**, 191.
106. F. S. Pullen, A. G. Swanson, M. J. Newman and D. S. Richards, *Rapid Commun. Mass Spectrom.*, 1995, **9**, 1003.
107. G. Bringmann and G. Lang, *Sponges (Porifers)*, 2003, 89.
108. M. Ludlow, D. Louden, A. Handley, S. Taylor, B. Wright and I. D. Wilson, *J. Chromatogr. A*, 1999, **857**, 89.
109. L. A. Allen, M. P. Spratt, T. E. Glass and H. C. Dorn, *Anal. Chem.*, 1988, **60**, 675.
110. D. A. Laude Jr. and C. L. Wilkins, *Macromolecules*, 1986, **19**, 2295.
111. M. Spraul, M. Hofmann, I. D. Wilson, E. Lenz, J. K. Nicholson and J. C. Lindon, *J. Pharm. Biomed. Anal.*, 1993, **11**, 1009.
112. S. Stevenson and H. C. Dorn, *Anal. Chem.*, 1994, **66**, 2993.
113. S. Stevenson, T. Glass and H. C. Dorn, *Anal. Chem.*, 1998, **70**, 2623.
114. J. K. Nicholson, P. J. D. Foxall, M. Spraul, R. D. Farrant and J. C. Lindon, *Anal. Chem.*, 1995, **67**, 793.
115. V. Blechta, J. Sykora, J. Hetflejs, S. Sabata and J. Schraml, *Magn. Reson. Chem.*, 2006, **44**, 7.
116. J. D. King and W. L. Rollwitz, *ISA Trans.*, 1983, **22**, 69.
117. C. G. Wade, R. D. Johnson, S. B. Philson, J. Strouse and F. J. McEnroe, *Anal. Chem.*, 1989, **61**, A107.
118. P. A. Keifer, *Drug Discov. Today*, 1997, **2**, 468.
119. P. A. Keifer, *Drugs Future*, 1998, **23**, 301.
120. P. A. Keifer, in: *Integrated Drug Discovery Technologies*, H. -Y. Mei and A. W. Czarnik, eds., Marcel Dekker Inc., New York, NY, 2002, p. 485.
121. S. A. Curran and D. E. Williams, *Appl. Spectrosc.*, 1987, **41**, 1450.
122. D. Louden, A. Handley, S. Taylor, E. Lenz, S. Miller, I. D. Wilson and A. Sage, *Analyst*, 2000, **125**, 927.
123. N. J. C. Bailey and I. R. Marshall, *Assay Drug Dev. Technol.*, 2005, **3**, 446.
124. N. J. C. Bailey and I. R. Marshall, *Anal. Chem.*, 2005, **77**, 3947.
125. D. W. Lachenmeier, W. Frank, E. Humpfer, H. Schaefer, S. Keller, M. Moertter and M. Spraul, *Eur. Food Res. Technol.*, 2005, **220**, 215.
126. C. Tisne and F. Dardel, *Comb. Chem. High Throughput Screen.*, 2002, **5**, 523.
127. B. J. Stockman, K. A. Farley and D. T. Angwin, *Methods Enzymol.*, 2001, **338**, 230.
128. P. A. Keifer, *J. Org. Chem.*, 1996, **61**, 1558.
129. R. A. Kautz, W. K. Goetzinger and B. L. Karger, *J. Comb. Chem.*, 2005, **7**, 14.
130. M. Spraul, M. Hofmann, M. Ackermann, J. P. Shockcor, J. C. Lindon, A. W. Nicholls, J. K. Nicholson, S. J. P. Damment and J. N. Haselden, *Anal. Commun.*, 1997, **34**, 339.
131. W. H. Gmeiner, W. Cui, D. E. Konerding, P. A. Keifer, S. K. Sharma, A. M. Soto, L. A. Marky and J. W. Lown, *J. Biomol. Struct. Dyn.*, 1999, **17**, 507.

132. B. C. Hamper, D. M. Snyderman, T. J. Owen, A. M. Scates, D. C. Owsley, A. S. Kesselring and R. C. Chott, *J. Comb. Chem.*, 1999, **1**, 140.
133. A. Combs and M. Rafalski, *J. Comb. Chem.*, 2000, **2**, 29.
134. K. Lewis, D. Phelps and A. Sefler, *Am. Pharm. Rev.*, 2000, **3**, 63.
135. G. R. Eldridge, H. C. Vervoort, C. M. Lee, P. A. Cremin, C. T. Williams, S. M. Hart, M. G. Goering, M. O'Neil-Johnson and L. Zeng, *Anal. Chem.*, 2002, **74**, 3963.
136. S. Kalelkar, E. R. Dow, J. Grimes, M. Clapham and H. Hu, *J. Comb. Chem.*, 2002, **4**, 622.
137. G. C. Leo, A. Krikava and G. W. Caldwell, *Anal. Chem.*, 2003, **75**, 1954.
138. G. K. Pierens, M. E. Palframan, C. J. Tranter, A. R. Carroll and R. J. Quinn, *Magn. Reson. Chem.*, 2005, **43**, 359.
139. B. J. Stockman, *Curr. Opin. Drug Disc. Dev.*, 2000, **3**, 269.
140. A. Ross, G. Schlotterbeck, W. Klaus and H. Senn, *J. Biomol. NMR*, 2000, **16**, 139.
141. D. G. Robertson, M. D. Reily, R. E. Sigler, D. F. Wells, D. A. Paterson and T. K. Braden, *Toxicol. Sci.*, 2000, **57**, 326.
142. B. C. M. Potts, A. J. Deese, G. J. Stevens, M. D. Reily, D. G. Robertson and J. Theiss, *J. Pharm. Biomed. Anal.*, 2001, **26**, 463.
143. S. Rezzi, D. E. Axelson, K. Heberger, F. Reniero, C. Mariani and C. Guillou, *Anal. Chim. Acta*, 2005, **552**, 13.
144. S. Rezzi, M. Spraul, D. E. Axelson, K. Heberger, C. Mariani, F. Reniero and C. Guillou, *Spec. Publ. – R. Soc. Chem.*, 2005, **299**, 124.
145. V. Exarchou, M. Krucker, T. A. Van Beek, J. Vervoort, I. P. Gerothanassis and K. Albert, *Magn. Reson. Chem.*, 2005, **43**, 681.
146. J. A. de Koning, A. C. Hogenboom, T. Lacker, S. Strohschein, K. Albert and U. A. T. Brinkman, *J. Chromatogr. A*, 1998, **813**, 55.
147. N. T. Nyberg, H. Baumann and L. Kenne, *Magn. Reson. Chem.*, 2001, **39**, 236.
148. V. Exarchou, M. Godejohann, T. A. Van Beek, I. P. Gerothanassis and J. Vervoort, *Anal. Chem.*, 2003, **75**, 6288.
149. N. T. Nyberg, H. Baumann and L. Kenne, *Anal. Chem.*, 2003, **75**, 268.
150. C. Clarkson, D. Strk, S. H. Hansen and J. W. Jaroszewski, *Anal. Chem.*, 2005, **77**, 3547.
151. M. Lambert, D. Staerk, S. H. Hansen and J. W. Jaroszewski, *Magn. Reson. Chem.*, 2005, **43**, 771.
152. R. J. Lewis, M. A. Bernstein, S. J. Duncan and C. J. Sleigh, *Magn. Reson. Chem.*, 2005, **43**, 783.
153. M. Sandvoss, B. Bardsley, T. L. Beck, E. Lee-Smith, S. E. North, P. J. Moore, A. J. Edwards and R. J. Smith, *Magn. Reson. Chem.*, 2005, **43**, 762.
154. C. Seger, M. Godejohann, L. H. Tseng, M. Spraul, A. Girtler, S. Sturm and H. Stuppner, *Anal. Chem.*, 2005, **77**, 878.
155. A. J. Alexander, F. Xu and C. Bernard, *Magn. Reson. Chem.*, 2006, **44**, 1.
156. S. R. Wilson, H. Maleroed, D. Petersen, N. Simic, M. M. Bobu, F. Rise, E. Lundanes and T. Greibrokk, *J. Sep. Sci.*, 2006, **29**, 582.
157. A. J. Simpson, L. H. Tseng, M. J. Simpson, M. Spraul, U. Braumann, W. L. Kingery, B. P. Kelleher and M. H. B. Hayes, *Analyst*, 2004, **129**, 1216.
158. T. E. Glass and H. C. Dorn, *J. Magn. Reson.*, 1983, **51**, 527.
159. A. G. Webb, *Magn. Reson. Chem.*, 2005, **43**, 688.
160. R. L. Haner, W. Llanos and L. Mueller, *J. Magn. Reson.*, 2000, **143**, 69.
161. B. Behnke, G. Schlotterbeck, U. Tallarek, S. Strohschein, L. H. Tseng, T. Keller, K. Albert and E. Bayer, *Anal. Chem.*, 1996, **68**, 1110.
162. D. L. Olson, M. E. Lacey and J. V. Sweedler, *Anal. Chem.*, 1998, **70**, 257A.
163. N. Wu, T. L. Peck, A. G. Webb, R. L. Magin and J. V. Sweedler, *Anal. Chem.*, 1994, **66**, 3849.
164. D. L. Olson, T. L. Peck, A. G. Webb, R. L. Magin and J. V. Sweedler, *Science*, 1995, **270**, 1967.
165. D. L. Olson, M. E. Lacey and J. V. Sweedler, *Anal. Chem.*, 1998, **70**, 645.
166. D. L. Olson, M. E. Lacey, A. G. Webb and J. V. Sweedler, *Anal. Chem.*, 1999, **71**, 3070.
167. R. Subramanian, W. P. Kelley, P. D. Floyd, Z. J. Tan, A. G. Webb and J. V. Sweedler, *Anal. Chem.*, 1999, **71**, 5335.
168. M. E. Lacey, Z. J. Tan, A. G. Webb and J. V. Sweedler, *J. Chromatogr. A*, 2001, **922**, 139.

169. A. M. Wolters, D. A. Jayawickrama, A. G. Webb and J. V. Sweedler, *Anal. Chem.*, 2002, **74**, 5550.
170. D. L. Olson, J. A. Norcross, M. O'Neil-Johnson, P. F. Molitor, D. J. Detlefsen, A. G. Wilson and T. L. Peck, *Anal. Chem.*, 2004, **76**, 2966.
171. M. E. Lacey, J. V. Sweedler, C. K. Larive, A. J. Pipe and R. D. Farrant, *J. Magn. Reson.*, 2001, **153**, 215.
172. A. B. Schefer and K. Albert, in: *On-Line LC-NMR and Related Techniques*, K. Albert ed., Wiley, West Sussex, England, 2002, p. 237.
173. N. Wu, A. Webb, T. L. Peck and J. V. Sweedler, *Anal. Chem.*, 1995, **67**, 3101.
174. P. Hentschel, M. Krucker, M. D. Grynbaum, K. Putzbach, R. Bischoff and K. Albert, *Magn. Reson. Chem.*, 2005, **43**, 747.
175. H. B. Xiao, M. Krucker, K. Putzbach and K. Albert, *J. Chromatogr. A*, 2005, **1067**, 135.
176. M. Sandvoss, A. D. Roberts, I. M. Ismail and S. E. North, *J. Chromatogr. A*, 2004, **1028**, 259.
177. Y. Li, M. E. Lacey, J. V. Sweedler and A. G. Webb, *J. Magn. Reson.*, 2003, **162**, 133.
178. R. A. Kautz, M. E. Lacey, A. M. Wolters, F. Foret, A. G. Webb, B. L. Karger and J. V. Sweedler, *J. Am. Chem. Soc.*, 2001, **123**, 3159.
179. A. M. Wolters, D. A. Jayawickrama, C. K. Larive and J. V. Sweedler, *Anal. Chem.*, 2002, **74**, 4191.
180. A. M. Wolters, D. A. Jayawickrama, C. K. Larive and J. V. Sweedler, *Anal. Chem.*, 2002, **74**, 2306.
181. A. M. Wolters, D. A. Jayawickrama and J. V. Sweedler, *J. Nat. Prod.*, 2005, **68**, 162.
182. A. K. Korir, V. K. Almeida, D. S. Malkin and C. K. Larive, *Anal. Chem.*, 2005, **77**, 5998.
183. V. K. Almeida and C. K. Larive, *Magn. Reson. Chem.*, 2005, **43**, 755.
184. L. A. Cardoza, V. K. Almeida, A. Carr, C. K. Larive and D. W. Graham, *TrAC, Trends Anal. Chem.*, 2003, **22**, 766.
185. J. Schewitz, P. Gfrorer, K. Pusecker, L. H. Tseng, K. Albert, E. Bayer, I. D. Wilson, N. J. Bailey, G. B. Scarfe, J. K. Nicholson and J. C. Lindon, *Analyst*, 1998, **123**, 2835.
186. P. Gfroerer, J. Schewitz, K. Pusecker, L. H. Tseng, K. Albert and E. Bayer, *Electrophoresis*, 1999, **20**, 3.
187. P. Gfrorer, J. Schewitz, K. Pusecker and E. Bayer, *Anal. Chem.*, 1999, **71**, 315A.
188. D. A. Jayawickrama, A. M. Wolters and J. V. Sweedler, *Electrokinetic Phenomena*, 2004, 311.
189. M. E. Lacey, R. Subramanian, D. L. Olson, A. G. Webb and J. V. Sweedler, *Chem. Rev.*, 1999, **99**, 3133.
190. T. L. Peck, R. L. Magin and P. C. Lauterbur, *J. Magn. Reson. B.*, 1995, **108**, 114.
191. R. Subramanian and A. G. Webb, *Anal. Chem.*, 1998, **70**, 2454.
192. R. Subramanian, J. V. Sweedler and A. G. Webb, *J. Am. Chem. Soc.*, 1999, **121**, 2333.
193. W. Peti, J. Norcross, G. Eldridge and M. O'Neil-Johnson, *J. Am. Chem. Soc.*, 2004, **126**, 5873.
194. J. F. Hu, E. Garo, H. D. Yoo, P. A. Cremin, M. G. Goering, M. O'Neil-Johnson and G. R. Eldridge, *Phytochemistry*, 2005, **66**, 1077.
195. M. Gronquist, J. Meinwald, T. Eisner and F. C. Schroeder, *J. Am. Chem. Soc.*, 2005, **127**, 10810.
196. A. Jansma, T. Chuan, R. W. Albrecht, D. L. Olson, T. L. Peck and B. H. Geierstanger, *Anal. Chem.*, 2005, **77**, 6509.
197. P. Froehlich, *Am. Lab.*, 2005, **37** 54, 56.
198. J. F. Hu, E. Garo, H. D. Yoo, P. A. Cremin, L. Zeng, M. G. Goering, M. O'Neil-Johnson and G. R. Eldridge, *Phytochem. Anal.*, 2005, **16**, 127.
199. Y. Li, T. M. Logan, A. S. Edison and A. Webb, *J. Magn. Reson.*, 2003, **164**, 128.
200. G. Fisher, C. Petucci, E. Macnamara and D. Raftery, *J. Magn. Reson.*, 1999, **138**, 160.
201. E. MacNamara, T. Hou, G. Fisher, S. Williams and D. Raftery, *Anal. Chim. Acta*, 1999, **397**, 9.
202. T. Hou, E. Macnamara and D. Raftery, *Anal. Chim. Acta*, 1999, **400**, 297.
203. T. Hou, J. Smith, E. Macnamara, M. Macnaughtan and D. Raftery, *Anal. Chem.*, 2001, **73**, 2541.
204. M. A. Macnaughtan, T. Hou, E. Macnamara, R. E. Santini and D. Raftery, *J. Magn. Reson.*, 2002, **156**, 97.
205. M. A. Macnaughtan, T. Hou, J. Xu and D. Raftery, *Anal. Chem.*, 2003, **75**, 5116.
206. M. A. Macnaughtan, A. P. Smith, P. B. Goldsbrough, R. E. Santini and D. Raftery, *Anal. Bioanal. Chem.*, 2004, **378**, 1520.
207. Y. Li, A. M. Wolters, P. V. Malawey, J. V. Sweedler and A. G. Webb, *Anal. Chem.*, 1999, **71**, 4815.

208. X. Zhang, J. V. Sweedler and A. G. Webb, *J. Magn. Reson.*, 2001, **153**, 254.
209. L. Ciobanu, D. A. Jayawickrama, X. Zhang, A. G. Webb and J. V. Sweedler, *Angew. Chem. Int. Ed. Engl.*, 2003, **42**, 4669.
210. D. A. Jayawickrama and J. V. Sweedler, *Anal. Chem.*, 2004, **76**, 4894.
211. N. Murali, W. M. Miller, B. K. John, D. A. Avizonis and S. H. Smallcombe, *J. Magn. Reson.*, 2006, **179**, 182.
212. H. Wang, L. Ciobanu, A. S. Edison and A. G. Webb, *J. Magn. Reson.*, 2004, **170**, 206.
213. H. Wang, L. Ciobanu and A. Webb, *J. Magn. Reson.*, 2005, **173**, 134.
214. P. Styles, N. F. Soffe, C. A. Scott, D. A. Cragg, F. Row, D. J. White and P. C. J. White, *J. Magn. Reson.*, 1984, **60**, 397.
215. W. A. Anderson, W. W. Brey, A. L. Brooke, B. Cole, K. A. Delin, L. F. Fuks, H. D. W. Hill, M. E. Johanson, V. Y. Kotsubo, R. Nast, R. S. Withers and W. H. Wong, *Bull. Magn. Reson.*, 1995, **17**, 98.
216. O. Corcoran and M. Spraul, *Drug Discov. Today*, 2003, **8**, 624.
217. M. Spraul, A. S. Freund, R. E. Nast, R. S. Withers, W. E. Maas and O. Corcoran, *Anal. Chem.*, 2003, **75**, 1536.
218. S. Bieri, E. Varesio, J. L. Veuthey, O. Munoz, L. H. Tseng, U. Braumann, M. Spraul and P. Christen, *Phytochem. Anal.*, 2006, **17**, 78.
219. J. Ruzicka and E. H. Hansen, *Anal. Chim. Acta*, 1975, **78**, 145.
220. J. Ruzicka and E. H. Hansen, *Flow Injection Analyses*, Wiley, New York, NY, 1988.
221. B. Karlberg and G. E. Pacey, *Flow Injection Analysis – A Practical Guide*, Elsevier, New York, 1989.
222. Z. Fang, *Flow Injection Separation and Preconcentration*, VCH, New York, 1993.
223. M. Trojanowicz, *Flow Injection Analysis: Instrumentation and Applications*, World Scientific, Singapore, 2000.
224. C. J. Patton and A. P. Wade, in: *Analytical Instrumentation Handbook*, G. W. Ewing ed., Marcel Dekker, Inc., New York, NY, 1997, p. 125.
225. T. L. Skeggs, *Anal. Chem.*, 1966, **38**, 31A.
226. C. Pasquini and W. A. de Oliveira, *Anal. Chem.*, 1985, **57**, 2575.
227. C. Pasquini, *Anal. Chem.*, 1986, **58**, 2346.
228. C. J. Patton and S. R. Crouch, *Anal. Chim. Acta*, 1986, **179**, 189.
229. L. -C. Tian, X. -P. Sun, Y. -Y. Xu and Z. -L. Zhi, *Anal. Chim. Acta*, 1990, **238**, 183.
230. Z. -L. Zhi, *Trends Anal. Chem.*, 1998, **17**, 411.
231. Y. Hsieh and S. R. Crouch, *Anal. Chim. Acta*, 1995, **303**, 231.
232. B. Behnia and A. G. Webb, *Anal. Chem.*, 1998, **70**, 5326.
233. M. Spraul, M. Hofmann, J. C. Lindon, R. D. Farrant, M. J. Seddon, J. K. Nicholson and I. D. Wilson, *NMR Biomed.*, 1994, **7**, 295.
234. J. K. Roberts and R. J. Smith, *J. Chromatogr. A*, 1994, **677**, 385.
235. N. Mistry, I. M. Ismail, M. S. Smith, J. K. Nicholson and J. C. Lindon, *J. Pharm. Biomed. Anal.*, 1997, **16**, 697.
236. C. L. Gavaghan, J. K. Nicholson, S. C. Connor, I. D. Wilson, B. Wright and E. Holmes, *Anal. Biochem.*, 2001, **291**, 245.
237. H. Pham-Tuan, L. Kaskavelis, C. A. Daykin and H. G. Janssen, *J. Chromatogr. B Anal. Tech. Biomed. Life Sci.*, 2003, **789**, 283.
238. K. E. Price, S. S. Vandaveer, C. E. Lunte and C. K. Larive, *J. Pharm. Biomed. Anal.*, 2005, **38**, 904.
239. J. D. Otvos, *Clin. Lab.*, 2002, **48**, 171.
240. D. S. Wishart, L. M. M. Querengesser, B. A. Lefebvre, N. A. Epstein, R. Greiner and J. B. Newton, *Clin. Chem.*, 2001, **47**, 1918.
241. R. D. Farrant, M. Spraul, I. D. Wilson, A. W. Nicholls, J. K. Nicholson and J. C. Lindon, *J. Pharm. Biomed. Anal.*, 1995, **13**, 971.
242. U. G. Sidelmann, C. Gavaghan, H. A. J. Carless, R. D. Farrant, J. C. Lindon, I. D. Wilson and J. K. Nicholson, *Anal. Chem.*, 1995, **67**, 3401.
243. U. G. Sidelmann, C. Gavaghan, H. A. J. Carless, M. Spraul, M. Hofmann, J. C. Lindon, I. D. Wilson and J. K. Nicholson, *Anal. Chem.*, 1995, **67**, 4441.

244. E. M. Lenz, D. Greatbanks, I. D. Wilson, M. Spraul, M. Hofmann, J. Troke, J. C. Lindon and J. K. Nicholson, *Anal. Chem.*, 1996, **68**, 2832.
245. J. L. Wolfender, E. F. Queiroz and K. Hostettmann, *Magn. Reson. Chem.*, 2005, **43**, 697.
246. K. Iwasa, W. Cui, M. Sugiura, A. Takeuchi, M. Moriyasu and K. Takeda, *J. Nat. Prod.*, 2005, **68**, 992.
247. J. W. Jaroszewski, *Planta Med.*, 2005, **71**, 795.
248. K. Putzbach, M. Krucker, M. D. Grynbaum, P. Hentschel, A. G. Webb and K. Albert, *J. Pharm. Biomed. Anal.*, 2005, **38**, 910.
249. J. F. Hu, H. D. Yoo, C. T. Williams, E. Garo, P. A. Cremin, L. Zeng, H. C. Vervoort, C. M. Lee, S. M. Hart, M. G. Goering, M. O'Neil-Johnson and G. R. Eldridge, *Planta Med.*, 2005, **71**, 176.
250. H. D. Yoo, P. A. Cremin, L. Zeng, E. Garo, C. T. Williams, C. M. Lee, M. G. Goering, M. O'Neil-Johnson, G. R. Eldridge and J. F. Hu, *J. Nat. Prod.*, 2005, **68**, 122.
251. J. F. Hu, E. Garo, M. G. Goering, M. Pasmore, H. D. Yoo, T. Esser, J. Sestrich, P. A. Cremin, G. W. Hough, P. Perrone, Y. S. Lee, N. T. Le, M. O'Neil-Johnson, J. W. Costerton and G. R. Eldridge, *J. Nat. Prod.*, 2006, **69**, 118.
252. H. Pasch, W. Hiller and R. Haner, *Polymer*, 1998, **39**, 1515.
253. L. C. M. Van Gorkom and T. M. Hancewicz, *J. Magn. Reson.*, 1998, **130**, 125.
254. W. Hiller, H. Pasch, T. Macko, M. Hofmann, J. Ganz, M. Spraul, U. Braumann, R. Streck, J. Mason and F. Van Damme, *J. Magn. Reson.*, 2006, **183**, 309.
255. J. C. Lindon, R. D. Farrant, P. N. Sanderson, P. M. Doyle, S. L. Gough, M. Spraul, M. Hofmann and J. K. Nicholson, *Magn. Reson. Chem.*, 1995, **33**, 857.
256. L. A. Cardoza, A. K. Korir, W. H. Otto, C. J. Wurrey and C. K. Larive, *Prog. Nucl. Magn. Reson. Spectrosc.*, 2004, **45**, 209.
257. L. A. Cardoza, B. J. Cutak, J. Ketter and C. K. Larive, *J. Chromatogr. A*, 2004, **1022**, 131.
258. T. Marquardsen, M. Hofmann, J. G. Hollander, C. M. P. Loch, S. R. Kiihne, F. Engelke and G. Siegal, *J. Magn. Reson.*, 2006, **182**, 55.
259. A. Hirayama, O. Shirota, M. Nomura, A. Nagadoi and Y. Nishimura, *Anal. Biochem.*, 2006, **353**, 99.
260. R. Gonzalez-Mendez, D. Wemmer, G. Hahn, N. Wade-Jardetzky and O. Jardetzky, *Biochim. Biophys. Acta*, 1982, **720**, 274.
261. A. A. De Graaf, R. M. Wittig, U. Probst, J. Strohhaecker, S. M. Schoberth and H. Sahm, *J. Magn. Reson.*, 1992, **98**, 654.
262. E. N. Lightfoot, A. M. Athalye, J. L. Coffman, D. K. Roper and T. W. Root, *J. Chromatogr.*, 1995, **707**, 45.
263. D. L. VanderHart, in: *Encyclopedia of Nuclear Magnetic Resonance*, D. M. Grant and R. K. Harris, eds., Wiley, West Sussex, England, 1996, p. 2938.
264. F. D. Doty, G. Entzminger and Y. A. Yang, *Concepts Magn. Reson.*, 1998, **10(3)**, 133.
265. D. A. Jayawickrama, A. M. Wolters and J. V. Sweedler, *Analyst*, 2003, **128**, 421.
266. M. E. Lacey, A. G. Webb and J. V. Sweedler, *Anal. Chem.*, 2000, **72**, 4991.
267. S. Akoka, L. Barantin and M. Trierweiler, *Anal. Chem.*, 1999, **71**, 2554.
268. V. Silvestre, S. Goupry, M. Trierweiler, R. Robins and S. Akoka, *Anal. Chem.*, 2001, **73**, 1862.
269. M. Maiwald, T. Grutzner, E. Strofer and H. Hasse, *Anal. Bioanal. Chem.*, 2006, **385**, 910.

This page intentionally left blank

Vanadium-51 NMR

D. REHDER[1], T. POLENOVA[2] AND M. BÜHL[3]

[1]*Department Chemie, Universität Hamburg, 20146 Hamburg, Germany*
[2]*Department of Chemistry and Biochemistry, Universitay of Delaware, Newark DE 19716, USA*
[3]*Max-Planck Institut für Kohlenforschung, 45470 Mülheim, Germany*

The quadrupolar nucleus ^{51}V is particularly well suited for NMR due to its rather small nuclear quadrupole moment and high sensitivity. The use of vanadium compounds in catalysis, and the biological and medicinal implications of the element vanadium, have initiated extensive studies into NMR characteristics of natural and model systems, revealing information on the (coordination) environment of inorganic, organic, and coordination compounds of vanadium in solution, in the solid state, and in meso-phases. We report here on chemical shift (shielding) data, scalar coupling constants, dipolar, first and second order quadrupole interactions in isotropic, partially ordered, and (crystalline and amorphous) solid systems. These fine structure constants are discussed in the context of electronic and steric influences imparted by the vanadium environments, and in conjunction with modern computational methods to approach a deeper understanding of the factors influencing NMR parameters.

ANNUAL REPORTS ON NMR SPECTROSCOPY
VOLUME 62 ISSN 0066 4103
DOI 10.1016/S0066-4103(07)62002-X

1. INTRODUCTION

Vanadium chemistry has experienced a drastic upswing during the last two decades, predominantly initiated by the discovery of vanadium-based enzymes (vanadate-dependent haloperoxidases and vanadium-nitrogenases in the early and mid-eighties), a possible general role of vanadium as a regulator of phosphate-metabolizing enzymes, including the potential of vanadium compounds in the treatment of *diabetes mellitus*, and the use of high- and low-valent vanadium compounds in oxidation and reduction catalysis, and as polymerization catalysts. Soluble "vanadium oxides" (polyoxovanadates) are intensely investigated for their properties as oxo-transfer catalysts in "green" chemistry and with respect to their intrinsic magnetic properties, as are solid vanadium oxide-based materials, which are now also employed in re-chargeable batteries. Inorganic and organovanadium compounds and, more generally, coordination compounds of vanadium have thus attained increasing importance in biological and medicinal chemistry as well as in material science and catalysis.

The scope of the present review, which is the first comprehensive one since Howarth's survey in 1991,[1] is to acquaint the vanadium chemist with vanadium-NMR as a powerful tool in elucidating the electronic structure at the vanadium nucleus as influenced by the inner and outer sphere electronic situation, reflecting electronic and steric factors induced by the nature and the arrangement of the ligands, the ligand periphery, and more remote spheres such as constituted by solvent molecules or next neighbors in a solid state structure. The survey is subdivided according to the nature of the phase under investigation: isotropic (common solutions), solid state, and meso-phases. A chapter on computational approaches is included to underline the benefits for inter-relating experimental and computational results.

The range of oxidation states covered by vanadium encompasses –III to +V, including three oxidation states (–III, d^8; –I, d^6; +V, d^0) where vanadium intrinsically is diamagnetic and thus susceptible to NMR, and three oxidation states in which vanadium may be diamagnetic under certain conditions, *viz.* +I (d^4 low spin), +III (d^2, low spin), and +IV (d^1, dinuclear anti-ferromagnetically coupled). There are actually two magnetic vanadium nuclei, ^{50}V and ^{51}V. Due to the sufficiently more favorable properties of the nucleus ^{51}V (Table 1), this is the one which is almost exclusively used in analytical vanadium NMR spectroscopy. For ^{50}V NMR see, e.g., Lutz *et al.*[2] The ^{51}V nucleus has a nuclear spin of 7/2 and thus belongs to the quadrupolar nuclei, for which relaxation times are short. This is an advantage as it comes to measuring times, but a disadvantage with respect to line widths and thus resolution in solution. This disadvantage is, at least in part, counter-balanced by the broad shift range (*cf.* Section 2.1). Among the quadrupolar transition metal nuclei, ^{51}V is unique because of its rather small quadrupole moment of $-4.8\,fm^2$ and high receptivity of 0.38 relative to ^1H.[3] These properties, along with the resonance frequency close to that of ^{13}C, make the nucleus ^{51}V easily accessible to both conventional NMR (one-dimensional in solution) and more sophisticated investigations (two-dimensional methods, solid-state NMR). The favorable properties of the ^{51}V nucleus as based on its high natural abundance, the

Table 1. Parameters for the nuclei ^{50}V and ^{51}V

	Nuclear spin	Q^a fm^2	γ^c 10^7 rad s^{-1} T^{-1}	Abundance (%)	Receptivity relative ^1H	Frequency (MHz)^d	Reference compound
^{50}V	6	+21	+2.6721	0.24	1.3×10^{-4}	9.988	–
^{51}V	7/2	−4.8^b	+7.0492	99.76	0.38	26.350	$VOCl_3$^{e}

[a]Nuclear quadrupole moment.
[b]Until recently, the adopted value for $Q(^{51}V)$ was −5.2 fm^2; for justification of the value −4.8(1), see ref. 3; for discussion, see also Section 3.1.
[c]Magnetogyric ratio.
[d]Measuring frequency at 2.35 T (where ^1H in TMS resonates at 100 MHz).
[e]$VOCl_3$ neat, $\delta = 0$ ppm. For convenience, an aqueous solution of 1 M sodium vanadate at pH 12, containing the VO_4^{3-} ($\delta = -535.7$ relative to $VOCl_3$) and $V_2O_7^{4-}$ anions ($\delta = -559.0$) may be employed.

small quadrupole moment, and the large shift range (high sensitivity to minor variations in the local electronic situation) allow for an easy acquisition of well resolved vanadium NMR spectra even in the sub-millimolar concentration range, often including access to resolved nuclear coupling to other magnetic nuclei in the coordination sphere of vanadium compounds of a comparatively high local symmetry.

The present review will concentrate on developments during the past decade and include earlier results only where needed for a comprehensive treatment and understanding of more recent applications. Previous reviews cover the state of the art in vanadium NMR,[1] vanadium NMR in the context of NMR studies of other transition metal nuclei,[4] vanadium compounds in biological systems,[5a] organovanadium compounds,[5b,c] polyoxovanadates,[6] and solid state studies on vanadia-based catalysts.[7]

2. ISOTROPIC SYSTEMS

Common solutions of vanadium compounds in water or organic solvents are isotropic, i.e., there are no favored orientations of the compounds due to irregular tumbling. As a consequence, the NMR parameters obtained from the spectra reflect averaged conditions. Parameters extracted from the experimental spectra are chemical shifts (shielding), nuclear spin–spin coupling (scalar coupling) constants, and line widths. The latter are related to the electric field gradient at the vanadium nucleus and the molecular correlation time, and – in the case of dynamic systems, i.e., exchange equilibria between two or more species on the sub-millisecond scale – kinetic and thermodynamic parameters. Due to its low nuclear quadrupole moment, ^{51}V is susceptible to NMR in almost every environment, including slowly tumbling vanadium-containing systems and vanadium compounds with virtually no local symmetry. In certain cases, such as in vanadium–protein complexes, special detection modes, centered on the central ($m = +1/2 \rightarrow -1/2$) quadrupole transition, have to be envisaged. Precondition for NMR sensitivity is, of course, the

diamagnetic nature of the vanadium compound. To a certain extent, however, paramagnetic impurities, such as $V^{IV}O^{2+}$ in V^{V} systems, are tolerable (although accompanied by a deterioration of the signal-to-noise), as long as there is no exchange between V^{IV} and V^{V}. The anionic polyoxovanadate $[GeV^{V}_{12}V^{IV}_{2}O_{40}]^{8-}$ is an example of a compound where three ^{51}V NMR signals corresponding to three distinct V^{V} sites have been detected despite of the presence of two isolated V^{IV} centers (which in turn are detectable by EPR).[8] Similarly, the dithiocarbazato (ONS) complex $[\{V^{IV}O(ONS)\}\mu\text{-}O\{V^{V}O(ONS)]^{-}$ provides signals in the EPR and ^{51}V NMR spectra.[9]

2.1. Shielding

Chemical shifts δ are related to shielding σ by $\delta = \sigma_{ref} - \sigma$, where σ_{ref} refers to the reference compound (standard). In compounds with negative δ values, i.e., those which resonate to high field (low frequency) of the standard, the vanadium nucleus is thus more shielded than the standard, and vice versa. The isotropic shielding constant σ, generally an unsymmetrical 3×3 tensor with the principal values σ_{11}, σ_{22}, and σ_{33} ($\sigma = 1/3/(\sigma_{11} + \sigma_{22} + \sigma_{33})$) can be expressed as the sum of three terms, Eq. (1):

$$\sigma = \sigma_{dia} + \sigma_{para} + \sigma_{nl} \tag{1}$$

where σ_{dia} and σ_{para} are the local diamagnetic and paramagnetic terms, respectively and σ_{nl} corresponds to non-local contributions (by ligand functions) to overall shielding. In $^{1,2}H$ NMR spectroscopy, σ_{dia} commonly is the dominant component. In $^{6,7}Li$ NMR, σ_{dia} and σ_{para} about equivalently influence variations in shielding. For all heavier nuclei, variation in shielding is predominantly governed by σ_{para}. For the diamagnetic contribution, Eq. (2a) applies.

$$\sigma_{dia} = \frac{e^2}{3mc^2} \times (<0|\sum r_i^{-1}|0> P_i). \tag{2a}$$

Here, $<r_i^{-1}>$ is the expectation value for the distance of the i-th electron from the nucleus, and P_i the population in the i-th orbital. The term σ_{dia} is essentially constant, because influenced by the inner shell electrons. The non-local term σ_{nl}, which amounts to several ppm only, again plays a secondary – and often negligible – role.

When dealing with variations in shielding, we are hence left with variations in the paramagnetic term σ_{para} which, following the crystal-field formalism introduced by Ramsey,[10] can be expressed, in a somewhat simplified way, by Eq. (2b),

$$\sigma_{para} = \frac{-e^2}{2mc^2} \times \sum (E_n - E_0)^{-1} <r^{-3}>_{3d} <0|\underline{L}^2|n> \tag{2b}$$

where r_{3d} refers to the distance of the $3d$ electrons, and $(E_n - E_0)^{-1} = \Delta E^{-1}$ is the energy separation between ground state ($<0|$) and relevant exited states ($|n>$).

Relevant excited states are those which have the transformation properties of the angular momentum operator L and can thus mix with the ground state. This condition restricts the number of excited states to be considered, in particular in compounds of high symmetry (such as cubic symmetry). In most cases, it is convenient to employ the average energy approximation, including covalent contributions by the so-called orbital reduction factor k'^2,[11] Eq. (2c), where $(\Delta E^{-1})_{av}$ is the mean excitation energy.

$$\sigma_{para} = -\text{const} \times (\Delta E^{-1})_{av} < r^{-3} >_{3d} k'^2. \quad (2c)$$

The parameters $(\Delta E^{-1})_{av}$, $< r^{-3} >_{3d}$ and k'^2 are respectively related to the strength of the ligand field, the nephelauxetic effect, and the covalency of the metal-ligand bond. In the light of these main factors influencing ^{51}V shielding, shielding trends will be discussed below. More elaborate expressions for σ_{dia} and σ_{para} have been derived within quantum-mechanical molecular orbital schemes; see discussion in Section 5.1.

The chemical shift observed under isotropic conditions, δ_{obs}, commonly is the isotropic shift δ_{iso}. In the condition of slow isotropic molecular motion (''far from extreme narrowing''), encountered with macromolecules such as V^V firmly coordinated to a protein, δ_{obs} and δ_{iso} differ. Under these conditions, the fairly sharp central transition corresponding to $m_I = +1/2 \rightarrow -1/2$ is the observable. Here δ_{obs} becomes a function of the applied magnetic field.

2.1.1. *Inorganic vanadium compounds*

The shielding range covered by inorganic vanadates(V) covers the range of +2570 ($[VSe_4]^{3-}$) to −895 (VF_5). Soft substituents (Se^{2-}, S^{2-}, Br^-, Cl^-) induce low shielding and thus low-field shifts (low-field referring to the magnetic field), while hard substituents (O^{2-}, OH^-, F^-) give rise to high-field shifts. These trends, which are sometimes referred to as ''inverse electronegativity dependence of shielding'' in high-valent (d^0) systems, can be interpreted in terms of increasing ΔE and decreasing k (decreasing covalency of the V-X bond) as the electronegativity of X increases.[12] According to Eq. (2b), both effects lead to a decrease of σ_{para} and thus to an increase of overall shielding; Eq. (1). Upfield shifts with respect to the oxo function are observed for the peroxo ligand O_2^{2-} and the isoelectronic hydroxylamido ligand R_2NO^-.

Depending on the pH, the concentration, and the ionic strength, aqueous vanadate solutions prepared by dissolving metavanadate (e.g., $NaVO_3$) or orthovanadate (e.g., Na_3VO_4) can contain a variety of vanadate species in different protonation and condensation states; compare Fig. 1a for a selection. The speciation of these systems has extensively and thoroughly been investigated by Pettersson, based on a combination of proton potentiometry and ^{51}V NMR.[12] Fig. 1b and Table 2 provide details on the pH/δ dependence in the vanadate system. The predominant species present in the vanadate system at ambient pH are monovanadate, divanadate, cyclic and linear tetravanadate, and pentavanadate. These species are in

(a)

H$_n$V$_{10}$O$_{28}$(6-n)-
H$_2$V$_2$O$_7^{2-}$/HV$_2$O$_7^{3-}$
V$_4$O$_{12}^{4-}$
V$_5$O$_{15}^{5-}$

Va
Vb
Vc

(b)

Shift/ppm
pH
V1
V2
I-V4/V3
V4
V5
V10
V10'
V10''

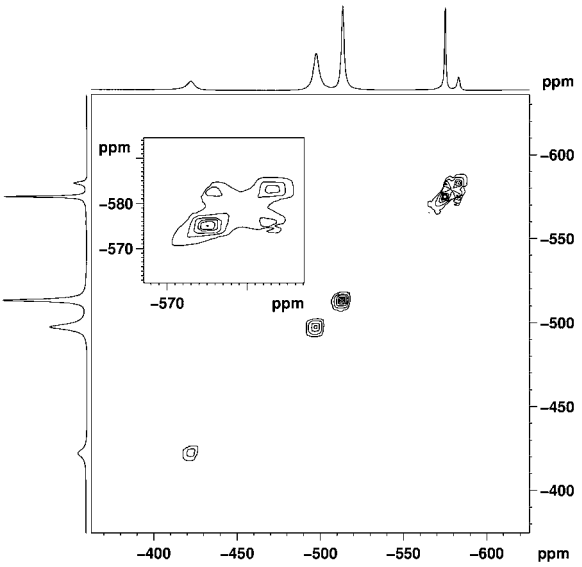

Fig. 2. The diagonal of the EXSY spectrum shows the three resonances of decavanadate (−422, −498, −513; *cf.* Fig. 1a) plus the resonances for di- (−575) and tetra-/pentavanadate (−583). Only the latter two exchange which each other (inset). The spectrum has been obtained at a mixing time of 1 msec. Conditions: 0.8 M aqueous vanadate, pH = 6.

exchange with each other on the millisecond scale, as has been shown by ^{51}V EXSY spectroscopy.[14] Below pH 6.3, decavanadate is formed at the expense of all of the remaining species, and in highly acidic medium, cationic $[VO_2(H_2O)_4]^+$ prevails. Decavanadate, easily detectable by is yellow color, contains three different vanadium sites (Fig. 1a) in the ratio 1 : 2 : 2, each of which is represented by a distinct ^{51}V NMR resonance. It is kinetically rather stable at pH values above its thermodynamically dictated range of existence. A transient situation, at pH 6, is shown in Fig. 2. In the presence of phosphate, mixed phosphovanadates form (Table 2).[15] The experimental chemical shift δ_{exp} of the monovanadate species can be employed to determine the pH of the medium.[16]

$$\mathrm{pH} = \mathrm{p}K_a + \frac{\log(\delta_2 - \delta_{exp})}{\delta_{exp} - \delta_1}$$

where $pK_a = 8.17$ (in 0.15 NaCl, i.e., isotonic conditions), and δ_1 and δ_2 are the shift values for HVO_4^{2-} (−538.8) and $H_2VO_4^-$ (−560.4).

Fig. 1. (a) Vanadate species present in aqueous solution. Right: Decavanadate; the labels indicate the three different vanadium and seven different oxo sites. The bridging oxo functions B and C are the protonation sites. (b) pH dependence of the species distribution and chemical shift in the aqueous vanadate system. For the V_n, *cf.* part a. l-V4/V3 stands for linear tetra-/trivanadate. (Courtesy by L. Pettersson, Umeå University, Sweden.)

Table 2. Chemical shift values of selected inorganic vanadium compounds (in water if not indicated otherwise)

Inorganic vanadium compounds	$\delta(^{51}V)$	References.	Inorganic vanadium compounds	$\delta(^{51}V)$	Reference
VO_4^{3-}	−541	[1,12]	$HVO_3(O_2)^{2-}$	−625	[20]
HVO_4^{2-}	−534	[1,12]	$HVO_2(O_2)_2^{2-}$	−765	[20]
$H_2VO_4^-$	−560	[1,13]	$H_2VO_2(O_2)_2^-$	−691	[20]
$V_2O_7^{4-}$	−561	[1,13]	$HVO(O_2)_3^{2-}$	−732	[20]
$HV_2O_7^{3-}$	−564	[1,13]	$HV_2O_6(O_2)^{3-}$	−622, −563[b]	[20]
$H_2V_2O_7^{2-}$	−573	[1,13]	$HV_2O_5(O_2)_2^{3-}$	−737, −555[b]	[20]
$V_3O_{10}^{5-}$	−556, −590	[1,13]	$HV_2O_3(O_2)_4^{3-}$	−755	[20]
$[Bu_4N]_n[V_3O_9]^{(3-n)-}$ (CD$_3$CN)	−555 ($n = 0$) to −628 ($n = 3$)	[17,18]	$V(O_2)_3^-$	−847	[22]
$V_4O_{13}^{6-}$	−569, −585	[1,13]			
$V_4O_{12}^{4-}$	−578	[1,13]	$H_2VO_3(NH_2O)$	−670	[23]
$V_5O_{15}^{5-}$	−586	[1,13]	$HVO_2(NH_2O)_2$	−819, −839[c]	[23]
$V_5O_{14}^{3-}$ (CD$_3$CN)	−538, −613	[18]	$HVO_2(NH_2O)_2(H_2O)$	−852, −861[c]	[23]
$V_{10}O_{28}^{6-}$	−418, −492, −510[a]	[12]			
$H_2V_{10}O_{28}^{4-}$	−422, −502, −519[a]	[12]	$VO_2F_2^-$	−595	[24]
$V_{12}O_{32}^{4-}$ (CD$_3$CN)	−590, −597, −605[a]	[17]	VOF_4^- (CD$_3$CN)	−797	[24]
$[VO_2(H_2O)_4]^+$	−546	[1,13]	$VO(O_2)_2F^{2-}$ (CD$_3$CN)	−714	[25]
$HPVO_7^{3-}$	−570	[15]	$H_2F_6NaVW_{17}O_{56}^{8-}$	−505, −516[d]	[24]
$H_2PVO_7^{2-}$	−583	[15]	$VO_2Cl_2^-$ (CD$_3$CN)	−364	[1]
$HP_2VO_{10}^{4-}$	−549	[15]	$VOCl_2F_2^-$ (CD$_3$CN)	−474/−424[e]	[1]
			$VOCl_4^-$ (CD$_3$CN)	+43	[1]
$VOBr_3$ (neat)	+432	[12]			
$VOCl_3$ (neat)	0	[12]	$VS_nO_{4-n}^{3-}$	+1395 to −250[f]	[26]
VOF_3 (THF)	−757	[12]	VS_4^{3-} (solid)	+1574	[26]
$VO(NO_3)_3$ (CD$_3$CN)	−749	[1]	$V_2S_7^{4-}$	+1457	[26]
			VSe_4^{3-}	+2570	[26]
VF_5 ($CDCl_3$)	−895	[1]			

[a]Intensity ratio $1(V_C):2(V_A):2(V_B)$ (*cf.* Fig. 1).
[b]The low field signal represents vanadium in the non-peroxo moiety of the divanadate.
[c]Two isomers.
[d]Intensity ratio approximately 1 : 2.
[e]For the *cis* and *trans* isomer, respectively.
[f]For $n = 4$–1.

In non-aqueous media, additional vanadate species can be detected and have been included in Table 2, such as cyclic trivanadate[17] and dodecavanadate.[18] Along with the protonation state, other factors influence the chemical shift: a counter-ion effect has been noted for solid state samples of $M^{II}[VO_4]_2$, ranging from comparatively low shielding for M = Zn (electronegativity (e.n.) = 1.7; $\delta_{iso} = -522$) to comparatively high shielding for M = Sr (e.n. = 1.0; $\delta_{iso} = -608$).[19] For the trivanadate $[V_3O_9]^{3-}$ shielding is sensitive to the extent of ion pairing;[17] *cf.* Table 2.

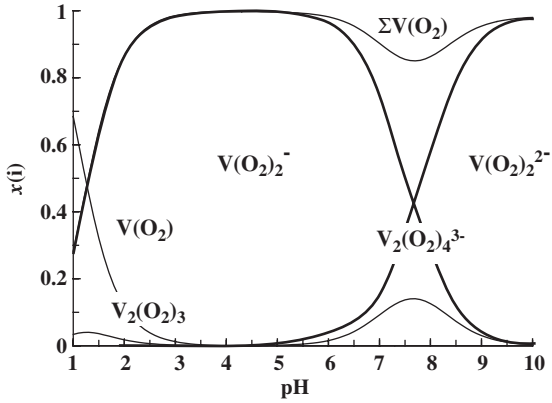

Fig. 3. Speciation diagram (mole fraction x(i) vs. pH) for peroxovanadium compounds at $c(V_{total}) = 10\,mM$, $c(H_2O_2)/c(V) = 2$, ionic strength 0.15 M Na(Cl), 25°C. Species containing less than 2% of V_{total} are not shown. (Courtesy by L. Pettersson, University of Umeå.)

Exchange of oxo for the η^2-peroxo groups gives rise to peroxovanadates, which exhibit a clearly higher shielding than the parent vanadates[20,21] (Table 2 and Fig. 3). The increase of shielding on introducing peroxo ligands is a generally observed phenomenon and will be addressed again in the context of coordination compounds containing the dioxo and oxo-peroxovanadium core (Section 2.1.2). A particularly high shielding, $\delta = -847$, has been reported for the *tris*(peroxo)metavanadate $[V(O_2)_3]^-$, which forms at pH 14. The species, the existence of which has been backed up by ESI-MS, is labile and decays to form $[VO(O_2)_2]^-$, $\delta = -764$.[22] The η^2-hydroxamido ligand H_2NO^-, which is isoelectronic to the peroxo ligand, induces a comparable high-field shift (see Table 2 for data). Contrasting peroxide, hydroxylamine can also coordinate in the end-on fashion via the oxygen, without any significant change in δ as compared with vanadate, i.e., $\delta = -569$ for $H_2VO_3(\eta^1\text{-}ONH_2)^{2-}$.[23] For a critical discussion on the existence of high pH peroxovanadates see also Section 5.2.

An upfield shift with respect to the parent vanadates is also observed for the fluorides derived from monovanadate and *bis*(peroxo)monovanadate[24,25] (Table 2), again a general observation in ^{51}V NMR spectroscopy. This trend has been exploited to assign the ^{51}V NMR signals for the Wells–Dawson type polyoxotungstate $[H_2F_6NaVW_{17}O_{56}]^{8-}$ to the vanadium centers disordered over the six end-capped positions (−502) and the twelve belt positions (−512), the latter experiencing a slightly higher shielding due to the proximity of the fluorides.[24]

As mentioned above, the soft sulfide and selenide functions induce effective deshielding, summarized in a recent review on binary vanadium chalcogenide complexes.[26] $[VSe_4]^{3-}$ $\delta = +2570$, in fact marks the low-field limit of the ^{51}V shielding scale. Note that, exemplified for $[VS_4]^{3-}$ the isotropic chemical shifts in solution (+1395) and in the solid state (+1574) differ from each other. In the cluster compound **1a** shown in Scheme 1, which derives from tetrathiovanadate, vanadium

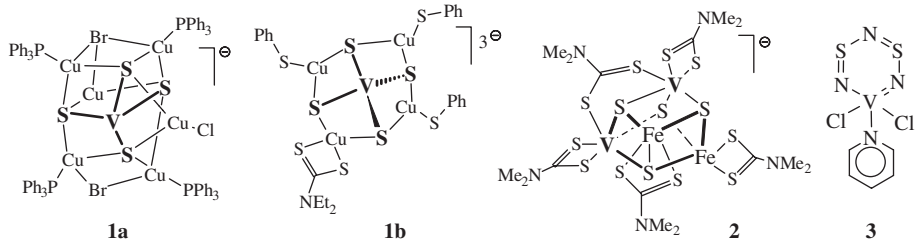

1a **1b** **2** **3**

Scheme 1.

is more shielded than in the parent $[VS_4]^{3-}$. Compound **1a** belongs to a larger family of clusters containing the core $\{VS_4Cu_n\}$, $n = 3-6$. Decreasing the number of copper centers leads to a decrease in shielding: $n = 6$ (**1a**), $\delta = +530$; $n = 3$, $\delta = +903$.[27] In the cluster anions **1b** ($\delta = +670$)[28] and **2** ($\delta = +663$),[29] a comparable shielding situation is observed. In **2**, sulfide ligands on vanadium are partially replaced by dithiocarbamate. Notably, shielding in **1b** (V^V) and **2** (V^{III}) are practically alike!

Deshielding is also observed in the series VOX_3, X = F, Cl, Br (Table 2), reflecting increasing softness of X. Shift values of mixed oxovanadiumtrihalides, such as $VOBr_nCl_{3-n}$, are ensued from linear interpolation between the limiting cases. There is a strong solvent dependence of shielding for $VOCl_3$. Solvents (*solv*) with donor functions, such as THF, MeCN, or pyridine can induce high-field shifts of up to 400 ppm as a consequence of (partial) exchange of Cl for *solv* and/or expansion of the coordination sphere by *solv*.[30] Finally, consistently low shielding comparable with that induced by the bromo ligand is also observed in cyclothiazeno vanadium complexes such as **3** ($\delta = +376$)[31] in Scheme 1.

2.1.2. *Vanadium coordination compounds*

In the presence of alcohols ROH, vanadate, in aqueous solution, forms weak esters typically of composition $HVO_3(OR)^-$ ($\delta = -551$), $VO_3(OR)^{2-}$ ($\delta = -528$), and $VO_2(OR)_2^-$ ($\delta = -543$).[32] The δ values indicated are for R = Me; for a more complete compilation of data see refs. 1, 4, and 5a. Under non-aqueous conditions, the triesters of "H_3VO_4", or oxovanadium-*tris*(alkoxides) $VO(OR)_3$ (−598 for R = Me), are obtained.

In Table 3, chemical shift values are summarized for neutral vanadium complexes of the general formula VEX_3, formally derived from hypothetic orthovanadium acid $H_3VO_4 \equiv VO(OH)_3$, where E is O^{2-} NR^{2-} or NPR_3^-, i.e., a function which is able to form double ($\sigma+\pi$) or triple ($\sigma+2\pi$) donor bonds to the V^V center. The three X ligands represent Cl^-, an alkoxo group OR^-, or an amino group NR_2^-. The following trends can be noted (*cf.* entry nos. in Table 3):

(1) Increasing replacement of Cl by OR increases shielding (entry no. 1), not unexpectedly, since the oxo function is harder (more electronegative) than

Table 3. Chemical shift values for vanadium compounds of the (idealized) composition VEX_3[a]

Entry	Vanadium compounds	δ [Ref.]	Entry	Vanadium compounds	δ [Ref.]
No. 1	$VOCl_3$ (neat)	0	No. 4a	Ph_3CNVCl_3 (CH_2Cl_2)	+49.3 [38]
	$VOCl_2$(O*i*Pr) (neat)	−309 [4c]		$Me_3SiNVCl_3$ (Tol)	+15.4 [38]
	{VOCl(O–O*i*Pr)(μ-Cl)}$_2$ **4**	−281 [33]			
	VOCl(O*i*Pr)$_2$ (neat)	−506 [4c]		*t*BuNVCl_3 (C_6D_6)	+9.5 [38]
	VO(O*i*Pr)$_3$ (neat)	−629 [4c]			
	VO(O*i*Pr)$_3$ ($CDCl_3$)	−597 [4c]	No. 4b	*t*BuNVCl_2N*i*Pr$_2$ (Tol)	−173 [38]
				*t*BuNV(N*i*Pr$_2$)$_3$ (Tol)	−272 [39]
No. 2	VO(OMe)$_3$ (solid)[b] **5**	−443, −451 [34]		*t*BuNVCl(N*i*Pr$_2$)O*t*Bu (Tol)	−436 [39]
	VO(OMe)$_3$ (*n*-pentane, $c = 0.52$)	−547.5 [36]			
	VO(OMe)$_3$ (*n*-pentane, $c = 0.012$)	−598.2 [36]	No. 5	$OVCl_4^-$ (CD_3CN)	+43 [1]
	VO(*cyclo*-C_5H_9)$_3$ ($CDCl_3$) **6** and **7**	−616, −623 [35]		Ph_3PNVCl_4	+228 [40]
				$Ph_3PNVCl_3(NPh_3)$ **8**	−225 [40]
No. 3	VO(O*n*Pr)$_3$ (neat)	−549 [4c,35]		$Ph_3PNVCl_2(NPh_3)_2$	−344 [40]
	VO(O*i*Pr)$_3$ (neat)	−629 [4c,36b]		$[V(NPh_3)_4]^+Cl^-$ **9**	−454 [40]
	VO(O*t*Bu)$_3$ (neat)	−672 [4c,36a]			
	VO(OAm)$_3$ (neat)	−684 [37]	No. 6	PhNV(O*i*Pr)$_3$ (CD_2Cl_2)	−628 [41]

[a]Bold numbers refer to structural formulae in Scheme 2. Abbreviations: Am, amyl; Tol, toluene.
[b]δ_{iso}.

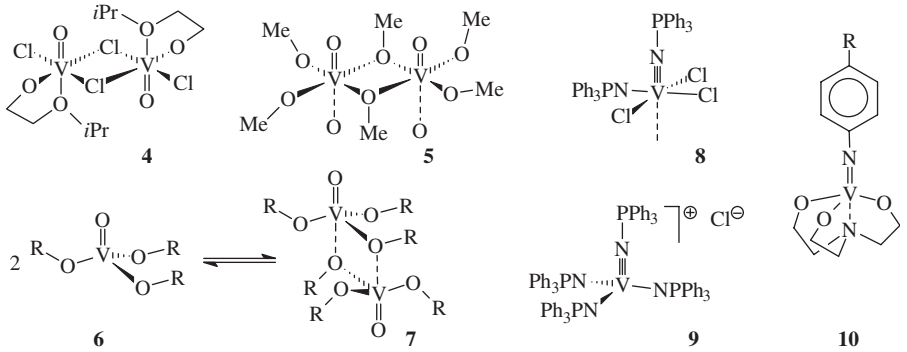

Scheme 2.

the chloro ligand (*cf.* ref. 3c). The dinuclear compound **4** (Scheme 2), which contains the 2-*iso*propoxyethanolato ligand,[33] smoothly fits into this series.

(2) Medium effects influence shielding, likely as a consequence of varying coordination numbers and geometrical arrangements of the alkoxo compounds, *viz.* distorted octahedral as in solid VO(OMe)$_3$ (**5** in Scheme 2)[34], distorted trigonal-bipyramidal as in VO(*cyclo*-C_5H_9)$_3$ (**7**)[35], or tetrahedral (**6**)

as for bulky groups R. In the case of sterically less demanding R, shielding is concentration dependent, i.e., shielding decreases with increasing concentration. This is due to a tendency for $VO(OR)_3$ to associate in solution at higher concentrations to form oligomers (preferentially dimers). Commonly, there is fast exchange (**6** and **7** in Scheme 2) at room temperature between monomers and dimers, and an intermediate signal is observed.[36] In specific cases, such as $VO(cyclo\text{-}C_5H_9)_3$, exchange is slow, and both species are characterized by distinct signals.

(3) Bulky substituents R induce high-field shielding.[4,36,37] Diols give rise to complex patterns, due to the parallel formation of several isomers of mono- and dinuclear (alkoxo-bridged) species. For the dinuclear species, with coordination numbers 6, chemical shifts fall within the range observed for solid $VO(OMe)_3$.[34]

(4) Replacement of the oxo group in $VOCl_3$ for the imido group leads to slight deshielding (no. 4a)[38]. As Cl is progressively replaced by amide or alkoxide, upfield shifts comparable with those discussed under entry no. 2 are observed (no. 4b).[38,39]

(5) In the phosphoranimidato compounds $Ph_3PNVCl_n(NPh_3)_n$ (**8** and **9** in Scheme 2),[40] which formally derive from $[VOCl_4]^-$ by replacing O^{2-} (and a varying number of Cl^-) by Ph_3PN^-, effects similar to those in entry no. 4 are observed: replacing the hard oxo group for Ph_3PN deshields the ^{51}V nucleus, while the substitution of the soft chloride induces increased shielding, although not to the extent observed on substituting chloride for alkoxide.

In the series 4–*R*-$C_6H_4N{=}V(tea)$ (H_3tea = triethanolamine), **10** in Scheme 2, shielding decreases with increasing electron donating capacity of R:[41]

R =	NO_2	CN	Br	Cl	H	OPh	OMe	NMe_2
δ =	−342	−340	−328	−328	−327	−310	−292	−224

Overall, shielding in this chelate complexes with coordination number (*cn*) 5 is substantially lower than in the corresponding open complexes 4-*R*-$C_6H_4N{=}V(OiPr)_3$ with $cn = 4$ (entry no. 6 in Table 2), an effect which is generally observed in otherwise similar systems. The superposition of electronic effects and effects accompanied with chelating ligands/changes in *cn* is also apparent in the following series (Scheme 3).[42]

While carboxylic acids without an additional function form tetrahedral anhydrides with vanadate, hydroxycarboxylic acids induce a change in coordination

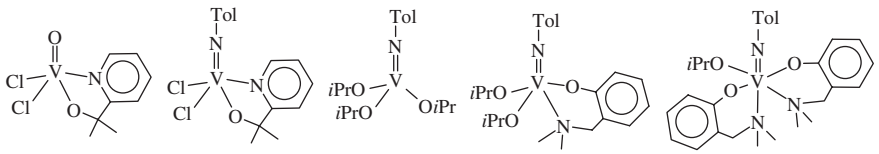

Scheme 3.

geometry (see below). Correspondingly, diols give rise to *cn* 4. For data collection see ref. 4. A comprehensive source of references, including glycols, carbohydrates, and nucleosides is provided by ref. 47b.

α-Hydroxycarboxylato complexes of vanadium have attracted specific interest because they model part of the active site in vanadium-nitrogenase, where vanadium is coordinated to three sulfide ligands (bridging to Fe), a histidine-N, and the alkoxo and carboxylato functions on the central carbon of homocitrate. Detailed speciation studies have appeared on the vanadate-lactate-peroxide,[43] the vanadate-citrate-peroxide,[44] and the vanadate-alanylserine-peroxide systems (with the peptide group as an additional function for coordination).[45] Hydroxy-carbonic acids form complexes with vanadate in aqueous solution at ambient pH, differing in stoichiometry, charge (i.e., protonation state), and *cn*/geometry.[46,47] The complexes can have the stoichiometries 1 : 1 (*cn* 5), 2 : 2 (*cn* 5), and 3 : 2 (*cn* 5 and 6), as shown for the complexes containing α-hydroxyisobutyric acid in Scheme 4, left.[47] As in the simple vanadate system, the peroxo ligand induces a high-field shift. Examples are the two mandelato complexes in Scheme 4, right,[48] the dinuclear monoperoxo–lactate complex, with a chemical shift of −520 for the dioxo, and −592 for the oxo-peroxo moieties,[49] and the corresponding α-hydroxyhippurato complex with shift values of −526 and −580.[50]

Aminoalcohols such as diethanolamines H_2L form penta-coordinate oxovanadium(V) complexes of composition VO(OR)L with, according to the X-ray structural data, a basic trigonal-bipyramidal geometry reminiscent of the active center of vanadate-dependent haloperoxidases.[51] Solutions of these complexes in non-aqueous solvents such as dichloromethane commonly exhibit two signals, possibly corresponding to the two structural isomers **11a** and **11b** shown for a glycine-derived complex in Scheme 5, and thus indicating flexibility. With organic hydroperoxides, the alkoxo ligand is replaced by the peroxo ligand; **12a** and **12b** in Scheme 5. The formation of the peroxo complexes **12** is accompanied by an upfield shift. Since, according to DFT calculations, the organic peroxo ligand RO_2^- coordinates in the end-on fashion, thus contrasting the common coordination mode observed for inorganic O_2^{2-}, the upfield shifts induced by peroxo groups do not reflect strains in a three-membered ring system, but primary electronic effects pertinent to the peroxo ligand.

In the context of modeling the active center of the haloperoxidases, where vanadate is covalently linked to a histidine in the active site pocket, extensive studies

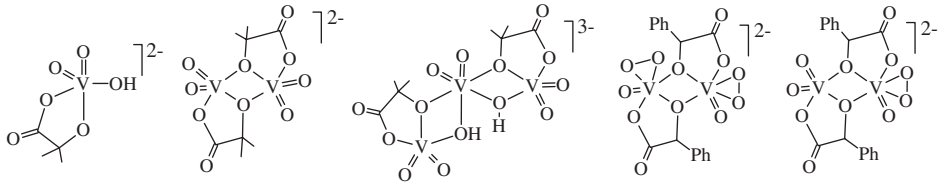

Scheme 4.

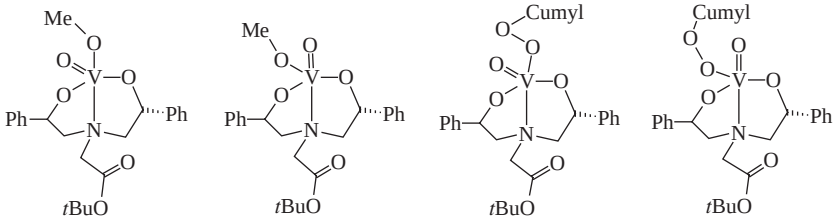

Scheme 5.

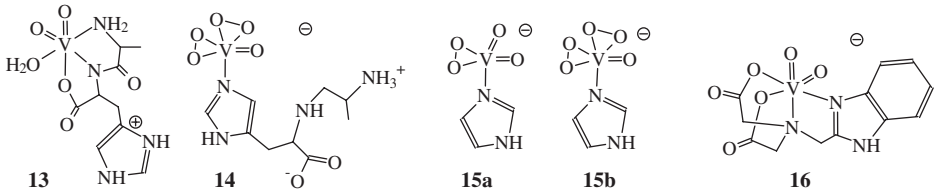

Scheme 6.

have been undertaken on vanadium complexes containing imidazole[20,52] or imidazole derivatives such as histidine,[53,54] alanylhistidine,[21] or benzimidazole,[55,56] including complexes which, along with the imidazole (derivative), contain peroxide, the latter modeling the *active* state of the enzyme. A selection is shown in Scheme 6. The chemical shift for the non-peroxo species (**13**, **16**) is in the range commonly observed for vanadium complexes of *cn* 5–6, containing a mixed *ON* donor set (*cf.* Table 3 and Schemes 4–7). As observed in simpler species (*vide supra*), exchange of one of the oxo ligands for peroxide (**15a**) leads to an upfield shift. An additional upfield shift is noted as a second peroxo ligand (**14**, **15b**) enters the coordination sphere.

The influence of the vanadium : ligand ratio and the number of peroxo ligands on the chemical shift is further demonstrated in the following series of picolinato complexes:[57]

	$\{VO_2(pic)\}$	$\{VO_2(pic)_2^-\}$	$\{VO(O_2)pic\}$	$\{V(O_2)pic_2^-\}$	$\{VO(O_2)_2pic^{2-}\}$
$\delta =$	−550	−513	−600	−632	−745

This pattern is essentially reproduced with other O_xN_y donor sets. The number of data available for the respective vanadium complexes is immense. On a general basis, shielding increases with the sum of the electronegativities of the donating function as a consequence of an increase of ΔE (decrease of σ_{para}; Eq. (2b)).[12] This is a rough conception, however, and several factors can be responsible for deviations from this trend, underlined by, e.g., peroxo and hydroxamido complexes

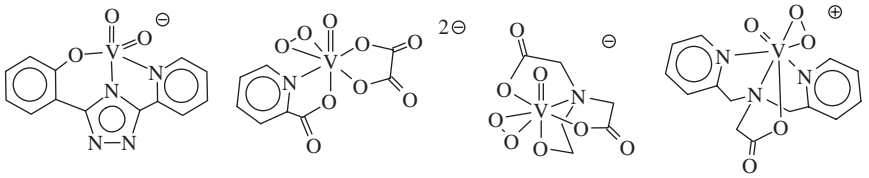

17 **18** **19** **20**
-450 **-620** **-569** **-545**

Scheme 7.

(for the latter the below). Chemical shifts for a few selected examples of complexes containing an O_xN_y donor sets are presented in Scheme 7: the 1,2,4-triazole derivative **17**,[58] the mixed picolinato–oxalato complex **18**,[59] a peroxo complex derived from the tetradentate O_3N ligand hydroxyethyliminodiacetic acid (H_3heida), **19**,[60] and a peroxo complex containing the tetradentate ON_3 ligand *bis*(picolyl-*β*-alaninate), **20**.[61] The examples provided in Schemes 6 and 7 also show that the shift ranges of non-peroxo and peroxo complexes may overlap; *cf.*, e.g., **16** and **20**.

Another large family of $\{VO(O_xN_y)\}$ complexes with abundant ^{51}V chemical shift data available is represented by complexes containing a Schiff-base or a related ligand, such as a hydrazone. Again, these species follow the general trends pointed out above. An interesting phenomenon, noted for the first time by Pecoraro and co-workers,[62] is an unprecedented down-field shift as a non-innocent ligand enters the coordination sphere. These down-field shifts have been observed for hydroxamato and, in particular, for catecholato ligands, and apparently root in the fact that efficient ligand-to-metal electron density transfer takes place, as demonstrated by the resonance hybrid in Scheme 8a. The chemical shifts correlate in fact linearly with the inverse energies of the LMCT bands in the visible and near IR, nicely demonstrating the influence of the ΔE term in Eq. (2b). Examples demonstrating this situation for Schiff base complexes with and without non-innocent co-ligands are depicted in Scheme 8b: while chemical shifts in the normal range are observed for compounds **21**,[63] **22**,[64] **23**,[62b] and **24**,[65] dramatic deshielding is present on going from the "innocent" systems **23** and **24** to the non-innocent hydroxamato (**23a**/**24a**) and catecholato complexes (**23b**/**24b**).

For type **23** complexes with substituents on the catecholate moiety exerting an inductive or mesomeric electron-withdrawing effect (Cl, Br, NO_2), deshielding is much less dramatic, since these substituents counter-act the transport of electron density to the vanadium center, i.e., a less pronounced participation of the V^{IV}(cat) form in the resonance hybrid, Scheme 8a. Deshielding with respect to the common situation, though to a lesser extent, has also been reported for the cationic non-oxo complex $[V(NN)(dtbc)_2]^+$ (**25** in Scheme 9) H_2dtbc = 3,5-di-*t*Bu-catechol, NN = bipy (= −235), *o*-phen (−202),[66] – and for the anionic oxovanadium–calix[4]arene complex **26**, Scheme 9.[67] In the latter case, the influence of the counter-cation is also noteworthy.

The deshielding in the non-oxo catecholato complex **25** is paralleled by a corresponding deshielding of the vanadium nucleus in the naturally occurring complex

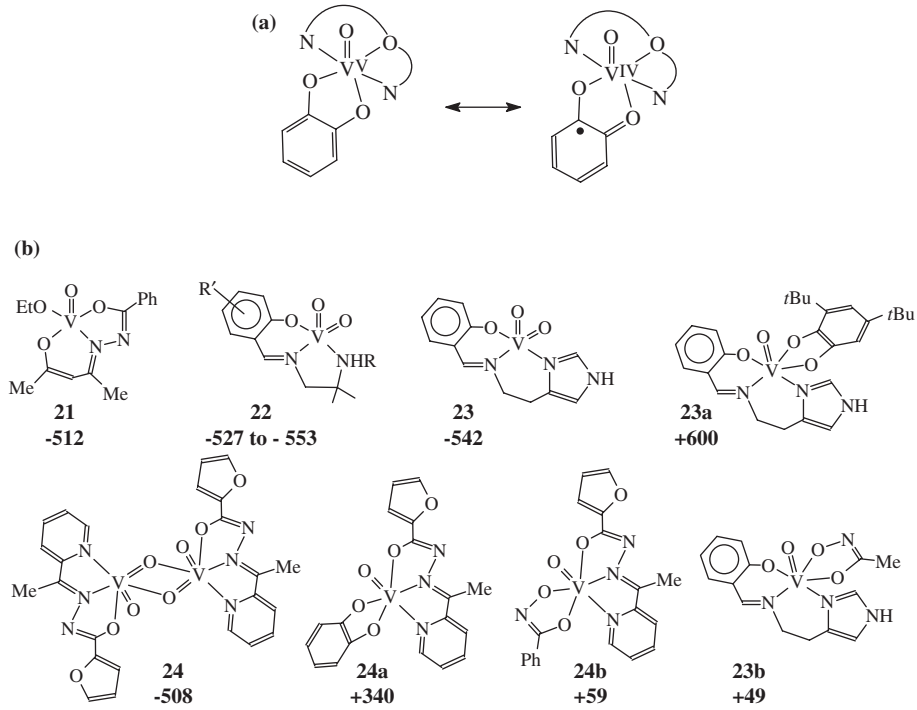

Scheme 8.

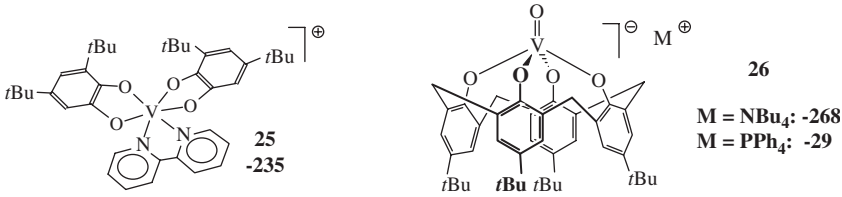

Scheme 9.

amavadin, contained in the fly agaric (toadstool) and other mushrooms belonging to the genus *Amanita*. Amavadin is an anionic non-oxovanadium complex of composition $[\Delta\text{-}V^{IV}(S,S\text{-hidpa})_2]^{2-}$ where H_3hidpa is 2,2′-(hydroxyimino)dipropionic acid, a derivative of hydroxylamine. On oxidation to $[\Delta\text{-}V^{V}(S,S\text{-hidpa})_2]^{-}$ (*cf.* complex **27** (R = H) in Scheme 10), a ^{51}V NMR signal at −281 is observed.[68] Model complexes obtained with *R,S*-H_3hidpa and *R,S*-H_3hidba (the corresponding butyric acid derivative; R = Me for **27** in Scheme 10), three signals are observed due to the presence of three diastereomers.[69] Given the fact that ligands derived from hydroxylamine induce high-field shifts up to −860 (Table 1; **28** in

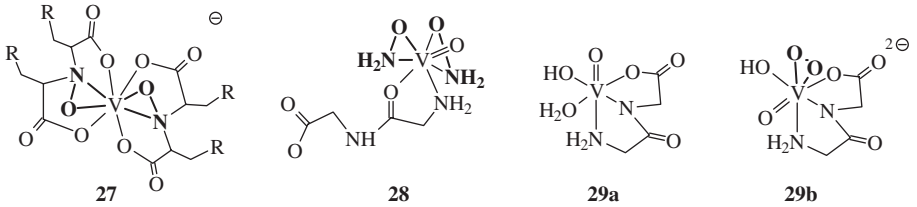

Scheme 10.

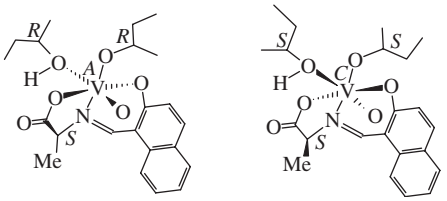

Fig. 4. The complex [VO(O*s*Bu)(HO*s*Bu)ala-naph] (ala-naph is the Schiff base formed from L-α-alanine and *o*-hydroxynaphthaldehyde) contains four centers of chirality. The two diastereomers present in the crystalline solid state are distinct by the chirality at the vanadium center (*A* vs. *C*), and the alkoxo and alcoholic ligands (*R* vs. *S*).

Scheme 6),[23,70,71] the consistently low shielding in **27** might be traced back to either the non-innocence of this specific hydroxamido ligand carrying two carbonic acid substituents on the nitrogen, or to the non-oxo nature of the complex.

The glycylglycinato complex **28** is an example of the peptide complexes which readily form in the ternary vanadate-hydroxylamine-peptide system.[71b] The high shielding compares to that of dipeptide complexes, where H_2NO^- is replaced by the isoelectronic O_2^{2-}.[13,44,71b] Interestingly, the mode of coordination for the peptide in the peroxo complexes (**29b**) compares to that in non-peroxo complexes (**29a** in Scheme 10), but differs from that in the hydroxamido complexes. The weak glycylglycine complex **29a** present in the binary vanadate-peptide system exhibits a "normal" chemical shift.[72] For a discussion of the possible coordination number and protonation state of **29a** see Section 5.2.

Distinction, by ^{51}V NMR, between diastereomers originating from complexes containing two or more elements of chirality, as in the case of the amavadin model compounds **27**, can be an important analytical tool, as demonstrated for the Schiff base–alkoxo complex (shown in Fig. 4), containing four centers of chirality. In CD_2Cl_2 solutions of this salicylidene complex, four of the eight possible diastereomers are represented by distinct NMR signals (−578.9, −583.4, −585.6, and −589.8).[73] Distinction between diastereomers by vanadium NMR will be re-addressed in the next section (organovanadium compounds).

2.1.3. *Organovanadium compounds*

In this section, vanadium complexes will be discussed, in which there is at least one direct vanadium-carbon bond. This includes carbonyl and isonitrile complexes, and complexes with σ-alkyl and -alkenyl ligands, alkylidyne, π-alkene, -alkyne and -acyl ligands, η^3-allyl and aromatic ligands such as cyclopentadienyl, η^5-Cp^-, in which vanadium may vary between the oxidation states +V and −III. The limiting shift values are +2382 for the dinuclear V^{IV} compound $(\eta^5\text{-CpV})_2(\mu\text{-O})(\mu\text{-Te})(\mu\text{-Te}_2)$[74] and −2054 for the V^{I} complex $[\eta^5\text{-CpV(CO)}_3\text{SnPh}_3]^-$,[75] thus clearly extending the high-field limit reported for the inorganic V^{V} compounds (VF_5, $\delta = -895$). The "record holder" in high-field shielding for a V^{V} compound is the alkylidyne complex **30** (Fig. 5). The chemical shift for $[V(CO)_5]^{3-}$ that contains V^{-III} is −1965.[76] It becomes again clear from these data that ^{51}V shielding cannot simply be related to electron density at the vanadium site.

For a comprehensive treatment of data on organovanadium compounds up to *ca.* 1995, see also ref. 5b,c. In the context of carbonylvanadates, complexes containing the isoelectronic nitrosyl (NO^+) or dinitrogen (N_2) ligand will also be discussed at the end of this sub-chapter.

Most of the high-valent organovanadium complexes contain a cyclopentadienyl unit. The alkylidyne complex **30**[77a] and the methyl complex **31**[77b] in Fig. 5 are examples for non-sandwich complexes. Table 4 summarizes data for cyclopentadienylvanadium(V) complexes formally derived from $O{=}VX_3$ and tBuN$=$$VX_3$ (*cf.* Table 3) by replacing one of the X substituents for η^5-Cp^-;[39,78,79] see, e.g., compound **32** in Fig. 5. The shielding trends are comparable with those noted for $O{=}VX_3$ and $RN{=}VX_3$: shielding increases in the series $Cl < NR_2 < OR$, i.e., in these d^0 systems, the electronegativity dependence of shielding is again "inverse". In addition, a steric effect is noted: in the series tBuN$=$VCpCl(NR_2), shielding increases with increasing bulkiness of R. In the series tBuN$=$VCp′Cl_2,

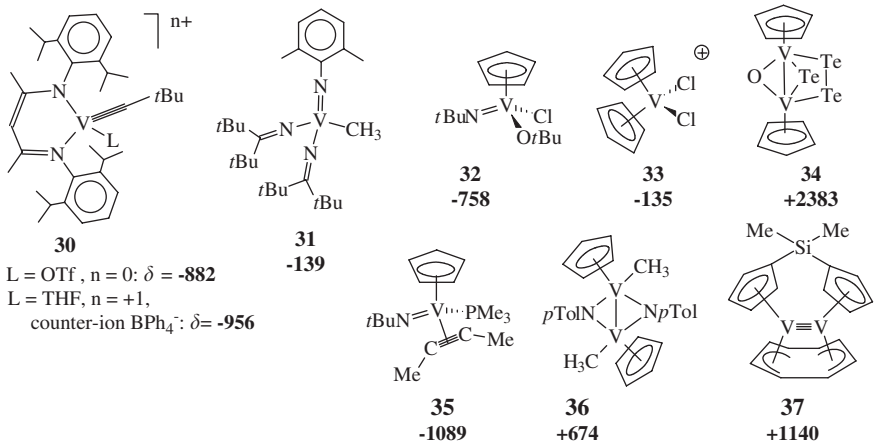

Fig. 5. Selection of high- to medium-valent organovanadium complexes. For data on cyclopentadienylvanadium(V), −(IV), and −(III) see also Table 4.

Table 4. Chemical shifts for $\{\eta^5$-CpV$\}$ and related complexes, containing vanadium in the oxidation state +V, +IV, or +III[a]

V^V		V^V	
$OVCpX_2$ [5b]		tBuNV(σ-CH_2CMe_3)NiPr$_2$ [39]	+329
X = OPh	−700	$[Cp_2VCl_2]^+[AsF_6]^-$ (lq. NH_3) **33** [80]	−135
F	−404		
Cl	−403	V^{IV}	
Br	−249	$Cp_2V_2(\mu$-S)(μ-$S_2)_2$ [81]	+417
SPh	−204	$Cp_2V_2(\mu$-S)$_2$(μ-S_2) [81]	+1454
tBuNVCp(OtBu)$_2$ [79a]	−904	$Cp_2V_2(\mu$-Se)$_2$(μ-Se_2) [81]	+2136
tBuNVCpCl(OtBu) **32** [78]	−758	$Cp_2V_2(\mu$-O)μ-Te)(μ-Te_2) **34** [81]	+2383
tBuNVCpCl(OtBu)NR_2 [39]		$Cp_2V_2(\mu$-S)$_3$ [81]	+1592
NR_2 = NH(tBu)	−785		
N(iPr)$_2$	−665	V^{III}	
NPh_2	−680	tBuNVCp(CO)$_2$ [82]	−1028
tBuNVCp′Cl_2 [79b]		tBuNVCp{P(OMe)$_3$}$_2$ [82]	−607
Cp′ = C_5H_5	−457	tBuNVCp(PMe_3)$_2$ [82]	−104
C_5H_4Me	−421	tBuNVCp(PMe_3)MeC≡CMe **35** [82]	−1089
C_5H_4iPr	−415	tBuNVCp(PMe_3)tBuC≡P [82]	−1055
C_5H_3(iPr)$_2$	−370, −344[b]	(CpVCl)$_2$(μ-NpTol)$_2$ [83]	+321
C_5H_2(iPr)$_3$	−279	(CpVMe)$_2$(μ-NpTol)$_2$ **36** [83]	+674
C_5Me_5	−182	**37** (Fig. 5) [84]	+1140

[a]References in square brackets. *cf.* Fig. 5 for selected complexes.
[b]For the 1,3- and 1,2-isomer, respectively.

where Cp′ represent alkyl-substituted Cp, shielding decreases with increasing the number of alkyl substituents, paralleling increasing +I effect. Low shielding is also observed for the "vanadocenium" cation $[(\eta^5\text{-Cp})_2V^VCl_2]^+$, **33**.[80] A particularly low shielding is induced by the presence of a σ-alkyl ligand, *cf.* tBuN=V(CH_2CMe_3)$_2$ (NiPr$_2$), indicating that these ligands should be classified as soft.

In dinuclear vanadium(IV) complexes of the type **34** (Fig. 5) where the η^5-CpV units are bridged by chalcogenide (E^{2-}) and dichalcogenide (E_2^{2-}), deshielding with increasing softness of E is again noted, i.e., enhanced deshielding according to $S^{2-} < Se^{2-} < Te^{2-}$ and $E_2^{2-} < E^{2-}$, Table 4.[81] Substituting CO in the vanadium(III) complex tBuN=VCp(CO)$_2$ by phosphite and further by phosphine leads to deshieding,[82] generally observed in the carbonylvanadium complexes (and discussed in more detail in the context of V^I and V^{-I} carbonyls below), while substitution of one of the trimethylphosphine ligands in tBuN=VCp(PMe_3)$_2$ by an alkyne (complex **35**) or phosphaalkyne restores the original shielding in the carbonyl derivative. Low shielding is also observed in the dinuclear V^{III} complex **36**,[83] containing a σ-methyl ligand in each of the vanadium moieties. The shielding is lower than in the corresponding chloro complex. In complex **37**, which formally contains a vanadium-vanadium triple bond ($\sigma^2\pi^2\delta^2$), vanadium is in a particularly low shielding situation. Furthermore, in **37**, shielding (and line width) strongly depend on the temperature, *viz.* δ = +1140 at 289 K, and +1283 at 200 K.[84]

Cyclopentadienyl and related vanadium(+I) complexes of the general formulation $[\eta^n\text{-}cyclo\text{-}C_nH_nV(CO)_m]^q$ (*cf.* **38–41** in Scheme 11) and derivatives thereof, in particular those derived from η^5-$CpV(CO)_4$ (**38a**) by either substituting one or two carbonyls for other ligands, or by adding alkyl and other $E^{IV}R_3$ (E^{IV} = group 14 element) substituents to the Cp ring, have systematically been studied.[5b,c,85–87] From the selection of representative data contained in Table 5 (and Scheme 11), the following trends can be derived:

(1) Shielding decreases as the Cp ring is substituted (Cp vs. indenyl and fluorenyl; Cp vs. alkyl and chloro substituted Cp). Since both, +I substituents (alkyl) and –I substituents (Cl) give rise to a down-field shift, this behavior may be considered primarily of steric origin. As shown for η^5-C_5H_3(*s*Bu)Me (**38b**) in Fig. 6, these steric effects can be exploited to distinguish between positional isomers, and diastereomers arising from optical isomerism.[88]

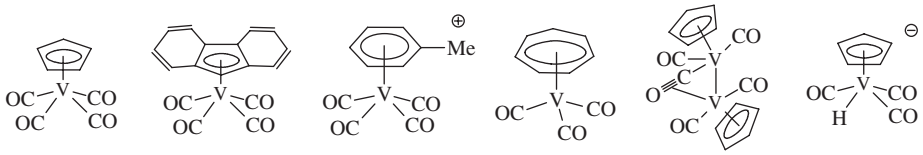

38 **-1534** **39** **-1118** **40** **-1660** **41** **-1485** **42** **-1664** **43** **-1730**

Scheme 11.

Table 5. Chemical shifts for sandwich complexes containing V^{I} and V^{-I}[a]

V^{I}		η^5-$CpV(CO)_2L_2$ [85]	
η^5-Cp′V(CO)$_4$ [5b]		L_2 = dppe	−1110
Cp = C_5H_5 **38a**	−1534	Alkynes	−598 to −626
C_5H_4Me	−1525	dad	−346 to −431
C_5H_3(*s*Bu)Me[b] **38b**		bipy	−63
C_5Me_5	−1492	$[\eta^5$-$CpV(CO)_3L]^-$	
C_5Cl_5	−1010	L = H^- **43** [5b,86]	−1730
Indenyl [5b]	−1375	$SnPh_3^-$ [5b,86]	−2059
Fluorenyl **39** [5b]	−1118	$SnCl_3^-$ [86]	−1340
η^5-$CpV(CO)_3L$		I^- [87]	−742
L = PF_3 [5c]	−1565	Cl^- [87]	−515
PMe_2Ph [85]	−1396	F^- [87]	+417
CNCy [5c]	−1401	$(C_5H_4CHNMe_2)V(CO)_3SnPh_3$[c] [88] **44**	−1560
NCMe [85]	−719	V^{-I}	
PhN=CHPh [87]	−491	η^7-$TpV(CO)_3$ **41** [85]	−1485
THF [85]	−136	η^5-$CpV(CO)(NO)_2$ [85]	−1294

[a] References in square brackets. Abbreviations: dppe, $Ph_2PCH_2CH_2PPh_2$; dad, diazadienes; bipy, 2,2′-bipyridyl; Tp, tropylium.

[b] Four isomers.

[c] *cf.* Fig. 6 and text.

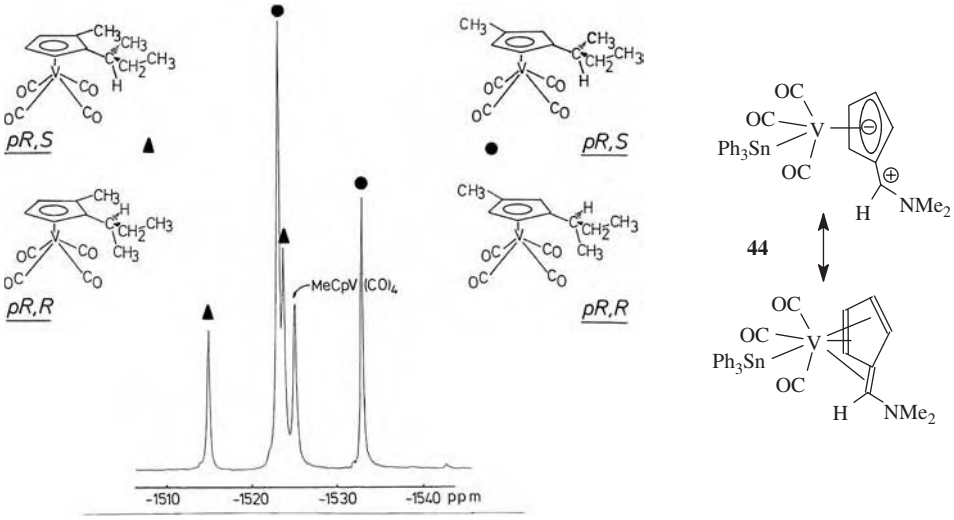

Fig. 6. Left: ^{51}V NMR spectrum of η^5-C_5H_3(*s*Bu)Me (**38b**). For each of the positional isomers (Me and *s*Bu in the 1,2- and 1,3-positions, respectively), there are diastereomers arising from a plane of chirality and a center of chirality. Right: Resonance hybrid for the η^5-Cp/η^6-fulvene complex **44**.

(2) Shielding decreases as CO is substituted by ligands which are less π-accepting. In this respect, PF_3 is the only ligand comparable with CO.
(3) Increasing substitution of CO leads to decreasing shielding, again reflecting a decrease of the overall vanadium-to-ligand π electron density transfer.
(4) Anionic ligands may either increase shielding (H^-, **43**; $SnPh_3^-$), or decrease shielding (halides). The complex $[\eta^5$-$CpV(CO)_3SnPh_3]^-$ marks the upper high-field limit, while $[\eta^5$-$CpV(CO)_3F]^-$ marks the low-field limit of chemical shifts for cyclopentadienyl–vanadium(I) complexes.
(5) As noted for $[\eta^5$-$CpV(CO)_3Hal]^-$, there is a normal electronegativity dependence for these d^4 systems, contrasting the inverse one noted above for d^0 systems.
(6) Fulvene complexes, such as **44** in Fig. 6, right, exhibit patterns similar to cyclopentadienyl complexes.[89]

Shielding patterns pertinent to the carbonyl-cyclopentadienyl-V^I (d^4) complexes are also observed in derivatives of the neutral complexes $XV^I(CO)_6$ (d^4)[90–92] and in the anionic d^6 systems $[V^{-I}(CO)_{6-n}L_n]^-$.[93,94] Generally, shielding reflects the "magnetochemical ligand strength", a composite of the π acceptor and σ donor strength, and the polarizability of the ligand (function). Since ligand fields in most cases are less "strong" than for the parent hexacarbonylvanadate, $[V(CO)_6]^-$, substitution of CO goes along with deshielding, i.e. (comparatively) weak σ-donors/π-acceptors induce deshielding, while more polarizable (softer) ligands induce additional shielding. The σ/π and polarizability effects may counter-act each other. As already

Table 6. Carbonylvanadium(−I and +I) complexes[a]

V^{-I}		$[V(PF_3)_6]^-$ [95]	−1946
$[V(CO)_5L]^-$ [4c,93]		η^3-AllylV(CO)$_3$dppe **45** [4a]	−1492 to −1343
L = PF_3	−1961	η^2-AcylV(CO)$_3$dppe **46** [94]	−1082 to −938
CO	−1955		
CNCy	−1908	V^{I}	
N_2	−1671	$HV(CO)_4$dppe [4a,91]	−1690
1-Hexyne	−1636	$IV(CO)_4$dppe [90]	−1706
Pyridine	−1461	$BrV(CO)_4$dppe [90]	−1698
η^2-CS_2	−1368	$BrV(CO)_4$pepe [90]	−1756
THF	−1367	$BrV(CO)_2(pepe)_2$ **47** [90]	−624
$[V(CO)_4dppe]^-$ [4a]	−1790	σ-AlkylV(CO)$_4p_2$ **48** [91]	−1172 to −1044
$[V(CO)_4dppb]^-$ [4a]	−1723	σ-AlkenylV(CO)$_4p_2$ **49** [90]	−1074 to −1042
$[V(CO)_4dppm]^-$ [4a]	−1590	σ-*i*hexylV(CO)$_2(p_2)_2$ [91]	−769
$[V(CO)_3tdmp]^-$ [91]	−1690	$IV(CO)_2p_2$(η^2-alkyne) **50** [92]	−455 to −321

[a]References in square brackets. For numbered complexes, see Fig. 7. Abbreviations: Cy, cyclohexyl; dppm, $Ph_2PCH_2PPh_2$; dppe, $Ph_2PCH_2CH_2PPh_2$; dppp, $Ph_2P(CH_2)_3PPh_2$; pepe, $Et_2PCH_2CH_2PPh_2$; tdmp, $P(CH_2CH_2CH_2PMe_2)_3$; p_2, any bidentate or two monodentate phosphines.

pointed out in the context of the $\{\eta^5$-$CpV^I\}$ complexes, these trends oppose those noted for the high-valent (in particular d^0) vanadium complexes. Thus, a series of increasing magnetochemical ligand strength has been derived for $XV(CO)_4$dppe (dppe = $Ph_2PCH_2CH_2PPh_2$), *viz.* X = σ-alkyl ≈ σ-alkenyl < $SiMe_3$ < H ≈ Br ≈ I < O_2CR < Cl ≈ N_3 < CN.[90] In hexacarbonylvanadates containing bi- to tetradentate ligands, such as $[V(CO)_4diphos]^-$, the "chelate effect" also plays a role, i.e., strained chelate four-rings give rise to deshielding with respect to chelate-five ring structures, while six-membered rings, which are subject to torsional strain, lie in-between. Finally, the local symmetry comes in, since the symmetry determines which of the excited states can mix with the ground state and thus contribute to σ_{para}; *cf.* Eq. (2a). Selected data underlining these trends are compiled in Table 6; *cf.* also Fig. 7. The chemical shift for $[V^{-III}(CO)_5]^{3-}$ (−1965)[76] and $[V^{-I}(PF_3)_6]^-$ (−1946)[95] are close to $[V^{-I}(CO)_6]^-$ (−1955).

In Table 7, NMR data of nitrosyl- and dinitrogen-complexes of V^{-I} are collated. In $V(CO)_5NO$, formally obtained by substituting one CO in $[V(CO)_6]^-$ by NO^+, clearly leads to a deshielding. Correspondingly, complexes of the general formulation $V(CO)_{5-n}(NO)L_n$ (n = 1, 2) are deshielded with respect to the anionic counterparts.[96] Matchable trends are noted for η^5-CpVL$(NO)_2$ vs. η^5-CpVL$(CO)_3$.[4a] The cationic *bis*(nitrosyl)vanadium(-I) complexes $[VL_4(NO)_2]X$ exhibit substantial deshielding as compared with the neutral compounds.[97] Within this family, however, the trends noted above for the low-valent carbonyl complexes prevail. Comparison of $[V(CO)_6]^-$ (δ = −1955) and $[V(CO)_5N_2]^-$ (−1671)[98] shows that dinitrogen is a somewhat weaker ligand than CO, even when taking into account that the lower symmetry of the latter (C_{4v}) will contribute to the deshielding. In the *bis*(dinitrogen) complexes $[V(N_2)_2(dmpe)_2]^-$ (dmpe = $Me_2PCH_2CH_2PMe_2$), which are isoelectronic to the carbonylvanadates $[V(CO)_2(dmpe)_2]^-$, this situation is

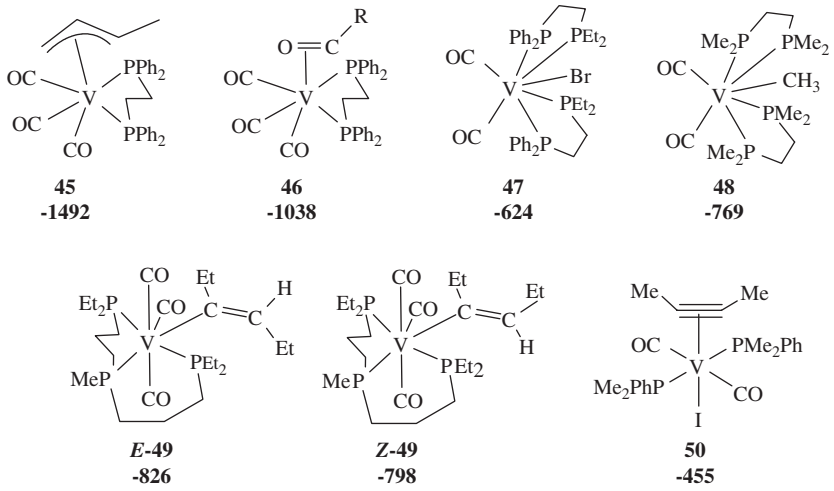

Fig. 7. Structures and chemical shifts of selected carbonylvanadium(−I and +I) complexes.

Table 7. Nitrosyl- and dinitrogen complexes of vanadium(-I)[a]

$V(CO)_5NO$ [96a]	−1489	$[V(thf)L_3(NO)_2]Br$ [97b]	−849 to −723
$V(CO)_4(NO)L$ [96a]	−1475 to −1085		
$V(CO)_3(NO)L_2$ [4a,96b]	−1480 to −1237	$[V(CO)_5N_2]^-$ [93,98]	−1671
η^5-$C_5H_5V(NO)_2CO$ [4a]	−1265	$[V(N_2)(dmpe)_3]^-$ [99]	−1032 (sxt)
η^5-$C_5H_5V(NO)_2L$ [4a,4c]	−1293 to −511	*cis*-$[V(N_2)_2(dmpe)_2]^-Na^+$ [99]	−982 (tt)
$[VL_4(NO)_2]X$ (X = Hal) [97]			
L = CNR	−1042 to −1038	*trans*-$[V(N_2)_2(dmpe)_2]^-Na^+$ [99]	−1183 (q)
NCMe	−276 to −272	*trans*-$[V(N_2)_2(dmpe)_2]^-Li^+$ [99]	−982 (q)
THF	+282 to +313		

[a]Abbreviations: dmpe, $Me_2PCH_2CH_2PMe_2$; sxt, sextet; tt, triplet of triplets; q, quartet.

retained.[99] The differences between *cis*- and *trans*-$[V(N_2)_2(dmpe)_2]^-$, and the fact that shielding depends on the counter-ion (Li^+ vs. Na^+) underlines the importance of local symmetry for the shielding situation.

2.2. Isotope and temperature effects

Shielding is also a function of temperature, and of isotopic substitution in the first or more distant coordination spheres. With decreasing temperature, shielding increases essentially in a practically linear fashion. An increase of shielding is also effective for a heavier isotopomer as compared with its lighter analog. Both effects can be traced back to changes in internuclear bonding parameters, in particular distances, and may thus be related, in a rovibrational frame, to variations in internal displacement coordinates Δr.[100,101] In addition, decreasing the temperature leads to a decrease of the population of excited vibronic levels of the electronic

Table 8. Temperature gradients t_g and isotope effects Δ

	t_g[a] ppm deg^{-1}	$^1\Delta$[b]	$^2\Delta$[b]	$^S\Delta$[c]
$[VO_4]^{3-}$ [101,103]		−0.19 (^{18}O)		−0.73 (D_2O)
η^5-CpV(CO)$_4$ [100a,101]	−0.61	−0.46 (^{13}C)	−0.13 (^{18}O)	
			−0.715 (^{2}H)	
η^5-CpV(CO)$_3$NH$_2$Bu [101]			−0.85 (^{2}H)	
$[\eta^5$-CpV(CO)$_3$H$]^-$ [101]		−4.7 (^{2}H)		
		−0.51 (^{13}C)		
η^7-TpV(CO)$_4$		−0.38 (^{13}C)		
[Et$_4$N][V(CO)$_6$] [100a,102a]	−0.31	−0.27 (^{13}C)	−0.10 (^{18}O)	−0.21 (CD_3OD)
[Me(C$_{10}$H$_{21}$)$_3$N][V(CO)$_6$] [101]				−0.09 (toluene[d$_8$])
Na[V(CO)$_6$]$^-$ [101]				−1.20 (D_2O)
[V(thf)$_4$(NO)$_2$]Br [100a]	−1.23			

[a]Temperature gradients of shielding ($\Delta\sigma/\Delta T$) are given per K. The minus sign indicates decreasing shielding with increasing temperature.

[b]Isotope shifts per isotopic substitution. The minus sign indicates deshielding for the lighter isotopomer.

[c]Solvent isotope shift per deuteron present in the solvent.

(ground) state(s) and thus to an increase in ΔE. For the consequences, *cf.* Eq. (2). In Table 8, temperature gradients, one- and two-bond isotope shifts, $^1\Delta$ and $^2\Delta$,[100,102] and solvent isotope shifts $^S\Delta$ induced by deuterated solvents[101] are listed. In the case of $[V(CO)_6]^-$, $^S\Delta$ are correlated to the polarity of the solvent, indicating differing degrees of solvation. Except for the orthovanadate,[103] all data available have been reported for the low valent vanadium complexes. Fig. 8 illustrates the mixture of isotopomers for $[V(CO)_n(C^{18}O)_{6-n}]^-$.

2.3. Relaxation and line widths

For quadrupolar nuclei relaxation is dominated by the quadrupole mechanism, originating from fast energy transfer from the nucleus to the environment by interaction between the electric nuclear field gradient tensor and the inhomogenous electric fields produced by polar molecules in motion. Relaxation is directly reflected in the line widths of the resonance line, usually indicated as the width at half-height, $W_{1/2}$. Under common isotropic conditions, the relaxation process can be described by Eq. (3),

$$W_{1/2} = (\pi T)^{-1} = 0.041\pi^2(e^2 q_{zz} Q/h)(1 + \eta^2/3)\tau_c \qquad (3)$$

where T is the relaxation time ($T_1 \approx T_2$ under isotropic conditions), $e^2 q_{zz} Q/h$ ($= C_Q$) the nuclear quadrupole coupling constant (q_{zz} = electric field gradient in zz direction, Q = nuclear quadrupole moment), η the asymmetry parameter ($\eta = 0$ for axial symmetry), and τ_c the molecular correlation time, a measure for the

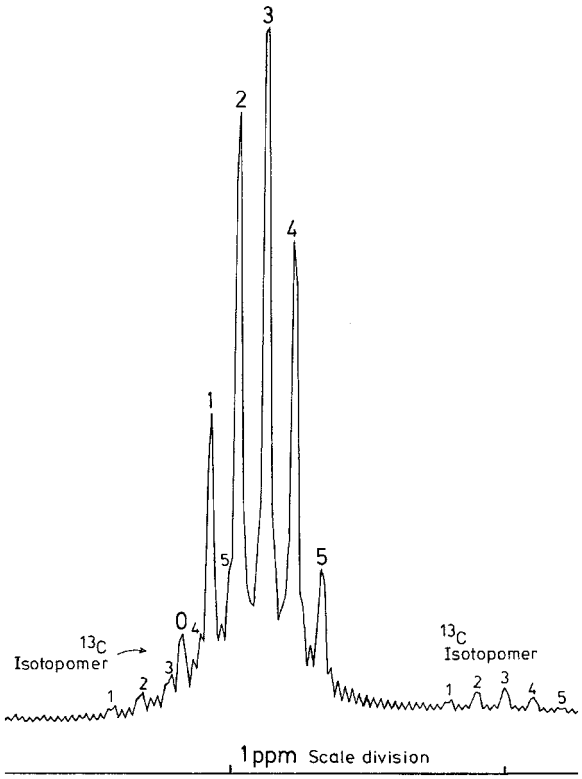

Fig. 8. ^{51}V NMR spectrum of a THF solution of $[V(^{12}C^{16}O)_n(^{12}C^{18}O)_{6-n}]^-$, $n = 0$–5. Also seen is the doublet for the natural abundance ^{13}C isotopomer, additionally reflecting the isotopomeric pattern due to ^{18}O (*cf.* ref. 102a).

interaction between solvent and solute molecules, i.e., the extent of tumbling of a molecule in a solvent.

From Eq. (3) it is clear that broad lines are to be expected for molecules of low point symmetry (via the influence of q), and for comparatively low molecular motion, as in case of large molecules and high viscosity of the solution (influence via τ_c). Since the viscosity increases as the temperature goes down, the line widths of the ^{51}V NMR signals increase with decreasing temperature and vice versa. Any adverse effect points toward slowing-down or acceleration of exchange equilibria between two or more chemical species present in solution. Qualitatively, the factors influencing $W_{1/2}$ can be summarized as follows; *cf.* Table 9 for selected data for vanadium(V)[104] and (-I)[105] compounds:

(1) A decrease of symmetry results in an increase of $W_{1/2}$. For cubic symmetry (T_d, O_h, I_h; $q = 0$), and certain cases of C_{nv} symmetry (e.g., *facial* octahedral complexes of C_{3v} symmetry), rather narrow lines are observed.
(2) Increasing the ligand bulkiness increases $W_{1/2}$.

Table 9. Line width $W_{1/2}$ (Hz) for selected vanadium compounds

Polyoxovanadates $H_nV_{10}O_{28}^{(6-n)-}$		
Tetrahedral sites	$V_4O_{12}^{4-}$	≈ 60
Isolated tetragonal sites	$VW_5O_{19}^{3-}$	60–80
Tetragonal with adjacent V sites	$V_{10}O_{28}^{6-}$, V_a/V_b[a]	100–200
Rhombic sites	$V_{10}O_{28}^{6-}$, V_c[a]	200–800
$[V(CO)_6]^-$	O_h	1.4
$[V(CO)_5PPh_2Me]^-$	C_{4v}	120
cis-$[V(CO)_4(PPh_2Me)_2]$	C_{2v}	775
η^3-$C_3H_5V(CO)_3$dppe	C_s	2,400
$[V(CO)_5PZ_3]^-$ (C_{4v})		
$PZ_3 = PPhMe_2$	Cone angle = 122	32
PPh_2Me	132	160
$P(tBu_3)_3$	182	420

[a] *cf.* Fig. 1.

(3) Increasing size of the donor function (increasing softness/nephelauxetic effect) leads to an increase of $W_{1/2}$.
(4) Strong π-accepting and σ-donating ligands (hard ligands) give rise to comparatively narrow lines.
(5) In chelates, an increase of ring strains goes along with an increase of $W_{1/2}$.

Equation (3) applies for the extreme narrowing case, characterized by $2\pi\nu_0\tau_c >> 1$ (ν_0 = NMR frequency). For very slow isotropic motion, $W_{1/2}$ for the central transition commonly observed under these conditions also becomes a function of ν_0, Eq. (4).

$$W_{1/2} \propto \frac{e^2 q_{zz} Q/h}{\nu_0^2 \tau_c}. \tag{4}$$

2.4. Scalar coupling

Nuclear spin–spin coupling (scalar coupling) J_{ML} between a spin M (such as vanadium) and L (a ligand function coordinated to vanadium) is dominated by the Fermi contact term, Eq. (5a), in which γ_M and γ_L are the magnetogyric ratios of the nuclei M and L, $^3\Delta E$ is the mean triplet excitation energy,$|S(0)_M|^2$ and$|S(0)_L|^2$ represent the *s*-electron densities at the M and L nuclei, and $\sigma(s)^2$ the $\sigma(s)$ contributions to the M-L bond. For a given set of nuclei M and L, J thus depends on three parameters, *viz.* ΔE, $S(0)$, and $\sigma(s)$, which are influenced by the bonding situation, with particular emphasis laid on $S(0)$ and $\sigma(s)$. Although π influences are not decidedly represented in Eq. (5a), π interactions between M and L do have a synergistic impact upon $\sigma(s)$ and $S(0)$, and thus contribute to the size of J.

$$J_{ML} \propto \gamma_M \times \gamma_L (^3\Delta E)^{-1} |S(0)_M|^2 |S(0)_L|^2 \sigma(s)^2. \tag{5a}$$

The dependence on the magnetogyric ratios can be eliminated by applying the reduced coupling constants K_{ML} (Eq. (5b)), which can be useful for comparative studies.

$$K_{ML} = \frac{4\pi^2}{h} \times \frac{J_{ML}}{\gamma_M \times \gamma_L}. \tag{5b}$$

An example is, the dinuclear diazenido complex $\{(t\text{BuCH}_2)_3\text{V}\}_2\mu\text{-N}_2$,[106] for which the coupling constants $J_{VN-14} = 48$ and $J_{VN-15} = 76$ Hz (**I** in Table 10) differ considerably, while the reduced coupling constants $K_{VN-14} = 21.0$ and $K_{VN-15} = 23.7$ $NA^{-2}m^{-3}$ are of comparable size.

The largest reported coupling involving the nucleus ^{51}V so far is $J_{VSn} = 900$ Hz in $[\eta^5\text{-CpV(CO)}_3\text{SnCl}_3]^-$. With respect to the size of the coupling constant, i.e., the extent of communication between the two nuclei, there are several common features in given series of complexes (*cf.* also Table 10):

(1) Electronegative ligands induce effective coupling (**II** in Table 10),[25,39,78,107,108] as a consequence of a contraction of Ψ_s and hence increase of $|S(0)_L|^2$. A comparable effect is observed for phosphite vs. phosphine complexes (**III**).[82a]
(2) In low-valent complexes, strongly π-accepting ligands (CO, PZ_3 [in particular for Z = F, OR; **IV**]) increase J mainly via an increase of $\left|S(0)_M\right|^2$.
(3) Enlarging the $\sigma(s)$ character of the M-L bond increases J.
(4) Bulky ligands, e.g., bulky phosphines, give rise to less effective coupling, likely a consequence of disturbed V-PR_3 overlap.
(5) Two-bond coupling constants are clearly smaller than one-bond coupling constants (**V**,[102a,109] **VI**,[95] **VII**[105]), in consent with expectation.

The observability of coupling is often hampered by unresolved coupling patterns due to line broadening. This can be a particular problem in the case where the coupling information is to be extracted from the L nucleus, for which an eight-line pattern (nuclear spin of $^{51}V = 7/2$) is to be expected. An example for a well resolved pattern both in the ^{13}C and ^{51}V NMR are η^5-$CpV(CO)_4$ and $[V(CO)_6]^-$;[102] for the ^{51}V NMR spectrum of the latter, see Fig. 8 in Section 2.2. If the spectra are unresolved, the resonance for the L nucleus appears as a plateau-like composite signal, from which the approximate coupling constant can be obtained by division of $W_{1/2}$ by 7, provided that coupling is fully effective, i.e., relaxation decoupling can be excluded. In the case of (partial) relaxation decoupling, a Gaussian-shaped signal is observed. Relaxation is faster at lower temperature, in polar solvents and with bulky molecules (see the previous section), and consequently relaxation decoupling is particularly effective under these conditions. Since line broadening by relaxation remains modulated by scalar spin–spin interaction, a rough estimate of the coupling constant J_{ML} is obtained from the half-widths of both coupled nuclei by applying Eq. (6).

$$J_{ML} = [f(I) \times W_{1/2}(V) \times W_{1/2}(L)]^{1/2} \quad \left(f(I) = \frac{1}{21} \text{ for M}=^{51}\text{V}\right). \tag{6}$$

Table 10. One-bond ($^1J_{VL}$) and two-bond ($^2J_{VL}$) coupling constants (in Hz)

L = ^{1}H		L = ^{31}P	
$[\eta^5$-CpV(CO)$_3$H$]^-$ **Va** [102a]	21.7 ($^1J_{VH}$)	$[V(N_2)_2(PR_3)_4]^-$ [99]	208–316 ($^1J_{VP}$)
η^7-$C_7H_7V(CO)_3$ **Vb** [109]	3 ($^2J_{VH}$)	$[V(PF_3)_6]^-$ **IVa** [95]	510 ($^1J_{VP}$)
L = ^{13}C		$[V(CO)_5PZ_3]^-$ [105]	
$[V(CO)_6]^-$ [102a]	116 ($^1J_{VC}$)	Z = F **IVb**	488 ($^1J_{VP}$)
η^5-CpV(CO)$_4$ [102b]	108 ($^1J_{VC}$)	OMe **IVc**	370 ($^1J_{VP}$)
O=V(CH$_3$)(O*t*Bu)$_2$ [107]	118 ($^1J_{VC}$)	Me	210 ($^1J_{VP}$)
L = $^{14/15}$N		H	170 ($^1J_{VP}$)
*t*BuN=V(η^5-Cp)(CO)$_2$ [82a]	82 ($^1J_{VN-14}$)	$[V(CO)_5P_2Me_4]^-$ **VII** [105]	341 ($^1J_{VP}$), 40 ($^2J_{VP}$)
{(*t*BuCH$_2$)$_3$V}$_2\mu$-N$_2$ **I** [106]	48 ($^1J_{VN-14}$), 76 ($^1J_{VN-15}$)	*t*BuN=V(η^5-Cp)P(OMe)$_3$ **IIIa** [82a]	593 ($^1J_{VP}$)
*t*BuN=VX$_3$ **II** [39,78]	74–103 ($^1J_{VN14}$)	*t*BuN=V(η^5-Cp)PMe$_3$ **IIIb** [82a]	397 ($^1J_{VP}$)
trans-$[V(N_2)_2(dmpe)_2]^-$[a] **Xa** [112]	57 ($^1J_{VN-15}$)	*t*BuN=V(η^5-Cp)(η^2-alkyne)PMe$_3$ [82a]	274–353 ($^1J_{VP}$)
cis-$[V(N_2)_2(dmpe)_2]^-$[a] **Xb** [112]	67 ($^1J_{VN-15}$)	$[V(NPPh_3)_4]^+$[c] [40]	120 ($^2J_{VP}$)
L = ^{17}O		L = $^{35/37}$Cl	
$[VO_4]^{3-}$ **VIII** [110]	62 ($^1J_{VO}$)	$VOCl_2$(but)[d] [36a]	100 ($^1J_{VCl-35}$) 83 ($^1J_{VCl-37}$)
L = ^{19}F		L = ^{119}Sn	
$[V(PF_3)_6]^-$ **VI** [95]	10.3 ($^2J_{VF}$)	$[\eta^5$-CpV(CO)$_3$SnCl$_3]^-$ [5c]	900 ($^1J_{VSn}$)
$[Cl_2FV(N_3S_2]^-$[b] [108]	79 ($^1J_{VF}$)	L = ^{183}W	
$[VOCl_2F_2]^-$ [111]	272 ($^1J_{VF}$)	$[VW_5O_{19}]^{3-}$ **IX** [105]	11 ($^2J_{VW}$)
$[VO(O_2)_2F]^{2-}$ [25]	163 ($^1J_{VF}$)		

Bold roman numbers refer to the discussion in the text.

[a] dmpe, $Me_2PCH_2CH_2PMe_2$.

[b] *cf.* **3** in Scheme 1, Section 2.1.1 (pyridine in **3** exchanged for F^-).

[c] See **9** in Scheme 2, Section 2.1.2.

[d] but, 2,3-butanediolate(1-).

Coupling information on inorganic vanadium compounds is scarce; examples are $^{1}J_{VO-17}$ in orthovanadate[110] (**VIII** in Table 10), $^{2}J_{VW}$ in the polyoxovanadotungstate **IX**,[105] J_{VF} in fluorovanadates(V),[25,111] and $^{1}J_{VP}$ and $^{2}J_{VF}$ in *hexakis* (trifluorophoshine)vanadate(-I) (**IVa/VI**).[95] Most data have been reported for high- and low-valent cyclopentadienyl- and carbonylvanadium complexes. For the *bis* (dinitrogen) complex $[V(N_2)_2(Me_2PCH_2CH_2PMe_2)_2]^-$ which exists in the *trans* (**Xa**) and *cis* configuration (**Xb**), the multiplet structure of the ^{51}V resonance allowed for an unequivocal assignment.[112] While, in the *trans* isomer, the signal ($\delta = -1123$) is split into a binominal quintet ($J_{VP} = 314$), the *cis* isomer ($\delta = 978$) is characterized by an A_2B_2X spin system ($J_{VP} = 316$ and 253 Hz). The larger shielding in the *trans* isomer (D_{4h} symmetry) as compared with the *cis* isomer (C_{2v} symmetry) is well in accord with the influence of symmetry upon shielding outlined previously.

2.5. Applications

2.5.1. *Biological and medicinal implications*

^{51}V NMR studies have been performed on several vanadate-oligopeptide systems such as alanylhistidine[21], alanyl-serine,[44] or valyl-glutamine,[113] invariably indicating coordination via the terminal carboxylate and amino groups, and the deprotonated amide-N, characterized by ^{51}V NMR signals at -510 ± 7, depending on the electronic and steric nature of the amino acid side-chains and the protonation state. Compound **13** in Scheme 6 (Section 2.1.2) illustrates this situation. With proteins, both unspecific binding of vanadate and coordination of vanadate into the metal binding site is feasible. Unspecific binding of vanadate has been detected for CuZn-superoxide dismutase,[114] where the signal for monovanadate (δ of *ca.* -555) is observed, considerably broadened due to effective relaxation and exchange with free vanadate. The down-field shifts in the systems vanadate/bovine prostatic acid phosphatase (-542; **51** in Fig. 9),[115] vanadate/ribonuclease-T_1 (-514),[116] and ribonuclease-A (-506)[117] are indicative of effective binding of vanadate to the protein. A detailed analysis of the strong coordination of vanadate has been carried out with transferrins.[118,119] These high molecular mass systems are in the motional narrowing limit (Eq. (4) in Section 2.3), where only one of the four transition components

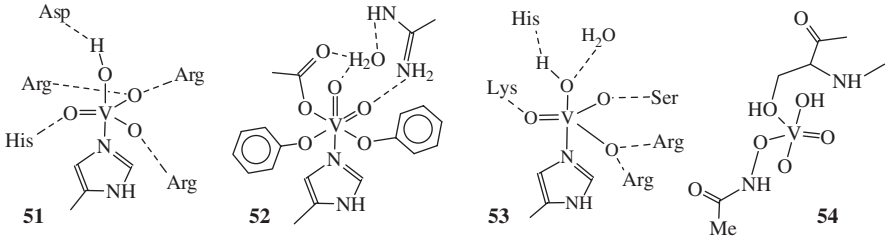

Fig. 9. Binding sites for vanadium in proteins: prostatic acid phosphatase (**51**; ref. 238), serum transferrin (**52**; ref. 120), bromoperoxidase from *Ascophyllum nodosum* (**53**; ref. 239), β-lactamase complex of vanadiumhydroxamate (**54**; ref. 123).

Table 11. Quadrupolar central transition NMR data for vanadate–protein complexes[a]

	7.05 T	9.4 T	11.7 T	References
Human serum transferrin, C-lobe, $\delta(W_{1/2})$	−536.0 (418)	−532.2 (226)	−529.9 (190)	[118,119]
Human serum transferrin, N-lobe, $\delta(W_{1/2})$	−536.0 (418)	−533.7 (328)	−531.4 (268)	[118,119]
Ovo transferrin, $\delta(W_{1/2})$	−537.7 (314)	−534.5 (265)	−532.7 (220)	[119]
A. nodosum bromoperoxidase[b]		−930 (5,100)		[115]

[a]Chemical shifts δ and line width $W_{1/2}$ (Hz; in parentheses).
[b]Peroxidase from the marine alga *Ascophyllum nodosum*.

$(+1/2 \rightarrow -1/2)$ is observed, the chemical shift and line width of which depend on the strength of the applied field, as demonstrated for the data presented in Table 11. Investigations of the vanadate-transferrin systems (see **52** in Fig. 9 for the proposed arrangement of the binding site[120]) have revealed a stronger binding of vanadate to the N-terminal than to the C-terminal site, and a stronger binding to human than to ovo-transferrin. While the chemical shifts for the transferrin complexes are in the expected range, an unprecedented and so far unexplained high shielding ($\delta = -930$) for the oxovanadium(V) center in the bromoperoxidase isolated from the marine alga *Ascophyllum nodosum* was reported.[115] For a more detailed discussion of the NMR features of vanadate-dependent haloperoxidases see Section 3.4.4.

Vanadium NMR has also been employed to investigate the nature of the inhibitory complexes formed between hydroxamatovanadates and lactamases or serineamidohydrolases.[121] The energy-minimized ternary complex **54** in Fig. 9, in which vanadium coordinates to a serine-hydroxyl, exhibits a chemical shift of −494, as compared with −518 for the binary complex formed between vanadate and methylhydroxamic acid.

The aqueous vanadate system shows an interesting pH-dependent behavior in the presence of humic acids. At a low pH (3.0), where decavanadate and $[VO_2(H_2O)_4]^+$ coexist, the latter is almost immediately reduced to V^{IV} while decavanadate slowly decomposes to the VO_2^+ species prior to reduction. At pH 7.2, where mono-, di-, and tetravanadate are present (*cf.* Fig. 1a in Section 2.1.1), the system is stable against reduction. Only monovanadate binds to the humic acid, as shown by line broadening. At pH 12, signals which are due to mono- and bis-peroxovanadates appear, apparently generated by redox reaction between dissolved O_2 and semichinone radicals present in the humic substance at high pH.[122]

The oxovanadium(IV)–pyridinone complex **55a** in Fig. 10 has been shown to be one of the many vanadium complexes to exhibit *in vitro* insulin-enhancing properties. In human blood, the complex is readily oxidized to the 1 : 2 and 1 : 1 oxovanadium(V) complexes **55b** and **55c**/**d**, plus some monovanadate, as evidenced by three distinct ^{51}V NMR signals.[123] Kinetic investigations show that only the neutral form **55c** enters the blood cells, presumably by diffusion through the membrane,

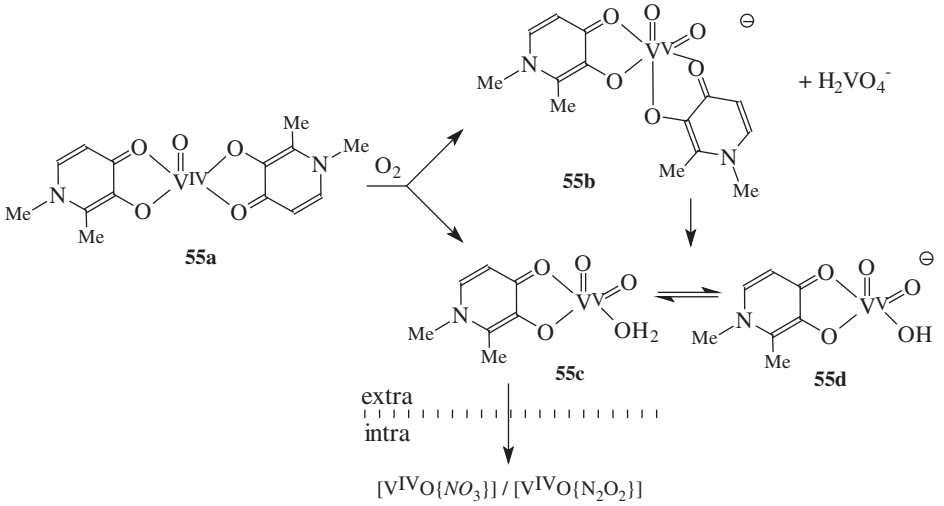

Fig. 10. Species distribution of oxovanadium–pyrimidone complexes in blood.

where it is reductively degraded to VO^{2+} species by intracellular reductants such as ascorbate and/or glutathione. In contrast, monovanadate (but not higher condensed vanadates) enter the cell through anion channels, again followed by reduction. Ascorbate has also been proven an effective reductant for dioxo-*bis*(maltolato)vanadate(V), $[VO_2(mal)_2]^-$ ($\delta = -496$) the precursor for another efficient *in vitro* and *in vivo* insulin-enhancing agent, the neutral $[VO(mal)_2]$.[124]

2.5.2. *Implications for catalysis*

The ability of vanadate-dependent haloperoxidases to catalyze the bromination of organic substrates and the sulfoxygenation of sulfides has initiated studies into structural/functional models with comparable properties. Scheme 12 provides two examples for bromination reactions: oxidation of bis*homo*allylalcohols with *tert*-butylhydroperoxide (tBuO$_2$H) in the presence of bromide and catalytic amounts of the Schiff base complex **56a** leads to the formation of brominated cyclic ethers.[125] The vanadium center in the pre-catalyst **56a** and the actual catalyst **56b** (which, according to ^{51}V NMR, forms on addition of tBuO$_2$H to **56a**) is dissymmetric, inducing stereoselectivity in the products. The substrate 1,3,5-trimethoxybenzene is often used as a test system for the catalytic activity of vanadium compounds[126] such as **56a**[127] and **57**[128] in oxidative bromination by H_2O_2; Scheme 12. In the case of the Schiff base complex **56a**, the active species is supposed to be the peroxo complex $[LVO(O_2)]^-$ ($\delta = -519$) while, in the case of the amidato complex **57** (genuine $\delta = -465$), the chemical shift of -726 indicates the presence of a free diperoxovanadate and thus detachment of the ligand.

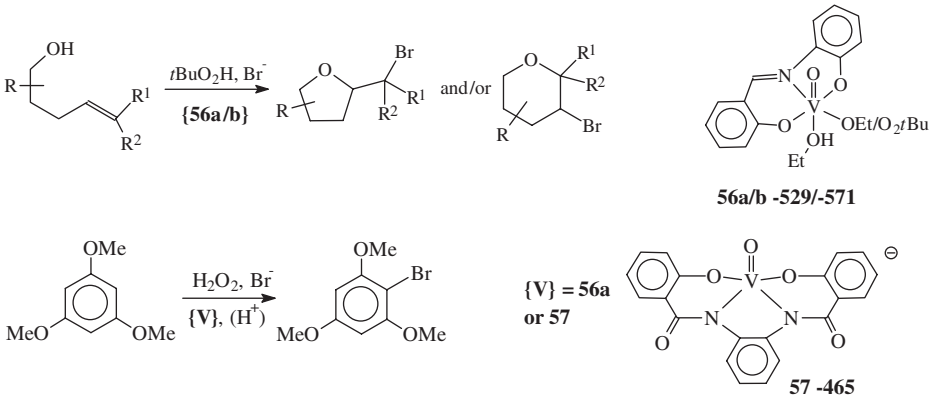

Scheme 12.

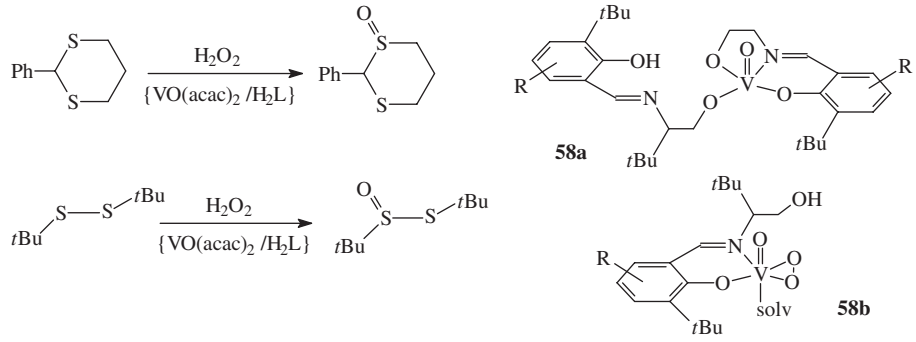

Scheme 13.

The formation of a peroxo complex as the actual catalyst by reacting a pre-catalyst with peroxide has also been detected, by ^{51}V NMR, in the oxidation of prochiral sulfides to chiral sulfoxides with RO_2H, catalyzed by trigonal-bipyramidal oxovanadium complexes derived from chiral aminoalcohols. The complexes **11** and **12** in Scheme 5, Section 2.1.2, are examples for pre- and active catalysts.[51,129] The catalyst system $VO(acac)_2/H_2L$, where H_2L is the chiral Schiff base ligand of the intermediately formed complexes **58** in Scheme 13, has been employed in the sulfoxygenation of prochiral sulfides, dithioacetals,[130] and disulfides.[131] A solution of $VO(acac)_2$, H_2L, and H_2O_2 in the biphasic H_2O/CD_2Cl_2 systems shows nine ^{51}V NMR resonances in the range from -460 to -580, associated with pre-catalysts such as VOL(HL) (**58a**)[131] and active catalysts of composition $VOL(O_2)$, **58b**.[130] Larger amounts of H_2O_2 induce displacement of the ligand and formation of free peroxovanadate ($\delta = -680$; *cf.* Table 2).[131]

In the absence of bromide, oxidative cyclization of bis*homo*allyl alcohols, such as depicted for **56a** in Scheme 12, results in the formation of hydroxylated cyclic ethers.[125b] Hydroxylation, e.g., of benzene to phenol, can otherwise also be

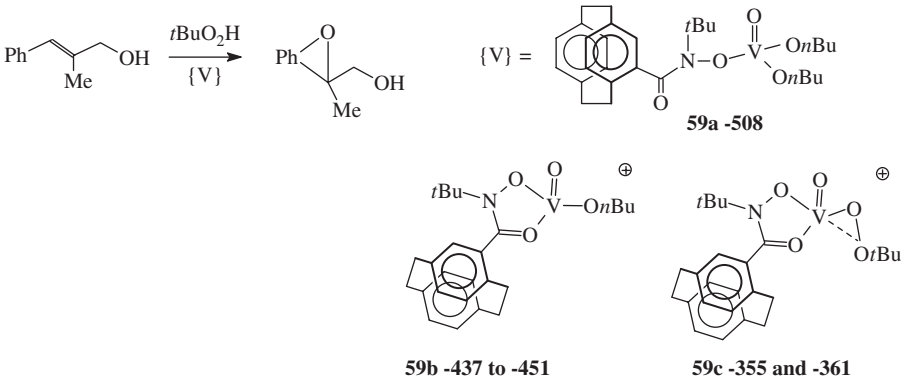

Scheme 14.

catalyzed by vanadate + H_2O_2 in acetonitrile under acidic conditions. The active species are peroxovanadates.[132] Enantio-selective epoxidation of geraniol has been achieved with the *in situ* system $VO(OR)_3$/hydroxamic acid/$tBuO_2H$, where again a vanadium(V)-alkylperoxo intermediate (**59c** in Scheme 14) is the active catalyst, formed from precursor complexes such as **59a** and **59b**.[133] Compound **59c**, which is present as two diastereomers, is a rare example for a down-field shift on replacing an oxo or alkoxo for a peroxo ligand.

3. SOLID-STATE PARAMETERS

3.1. General introduction

^{51}V solid-state NMR lineshapes are dominated by two anisotropic tensorial interactions: quadrupolar and chemical shielding. Dipolar interaction may introduce additional broadening of the spectral lines. Because of the relatively small quadrupole moment of ^{51}V ($-4.8\,fm^2$), ^{51}V solid-state NMR spectra can be readily detected. The above value is based on the recent work by Skibsted, Jacobsen, and colleagues,[3] combining NMR experiments and high-level DFT calculations, allowing the determination of the ^{51}V quadrupole moment with high precision. This value is in general agreement with the quadrupole moment of $-4.3\,fm^2$ determined from laser-induced resonance-fluorescence spectroscopy.[236] We note that the majority of the reports on ^{51}V NMR to date quote a quadrupole moment of $-5.2\,fm^2$ determined in 1967, based on atomic-beam magnetic resonance measurements.[237]

A wealth of information can be extracted from the analysis of the quadrupolar and chemical shielding interactions, making ^{51}V solid-state NMR spectroscopy a very valuable structural probe in a variety of inorganic and biological systems as discussed below. In conjunction with density functional theory (DFT) calculations, ^{51}V solid-state NMR experiments can reveal important details about the vanadium

sites not readily available from the X-ray structures, such as protonation states of the coordinated ligands, electronic structure, and dynamics.

For detailed general treatments of the effects of quadrupolar interaction on the solid-state NMR spectra, we refer the reader to excellent monographs and reviews.[134,135] Here we present only a brief summary relevant to observation and interpretation of ^{51}V solid-state NMR spectra.

The total Hamiltonian in the solid state can be expressed as

$$H = H_{\text{Zeeman}} + H_{\text{RF}} + H_{\text{DIP}} + H_{\text{Q}} + H_{\text{CSA}} \tag{7}$$

where H_{Zeeman} is the Zeeman term, H_{RF} the radiofrequency field, H_{DIP} the dipolar interaction. H_Q and H_{CSA} the quadrupolar and chemical shielding anisotropies (CSA), respectively. These two terms are dominant and dictate the spectral lineshape. As pointed out above, the dipolar interactions are generally much smaller than the quadrupolar and the CSA terms, and usually give rise to additional broadening of the spectral lines. The quadrupolar and CSA terms are commonly expressed as spherical tensors composed of the spatial (R_{mn}) and spin (T_{mn}) variables:[135b]

$$H_Q^{(1)} = \frac{eQ}{4S(2S-1)} \times R_{20}^Q T_{20}^S = \omega_Q[3S_z^2 - S(S+1)] \tag{8}$$

$$H_Q^{(2)} = \frac{C_Q}{\omega_0} \sum_{m \neq 0} \frac{R_{2m} R_{2-m}[T_{2m}, T_{2-m}]}{2m} \tag{9}$$

$$H_{\text{CSA}} = -\gamma\left(R_{00}^{\text{CS}} T_{00}^{\text{S}} + R_{20}^{\text{CS}} T_{20}^{\text{S}}\right) = \left(\omega_{\text{CS}}^{\text{iso}} + \omega_{\text{CS}}^{\text{aniso}}\right) S_Z \tag{10}$$

where $H_Q^{(1)}$ and $H_Q^{(2)}$ are the first- and second-order quadrupolar interactions.

The quadrupolar and CSA tensors according to the standard notation are:

$$C_Q = \frac{eQ\text{V}_{zz}}{h}; \quad \eta_Q = \frac{\text{V}_{yy} - \text{V}_{xx}}{\text{V}_{zz}}; \tag{11}$$

$$\delta_\sigma = \delta_{zz} - \delta_{\text{iso}}; \quad \eta_\sigma = \frac{\delta_{yy} - \delta_{xx}}{\delta_{zz} - \delta_{\text{iso}}}; \quad \delta_{\text{iso}} = \frac{1}{3}(\delta_{xx} + \delta_{yy} + \delta_{zz}) \tag{12}$$

where C_Q is the quadrupolar coupling constant (in MHz); V_{xx}, V_{yy}, and V_{xx} the principal components of the electric field gradient (EFG) tensor, where $\text{V}_{xx} = eq$ is its largest principal component, and $|\text{V}_{zz}| \geq |\text{V}_{yy}| \geq |\text{V}_{xx}|$. Q is the vanadium quadrupole moment given above; e the electronic charge; h the Planck constant.

In Fig. 11, the simulated ^{51}V NMR spectra are presented for an unoriented powder sample to illustrate the typical lineshapes in the solid state. The first-order quadrupolar interaction gives rise to seven transitions (termed the central and the satellite transitions), usually all observable in the resulting NMR spectrum because of the generally small quadrupolar coupling constants in vanadium-containing

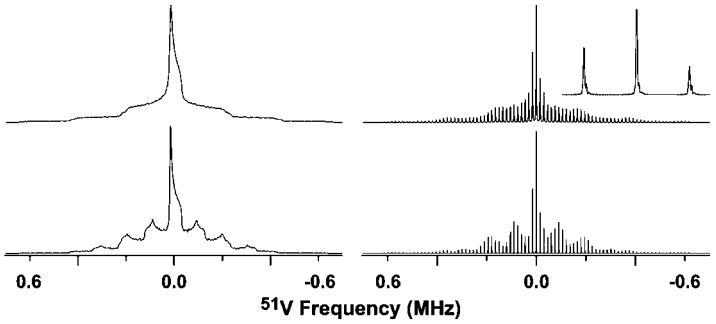

Fig. 11. Simulated 9.4 T ^{51}V static (left) and 15 kHz magic angle spinning (right) solid-state NMR spectra for $C_Q = 3$ MHz, $\delta_\sigma = 300$ ppm, $\eta_\sigma = 0$, $\alpha = 0$, $\beta = 60$, and $\gamma = 0$. The bottom spectra correspond to $\eta_\sigma = 0$, the top spectra to $\eta_\sigma = 1$. The inset is an expansion of the MAS spectrum around the central transition illustrating the second-order quadrupolar broadening of the spinning sidebands.

systems. The overall breadth of the spectral envelope is determined by C_Q; the breadth of the central transition by δ_σ. The asymmetry parameters of the quadrupolar and CSA tensors, η_Q and η_σ reflect the deviations from the axial symmetry and dictate the shape of the overall spectral envelope, and of the central transition, respectively. The second-order quadrupolar interaction results in additional line broadening, yielding the characteristic second-order lineshapes.

Under magic angle spinning, the spectral broadening due to the second-rank spatial components R_{20} of tensorial anisotropies of H_Q^1 and H_{CSA} is averaged into a spinning sideband manifold (illustrated in Fig. 11, right). The fourth-rank terms of $H_Q^{(2)}$ are not completely averaged out, and give rise to the asymmetric second-order lineshapes (shown in the inset in Fig. 11, right). The functional forms of the time-dependent Hamiltonians $H_Q^{(1)}$ and $H_Q^{(2)}$ under MAS have been previously derived by Skibsted and colleagues[136] and can be found in the corresponding article.

A number of experimental methods have emerged in the past decade and a half for the detection of ^{51}V solid-state NMR signals and for extracting the NMR observables from the spectra. Below we summarize the representative single- and double-resonance approaches.

3.2. Single resonance techniques

3.2.1. *^{51}V Magic angle spinning satellite transition spectroscopy (SATRAS)*

For ^{51}V sites with small or moderate quadrupolar constants (in practice, $C_Q < 10$–15 MHz), the modern spectrometer hardware and MAS probes permit efficient excitation and detection of the complete manifold of satellite transitions in the NMR spectra. As demonstrated by Skibsted, Nielsen, Jacobsen, and their colleagues[136–138] as well as in our recent work,[139–141] the elements of the quadrupolar

and the CSA tensor as well as the relative orientations of the two tensors can be readily extracted by numerical analysis of the SATRAS spectra, due to the orders of magnitude differences in the two interactions. The NMR observables are typically determined via the systematic grid search of the spectral parameter space followed by the least-squares optimization of the calculated spinning sideband intensities or the integrated intensities. A number of programs are currently available for simulations of SATRAS spectra, including SIMPSON,[142] STARS (currently incorporated into the Varian software and originally developed by Skibsted, Jakobsen and colleagues[136,137,143]), QUASAR,[144] and NMR5.[145]

3.2.2. *Off-MAS spectroscopy*

Oldfield and later Hayashi demonstrated that preferential broadening of the first-order quadrupolar interaction can be accomplished via a rotation of the sample around an axis that deviates slightly (by 0.5−1°) from the magic angle (54.7°).[146,147] Under these conditions, the intensities of the satellite transitions are greatly attenuated resulting in the selective observation of the spinning sidebands of the central transition whose intensities are dominated by the CSA term and whose lineshape by the second order quadrupolar interaction. This approach permits to extract the chemical shielding anisotropy tensor via the Herzfeld–Berger analysis of the spinning sideband intensities,[148] and the quadrupolar interaction via the lineshape calculations.[147]

3.2.3. *Nutation spectroscopy*

An alternative approach for estimating the value of the quadrupolar interaction involves nutation spectroscopy under static or MAS conditions, the former reviewed in depth by Samoson and Lipmaa.[149] In quadrupolar nuclei, the length of the excitation pulse dictates whether and to what extent the satellite transitions will be excited. For example, selective excitation of the central transition in ^{51}V solids is accomplished by a pulse smaller by a factor of $4(I+1/2)$ compared with the non-selective $\pi/2$ pulse, the latter typically determined from the spectra of a vanadium-containing compound where $C_Q = 0$, e.g., a neat liquid such as $VOCl_3$. The relative contributions of the satellite transitions to the overall intensity of the signal are a function of the excitation pulse length. The nutation profile is determined by the quadrupolar frequency $\nu_Q = 3C_Q/2I(I-1)$ (where $I = 7/2$ for ^{51}V) and the radio frequency $\nu_{RF} = \gamma B_1/2\pi$ (where γ is the gyromagnetic ratio and B_1 the rf field strength). In the limit of a very large or a very small quadrupolar frequency ($\nu_Q >> \nu_{RF}$ or $\nu_Q << \nu_{RF}$), the nutation curve is a sinusoid with the oscillation frequency of $(I+1/2)\nu_{RF}$ or ν_{RF}, respectively.[149] When $\nu_Q \approx \nu_{RF}$ (the so-called intermediate regime), the nutation curve exhibits complex oscillation pattern dependent on C_Q, δ_σ, and (to a smaller extent) on η_Q, as illustrated in Fig. 12. The quantity C_Q, and in some cases η_Q, can be estimated from the nutation curve by numerical simulations as described in a number of reports.[134,140,149–151]

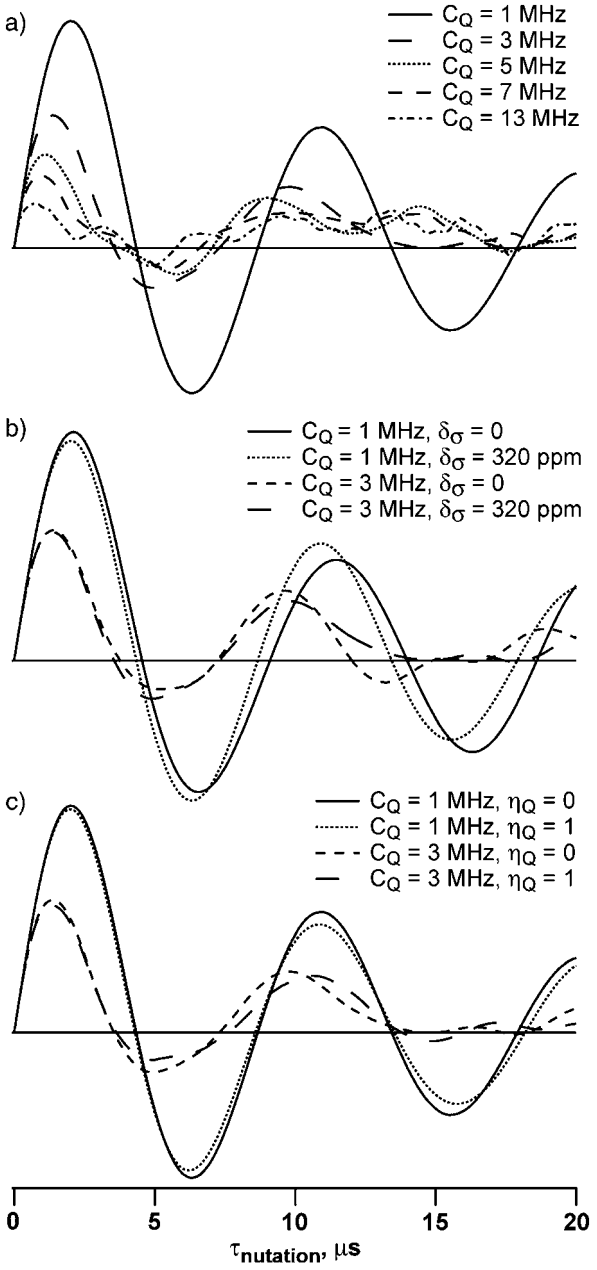

Fig 12. Simulated ^{51}V nutation curves in the presence of magic angle spinning illustrating the effect on the nutation profiles of (a) the magnitude of the quadrupolar coupling constant C_Q (the other NMR parameters are $\eta_\sigma = 0$, $\delta_\sigma = 320$ ppm, and $\eta_\sigma = 0$), (b) chemical shielding anisotropy δ_σ (for $C_Q = 1$ and 3 MHz), and (c) asymmetry parameter η_σ (for $C_Q = 1$ and 3 MHz). The radiofrequency field strength is 100 kHz, and the MAS spinning frequency is 15 kHz.

The main limitation of nutation spectroscopy is its generally poor accuracy, especially in the cases when signals are weak;[140] nevertheless, the method is quite useful for qualitative estimates of the quadrupolar interaction parameters.

3.2.4. *MQMAS*

In the presence of several non-equivalent sites, the analysis of the one-dimensional MAS and off-MAS spectra may be complicated due to the signal overlap. The two-dimensional multiple-quantum MAS (MQMAS) experiment developed by Frydman and co-workers combines space and spin averaging, and correlates the multiple-quantum coherences with the single-quantum coherence corresponding to the central transition.[152,153] The resulting high-resolution spectrum is composed of an isotropic and anisotropic dimension. From the two frequencies defining each peak in the 2D MQMAS spectra, the combined quadrupolar coupling constant and isotropic chemical shift are readily inferred. Static-mode multiple-quantum experiments correlating the highest $-S \rightarrow +S$ multiple quantum transition in the spin manifold with the $-1/2 \rightarrow +1/2$ central transition can be used in conjunction with MQMAS to distinguish the second-order quadrupolar and the CSA.[154]

MQMAS is a powerful approach for the analysis of a large number of half-integer quadrupolar nuclei. However, practically this technique is restricted to systems with moderate or large C_Q and small δ_σ,[154] and therefore MQMAS is not very commonly utilized for investigations of vanadium-containing solids.[155]

3.2.5. *Hahn spin echo decay spectroscopy for homonuclear ^{51}V-^{51}V dipolar couplings*

Homonuclear ^{51}V-^{51}V dipolar interaction in vanadium solids are typically much smaller than the quadrupolar and CSA. Therefore, it is generally difficult if impossible to infer the dipolar coupling constant from the static or MAS spectra. Gee has demonstrated that Hahn spin echo decay spectroscopy can be employed for selective excitation of the central transition, and the analysis of the resulting decay curves yields quantitative estimates of the homonuclear dipolar second moments.[156] This approach is particularly useful for compounds with small or moderate CSA and second-order quadrupolar interaction where the vanadium site at the same time does not exhibit additional heteronuclear dipolar couplings (or these are relatively weak).

3.3. Heteronuclear double resonance techniques

Double- and multiple-resonance methods are generally employed in order to simplify spectral assignments in complex materials, to infer heteronuclear distances, and in some instances to gain information about the dynamics of the half-integer quadrupolar sites. In the past decade and a half, a number of heteronuclear multiple-resonance methods were developed and applied to various half-integer

quadrupolar nuclei; these techniques include SEDOR,[157] REDOR,[158,159] TEDOR,[159,160] TRAPDOR,[161] and REAPDOR.[162] Of these, REDOR and TRAPDOR experiments have been reported in vanadium-containing solids, and are discussed below.

3.3.1. *REDOR*

REDOR developed by Gullion and Schaefer[158] is a double-resonance MAS experiment widely used for quantitative distance measurements in heteronuclear dipolar-coupled spin systems. The REDOR pulse sequence is depicted in Fig. 13a. During the experiment, dipolar dephasing of the magnetization on spin I is accomplished by recoupling of its heteronuclear dipolar interaction with the second spin S via application of rotor-synchronized π pulses on both radiofrequency channels. The

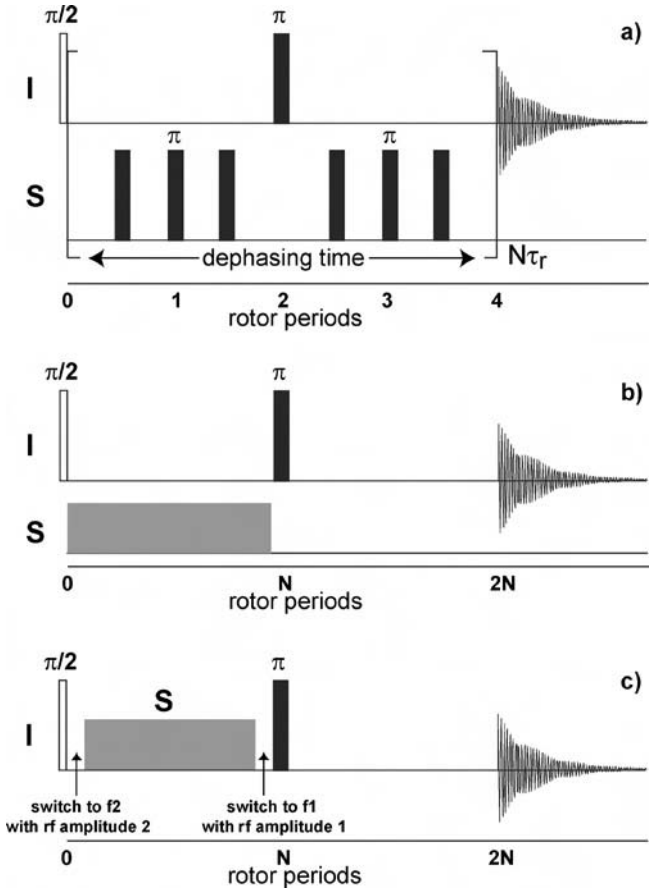

Fig. 13. Pulse sequences for the REDOR (a), TRAPDOR (b), and single-channel TRAPDOR (c) experiments.

intensity of the dephased signal is determined by the dipolar coupling constant (which in turn is dictated by the internuclear distance), and by the total dephasing time. Two sets of spectra are typically recorded as the function of the total dephasing time determined by the number of rotor periods and the MAS frequency: the control spectrum without the application of the recoupling pulses on the *S* channel (called an $\mathbf{S}_0$ spectrum), and the recoupling experiment where the *S* channel is irradiated for the restoration of the heteronuclear dipolar interaction (called an $\mathbf{S}_\mathbf{r}$ spectrum). The REDOR ratios are subsequently defined as $(\mathbf{S}_0 - \mathbf{S}_\mathbf{r})/\mathbf{S}_0$, and from their dependence on the total dipolar evolution time, the dipolar coupling constant and hence the internuclear distance are extracted.

In the modification to the original REDOR sequence, the so-called θ-REDOR experiment developed for the ^{13}C-^{2}H spin pair,[163] a dephasing pulse of a flip angle θ different from π is applied to ^{2}H resulting in superior recoupling performance. For spin 1/2 – half integer quadrupolar spin pairs, REDOR is generally applicable only when the quadrupolar interaction is small, as complete magnetization inversion cannot otherwise be attained.

3.3.2. *TRAPDOR*

In the TRAPDOR experiment developed by Grey and co-workers,[161] and designed specifically for a spin-1/2 – quadrupolar spin nuclear pair, the heteronuclear dipolar interaction is recoupled in the regime of slow MAS by the continuous irradiation of the quadrupolar nucleus leading to adiabatic population transfer between all transitions (central and satellite). The pulse sequence is illustrated in Fig. 13b. While TRAPDOR dephasing is more efficient than REDOR, the drawbacks of the TRAPDOR experiment are the complex dephasing dynamics and the dependence of the dephasing efficiency on the adiabaticity parameter α, which in practice makes quantitative estimates of dipolar coupling constant difficult if impossible. Nevertheless, TRAPDOR found widespread use as a qualitative distance probe,[164] and as a probe of dynamics[165] in various vanadium-containing systems.

It is worth noting that the gyromagnetic ratio of ^{51}V is similar to those of several other nuclei, such as ^{13}C, ^{23}Na, and ^{79}Br, making the double resonance experiments between the corresponding nuclei difficult from the hardware (probe and filters) standpoint. Nevertheless, van Wüllen demonstrated that ^{23}Na-^{51}V TRAPDOR experiment can be readily conducted in a single-resonance probe via frequency and rf-amplitude switching during the pulse sequence, as illustrated in Fig. 13c.[166]

3.3.3. *Heteronuclear ^{51}V decoupling*

^{51}V decoupling has been recently demonstrated in ^{1}H-^{29}Si CPMAS experiments leading to simplified ^{29}Si spectra.[167] In contrast to decoupling from spin-1/2 nuclei, low radiofrequency power generally has to be employed when the decoupled nucleus is a quadrupole.[168]

3.4. Applications

3.4.1. *Inorganic vanadates*

A number of inorganic vanadate solids of different composition and structure have been addressed to date by ^{51}V static and MAS solid-state NMR spectroscopy, including monovalent and divalent metavanadates,[137a,b,146,151,169–171] pyrovanadates,[19,137c,138a,b,151] and orthovanadates.[19,137c,151,172] ^{51}V solid-state NMR parameters shed light on local structural and electronic environments in these vanadates. Eckert and Wachs[151] demonstrated that in meta-, ortho-, and pyrovanadates the ^{51}V chemical shielding anisotropy correlates with the degree of polymerization, and in turn the degree of polymerization as well as the coordination environment of the VO_n structural units can be inferred from the anisotropy and asymmetry parameters of the ^{51}V CSA tensor.[19,170] Skibsted, Jakobsen, and colleagues demonstrated that in metavanadates and KV_3O_8,[137b] ^{51}V solid-state NMR spectroscopy is a powerful technique for distinguishing polymorphs as well as crystallographically non-equivalent sites in a single polymorph.

Interestingly, the inorganic meta- and orthovanadates characterized in the above studies exhibit relatively small quadrupolar interaction. For example, in orthovanadates C_Q varies from 0.85 MHz in $TaVO_5$ to 4.94 MHz in $BiVO_4$.[137c] In metavanadates and KV_3O_8, fairly small variations in C_Q were observed as well: from 2.45 MHz in KV_3O_8[137b] to 4.23 MHz in $RbVO_3$.[137c] δ_σ varies to a greater extent: from 221 in $LiVO_3$ to 512 in β-$NaVO_3$. α- and β-$NaVO_3$ polymorphs are readily distinguishable from their different C_Q (3.8 and 4.2 MHz, respectively) and different δ_σ (259 and 512, respectively).[137b] In pyrovanadates, C_Q are generally larger (reflecting the more distorted vanadium geometry) and vary considerably from 1.58 MHz in the V(1) site of $Ca_2V_2O_7$ to 10.1 MHz in the V(2) site of β-$Mg_2V_2O_7$. δ_σ are also significantly larger than in meta- and orthovanadates. Furthermore, ''thortveitite'' and ''dichromate'' type pyrovanadates are characterized by the different sign of δ_σ.[138a]

In the inorganic vanadates, correlations between the quadrupolar interaction parameters and the local structure for homologous compounds can be established from the classical electrostatic calculations including the first coordination sphere of vanadium.[137,138] These reproduced (by DFT) trends were found to be in excellent agreement with the experimental observations in the inorganic vanadates. The quadrupolar coupling constant C_Q correlates with the local geometry of the VO_n polyhedra in vanadates. The quadrupolar asymmetry parameter η_Q represents the deviation of the electric field gradient tensor from the axial symmetry and reflects the local symmetry of the vanadium site. For example, for the VO_4 tetrahedra in metavanadates, the symmetry is C_{2v}, and the asymmetry parameter is very sensitive to the O-V-O bond lengths and bond angles. In KVO_3, NH_4VO_3, and $TlVO_3$, the experimentally observed η_Q are considerably lower than 1.0, indicating deviations in the O-V-O bond angles from that of a perfect tetrahedron.[137b]

In the absence of single-crystal X-ray diffraction data, ^{51}V MAS and MQMAS NMR spectroscopy can be used to derive structural information in the mixed

vanadium oxides, as has been demonstrated in aluminum orthovanadate $AlVO_4$, the structure of whose asymmetric unit was derived from a combination of solid-state NMR, spectroscopic and powder XRD measurements.[138c]

3.4.2. *Hybrid organic–inorganic and bioinorganic solids*

In contrast to the abundant literature on ^{51}V solid-state NMR investigations of inorganic vanadates (discussed above) and on vanadium-containing catalysts, ceramic and nanocomposite materials (addressed below), there have been only a handful of reports focusing on ^{51}V SSNMR spectroscopy of vanadium(V) solids complexed with organic or bioinorganic ligands.

Rehder and colleagues examined ^{51}V solid-state NMR parameters of vanadyl esters and chlorides $VOCl_3$, $VO(OiC_3H_7)_3$, and $VOCl(OiC_3H_7)_2$.[173] Interestingly, the ^{51}V quadrupolar interaction parameters were found to be of the same order of magnitude (4.4–5.7 MHz) as those for polycrystalline meta- and orthovanadates, and the quadrupolar coupling constants were correlated to the sum of the electronegativities of the groups attached to vanadium.

Crans *et al.* [34] reported syntheses, and established ^{51}V solid-state NMR spectroscopy for the structural characterization of vanadium environments in a large series of new oxovanadium(V) 1,2-diolates. According to the solid-state NMR results, vanadium in these compounds is six-coordinate. In this series, the quadrupolar coupling constants were found to vary considerably between 1.6 and 5.1 MHz, reflecting the differences in the local vanadium geometry and ligand environment. Importantly, this study demonstrated that plausible molecular structures for oxovanadium(V) 1,2-diolates can be proposed, based on solution and solid-state NMR spectroscopy, in the absence of the X-ray crystallographic data.

Polenova, Rehder and co-workers addressed an extensive series of novel bioinorganic oxovanadium(V) solids with various donor sets and mimicking the active sites of vanadium haloperoxidases,[139] by a combination of ^{51}V solid-state NMR spectroscopy and quantum mechanical DFT calculations. It was found that the ^{51}V NMR spectroscopic parameters (and hence the electrostatic environment of the metal) vary significantly as a function of both the proximal and the distal substituents in this series, even for compounds with similar geometries (examples of ^{51}V MAS spectra are illustrated in Fig. 14). Furthermore, it was demonstrated that, while classical electrostatic calculations do not adequately account for the experimentally observed quadrupolar interaction parameters in these covalent complexes, the DFT calculations yield accurate values for the anisotropy and asymmetry parameters of the quadrupolar and CSA tensors. These results may potentially be important in understanding how the substrate specificities of vanadate-dependent haloperoxidases from different microorganisms are fine-tuned by subtle variations of the active site structure in these proteins.[139]

Recently, Mafra *et al.*[174] examined a novel pentanuclear oxovanadium(V) phosphate complex with phenanthroline. ^{51}V solid-state NMR spectra revealed the presence of two types of coordination environments with distorted tetrahedral and

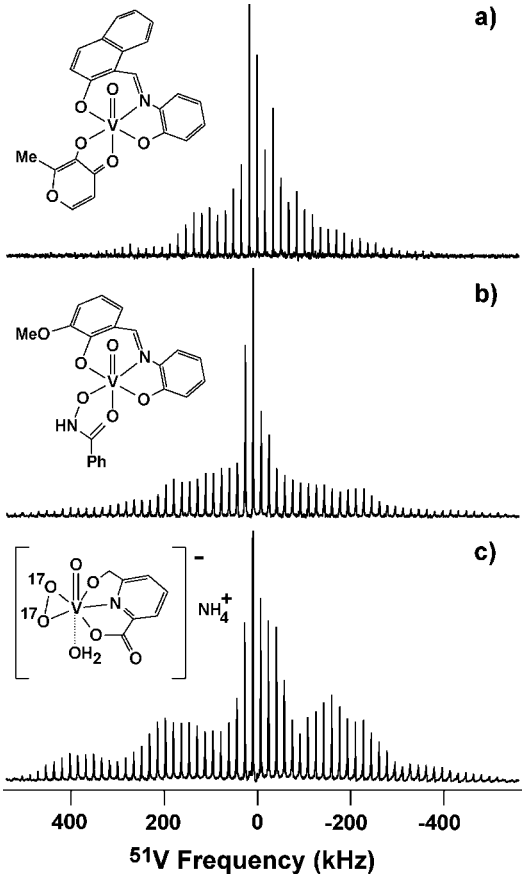

Fig. 14. ^{51}V solid-state NMR spectra of bioinorganic oxovanadium(V) complexes SJZ0040 (a) and SJZ0032 (b) mimicking the resting state, as well as HS003 (c) mimicking the peroxo intermediate of vanadium haloperoxidases. The spectra were acquired at 9.4 T with the MAS spinning frequency of 17 kHz.

distorted octahedral geometry, in agreement with the X-ray crystal structure of the complex.

3.4.3. *Polyoxoanionic solids*

Vanadium-substituted polyoxoanionic solids have found widespread use as oxidation catalysts,[175,176] and are attaining interest for potential applications as solid nanocomposite molecular devices due to their putative electro-, photo-, and thermochromism.[177–180] The degree of vanadium substitution in the polyoxoanion and the counter-ion environment have been empirically determined to be key factors influencing the chemical properties of these solids;[176] however, the molecular basis

of these results could not be established with traditional techniques, such as EPR, FTIR, Raman spectroscopy, and powder X-ray diffraction.

Polenova, Francesconi, Teplyakov, Dmitrenko and co-workers explored the utility of ^{51}V solid-state NMR spectroscopy, FTIR spectroscopy, and DFT calculations for probing the effects of counter-ions and of vanadium substitution on the electronic environment of vanadium sites in oxotungstates of Lindqvist and Keggin families.[141,181] ^{51}V solid-state NMR and FTIR unequivocally demonstrate that the NMR parameters (C_Q, η_Q, δ_σ, and η_σ) as well as the IR vibrational frequencies are dictated by the counter-ions, providing the first direct experimental evidence that counter-ions modulate the electronic structure of the anion. Furthermore, vibrational IR frequencies were accurately predicted by the DFT, when counter-ions were included in the calculations. The degree of vanadium substitution has a profound effect on the quadrupolar and CSA tensor parameters as well.[141] In vanadium-substituted Lindqvist solids, the quadrupolar coupling constants were found to be quite small and ranging from 0.60 MHz in mono-vanadium substituted $[(nC_4H_9)_4N]_3[VW_5O_{19}]$ to 1.55 MHz in di-vanadium substituted $Na_2Cs_2[V_2W_4O_{19}] \cdot 6H_2O$.[141a] In Keggin solids, C_Q was considerably larger and ranged from 0.79 MHz in mono-vanadium substituted $K_4[PVW_{11}O_{40}]$ to 5.50 MHz in tri-vanadium substituted α-1,2,3-$[(nC_4H_9)_4N]_6[PV_3W_9O_{40}]$.[141b] In Fig. 15, selected ^{51}V solid-state NMR spectra are presented for mono-vanadium substituted Lindqvist polyoxotungstates, illustrating the counter-ion effect.

It is worth noting that counter-ions are generally ignored in the DFT analysis of polyoxometalates; however, the above work highlights the importance of counter-ions

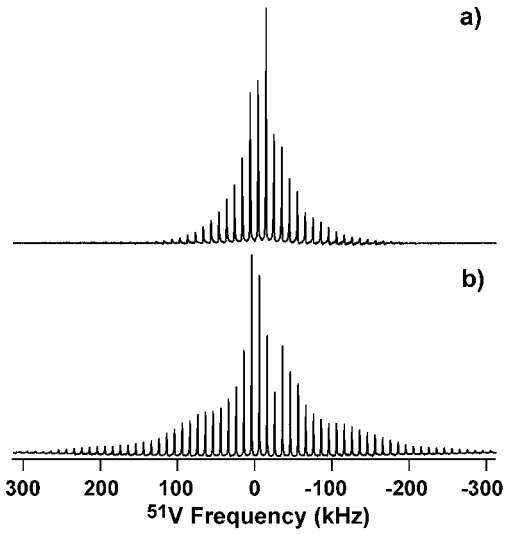

Fig. 15. ^{51}V solid-state NMR spectra of mono-vanadium substituted Lindqvist polyoxotungstates $[(n\text{-}C_4H_9)_4N]_3[VW_5O_{19}]$ (a) and $Cs_3[VW_5O_{19}]$ (b) illustrating that counter-ion dictates the ^{51}V NMR parameters in these solids. The spectra were acquired at 9.4 T with the MAS spinning frequency of 10 kHz.

in defining the electronic structure of the anion and suggests that counter-ions should be considered for accurate description of the system.

Recently, Bonhomme *et al.*[167] illustrated that ^{51}V decoupling can be beneficial in ^{29}Si NMR of a vanadium-containing polyoxometalate solid $[AsW_9O_{33}(t\text{BuSiO})_3(VO)][n\text{Bu}_4\text{N}]_3$, yielding greatly simplified ^{29}Si spectra and permitting to distinguish between the three crystallographically non-equivalent Si sites whose resonances otherwise overlap.

3.4.4. *Proteins: vanadium haloperoxidases*

To date, there is only one example where ^{51}V solid-state NMR spectroscopy has been employed to address vanadium sites in proteins, vanadium-containing haloperoxidases.[140,182] Polenova, Pooransingh-Margolis, Wever, and colleagues demonstrated that ^{51}V MAS spectra can be detected in vanadate-dependent chloro- and bromoperoxidases despite of the low concentration of vanadium sites in the proteins, one per active subunit (*M ca.* 60 kDa), and the large quadrupolar interaction in both proteins, as illustrated in Fig. 16. Experimental NMR parameters describing the quadrupolar and CSA interactions were used in conjunction with the DFT-predicted values for a large number of models representing the possible coordination environments of the vanadium site, to extract the protonation states of the vanadate cofactor in chloroperoxidase. Interestingly, the most

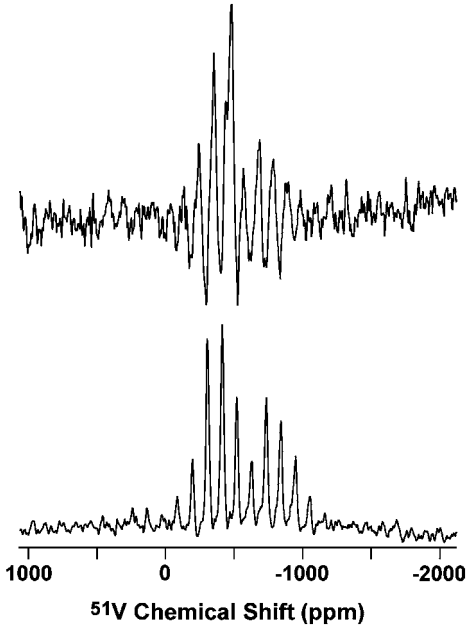

Fig. 16. Comparison of 14.1 T ^{51}V NMR spectra of (a) vanadium chloroperoxidase and (b) vanadium bromoperoxidase. The spectra were acquired with 1.5 million scans; the temperature was −25°C, and the MAS frequency 17 kHz.

probable coordination environment is an anionic vanadate cofactor with the axial hydroxo ligand, while one hydroxo and two oxo groups are present in the equatorial plane. This is different from the anionic fully deprotonated vanadate proposed previously based on the bond-length analysis of the X-ray structure of vanadium chloroperoxidase,[183] but in agreement with recent computational predictions (see also Section 5.2).[184–186] Furthermore, the solid-state NMR spectra reveal that the active sites of vanadium chloro- and bromoperoxidases have unique electronic environments, despite their similar geometries.[182] These results illustrate the promise of an integrated approach involving ^{51}V spectroscopy and DFT calculations for the analysis of diamagnetic vanadium sites in proteins.

3.4.5. *Catalysts, ceramic, and nanocomposite materials*

Traditionally, ^{51}V solid-state NMR spectroscopy has been most widely employed for the analysis of various vanadia-based catalysts, as well as of ceramic and nanocomposite materials, with extensive literature addressing various spectroscopic and chemical aspects of these solids. These systems are not the primary focus of this overview, and we therefore refer the reader to the beautiful detailed reviews of this field,[155,169] as well as to judiciously chosen recent reports.[150,187,188] In addition, we point the reader to the interesting work of Grey and Kim, who demonstrated ^{17}O-^{51}V TRAPDOR NMR in anionic conductors to be a sensitive probe of dynamics of oxo anions coordinated to the different vanadium polyhedra.[165]

4. MESOPHASES

For ^{51}V NMR spectroscopy of mesophases, both solution and solid-state approaches are employed. In the solid-like amorphous systems, the lines are typically broad due to the conformational heterogeneity, and extracting the anisotropic parameters may therefore be challenging. If some intrinsic order is present, as in liquid crystalline systems, seven separate, equidistant resonance lines corresponding to the seven quadrupolar transitions can be observed, the separation of which reflects first order quadrupole perturbation, which can be exploited to evaluate the quadrupole coupling constant in the specific vanadium compound and the order parameter of the liquid crystalline phase; Eq. (13).[189]

$$\Delta\nu_{\mathrm{LC}} = S_a \times \frac{3e^2qQ}{4I(2I-1)h} \tag{13}$$

$\Delta\nu_{\mathrm{LC}}$ is the splitting, S_a the ordering parameter, $e^2qQ/h = C_Q$ the quadrupole coupling constant, and I the nuclear spin.

A typical example, VO(O*i*Pr)$_3$ in the nematic liquid crystal MBBA, is depicted in Fig. 17. The majority of the reports in the literature focus on analyses of isotropic NMR parameters for inferring local coordination geometry of the vanadium sites, and on studies of kinetics of formation of mesophases by simple one-dimensional experiments. Below we describe the applications of ^{51}V NMR in specific systems.

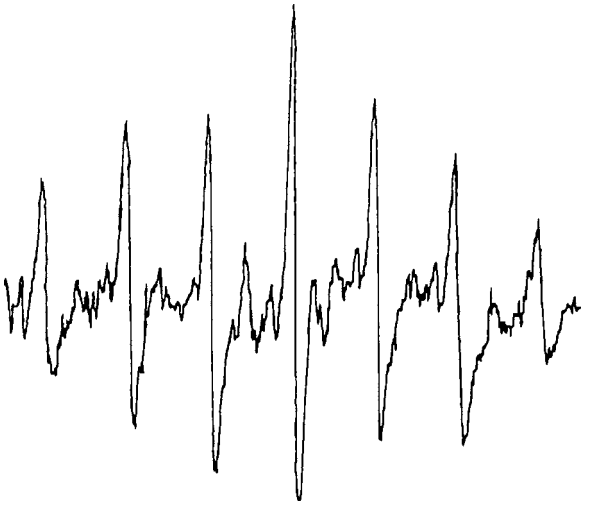

Fig. 17. 11.2 MHz ^{51}V NMR spectrum (1st derivative) of VO(O*i*Pr)$_3$ in the liquid crystal 4-methoxybenzylidene-4′-butylamin (MBBA) at 295 K; vanadium content 8.3%; 23°C. The splitting amounts to 12 kHz.

4.1. Applications

4.1.1. *Sols and gels*

Vanadium pentoxide gels have been a subject of interest and numerous studies due to their interesting physical properties, including proton and electron conduction,[190] defining their applications as antistatic coatings in photography,[191] as well as potential importance in lithium batteries[192] and in electrochromic devices.[193] ^{51}V NMR spectroscopy has been an essential method for probing the composition and local structure of these gels, as well as the gelation kinetics.

Mege and co-workers[194] addressed the effect of surfactants on the formation of vanadium alkoxide gels. The authors conclude that surfactant modifies the gel porosity and affects the gelation rate. ^{51}V NMR spectra revealed that, in the presence of surfactant, hydrolysis is slowed down and the precursor as well as intermediate species VO(OAm)$_3$ and VO(OAm)$_{3-x}$(OH)$_x$ (Am = amyl) are present after 6 h.

Alonso *et al*. explored the synthesis of vanadium pentoxide nematic gels and the mechanism of polymerization of vanadium species.[195–197] ^{51}V NMR spectroscopy was employed to address the speciation in solution, by the characteristic vanadate and peroxovanadate isotropic chemical shifts. Kinetics of gel formation has been traced by monitoring the decrease in intensities of the ^{51}V isotropic peaks corresponding to $[H_2V_{10}O_{28}]^{4-}$ Formation of vanadia–silica composite gels was addressed by Choi *et al*.[198] ^{51}V isotropic chemical shifts revealed that the predominant vanadium species in the gel is dependent on the original vanadium content, and is identified as $V_{10}O_{28}^{6-}$ at low V/(V + Si) ratios, while an additional V(V) in distorted octahedral coordination species emerges when V/(V + Si) = 48%.

Dubarry *et al.*[199] used ^{51}V magic angle spinning NMR spectroscopy to probe the local environments of vanadium in $Li_{1+\alpha}V_3O_8 \cdot nH_2O$ xerogels. The authors observed several vanadium sites, and are able to assign their symmetries based on the chemical shift anisotropy and quadrupolar coupling constant. The interesting conclusion of this work is that the vanadium environments in the xerogels under investigation differ from those in vanadium pentoxide gels.

4.1.2. *Foams*

Carn *et al.*[200] developed a non-static patterning method for the synthesis of macroporous vanadium oxide foams. ^{51}V MAS NMR spectroscopy revealed four distinct vanadium environments in the foam: square pyramidal VO_5 with a water molecule in a *trans* position with respect to the vanadyl V═O bond; a highly distorted VO_5 environment; a square pyramid VO_5 with a water molecule interacting with the vanadyl bond; and a square pyramid environment of vanadium close to that in the crystalline V_2O_5. These types of vanadium species are similar to those observed in the V_2O_5 xerogels.

4.1.3. *Micelles*

Crans, Levinger and coworkers utilized ^{51}V solution NMR spectroscopy to probe interactions of dipicolinatodioxovanadium(V) complexes in reverse micelles.[201,202] Based on the analysis of the ^{51}V longitudinal and transverse relaxation rates and ^{1}H-^{1}H NOEs, the authors conclude that the oxovanadium complex is buried in the hydrophobic part of the interfacial region of the Aerosol OT microemulsions,[203] while in the water/cetyltrimethylammonium bromide (CTAB)/*n*-pentanol/cyclohexane quarternary microemulsions, the complex is located near the lipid interface, with the hydrophobic portion of the dipicolinato ligand facing the aqueous micellar interior.

4.1.4. *Hexagonal mesostructured phases*

Luca and Hook[204] reported on the synthesis of a novel hexagonal meso-structured vanadium oxide (HMVO). ^{51}V MAS NMR spectroscopy was employed to address the local geometry of vanadium in this phase. Interestingly, reduced quadrupolar interaction was observed compared with the crystalline and gel V_2O_5 samples, indicating that the coordination geometry in HMVO is square pyramidal but somewhat less distorted than in V_2O_5.

4.1.5. *Liquid crystals*

As noted above, first order quadrupole perturbation influences the seven Zeeman levels in such a way that seven equidistant transitions are generated, comparable

with first order interaction in crystalline samples, by several orders of magnitude smaller however than in the crystalline solid state.[189] Ordering factors S_a for oxovanadium*tris*(alkoxides) $VO(OR)_3$ (R = *n*Pr, *n*Bu, *t*Bu) dissolved in liquid crystals such as nematic phase 4 (Merck), obtained by employing Eq. (13), are concentration and temperature dependent. Typical S_a values at ambient temperature and concentrations of *ca.* 10% w/w amount to 0.1. Interestingly, an S_a of the same magnitude has been reported for a solution of η^5-$C_5H_5V(CO)_4$ in nematic phase 4.[205]

5. COMPUTATIONAL METHODS

5.1. Methodological aspects

For a long time, computational chemistry of transition metal complexes used to be less well developed than that of common organic molecules, because the former require highly sophisticated, and hence, expensive, quantum chemical methods from the conventional *ab initio* hierarchy. This situation has changed with the advent of DFT in its modern Kohn–Sham implementation, which turned out to be extremely fruitful for the study of geometries, energies, and properties of transition metal complexes.[206] NMR parameters such as chemical shifts and spin–spin coupling constants are important properties that can now be routinely computed with DFT, and several reviews of this field mention transition–metal complexes explicitly.[207–209] In fact, the very first DFT-based method for the calculation of chemical shifts, Sum-Over-States Density Functional Perturbation Theory (SOS-DFPT), had been validated right from the start against known ^{51}V chemical shift tensors.[210] Occasionally, newly developed exchange-correlation functionals are assessed by their performance in reproducing chemical shifts of transition–metal nuclei, including ^{51}V.[211] It therefore seemed appropriate to include a summary of the body of theoretical literature on this nucleus in the present review.

As the details of the underlying theoretical machinery have been often summarized and documented,[212,213] we will only briefly touch some of the basic aspects of chemical-shift computations. Formally, the magnetic shielding tensor, $\boldsymbol{\sigma}$, is obtained as second derivative of the total quantum-mechanical energy of a system with respect to the external magnetic field and the magnetic momenta of the nuclei present.[214] This derivative is conveniently evaluated by means of double perturbation theory, and can in principle be formulated for any desired quantum-mechanical approximation. In order to circumvent the so-called gauge problem, one usually employs sets of gauge origins for the magnetic perturbations that are distributed over the molecular system, either at the level of Hartree–Fock or Kohn–Sham-DFT molecular orbitals (MOs), in the Individual Gauge for Localized Orbitals (IGLO) or Localized Orbitals/Local origin (LORG) approaches, or, more commonly, at the level of the atomic basis set, in the Gauge-Including Atomic Orbitals (GIAO) framework.[212–214] The tensor components of $\boldsymbol{\sigma}$ are obtained as the sum of two parts, a diamagnetic (shielding) part, which depends only on the ground-state wave function, and a paramagnetic (deshielding) part, which depends,

in addition, on the excited states, expressed in terms of the virtual (unoccupied) MOs (*cf.* the approximations to σ_{dia} and σ_{para}, Eqs. (2a–c) in Section 2.1). As with lighter nuclei, it is usually the latter paramagnetic part that is decisive for the actual δ(metal) value and the considerable range frequently observed for such nuclei. Individual matrix elements to these paramagnetic contributions become important when occupied and virtual MOs have the proper symmetry (i.e., when they can mix upon action of the angular operator of the magnetic perturbation) and a small energetic separation (which appears as "energy denominator" in the salient expressions; *cf.* Eq. (2b)). Selected pictorial rationalizations of such contributions, notwithstanding[215] a comprehensive interpretation of metal shielding tensors on this basis is difficult, because there is usually a plethora of significant MO contributions, quite often unique to a particular structure. Besides validation of the available theoretical methods, the main body of computational ^{51}V NMR spectroscopy has thus concentrated on selected applications, e.g., to structural questions or to reactivities in homogeneous catalysis, rather than on detailed interpretations.

In the absence of an empirical absolute shielding scale for ^{51}V, only calculated relative chemical shifts, δ, can be compared with experiment. In computations, the common standard, neat $VOCl_3$, is almost invariably modeled as an isolated molecule (see below for a discussion of medium effects), the isotropic σ value of which is used as reference. The σ value(s) computed for the complex under scrutiny is then subtracted from this reference, affording the desired $\delta(^{51}V)$ value. Because the chemical shift is thus obtained as difference of two σ values, it can benefit to some extent from a cancellation of errors. Such errors could for instance arise from the neglect of relativistic effects. To our knowledge, no such relativistic calculations have been reported for a ^{51}V chemical shift so far, but it is known for other 3d metals that relativistic effects, while noticeable for the magnetic shieldings σ, cancel to a large extent for relative δ values.[208,216] A selection of computed absolute σ values for $VOCl_3$ is collected in Table 12, illustrating the sensitivity of this property to details of geometrical parameters, exchange-correlation functional, and basis set.

Apart from the singular result with the (probably too unflexible) deMon basis set (entry 1 in Table 12), the magnitude of σ is mainly governed by the nature of the exchange-correlation functional employed in the NMR computation: typical "pure" density functionals (entries 2–6) yield σ values around *ca.* −2,000, while popular hybrid functionals (entries 7–15) afford values around *ca.* −2,300. The concomitant deshielding of the metal nucleus upon inclusion of Hartree–Fock exchange in the hybrid functional has been noted for many other transition metal complexes as well, for instance in ferrocene, where this effect has been analyzed in detail.[217]

The first systematic study of ^{51}V equilibrium chemical shifts, published in 1998,[218] has been conducted for a set of seven vanadium complexes that are known experimentally ($VOCl_2F$, $VOClF_2$, VOF_3, VF_5, $VO(OCH_2CH_2)_3N$, $[V(CO)_6]^-$, and $[V(CO)_5(N_2)]^-$) and eight complexes of the general type $V(O\cdots X)Me_n(OMe)_{4-n}$ (X = vacancy or AlH_3, $n = 0 - 4$), the latter modeling known species with bulkier alkyl groups (CH_2SiMe_3 instead of CH_3 or H). Later it has been shown that the use

Table 12. Computed absolute isotropic ^{51}V shielding constants σ for $VOCl_3$

Entry	Method	Functional	Basis[a]	Geometry[b]	σ	Reference
1	IGLO-SOS-DFPT	PW91	deMon/II	Experiment	−1505	[210]
2	IGLO-SOS-DFPT	PW91	WTB/II	BP86 opt	−2010	[218]
3	LORG-DFT	PBE	Wachters/6-31G*	Experiment	−2023	[211]
4	LORG-DFT	BLYP	Wachters/6-31G*	Experiment	−2073	[211]
5	LORG-DFT	BP86	Wachters/6-31G*	Experiment	−2037	[211]
6	GIAO-DFT	BP86	Wachters/6-31G*	BP86 opt	−1959	[218]
7	LORG-DFT	B3LYP	Wachters/6-31G*	Experiment	−2392	[211]
8	LORG-DFT	PBE0	Wachters/6-31G*	Experiment	−2405	[211]
9	GIAO-DFT	B3LYP	Wachters/6-31G*	BP86 opt	−2317	[218]
10	GIAO-DFT	B3LYP	Wachters/II	BP86 opt	−2306	[219]
11	GIAO-DFT	B3LYP	WTB/II	BP86 opt	−2418	[218]
12	GIAO-DFT	B3LYP	Wachters/II	BP86 CP-opt	−2264	[219]
13	GIAO-DFT	B3LYP	Wachters/II	BLYP CP-opt	−2346	[221]
14	GIAO-DFT	B3LYP	Wachters/II	BP86 CPMD	−2292(±1)	[219]
15	GIAO-DFT	B3LYP	Wachters/II	BP86 CPMD(*l*)	−2334(±1)	[227]

[a]Denoted metal/ligands; deMon, Wachters, and WTB stand for a decontracted (6s6p5d) basis from the deMon library, the augmented (8s7p4d) Wachters basis, and a contracted (14s11p8d) well-tempered basis, respectively. 6-31G* and II are standard polarized double- and triple-zeta bases, respectively; see refs. for details.

[b]Experiment from gas-phase electron diffraction; opt and CP-opt stand for optimized with all-electron-Wachters/6-31G* and pseudopotential/plane-wave basis sets, respectively; CPMD denotes a mean value over snapshots from a corresponding trajectory, (*l*) designating a model for the bulk liquid (see text).

of these models is indeed justified, as equilibrium $\delta(^{51}V)$ values computed for $VOMe_3$ and $VO(CH_2SiMe_3)$ agree within better than 20 ppm,[219] a rather insignificant difference compared with the total ^{51}V chemical-shift range of *ca.* 3,500 covered by the test set. For the total set of 15 complexes, a number of the IGLO- and GIAO-based methods detailed in Table 12 were assessed by correlations between equilibrium ^{51}V chemical shifts, computed for DFT-optimized geometries, and the corresponding experimental $\delta(^{51}V)$ values. Little discrimination between the various methods was apparent, both in terms of the slopes of the linear regression lines (which were all close to the ideal value of 1) and the mean absolute deviations from experiment. For the GIAO-BP86 and -B3LYP methods, the errors were between 114 and 119 ppm,[218] a quite satisfactory agreement (*ca.* 3% of the total chemical shift range covered). Whereas both "pure" and hybrid functionals thus performed similarly well for $\delta(^{51}V)$, the latter variants, B3LYP in particular, had been found clearly superior for many other transition–metal nuclei.[220] Therefore, the GIAO-B3LYP level was also recommended for the calculation of ^{51}V chemical shifts.[218]

These comparisons involved computed equilibrium chemical shifts in the gas phase, δ_e, whereas the experiments refer to thermally averaged values in a solvent. Inert organic solvents had been used in the experiments for this test set, and little effect on the trends in $\delta(^{51}V)$ is to be expected. Thermal averaging, however, could affect the metal chemical shift noticeably, in particular when this nucleus is very

sensitive to small structural changes, such as thermally induced elongations of bonds from their equilibrium values. The first study of such thermal effects on transition–metal chemical shifts was conducted for vanadium complexes, where such thermal fluctuations were modeled by short-time (a few picoseconds) classical molecular dynamics (MD) simulations based on DFT-derived energies and gradients, specifically in the Car-Parrinello MD (CPMD) scheme.[221] Mean isotropic shielding constants were obtained by averaging the instantaneous σ values over a sufficient number of snapshots from the MD trajectory. For $VOCl_3$ and three small vanadates, $[VO_2(OH)_2]^-$, $[VO_2(H_2O)_4]^+$, and $[VO(O_2)_2(H_2O)]^-$, only small differences were found in the gas phase between these thermal averages (σ_{av}) and the corresponding equilibrium values (σ_e), e.g., less than 30 ppm for $VOCl_3$ (compare entries 12 and 14 in Table 12). Even smaller effects were obtained when zero-point corrections to σ_e values (which are not included in the MD simulations with their classical propagation scheme) were computed using a perturbational approach.[222] For $VOCl_3$, for instance, such corrections (affording σ_0) amounted to less than 20 ppm. Subsequently, zero-point and classical thermal effects were evaluated for the above-mentioned test set (excluding the OMe derivatives).[219] For most complexes, similarly small changes to σ_{av} and σ_0 were obtained (up to *ca.* 40 ppm), resulting in even smaller changes in the corresponding δ values. Somewhat larger effects, exceeding 100 ppm, were obtained for the carbonyl complexes, $[V(CO)_6]^-$ and $[V(CO)_5(N_2)]^-$, and for the model Lewis-acid complex $V(O\cdots AlH_3)Me_3$, in which cases the thermally averaged chemical shifts agreed better with experiment than the equilibrium ones. Over the whole, smaller test set, however, these improvements were only moderate: for instance, on going from δ_e(CP-opt) to δ_{av}(CPMD) values, the mean absolute deviation decreased from 165 to 134 ppm.[219]

In terms of σ values, zero-point and thermal effects are deshielding in essentially all cases, due to enhanced paramagnetic contributions upon the concomitant elongations of the vanadium-ligand bonds. The sensitivity of the ^{51}V nucleus toward these geometrical parameters has been evaluated in terms of shielding/bond-length derivatives, $\partial\sigma_V/\partial r_{V-L}$, which were found to account to a large extent for the calculated changes in σ.[219] For the six V-C bonds in $[V(CO)_6]^-$, e.g., such a derivative of $-44.5\,ppm\,pm^{-1}$ has been obtained. This number is about twice as large as an earlier empirical estimate ($-20\,ppm\,pm^{-1}$),[100a] but is definitely on the same order of magnitude. For a peroxovanadate–imidazole complex, the computed ^{51}V chemical shift has also been shown to depend noticeably on the particular conformation of the imidazole ligand, i.e., its rotation about the V-N axis.[223]

When ^{51}V NMR spectra are recorded in polar protic solvents such as water, the effects of the latter on the chemical shifts may no longer be negligible. With this possibility in mind, the MD-based protocol has been extended to model ^{51}V chemical shifts in water.[221] This was achieved by filling the periodic boxes in the CPMD setup with an appropriate number of water molecules, thus modeling an infinite bulk solution. In this approach, solvent and solute are treated on an equal quantum-chemical footing and are free to interact or react, at least on the short time scales accessible. In fact, spontaneous processes observed in such simulations

can provide interesting insights into structure and speciation of the species under scrutiny (see below). NMR properties were then averaged over snapshots without periodic boundary conditions, i.e., containing a single complex each, and with the surrounding water molecules represented as point charges. Initially, the underlying CPMD simulations had been performed with the BLYP functional,[221] but the BP86 combination, preferable for transition–metal complexes, has later been shown[224] to provide very similar results in conjunction with GIAO-B3LYP NMR computations. Up until now, this approach has been applied to a number of oxo- and peroxovanadium(V) complexes,[221,223,225,226] the data of which are summarized in Table 13 and displayed graphically in Fig. 18.

In general, the combined thermal and solvent effects on the computed ^{51}V chemical shifts are not large (compare δ_e (g) and δ_{av} (aq) values in Table 13), exceeding 100 ppm only for the *bis(*peroxo) complexes, $[VO(O_2)_2L]^-$ (L = water or imidazole, see last two entries in Table 13). In the latter cases, a very large decrease of the V-L bond lengths upon solvation has been noted (by *ca.* 0.3 and 0.1 Å, respectively),[221,223] consistent with the concomitant shielding of the ^{51}V nucleus in water.

When comparing simulated and experimental $\delta(^{51}V)$ values in water, it turns out that most peroxo species are described very well (filled circles in Fig. 18), whereas a systematic shift of *ca.* 140 ppm to lower field is apparent for the theoretical $\delta(^{51}V)$ data of "normal" vanadates (filled squares in Fig. 18). The reasons for this discrepancy are not understood at present. Initially it had been speculated that systematic errors in $\delta(^{51}V)$ might be introduced by a different treatment of the aqueous substrate and the standard, $VOCl_3$, because the latter was only modeled in the gas phase, not as the neat liquid it is used experimentally.[221] Preliminary efforts to model such a neat liquid with CPMD, however, produced no evidence for

Table 13. Equilibrium (δ_e) and thermally averaged (δ_{av}) ^{51}V chemical shifts, computed at the GIAO-B3LYP level for minima or snapshots from optimizations or CPMD simulation with the BP86 functional[a]

Compound	Reference	δ_e (g) (CP-opt)	δ_{av} (g) (CPMD)	δ_{av} (aq) (CPMD)	Experiment[b]
$[VO_2(glygly')]^-$	[226]	−637	n.a.	−627	−505
$[VO_2(H_2O)_n]^{+c}$	[221]	−664	−662	−694	−545
$[VO_2(OH)_2]^-$	[224]	−659	−669	−715	−560
$[VO(O_2)(H_2O)_3]^+$	[225]	−484	n.a.	−560	−543
$[VO(O_2)(glygly')]^-$	[225]	−616	n.a.	−656	−649
$[VO(O_2)_2(H_2O)]^-$	[224]	−588	−561	−682	−692
$[VO(O_2)_2(im)]^-$	[223]	−722	−696	−833	−748

[a]Relative to gaseous $VOCl_3$, optimized or modeled at the corresponding level; (g) and (aq) denote gaseous and aqueous phase, respectively. im, imidazole; glygly', NH_2-CH_2-CO-N-CH_2-COO^-.
[b]In water; see cited references for the experimental sources.
[c]BLYP functional employed in CPMD optimizations and simulations, where *n* was equal to 3 in the gas phase, and approximately 3.5 in water.

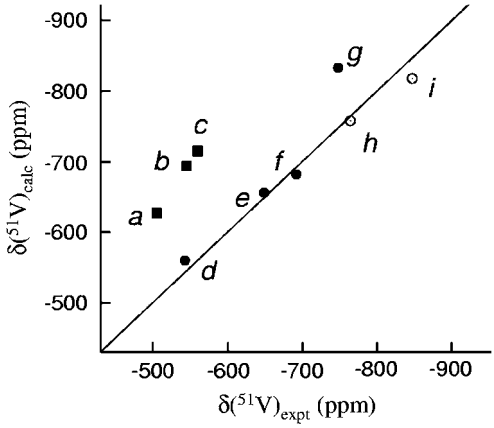

Fig. 18. Plot of calculated (B3LYP/CPMD) vs. experimental ^{51}V chemical shifts of aqueous vanadate (squares) and peroxovanadate complexes (circles) from Table 13, together with the ideal line (no fit); *a* $[VO_2(glygly')]^-$, *b* $[VO_2(H_2O)_n]^+$, *c* $[VO_2(OH)_2]^-$, *d* $[VO(O_2)(H_2O)_3]^+$, *e* $[VO(O_2)(glygly')]^-$, *f* $[VO(O_2)_2(H_2O)]^-$, *g* $[VO(O_2)_2(H_2O)]^-$, *h* $[VO(O_2)_2(OOH)]^{2-}$, *i* $[V(O_2)_4]^{3-}$; for assignments of the latter two resonances see text.

a substantial gas-to-liquid-shift for that compound: only a slight deshielding of *ca.* 40 ppm was predicted upon going into the bulk (compare last two entries in Table 13),[227] albeit with an unknown error margin due to a possibly incomplete equilibration of the MD simulation. At present, the search for better exchange-correlation functionals appears to be the most promising route to identify theoretical methods and levels that allow computation of ^{51}V NMR properties with a uniform, high accuracy.

Compared with studies on isotropic ^{51}V chemical shifts, assessment of computed tensor elements is much less well developed (see also preceding section on experimental solid-state ^{51}V NMR spectroscopy). In the first SOS-DFPT study, experimental chemical shift anisotropies and asymmetry parameters of some metavanadates MVO_3 (M = Li and Na) were reasonably well predicted (better than 60 ppm and 0.01 for $\Delta\delta$ and η, respectively), even though only a minimal cluster model without cations was considered in the computations.[210] In a more recent solid-state NMR study, observed and GIAO-B3LYP computed chemical shielding anisotropy (CSA) parameters of three oxovanadium(V) complexes with O and N donors were also found in respectable agreement, within *ca.* 70 ppm and 0.15 for δ_σ and η_σ, respectively (see preceding section for definition of these parameters).[139] Larger errors were apparent in the theoretical isotropic chemical shifts of these complexes (exceeding 300 ppm), part of which may be related to the fact that the geometries of substrates and standard were taken from different sources, namely experiments in the solid and a DFT-optimization in the gas phase, respectively. Even larger discrepancies were found for one complex containing, in addition to O- and N-donors, an S-donor atom coordinated to the metal. Because in this case, the results were also quite basis-set dependent, more definite conclusions

concerning the DFT performance would have to await more systematic studies involving larger basis sets and, possibly, complexes with other donors from the second main row.

To summarize this section, the theoretical methods to compute ^{51}V chemical shifts from first principles are well advanced, and it is now possible to model this property under the conditions of the NMR experiment, i.e., at ambient temperature and in solution. For essentially all vanadium complexes studied so far, effects of solvation and/or thermal averaging on $\delta(^{51}V)$ are rather small, rarely approaching or exceeding 100 ppm. Occasional, larger deviations notwithstanding, the intrinsic accuracy of the currently employed flavors of DFT appear to be on the same order of magnitude, and a further reduction of this "theoretical uncertainty" is a challenge worth pursuing. Within the limits set by this error margin, however, structural and functional applications of ^{51}V NMR calculations are already possible, as will be discussed in the following section.

5.2. Applications

The first chemical applications of ^{51}V chemical shift calculations were directed toward homogeneous catalysis, emphasizing the potential usefulness of ^{51}V NMR spectroscopy for a screening of potential catalysts. Inspired by empirical correlations between transition–metal chemical shifts and reactivities,[228] and by observations that oxo- and imidovanadium(V) complexes can be active catalysts for olefin polymerization, attempts have been made to correlate computed $\delta(^{51}V)$ values in model catalysts $VXMe_3$ with the barriers ΔE^{a} for ethylene insertion into one of the V-C bonds, believed to be the rate-limiting step in the catalytic cycle.[229–231]

For the model oxovanadium(V) species (X = O), coordination of a Lewis acid of increasing strength to the terminal oxo ligand was computed to successively reduce this barrier and to produce an ever more deshielded ^{51}V nucleus in the adduct complex.[229] A similar trend between computed barriers and $\delta(^{51}V)$ values has been found in imidovanadium(V) complexes, depending on the electron-withdrawing capabilities of the alkyl and aryl groups attached to the imido nitrogen atom and the possibility of forming additional intramolecular contacts between *ortho*-aryl substituents and the metal center.[230] The common trend for both systems, which extends to the respective protonated species as limiting cases with lowest barriers, is depicted in Fig. 19 (open squares and circles). In these systems, ^{51}V NMR could be useful to screen potential catalysts, as more active catalysts should be characterized by higher metal chemical shifts. In particular for imidovanadium complexes, the use of which as olefin-polymerizing catalysts has flourished recently,[232] it would be rewarding if this property could be exploited for catalyst design and optimization.

For the parent systems with X = NH, O, S, and Se a similar trend was predicted, but with a much smaller sensitivity of the computed barrier toward $\delta(^{51}V)$[231] (see filled triangles in Fig. 19). Thus, NMR/reactivity correlations in general will be limited to closely related species within specific families of compounds. Such limitations became even more apparent in the $[VO(O_2)_2L]^-$ system, which was

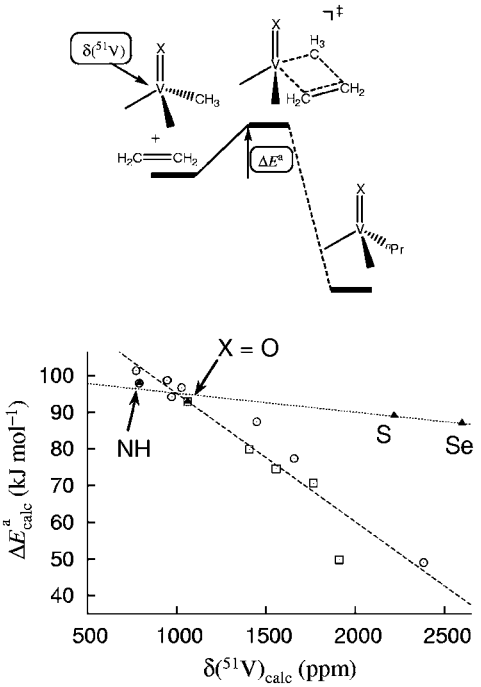

Fig. 19. Top: Schematic sketch of olefin insertion into $VXMe_3$. Bottom: Correlations of predicted activation barriers for ethylene insertion (BP86 + ZPE level) and ^{51}V chemical shifts (GIAO-B3LYP) in such $VXMe_3$ systems; triangles: parent systems (dotted line: linear correlation); squares: Lewis adducts of oxo species; circles: imido derivatives (dashed line: linear correlation for the latter two systems combined). Data taken from refs. 229–231.

predicted to be a viable catalyst for ethylene epoxidation in the case of L = imidazole.[223] General trends between O-transfer barriers and $\delta(^{51}V)$ were only found for very closely related ligands L, notably neutral N-heterocyclic aromatic species, suggesting that in this case ^{51}V NMR will probably be less useful in catalyst design.

Besides these reactivity studies, ^{51}V chemical shift computations have been applied to structural problems, i.e., to cases where ^{51}V NMR spectra are known, but not the precise structure of the species producing them. Even though no definite structural proof is possible in this way, a good accord between calculated and experimental shifts can be taken as evidence for the plausibility of the structure employed in the computation. This approach has furnished support for the assignment of complexes between vanadate and the simplest dipeptide, glycylglycine, to anionic, five-coordinated species $[VO_2(glygly')]^-$ (glygly′ = NH_2-CH_2-CO-N-CH_2-COO^-), *cf.* **XIII** in Fig. 20).[233,226] Specifically, static computations in the gas phase have strongly disfavored a structure with a *fac* orientation of the tridentate dipeptide ligand (which optimized to a *mer* conformation) and to a complex with intact peptide linkage, i.e., protonated at the peptide nitrogen atom

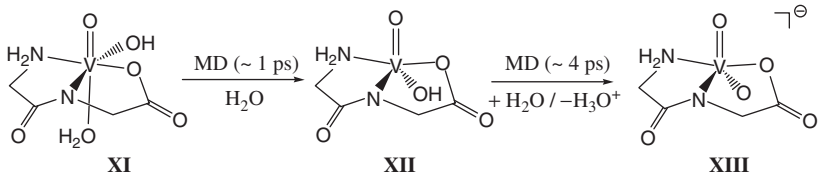

Fig. 20. Plausible structural candidates for the complex formed between vanadate and glycylglycinate, validated by computed ^{51}V chemical shifts. According to CPMD simulations (ref. 226), species **XIII** is favored in water, where it is formed spontaneously from **XI** and **XII**.

(which showed a deviation of *ca.* 200 ppm between the calculated and the observed ^{51}V chemical shift).[233]

Similar results have been obtained for the related glycylserine complex, for which the calculations corroborated the presence of two structural isomers, namely one coordinated via an O atom of the carboxylate group (as depicted in Fig. 20), and one coordinated via the O atom of the hydroxymethyl side-chain.[234] Further distinction of details concerning type and number of other O-donor ligands about the metal, however, were not possible with these static gas-phase studies, as the computed $\delta(^{51}V)$ values of several such possibilities (e.g., **XI** – **XIII** in Fig. 20) were all found within 100 ppm of experiment, i.e., within the previously established uncertainty of the DFT-based approach (see above). Progress toward such a distinction has subsequently been made in a CPMD study of the glycylglycine complex in water: in these simulations, the neutral species **XI** with six-coordination about the metal turned out to be unstable, quickly losing the labile water ligand and a proton to the surrounding solvent.[226] The resulting species **XIII** was also validated by its computed ^{15}N chemical shift.

The combination of CPMD simulations and chemical shift calculations was also used to study peroxovanadate complexes, which are present at high pH and H_2O_2 concentrations and which are characterized by high-field ^{51}V resonances, between *ca.* −710 and −850 (*cf.* Table 2 and text in Section 2.1.1).[235] According to the computational results, some of the original (largely tentative) assignments of the signals in that region may need revision. For instance, species formulated as $[VO(O_2)_3]^{3-}$ or $[V(OH)(O_2)_3]^{2-}$ were either not stable in the simulations or afforded predicted $\delta(^{51}V)$ values outside this characteristic, strongly shielded region.[225] Two stable high pH structures with computed chemical shifts in that region, $[V(O_2)_4]^{3-}$ and $[VO(O_2)_2(OOH)]^{2-}$ are depicted in Scheme 15. When the latter is identified with the species originally believed to be $[VO(O_2)_3]^{3-}$ (from which it formed spontaneously within a few picoseconds in a CPMD simulation), and when both assignments are switched, excellent accord with experiment is obtained (see data points labeled *h* and *i* in Fig. 18).

In these CPMD-based structural applications, the inclusion of thermal and solvation effects was not so critical for the accuracy of the ^{51}V chemical shift of a given minimum, but rather allowed to explore the intrinsic stability of a given species under the experimental conditions. Both aspects combined, apparent kinetic

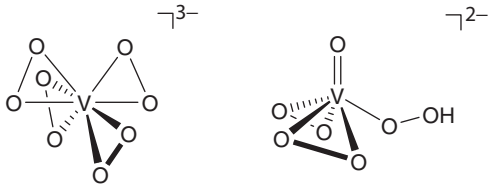

Scheme 15.

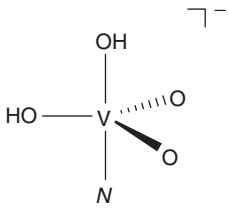

Fig. 21. Probable first coordination sphere of vanadium in a V-containing enzyme, as suggested by the NMR computations in ref. 140 (*N*: nitrogen donor, histidine in the actual enzyme).

stability and well-reproduced experimental $\delta(^{51}V)$ values, are thus a promising tool to study structures and speciation of vanadium complexes in solution.

For a large set of small oxovanadium(V) complexes modeling the active site of a vanadium-dependent chloroperoxidase (VCPO), the GIAO-B3LYP computed CSA (and nuclear quadrupole coupling) tensor components have been compared with the corresponding quantities derived experimentally for the actual enzyme.[140] This comparison can provide insights into details of protonation state and hydrogen-bond network involving the active center, information that is not available from the positions of the heavy atoms, as located by X-ray crystallography in a VCPO single crystal. Of the 86 optimized model complexes, just 16 were found to match the experimental tensorial NMR data reasonably well (within 15–20% of the respective values). The majority of these candidates, and the most plausible ones based on other considerations such as accessibility at the given pH, have an overall singly negatively charged vanadate core (see Fig. 21), in accordance with energetic preferences obtained in quantum-mechanical/molecular-mechanical calculations[185] of larger sections from the whole enzyme.

6. CONCLUDING REMARKS

The numerous investigations reviewed here illustrate the power of ^{51}V both in solution and in solid-state NMR spectroscopy for analyses of various vanadium-containing systems encompassing virtually all classes of inorganic, organovanadium and biological materials. As demonstrated, a plethora of modern ^{51}V solid-state NMR methods is available to the experimentalist, and a careful choice of the

method suited to a particular system yields a wealth of information about the geometrical and electronic aspects of local structure of vanadium sites. ^{51}V NMR spectroscopy is especially beneficial when used in conjunction with modern computational methods for calculations of the electric field gradients and of the chemical shielding anisotropy tensors. This integrated approach has great promise for providing the accurate description of geometry and electronic structure of complex vanadium solids intractable by the traditional crystallographic methods. Given the large amount of shielding, coupling, and relaxation data now available for classification of vanadium centers in specific environments, future applications will concentrate on geometric and electronic structure elucidation of insufficiently characterized materials such as those stemming from biological sources and present as active (transient) species in catalytically conducted reactions.

ACKNOWLEDGMENTS

Part of the work reported herein has been carried out in the frame of projects supported by the Deutsche Forschungsgemeinschaft (grants to D.R.). T.P. acknowledges financial support of the National Science Foundation (NSF-CAREER CHE-0237612) and the National Institutes of Health (P20-17716 under COBRE program). M.B. wishes to thank Prof. W. Thiel and the MPI in Mülheim for continuous support.

REFERENCES

1. O. W. Howarth, *Prog. Nucl. Magn. Reson. Spectrosc.*, 1991, **22**, 453.
2. O. Lutz, W. Messner, K. R. Mohn and P. Kroneck, *Z. Phys. A*, 1981, **300**, 111.
3. M. R. Hansen, G. K. H. Madsen, H. J. Jakobsen and J. Skibsted, *J. Phys. Chem.*, 2006, **110**, 5975.
4. (a) D. Rehder, *Magn. Reson. Rev.*, 1984, **9**; (b) D. Rehder, *Chimia*, 1986, **40**, 186; (c) D. Rehder, in: *Transition Metal Nuclear Magnetic Resonance*, P. S. Pregosin ed., Elsevier, Amsterdam, 1991, p. 1.
5. (a) D. Rehder, in: *Vanadium in Biological Systems*, N. D. Chasteen ed., Kluwer Academic, Dordrecht, 1990, p. 173; (b) D. Rehder, *Coord. Chem. Rev.*, 1991, **110**, 161; (c) D. Rehder and D. Rodewald, in: *Advanced Applications of NMR to Organometallic Chemistry*, M. Gielen, R. Willem and B. Wrackmeyer, eds., Wiley, New York, 1996 Ch. 10.
6. L. Pettersson, in: *Polyoxometalates: From Platonic Solids to Anti-Retroviral Activity*, M. T. Pope and A. Müller, eds., Kluwer Academic, Dordrecht, 1994, p. 27.
7. O. B. Lapina, V. M. Mastikhin, A. A. Shubin, V. N. Krasilnikov and K. I. Zamaraev, *Prog. NMR Spectrosc.*, 1992, **24**, 525.
8. L. -H. Bi, U. Kortz, M. H. Dickmann, S. Nellutla, N. S. Dalal, B. Keita, L. Nadjo, M. Prinz and M. Neumann, *J. Cluster Sci.*, 2006, **17**, 143.
9. S. K. Dutta, S. Samanta, S. B. Kumar, O. H. Han, P. Burckel, A. A. Pinkerton and M. Chaudhury, *Inorg. Chem.*, 1999, **38**, 1982.
10. (a) N. F. Ramsay, *Phys. Rev*, 1950, **78**, 699; (b) N. F. Ramsay, *Phys. Rev.*, 1952, **86**, 243; (c) J. S. Griffith and L. E. Orgel, *Trans. Farad. Soc.*, 1957, **53**, 601.
11. J. S. Griffith, in: *The Theory of Transition Metal Ions*, Cambridge University Press, London, 1964, p. 284.
12. D. Rehder, C. Weidemann, A. Duch and W. Priebsch, *Inorg. Chem.*, 1988, **27**, 584.

13. (a) K. Elvingson, A. Gonzáles-Baro and L. Pettersson, *Inorg. Chem.*, 1996, **35**, 3388; (b) H. Schmidt, I. Anderson, D. Rehder and L. Pettersson, *Chem. Eur. J.*, 2001, 7.
14. D. C. Crans, C. D. Rithner and L. A. Theisen, *J. Am. Chem. Soc.*, 1990, **112**, 2901.
15. M. J. Gresser and A. S. Tracey, *J. Am. Chem. Soc.*, 1986, **108**, 1935.
16. B. Galeffi and A. S. Tracey, *Inorg. Chem.*, 1989, **28**, 1726.
17. E. E. Hamilton, P. E. Fanwick and J. J. Wilker, *J. Am. Chem. Soc.*, 2002, **124**, 78.
18. E. E. Hamilton, P. E. Fanwick and J. J. Wilker, *J. Am. Chem. Soc.*, 2006, **128**, 3388.
19. S. Hayakawa, T. Yoko and S. Sakka, *Bull. Chem. Soc. Jpn.*, 1993, **66**, 3393.
20. I. Andersson, S. Angus-Dunne, O. Howarth and L. Pettersson, *J. Inorg. Biochem.*, 2000, **80**, 51.
21. H. Schmidt, I. Andersson, D. Rehder and L. Pettersson, *Chem. Eur. J.*, 2001, **7**, 251.
22. M. Bonchio, O. Bortolini, V. Conte and S. Moro, *Eur. J. Inorg. Chem.*, 2001, 2913.
23. S. J. Angus-Dunne, C. P. Paul and A. S. Tracey, *Can. J. Chem.*, 1997, **75**, 1002.
24. A. M. Khenkin and R. Neumann, *Inorg. Chem.*, 2000, **39**, 3455.
25. J. Chrappova, P. Schwendt and J. Marek, *J. Fluorine Chem.*, 2005, **126**, 1297.
26. C. Simonnet-Jegat and F. Secheresse, *Chem. Rev.*, 2001, **101**, 2601.
27. Z. Chen, S. -H. Cai, J. -L. Ye, P. -Q. Huang, F. -K. Zheng and J. -S. Huang, *Polyhedron*, 1999, **18**, 1339.
28. Q. Liu, Y. Yang, L. Huang, D. Wu, B. Kang, C. Chen, Y. Deng and J. Lu, *Inorg. Chem.*, 1995, **34**, 1884.
29. Y. Deng, Q. Liu, Y. Yang, Y. Wang, Y. Cai, D. Wu, C. Chen, D. Liao, B. Kang and J. Lu, *Inorg. Chem.*, 1997, **36**, 214.
30. C. Weidemann and D. Rehder, *Inorg. Chim. Acta*, 1986, **120**, 15.
31. R. Christophersen, P. Klingelhöfer, U. Müller, K. Dehnicke and D. Rehder, *Z. Naturforsch.*, 1985, **40b**, 1631.
32. A. S. Tracey and M. J. Gresser, *Can. J. Chem.*, 1988, **66**, 2294.
33. E. C. E. Rosenthal, H. Cui, J. Koch, G. Escarpa, M. Hummert and S. Dechert, *Dalton Trans.*, 2005, 3108.
34. C. C. Crans, R. A. Felty, H. Chen, H. Eckert and N. Das, *Inorg. Chem.*, 1994, **33**, 2427.
35. F. Hillerns, F. Olbrich, U. Behrens and D. Rehder, *Angew. Chem. Int. Ed. Engl.*, 1992, **31**, 447.
36. (a) W. Priebsch and D. Rehder, *Inorg. Chem.*, 1990, **29**, 3013; (b) F. Hillerns and D. Rehder, *Chem. Ber.*, 1991, **124**, 2249.
37. L. Albaric, N. Hovnanian, A. Julbe and G. Volle, *Polyhedron*, 2001, **20**, 2261.
38. D. Gudat, U. Fischbeck, F. Tabellion, M. Billen and F. Preuss, *Magn. Reson. Chem.*, 2001, **40**, 139.
39. F. Preuss, M. Vogel, U. Fischbeck, J. Perner, G. Overhoff, E. Fuchslocher, F. Tabellion, B. Geiger and G. Wolmershäuser, *Z. Naturforsch. B*, 2001, **56b**, 1100.
40. A. Aistars, R. J. Doedens and M. N. Doherty, *Inorg. Chem.*, 1994, **33**, 4360.
41. T. Moriuchi, K. Ishino, T. Beppu and T. Hirao, 232nd ACS National Meeting, San Francisco, 2006, INOR-982.
42. H. Hagen, C. Bezemer, J. Boersma, H. Kooijman, M. Lutz, A. L. Spek and G. van Koten, *Inorg. Chem.*, 2000, **39**, 3970.
43. A. Gorzsás, I. Andersson and L. Pettersson, *Dalton Trans.*, 2003, 2530.
44. A. Gorzsás, K. Getty, I. Andersson and L. Pettersson, *Dalton Trans.*, 2004, 2873.
45. A. Gorzsás, I. Andersson, H. Schmidt, D. Rehder and L. Pettersson, *Dalton Trans.*, 2003, 1161.
46. M. H. Lee and I. W. Kim, *Bull. Korean Chem. Soc.*, 1993, **14**, 557.
47. (a) S. Hati, R. J. Batchelor, F. W. B. Einstein and A. S. Tracey, *Inorg. Chem.*, 2001, **40**, 6258; (b) A. S. Tracey, *Coord. Chem. Rev.*, 2003, **237**, 113.
48. M. Ahmed, P. Schwendt, J. Marek and M. Sivák, *Polyhedron*, 2004, **23**, 655.
49. L. L. G. Justino, M. S. Ramos, M. M. Caldeira and V. M. S. Gil, *Eur. J. Inorg. Chem.*, 2000, 1617.
50. M. Ahmed, P. Schwendt and M. Sivak, *Trans. Met. Chem.*, 2004, **29**, 675.
51. C. Wikete, P. Wu, G. Zampella, L. De Gioia, G. Licini and D. Rehder, *Inorg. Chem.*, 2007, **46**, 196.
52. D. C. Crans, A. D. Keramidas, H. Hoover-Litty, O. P. Anderson, M. M. Miller, L. M. Lemoine, S. Pleasic-Williams, M. Vandenberg, A. J. Rossomando and L. J. Sweet, *J. Am. Chem. Soc.*, 1997, **119**, 5447.

53. O. Bortolini, M. Carraro, V. Conte and S. Moro, *Eur. J. Inorg. Chem.*, 1999, 1489.
54. M. Fritzsche, V. Vergopoulos and D. Rehder, *Inorg. Chim. Acta*, 1993, **211**, 11.
55. D. C. Crans, A. D. Keramidas, S. S. Amin, O. P. Anderson and S. M. Miller, *Dalton Trans.*, 1997, 2799.
56. M. R. Maurya, A. Kumar, M. Ebel and D. Rehder, *Inorg. Chem.*, 2006, **45**, 5924.
57. I. Andersson, A. Gorzcás and L. Pettersson, *Dalton. Trans.*, 2004, 421.
58. W. R. Browne, A. G. J. Ligtenbarg, J. W. De Boer, T. A. Van den Berg, M. Lutz, A. L. Spek, F. Hartl., R. Hage and B. L. Feringa, *Inorg. Chem.*, 2006, **45**, 2903.
59. J. Tatiersky, P. Schwendt, M. Sivak and J. Marek, *Dalton Trans.*, 2005, 2305.
60. (a) G. J. Colpas, B. J. Hamstra, J. W. Kampf and V. L. Pecoraro, *J. Am. Chem. Soc.*, 1996, **118**, 3469; (b) B. J. Hamstra, A. L. P. Houseman, G. J. Colpas, J. W. Kampf, R. LoBrutto, W. D. Frasch and V. L. Pecoraro, *Inorg. Chem.*, 1997, **36**, 4866.
61. M. Časný and D. Rehder, *Dalton Trans.*, 2004, 839.
62. (a) C. R. Cornman, J. Kampf and V. L. Pecoraro, *Inorg. Chem.*, 1992, **31**, 1983; (b) C. R. Cornman, G. J. Colpas, J. D. Hoeschele, J. Kampf and V. L. Pecoraro, *J. Am. Chem. Soc.*, 1992, **114**, 9925; (c) A. Butler, R. de la Rosa, Q. Zhou, A. Jhanji and C. J. Carrano, *Inorg. Chem.*, 1992, **31**, 5072.
63. M. Moon, M. Pyo, Y. C. Myoung, C. Ahn II and M. S. Lah, *Inorg. Chem.*, 2001, **40**, 554.
64. E. Kwiatkowski, G. Romanowski, W. Nowicki, M. Kwiatkowski and K. Suwinska, *Polyhedron*, 2003, **22**, 1009.
65. M. R. Maurya, S. Agarwal, M. Abid, A. Azam, C. Bader, M. Ebel and D. Rehder, *Dalton Trans.*, 2006, 937.
66. T. A. Kabanos, A. M. Z. Slawin, D. J. Williams and J. D. Woollins, *J. Chem. Soc. Dalton Trans.*, 1992, 1423.
67. (a) E. Hoppe, C. Limberg and B. Ziemer, *Inorg. Chem*, 2006, **45**, 8308; (b) E. Hoppe, C. Limberg, B. Ziemer and C. Mügge, *J. Mol. Catal. A*, 2006, **251**, 34.
68. E. M. Armstrong, R. L. Beddoes, L. J. Calviou, J. M. Charnock, D. Collison, S. N. Ertok, J. H. Naismith and C. D. Garner, *J. Am. Chem. Soc.*, 1993, **115**, 807.
69. P. D. Smith, R. E. Berry, S. M. Harben, R. L. Beddoes, M. Helliwell, D. Collison and C. D. Garner, *J. Chem. Soc. Dalton Trans.*, 1997, 4509.
70. P. C. Paul, S. J. Angus-Dunne, R. J. Batchelor, F. W. B. Einstein and A. S. Tracey, *Can. J. Chem.*, 1997, **75**, 183.
71. (a) A. D. Keramidas, S. M. Miller, O. P. Anderson and D. C. Crans, *J. Am. Chem. Soc.*, 1997, **119**, 8901; (b) A. S. Tracey and J. S. Jaswal, *J. Am. Chem. Soc.*, 1992, **114**, 3835.
72. (a) D. Rehder, *Inorg. Chem.*, 1988, **27**, 4312; (b) J. S. Jaswal and A. S. Tracey, *Can. J. Chem.*, 1991, **69**, 1600.
73. R. Fulwood, H. Schmidt and D. Rehder, *J. Chem. Soc. Chem. Commun.*, 1995, 1443.
74. M. Herberhold, M. Schrepfermann and J. Darkwa, *J. Organomet. Chem.*, 1992, **430**, 61.
75. R. Talay and D. Rehder, *J. Organomet. Chem.*, 1984, **262**, 25.
76. G. F. P. Warnock, S. B. Philson and J. E. Ellis, *J. Chem. Soc. Chem. Commun.*, 1984, 893.
77. (a) F. Basuli, B. C. Bailey, D. Brown, J. Tomaszewski, J. C. Huffman, M. -H. Baik and D. J. Mindiola, *J. Am. Chem. Soc.*, 2004, **126**, 10506; (b) J. Yamada and K. Nomura, *Organometallics*, 2005, **24**, 3621.
78. D. Gudat, U. Fischbek, F. Tabellion, M. Billen and F. Preuss, *Magn. Reson. Chem.*, 2002, **40**, 139.
79. (a) F. Preuss, M. Scherer, C. Klingshirn, G. Hornung, M. Vogel, W. Frank and G. Reiß, *Z. Naturforsch.*, 1999, **54b**; (b) F. Preuss and J. Perner, *Z. Naturforsch.*, 1999, **55b**, 1.
80. P. Gowick, T. M. Klapötke, K. Siems and U. Thewaldt, *J. Organomet. Chem.*, 1992, **431**, 47.
81. M. Herberhold, M. Schrepfermann and J. Darkwa, *J. Organomet. Chem.*, 1992, **430**, 61.
82. (a) M. Billen, G. Hornung and F. Preuss, *Z. Naturforsch.*, 2003, **58b**, 975; (b) M. Billen, G. Hornung, G. Wolmershäuser and F. Preuss, *Z. Naturforsch.*, 2003, **58b**, 237.
83. J. -K. F. Buijink, A. Meetsma, J. H. Teuben, H. Kooijman and A. L. Spek, *J. Organomet. Chem.*, 1995, **497**, 161.
84. B. Bachmann, F. Hahn, J. Heck and M. Wünsch, *Organometallics*, 1989, **8**, 2533.

85. C. Woitha, U. Behrens, V. Vergopoulos and D. Rehder, *J. Organomet. Chem.*, 1990, **393**, 97.
86. M. Hoch and D. Rehder, *J. Organomet. Chem.*, 1985, **288**, C25.
87. M. Talay and D. Rehder, *Inorg. Chim. Acta*, 1983, **77**, L175.
88. D. Rehder, M. Hoch and M. Link, *Organometallics*, 1988, **7**, 233.
89. D. Rehder and D. Wenke, *J. Organomet. Chem.*, 1988, **348**, 205.
90. F. Süßmilch, F. Olbrich, H. Gailus, D. Rodewald and D. Rehder, *J. Organomet. Chem.*, 1994, **472**, 119.
91. F. Süßmilch, F. Olbrich and D. Rehder, *J. Organomet. Chem.*, 1994, **481**, 125.
92. H. Gailus, H. Maelger and D. Rehder, *J. Organomet. Chem.*, 1994, **465**, 181.
93. (a) K. Ihmels and D. Rehder, *Organometallics*, 1985, **4**, 1334; (b) K. Ihmels and D. Rehder, *Organometallics*, 1985, **4**, 1340.
94. J. Schiemann and E. Weiss, *J. Organomet. Chem.*, 1983, **255**, 179.
95. D. Rehder, H. -Ch. Bechthold and K. Paulsen, *J. Magn. Reson.*, 1980, **40**, 305.
96. (a) D. Rehder, K. Ihmels, D. Wenke and P. Oltmanns, *Inorg. Chim. Acta*, 1985, **100**, L11; (b) F. Näumann, D. Rehder and V. Pank, *Inorg. Chim. Acta*, 1984, **84**, 117.
97. (a) F. Näumann and D. Rehder, *Z. Naturforsch.*, 1984, **39b**, 1647; (b) F. Näumann and D. Rehder, *Z. Naturforsch.*, 1984, **39b**, 1654.
98. K. Ihmels and D. Rehder, *Chem. Ber.*, 1985, **118**, 895.
99. H. Gailus, C. Woitha and D. Rehder, *J. Chem. Soc. Dalton Trans.*, 1994, 3471.
100. (a) C. J. Jameson, D. Rehder and M. Hoch, *J. Am. Chem. Soc.*, 1987, **109**, 2589; (b) C. J. Jameson, D. Rehder and M. Hoch, *Inorg. Chem.*, 1988, **27**, 3490.
101. D. Rehder, M. Hoch and C. J. Jameson, *Magn. Reson. Chem.*, 1990, **28**, 138.
102. (a) M. Hoch and D. Rehder, *Inorg. Chim. Acta*, 1986, **111**, L13; (b) K. Ihmels, D. Rehder and V. Pank, *Inorg. Chim. Acta*, 1986, **111**, L13.
103. V. P. Tarasov, V. I. Privalov, Yu. A. Buslaev and U. Eichoff, *Z. Naturforsch.*, 1984, **39b**, 1230.
104. S. E. O'Donnell and M. T. Pope, *J. Chem. Soc. Dalton Trans.*, 1976, 2290.
105. D. Rehder, *Bull. Magn. Reson.*, 1982, **4**, 33.
106. J. -K. F. Buijink, A. Meetsma and J. H. Teuben, *Organometallics*, 1993, **12**, 2004.
107. F. Preuss and L. Ogger, *Z. Naturforsch.*, 1982, **37b**, 957.
108. D. Rehder, D. Fenske, G. Baum, H. Borgholte and K. Dehnicke, *Z. Naturforsch.*, 1989, **44b**, 1385.
109. G. M. Whitesides and H. L. Mitchell, *J. Am. Chem. Soc.*, 1969, **91**, 2245.
110. O. Lutz, W. Nepple and A. Nolle, *Z. Naturforsch.*, 1976, **31a**, 1046.
111. R. C. Hibbert, *J. Chem. Soc. Dalton Trans.*, 1986, 751.
112. C. Woitha and D. Rehder, *Angew. Chem. Int. Ed.*, 1990, **29**, 1438.
113. O. Durupthy, A. Coupé, L. Tache, M. -N. Rager, J. Maquet, T. Coradin, N. Steunou and J. Livage, *Inorg. Chem.*, 2004, **43**, 2021.
114. L. Wittenkeller, A. Abraha, R. Ramasamy, D. Mota de Freitas, L. A. Theisen and D. C. Crans, *J. Am. Chem. Soc.*, 1991, **113**, 7872.
115. D. Rehder, M. Časný and R. Grosse, *Magn. Reson. Chem.*, 2004, **42**, 745.
116. D. Rehder, H. Holst, R. Quaas, W. Hinrichs, U. Hahn and W. Saenger, *J. Inorg. Biochem.*, 1989, **37**, 141.
117. B. Borah, C. W. Chen, W. Egan, M. Millar, A. Wlodawer and J. S. Cohen, *Biochemistry*, 1985, **24**, 2058.
118. A. Butler and H. Eckert, *J. Am. Chem. Soc.*, 1989, **111**, 2802.
119. J. A. Saponja and H. J. Vogel, *J. Inorg. Biochem.*, 1996, **62**, 253.
120. A. Butler and C. J. Carrano, *Coord. Chem. Rev.*, 1991, **109**, 61.
121. (a) J. H. Bell and R. F. Pratt, *J. Am. Chem. Soc.*, 2002, **41**, 4329; (b) J. H. Bell and R. F. Pratt, *Inorg. Chem.*, 2002, **41**, 2747.
122. X. Lu, W. D. Johnson and J. Hook, *Environ. Sci. Technol.*, 1998, **32**, 2257.
123. T. C. Delgado, A. I. Tomaz, I. Correira, J. Costa Pessoa, J. G. Jones, C. F. G. C. Geraldes and M. M. C. A. Castro, *J. Inorg. Biochem.*, 2005, **99**, 2328.
124. B. Song, N. Aebischer and C. Orvig, *Inorg. Chem.*, 2002, **41**, 1357.
125. (a) M. Greb, J. Hartung, F. Koehler, K. Spehar, R. Kluge and R. Csuk, *Eur. J. Org. Chem.*, 2004, 3799.; (b) J. Hartung, *Pure Appl. Chem.*, 2005, **77**, 1559.

126. A. G. J. Ligtenbarg, R. Hage and B. L. Feringa, *Coord. Chem. Rev.*, 2003, **237**, 89.
127. M. J. Clague, N. L. Keder and A. Butler, *Inorg. Chem.*, 1993, **32**, 4754.
128. A. D. Keramidas, A. B. Papaioannou, A. T. Vlahos, T. A. Kabanos, G. Bonas, A. Makriyannis, C. P. Rapropoulou and A. Terzis, *Inorg. Chem.*, 1996, **35**, 357.
129. G. Santoni, G. Licini and D. Rehder, *Chem. Eur. J.*, 2003, **9**, 4700.
130. C. Bolm, *Coord. Chem. Rev.*, 2003, **237**, 245.
131. S. A. Blum, R. C. Bergman and J. A. Ellmann, *J. Org. Chem.*, 2003, **68**, 150.
132. M. Jian, L. Zhu, J. Wang, J. Zhang, G. Li and C. Hu, *J. Mol. Catal. A*, 2006, **253**, 1.
133. K. P. Bryliakov, E. P. Talsi, T. Kuehn and C. Bolm, *New J. Chem.*, 2003, **27**, 609.
134. M. E. Smith and E. R. H. van Eck, *Prog. Nucl. Magn. Reson. Spectrosc.*, 1999, **34**, 159.
135. (a) M. H. Cohen and F. Reif, *Solid State Phys.*, 1957, **5**, 321; (b) L. Frydman, *Annu. Rev. Phys. Chem.*, 2001, **52**, 463–498; (c) A. P. M. Kentgens, *Geoderma*, 1997, **80**, 271.
136. J. Skibsted, N. C. Nielsen, H. Bildsoe and H. J. Jakobsen, *J. Magn. Reson.*, 1991, **95**, 88.
137. (a) J. Skibsted, N. C. Nielsen, H. Bildsoe and H. J. Jakobsen, *Chem. Phys. Lett.*, 1992, **188**, 405; (b) J. Skibsted, N. C. Nielsen, H. Bildsoe and H. J. Jakobsen, *J. Am. Chem. Soc.*, 1993, **115**, 7351; (c) J. Skibsted, C. J. H. Jacobsen and H. J. Jakobsen, *Inorg. Chem.*, 1998, **37**, 3083.
138. (a) U. G. Nielsen, H. J. Jakobsen and J. Skibsted, *J. Phys. Chem. B*, 2001, **105**, 420; (b) U. G. Nielsen, H. J. Jakobsen, J. Skibsted and P. Norby, *J. Chem. Soc. Dalton Trans.*, 2001, 3214.; (c) U. G. Nielsen, A. Boisen, M. Brorson, C. J. H. Jacobsen, H. J. Jakobsen and J. Skibsted, *Inorg. Chem.*, 2002, **41**, 6432.
139. N. Pooransingh, E. Pomerantseva, M. Ebel, S. Jantzen, D. Rehder and T. Polenova, *Inorg. Chem.*, 2003, **42**, 1256.
140. N. Pooransingh-Margolis, R. Renirie, Z. Hasan, R. Wever, A. J. Vega and T. Polenova, *J. Am. Chem. Soc.*, 2006, **128**, 5190.
141. (a) W. L. Huang, L. Todaro, L. C. Francesconi and T. Polenova, *J. Am. Chem. Soc.*, 2003, **125**, 5928; (b) W. L. Huang, L. Todaro, G. P. A. Yap, R. Beer, L. C. Francesconi and T. Polenova, *J. Am. Chem. Soc.*, 2004, **126**, 11564.
142. M. Bak, J. T. Rasmussen and N. C. Nielsen, *J. Magn. Reson.*, 2000, **147**, 296.
143. (a) J. Skibsted, T. Vosegaard, H. Bildsoe and H. J. Jakobsen, *J. Phys. Chem.*, 1996, **100**, 14872; (b) T. Vosegaard, J. Skibsted, H. Bildsoe and H. J. Jakobsen, *J. Phys. Chem.*, 1995, **99**, 10731.
144. J. P. Amoureux, C. Fernandez, L. Carpentier and E. Cochon, *Phys. Status Solid A*, 1992, **132**, 461.
145. A. A. Shubin, O. B. Lapina, E. Bosch, J. Spengler and H. Knozinger, *J. Phys. Chem. B*, 1999, **103**, 3138.
146. E. Oldfield, R. A. Kinsey, B. Montez, T. Ray and K. A. Smith, *J. Chem. Soc. Chem. Commun.*, 1982, 254.
147. S. Hayashi, *Magn. Reson. Chem.*, 1996, **34**, 791.
148. J. Herzfeld and A. E. Berger, *J. Chem. Phys.*, 1980, **73**, 6021.
149. A. Samoson and E. Lippmaa, *J. Magn. Reson.*, 1988, **79**, 255.
150. F. D. Hardcastle, I. E. Wachs, H. Eckert and D. A. Jefferson, *J. Solid State Chem.*, 1991, **90**, 194.
151. H. Eckert and I. E. Wachs, *J. Phys. Chem.*, 1989, **93**, 6796.
152. L. Frydman and J. S. Harwood, *J. Am. Chem. Soc.*, 1995, **117**, 5367.
153. A. Medek, J. S. Harwood and L. Frydman, *J. Am. Chem. Soc.*, 1995, **117**, 12779.
154. A. Medek and L. Frydman, *J. Magn. Reson.*, 1999, **138**, 298.
155. O. B. Lapina, A. A. Shubin, D. F. Khabibulin, V. V. Terskikh, P. R. Bodart and J. P. Amoureux, *Catal. Today*, 2003, **78**, 91.
156. B. Gee, *Solid State Nucl. Magn. Reson.*, 2001, **19**, 73.
157. (a) D. E. Kaplan and E. L. Hahn, *J. Phys. Paris*, 1958, **19**, 821–825; (b) M. Emshwiller, E. L. Hahn and D. Kaplan, *Phys. Rev.*, 1960, **118**, 414; (c) P. K. Wang, C. P. Slichter and J. H. Sinfelt, *Phys. Rev. Lett.*, 1984, **53**, 82.
158. T. Gullion and J. Schaefer, *J. Magn. Reson.*, 1989, **81**, 196.
159. E. R. H. van Eck and W. S. Veeman, *Solid State Nucl. Magn. Reson.*, 1993, **2**, 307.
160. (a) A. W. Hing, S. Vega and J. Schaefer, *J. Magn. Reson. Ser. A*, 1993, **103**, 151; (b) A. W. Hing, S. Vega and J. Schaefer, *J. Magn. Reson.*, 1992, **96**, 205.

161. (a) C. P. Grey, W. S. Veeman and A. J. Vega, *J. Chem. Phys.*, 1993, **98**, 7711; (b) C. P. Grey and W. S. Veeman, *Chem. Phys. Lett.*, 1992, **192**, 379.
162. (a) T. Gullion, *Chem. Phys. Lett.*, 1995, **246**, 325–330; (b) T. Gullion, *J. Magn. Reson. Ser. A*, 1995, **117**, 326.
163. (a) T. Gullion and C. H. Pennington, *Chem. Phys. Lett.*, 1998, **290**, 88; (b) T. Gullion, *J. Magn. Reson.*, 1999, **139**, 402.
164. R. D. Gougeon, P. R. Bodart, R. K. Harris, D. M. Kolonia, D. E. Petrakis and P. J. Pomonis, *Phys. Chem. Chem. Phys.*, 2000, **2**, 5286.
165. N. Kim and C. P. Grey, *Science*, 2002, **297**, 1317.
166. L. van Wüllen, *Solid State Nucl. Magn. Reson.*, 1998, **10**, 235.
167. C. Bonhomme, C. Coelho, T. Azais, L. Bonhomme-Coury, F. Babonneau, J. Maquet and R. Thouvenot, *C.R. Chimie*, 2006, **9**, 466.
168. L. Delevoye, C. Fernandez, C. M. Morais, J. P. Amoureux, V. Montouillout and J. Rocha, *Solid State Nucl. Magn. Reson.*, 2002, **22**, 501.
169. O. B. Lapina, V. M. Mastikhin, A. A. Shubin, V. N. Krasilnikov and K. I. Zamaraev, *Prog. Nucl. Magn. Reson. Spectrosc.*, 1992, **24**, 457.
170. S. Hayakawa, T. Yoko and S. Sakka, *J. Solid State Chem.*, 1994, **112**, 329.
171. U. G. Nielsen, H. J. Jakobsen and J. Skibsted, *Inorg. Chem.*, 2000, **39**, 2135.
172. U. G. Nielsen, H. J. Jakobsen and J. Skibsted, *Solid State Nucl. Magn. Reson.*, 2003, **23**, 107.
173. W. Basler, H. Lechert, K. Paulsen and D. Rehder, *J. Magn. Reson.*, 1981, **45**, 170.
174. L. Mafra, F. A. A. Paz, F. N. Shi, C. Fernandez, T. Trindade, J. Klinowski and J. Rocha, *Inorg. Chem. Commun.*, 2006, **9**, 34.
175. K. Inumaru, A. Ono, H. Kubo and M. Misono, *J. Chem. Soc. Faraday*, 1998, **94(12)**, 1765.
176. (a) K. Nomiya, Y. Nemoto, T. Hasegawa and S. Matsuoka, *J. Mol. Catal. A Chem.*, 2000, **152**, 55; (b) K. Nomiya, K. Hashino, Y. Nemoto and M. Watanabe, *J. Mol. Catal. A Chem.*, 2001, **176**, 79.
177. D. E. Katsoulis, *Chem. Rev.*, 1998, **98**, 359.
178. P. Gomez-Romero, *Adv. Mater.*, 2001, **13**, 163.
179. T. Yamase, *Chem. Rev.*, 1998, **98**, 307.
180. S. Q. Liu, D. G. Kurth, H. Mohwald and D. Volkmer, *Adv. Mater.*, 2002, **14(3)**, 225.
181. O. Dmitrenko, W. L. Huang, T. E. Polenova, L. C. Francesconi, J. A. Wingrave and A. V. Teplyakov, *J. Phys. Chem. B*, 2003, **107**, 7747.
182. N. Pooransingh-Margolis, *^{51}V Solid-State Magic Angle Spinning NMR Spectroscopy of Vanadium Haloperixodases and Oxovanadium (V) Haloperoxidase Mimics*, Ph.D. Thesis, University of Delaware, Newark, 2006.
183. A. Messerschmidt and R. Wever, *Proc. Natl. Acad. Sci. USA*, 1996, **93**, 392.
184. G. Zampella, J. Y. Kravitz, C. E. Webster, P. Fantucci, M. B. Hall, H. A. Carlson, V. L. Pecoraro and L. De Gioia, *Inorg. Chem.*, 2004, **43**, 4127.
185. J. Y. Kravitz, V. L. Pecoraro and H. A. Carlson, *J. Chem. Theory Comput.*, 2005, **1**, 1265.
186. (a) S. Raugei and P. Carloni, *J. Phys. Chem. B*, 2006, **110**, 3747; (b) M. Bangesh and W. Plass, *J. Mol. Struct. Theochem.*, 2005, **725**, 163.
187. (a) A. A. Shubin, O. B. Lapina and V. M. Bondareva, *Chem. Phys. Lett.*, 1999, **302**, 341; (b) A. A. Shubin, O. B. Lapina and D. Courcot, *Catal. Today*, 2000, **56**, 379.
188. (a) V. V. Terskikh, O. B. Lapina and V. M. Bondareva, *Phys. Chem. Chem. Phys.*, 2000, **2**, 2441; (b) B. M. Weckhuysen and D. E. Keller, *Catal. Today*, 2003, **78**, 25; (c) N. Dajda, J. M. Dixon, M. E. Smith, N. Carthey and P. T. Bishop, *Phys. Rev. B*, 2003, **67**, 024201; (d) R. Cousin, D. Courcot, E. Abi-Aad, S. Capelle, J. P. Amoureux, M. Dourdin, M. Guelton and A. Aboukais, *Colloid Surface A*, 1999, **158**, 43; (e) O. H. Han, S. Kim, S. G. Lee and Y. U. Kwon, *J. Non-Cryst. Solids*, 2005, **351**, 3365; (f) J. Matta, D. Courcot, E. Abi-Aad and A. Aboukais, *Chem. Mater.*, 2002, **14**, 4118; (g) F. Delmaire, M. Rigole, E. A. Zhilinskaya, A. Aboukais, R. Hubaut and G. Mairesse, *Phys. Chem. Chem. Phys.*, 2000, **2**, 4477; (h) U. G. Nielsen, N. Y. Topsoe, M. Brorson, J. Skibsted and H. J. Jakobsen, *J. Am. Chem. Soc.*, 2004, **126**, 4926; (i) C. Hudalla, H. Eckert and R. Dupree, *J. Phys. Chem.*, 1996, **100**, 15986; (j) C. Marichal, J. Y. Kempf, B. Maigret and J. Hirschinger, *Solid State Nucl. Magn. Reson.*, 1997, **8**, 33.

189. (a) K. Paulsen and D. Rehder, *Z. Naturforsch.*, 1981, **37a**, 139–149; (b) D. Rehder, K. Paulsen and H. Lechert, *Z. Naturforsch.*, 1978, **33a**, 1597.
190. J. Livage, *Chem. Mater.*, 1991, **3**, 578.
191. C. Guestaux, J. Leaute, C. Virey and J. Vial, *Support Provided with Antistatic Layer*, 1972, US Patent 03658573.
192. R. Baddour, J. P. Pereiraramos, R. Messina and J. Perichon, *J. Electroanal. Chem.*, 1991, **314**, 81.
193. A. Azens, A. Talledo, A. M. Andersson, G. A. Niklasson, B. A. Stjerna and C. -G. Granqvist, *Proc. SPIE*, 1992, **1728**, 103.
194. S. Mege, M. Verelst, P. Lecante, E. Perez, F. Ansart and J. M. Savariault, *J. Non-Cryst. Solids*, 1998, **238**, 37.
195. B. Alonso and J. Livage, *J. Solid State Chem.*, 1999, **148**, 16.
196. O. Pelletier, P. Davidson, C. Bourgaux, C. Coulon, S. Regnault and J. Livage, *Langmuir*, 2000, **16**, 5295.
197. J. Livage, O. Pelletier and P. Davidson, *J. Sol-Gel Sci. Technol.*, 2000, **19**, 275.
198. H. Choi, Y. Y. Chang, Y. U. Kwon and O. H. Han, *Chem. Mater.*, 2003, **15**, 3261.
199. M. Dubarry, J. Gaubicher, D. Guyomard, O. Durupthy, N. Steunou, J. Livage, N. Dupre and C. P. Grey, *Chem. Mater.*, 2005, **17**, 2276.
200. F. Carn, N. Steunou, J. Livage, A. Colin and R. Backov, *Chem. Mater.*, 2005, **17**, 644.
201. D. C. Crans, C. D. Rithner, B. Baruah, B. L. Gourley and N. E. Levinger, *J. Am. Chem. Soc.*, 2006, **128**, 4437.
202. J. Stover, C. D. Rithner, R. A. Inafuku, D. C. Crans and N. E. Levinger, *Langmuir*, 2005, **21**, 6250.
203. F. Carn, N. Steunou, J. Livage, A. Colin and R. Backov, *Chem. Mater.*, 2005, **17**, 644.
204. V. Luca and J. M. Hook, *Chem. Mater.*, 1997, **9**, 2731.
205. D. Rehder, K. Paulsen and W. Basler, *J. Magn. Reson.*, 1983, **53**, 500.
206. W. Koch and M. C. Holthausen, *A Chemist's Guide to Density Functional Theory*, Wiley-VCH, Weinheim, 2000.
207. M. Bühl, M. Kaupp, V. G. Malkin and O. L. Malkina, *J. Comput. Chem.*, 1999, **20**, 91.
208. J. Autschbach, *Struct. Bonding*, 2004, **112**, 1.
209. M. Bühl, in: *Calculation of NMR and EPR Parameters. Theory and Applications*, M. Kaupp, M. Bühl and V. G. Malkin, eds., Wiley-VCH, Weinheim, 2004, p. 421.
210. V. G. Malkin, O. L. Malkina, M. E. Casida and D. R. Salahub, *J. Am. Chem. Soc.*, 1994, **116**, 5898.
211. P. J. Wilson, R. D. Amos and N. C. Handy, *Phys. Chem. Chem. Phys.*, 2000, **2**, 187.
212. T. Helgaker, M. Jaszunski and K. Ruud, *Chem. Rev.*, 1999, **99**, 293.
213. M. Kaupp, M. Bühl and V. G. Malkin, eds., *Calculation of NMR and EPR Parameters. Theory and Applications*, Wiley-VCH, Weinheim, 2004.
214. J. Gauss, *Modern Methods and Algorithms of Quantum Chemistry*, J. Grotendorst, ed., NIC Series Vol. 1, Jülich (Germany), 2000, p. 509.
215. Y. Ruiz-Morales and T. Ziegler, *J. Phys. Chem. A*, 1998, **102**, 3970.
216. G. Schreckenbach and T. Ziegler, *Int. J. Quantum Chem.*, 1997, **61**, 899.
217. G. Schreckenbach, *J. Chem. Phys.*, 1999, **110**, 11936.
218. M. Bühl and F. A. Hamprecht, *J. Comput. Chem.*, 1998, **119**, 113.
219. S. Grigoleit and M. Bühl, *Chem. Eur. J.*, 2004, **10**, 5541.
220. M. Bühl, *Chem. Phys. Lett.*, 1997, **267**, 25.
221. M. Bühl and M. Parrinello, *Chem. Eur. J.*, 2001, **7**, 4487.
222. M. Bühl, P. Imhof and M. Repisky, *Chem. Phys. Chem.*, 2004, **5**, 414.
223. M. Bühl, R. Schurhammer and P. Imhof, *J. Am. Chem. Soc.*, 2004, **126**, 3310.
224. M. Bühl, F. T. Mauschick, and R. Schurhammer, *High Performance Computing in Science and Engineering, Munich 2002*, S. Wagner, W. Hanke, A. Bode, F. Durst, eds., Springer, Berlin, 2003, p. 189.
225. M. Bühl, *Vanadium the Versatile Metal*, K. Kustin, D. C. Crans, J. C. Pessoa, eds., ACS Symposium Series, Washington DC, 2007, **947**.
226. M. Bühl, *Inorg. Chem.*, 2005, **44**, 6277.
227. M. Bühl, R. Schurhammer and P. Imhof, in: *High Performance Computing in Science and Engineering, Munich 2004*, S. Wagner, W. Hanke, A. Bode and F. Durst, eds., Springer, Berlin, 2004, p. 189.

228. W. von Philipsborn, *Chem. Soc. Rev.*, 1999, 95.
229. M. Bühl, *Angew. Chem. Int. Ed.*, 1998, **37**, 142.
230. M. Bühl, *Organometallics*, 1999, **18**, 4894.
231. M. Bühl, *Modeling NMR Chemical Shifts: Gaining Insights into Structure and Environment*, J. C. Facelli, A. DeDios, eds., ACS Symposium Series, Vol. 732, Washington DC, 1999, p. 240.
232. P. D. Bolton and P. Mountford, *Adv. Synth. Catal.*, 2005, **347**, 355 Review.
233. M. Bühl, *J. Comput. Chem.*, 1999, **20**, 1254.
234. M. Bühl, *J. Inorg. Biochem.*, 2000, **80**, 137.
235. N. J. Campbell, A. C. Dengel and W. P. Griffith, *Polyhedron*, 1989, **11**, 1379.
236. P. Unkel, P. Buch, J. Dembczynski, W. Ertmer and U. Johann, *Z. Phys. D*, 1989, **11**, 259.
237. W. J. Childs, *Phys. Rev.*, 1967, **156**, 71.
238. Y. Lindquist, G. Schneider and P. Vihko, *Eur. J. Biochem.*, 1994, **221**, 139.
239. M. Weyand, H. -J. Hecht, M. Kieß, M. -F. Liaud, H. Vilter and D. Schomburg, *J. Mol. Biol.*, 1999, **293**, 595.

Solid-State Effects on NMR Chemical Shifts

A.M. ORENDT[1,2] AND J.C. FACELLI[1,2,3]

[1]*Center for High Performance Computing, University of Utah, Salt Lake City, UT 84112, USA*
[2]*Department of Chemistry, University of Utah, Salt Lake City, UT 84112, USA*
[3]*Department of Biomedical Informatics, University of Utah, Salt Lake City, UT 84112, USA*

This review presents first a qualitative description of the changes observed in the measured chemical shifts in solid state when compared with those obtained in solution. This qualitative description of the intermolecular interactions that affect the chemical shifts is followed by a comprehensive description of the theoretical methods available to analyze the solid-state effects on the chemical shifts.

ANNUAL REPORTS ON NMR SPECTROSCOPY
VOLUME 62 ISSN 0066 4103
DOI 10.1016/S0066-4103(07)62003-1

There are numerous examples of solid-state effects in the literature; here we have selected some of the most notable ones, which are presented as case studies. These case studies are classified by nuclei and by the dominant interaction that defines the solid-state effects. Examples are presented for ^{13}C, $^{15/14}N$, ^{1}H, ^{17}O, ^{31}P, and ^{19}F. In addition to the effects discussed for chemical shifts the review also presents examples of the solid-state effects on the quadrupolar constants in the case of non 1/2 spin nuclei.

1. INTRODUCTION

Information available from solid-state nuclear magnetic resonance (SSNMR) is being increasingly used to provide information on molecular and crystal structure[1] of materials not amenable to single crystal or high resolution powder diffraction X-ray spectroscopy studies. One reason for this increase is that the availability of SSNMR, once restricted only to a relatively small number of NMR research groups, is becoming much more widespread. A second reason is the sensitivity of the NMR parameters, especially the chemical shift and quadrupolar constants, to the local environment, making these parameters good probes of local structural features[2,3] not easily obtainable from other methods such as powder diffraction X-ray. In addition, the state of the art in quantum chemical calculations of shielding is such that theory can be used to accurately reproduce the experimentally measured data. This accuracy allows for confidence in making assignments, as well as for providing insight into the relationship between the molecular structure and chemical shifts. This is at the point that quantitative structural predictions are a realistic expectation in the near future. This type of analysis is currently being extended beyond the structure of a single molecule and is being used to gain information on crystal structures,[4–8] an extension which requires an understanding of the intermolecular interactions present in solids and how they affect the NMR parameters.

There are a number of NMR parameters that can be used to obtain structural information: the chemical shift (both the isotropic shift and the tensor components), J couplings, dipolar couplings, and quadrupolar parameters. Any change in the local structure, symmetry, and/or electronic distribution of a chemical species due to intermolecular interactions can have an effect on any of these NMR parameters. These effects can be either indirect effects, the ones resulting from changes in the molecular structure, or direct effects, involving changes in the distribution of the electron density due to the crystalline field. While the dipolar and J couplings have a direct relationship with structure and are widely used for structural characterization in solution studies,[9] they are very difficult to measure in solids and are seldom used in structural studies. The most widely used of the NMR parameters in the solid state is the chemical shift, but with the increased use of NMR spectroscopy in nuclei with spin larger than 1/2, quadrupolar parameters are becoming of greater importance. This article will focus on the use of SSNMR measurement of chemical shift and quadrupolar coupling constants along with the quantum chemical calculation of these parameters to gain insight into the effects of intermolecular

interactions and their implication on structure determination. Finally, in this article we report only results on crystalline or microcrystalline materials, for which the intermolecular environment is well characterized, neglecting any discussion on amorphous samples. We also refrain from discussing those studies using SSNMR in which external probes such as ^{129}Xe have been used to probe the structure of materials.[10]

For crystalline solids, the solid-state spectra of spin-1/2 nuclei such as ^{13}C or ^{15}N, under conditions of fast magic angle spinning (MAS) and high power proton decoupling, becomes very much like a proton decoupled solution spectra in terms of spectral resolution and line widths. In the absence of solid-state effects, the number of lines and their frequencies or chemical shifts do not change when going between solution and solid state. However, there are cases where one or both of the above change in going between solution and solid state; this article describes all the possible known reasons for these changes. For nuclei with spin greater than 1/2 the SSNMR spectrum is further complicated by the presence of the residual quadrupolar coupling, which is also influenced by the same intermolecular factors.

The shielding is a tensor quantity, resulting in the observed chemical shifts in a solid being dependent on the orientation of the magnetic field in the molecular frame.[11] The shielding is due to the induced electronic circulation around the nuclei in the plane perpendicular to the magnetic field for any given orientation. For a single crystal sample this gives spectra with as many lines as the number of magnetically inequivalent nuclei in the asymmetric unit, with the individual resonance frequencies depending on the orientation of the crystal with respect to the external field. For a microcrystalline sample, all orientations of the molecule with respect to the magnetic field co-exist in the sample; this results in a so-called powder pattern of all possible chemical shielding values for each magnetically inequivalent nuclei. These powder patterns can be very broad, depending on the electronic environment of a given nuclei. In many cases a given powder pattern spans the entire isotropic chemical shift range typical of that nuclei, e.g., ~200 ppm for the case of a ^{13}C nuclei in olefinic compounds. The powder pattern is characterized by the three principal values of the chemical shift tensor; the isotropic chemical shift measured in a solution or MAS experiment is the average of these three principal values. It is often found that a change due to intermolecular effects is concentrated in only one of the principal values or shows up as opposite effects in two of the components, with one increasing and one decreasing. This leads to changes in the isotropic chemical shift often being magnified in the individual components of the shielding tensor; therefore, much more detailed information can be obtained in the case where the components are measured instead of just the isotropic chemical shifts.

The quadrupolar coupling of nuclei possessing a quadrupole moment is also very sensitive to the local environment. The readers are referred to general SSNMR books for a detailed description of the quadrupolar coupling.[12,13] Briefly, the magnitude of the coupling constant depends on the size of the quadrupolar moment of the nucleus as well as the size and orientation of the electric field gradient (EFG) at the nucleus. The EFG, generated by the nonspherical electron distribution about

the nucleus, is very sensitive to variations in the electronic environment that arise due to changes in the structure and/or intermolecular interactions. The use of SSNMR on quadrupolar nuclei has been limited, especially on organic materials. This, however, is changing, with ^{17}O the most popular quadrupolar nuclei being investigated. Under MAS conditions, the isotropic chemical shift, the quadrupolar coupling constant, and the asymmetry factor of the quadrupolar interaction are obtained. The lineshape of the solid-state spectra of spin 1/2 nuclei in the vicinity of quadrupolar nuclei is also affected through the dipolar coupling between the two magnetic species; from the spectal analysis both the coupling constant and the EFG tensor can also be extracted. This is commonly done in samples with ^{13}C-^{14}N bonds. This effect on the spectra can be quite large for directly bonded nuclei at low magnetic fields, but is greatly diminished by going to higher fields as the coupling is not field dependent. Therefore, the choice is often made to go to higher magnetic fields where this dipolar coupling can be ignored, if possible, making for an easier spectral interpretation.

Advances in NMR spectroscopy have allowed for determination of chemical shift data in increasingly complex compounds. The use of higher magnetic field strengths and higher spinning speeds has allowed for the high resolution MAS of large molecules on limited amounts of material. When measuring the tensor data, the primary advance is in the use of two dimensional spectroscopic techniques to allow for the separation of the tensor data in a second dimension based on the isotropic chemical shift. There are a number of experimental methods that achieve this separation, including the magic angle turning family of experiments (FIREMAT)[14] and the PASS[15] method.

Advances in both computational resources and methodology have allowed for the accurate calculation of chemical shielding in large chemical systems. The use of density functional theory (DFT) methods to efficiently include electron correlation has been a major advance. Currently, calculations in light nuclei typically agree to within $\sim$5 ppm on shift tensor components[16,17] when calculations are done on an isolated molecule provided there are no significant intermolecular effects that need to be considered, as is the case for most rigid, neutral, nonpolar molecules. When intermolecular interactions are a factor, however, the agreement between experiment and theory on an isolated molecule degrades, making the use of theory an important tool in the interpretation and analysis of the NMR data that would be difficult if not impossible to interpret otherwise. Therefore, there has been much work focused on methodology to include intermolecular effects into the calculations, so that theory can accurately reproduce experimental results in these cases, resulting in a number of useful models. The use of these different models can serve as a guide for the interpretation of the experimental values and for the role the different intermolecular effects play in the measured solid-state NMR parameters.

It should also be noted that the NMR parameters of quadrupolar nuclei can also be calculated. However, the amount of data available, both experimental and theoretical, on these quadrupolar parameters is much less than the amount of chemical shift data that is available. Therefore not as much information is known on the correlation and agreement between experiment and theory for the coupling

constant and the EFG tensor, or about the affect of including intermolecular effects into the calculations.

This article will start with a general discussion of how the solid-state spectra can differ from the solution state spectra with which most chemists are much more familiar, focusing on the changes that are due to intermolecular effects. This will be followed by a discussion of the most commonly used theoretical treatments that calculate the effect of intermolecular interactions on the NMR parameters. Finally, a presentation of case studies from the literature, sorted by nuclei, will be made. The cases presented are by no means a complete literature survey; they are, however, a sampling to illustrate the effect that intermolecular interactions have on the chemical shift and to hopefully act as a source of information to guide future studies.

2. ORIGIN OF SOLID-STATE EFFECTS ON CHEMICAL SHIFTS

The majority of the time there will be no or only very minor differences between the isotropic chemical shifts measured in solution (in a nonpolar solvent) versus those measured in the solid state via either a MAS spectrum or from the average of a measurement of the principal values of the chemical shift tensor. When this is the case, it is an indication that intermolecular effects are probably not a factor for the chemical system being studied and that there are not crystal effects complicating the interpretation of the SSNMR spectra. In these cases there is often also good agreement (typically within 5 ppm for principal values) between the experimental chemical shift values and the results of calculations done on a single isolated molecule. However, there are many examples in the literature where substantial differences are measured between solution and solid-state chemical shifts and/or between experimental solid-state data and single molecule theoretical measurements. In some cases these differences in the isotropic chemical shift values are of such magnitude, that duplication of lines may be observed in the SSNMR spectra. In other cases only a detailed study of the principal components and comparison between experiment and theory reveals differences. When such differences are observed one must look to the structure of the molecule and its local environment for reasons to explain the differences. Some of the differences are due to changes in the molecule itself (structure and/or dynamics) upon going from solution/liquid to solid; others are due to strong intermolecular interactions in the solid state.

In this section, a discussion of the solid-state effects which can impact the observed SSNMR spectra is presented. First the effects observed due to changes in the molecule and its structure between solution and solid state will be discussed. These effects include differences in molecular and crystal symmetry, multiple molecules present in the crystal asymmetric unit, conformational and/or tautomeric freezing, polymorphism, and phase changes. This will be followed by a discussion of the intermolecular interactions present in the solid that lead to the observed changes: electrostatic effects, hydrogen bonding (HB), and molecular magnetic susceptibility or ring current effects. It should be noted that these two discussions are very much inter-related, as

the crystal structure or structures of a substance in the solid state are also a direct result of the intermolecular forces present in the material.

2.1. Conformational and tautomeric averaging

One factor that can cause changes in the chemical shifts as well as in the number of resonances observed between solution and solid state is conformational averaging due to motion that it is present in solution but absent or different in the solid state. In addition, most tautomeric exchange processes are only observed in solution. Both mechanisms can lead to different nuclei being equivalent in solution, but nonequivalent in the solid state. If the motion or the tautomeric process is stopped, the averaging will be removed and therefore the magnetic equivalency lifted. There are cases where these processes do not even stop in the solid state, or at least not at room temperature, especially in the case of motional averaging. One such example is the rotation about the threefold symmetry axis in methyl groups. Depending on the differences in the environment that the individual nuclei sample, the change in the chemical shift when these processes are stopped can be of varying magnitudes. Fig. 1 shows the difference observed in anisole in going from the solution state, where the twofold stochastic jumping of the methoxy group leads to averaging of the two *ortho* carbons, to a low temperature SSNMR where this motion is stopped.[18]

2.2. Crystal symmetry

In some cases the molecule of interest has higher symmetry as an isolated molecule than it does in the solid state, which affects the number of resonances observed. An example of this situation is naphthalene.[2,19] The isolated molecule has D_{2h} symmetry, and as such a solution ^{13}C NMR spectrum shows a total of three resonances, one for the bridgehead carbons, one for the *alpha* protonated carbons, and one from the *beta* protonated carbons. In the solid state the molecular symmetry is reduced from D_{2h} to C_i; this reduction in symmetry leads to the observation of five resolvable chemical shift tensors. The change in the molecular symmetry can be due to slight changes in the bond lengths and angles within the molecule and/or due to differences in the crystal environment; often it is a mixture of the two.

2.3. Multiple molecules per asymmetric unit

A second possible effect imposed by the crystal structure is that there can be more than one molecule per asymmetric unit. The asymmetric unit contains all nonsymmetry related atoms in the unit cell; it is therefore the smallest part of the unit cell which can be used to generate the entire cell. The number of molecules per asymmetric unit, designated Z', is most commonly one; however it can be a fraction of a

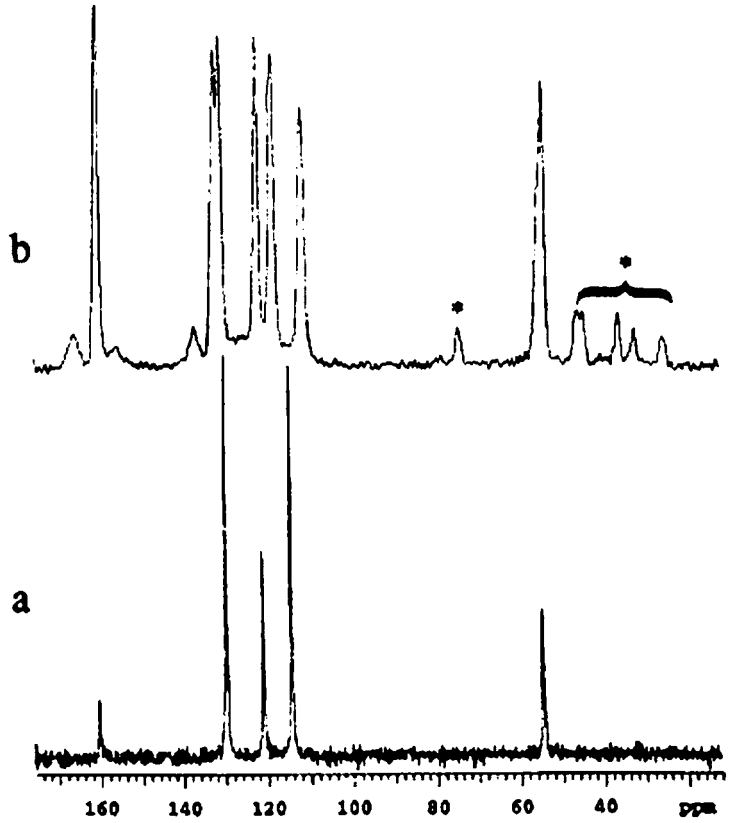

Fig. 1. High resolution spectra of anisole at (a) room temperature liquid and (b) MAS spectrum at 180 K showing the splitting of the aromatic carbons upon freezing out the motion of the methoxy group. Peaks marked with asterisks are MAS side bands. (Reproduced with permission from ref. 18.)

molecule (in cases where there are molecular symmetry elements which coincide with crystallographic symmetry elements and therefore relate a portion of the molecule to the rest) or it can be two or more. When Z' is greater than one there is the potential to see multiple lines for each nuclei in the molecule. Typically, multiple resonances are observed for only some of the nuclei, namely those whose environment differ enough to lead to an observable change in the chemical shift, while other of the resonances remain accidentally degenerate (see Fig. 2).

2.4. Presence of polymorphs

Polymorphism is another phenomenon that can only be observed in the solid state.[20–22] While there are still discussions of a precise definition of what constitutes polymorphism, one very general definition is the existence of different crystal

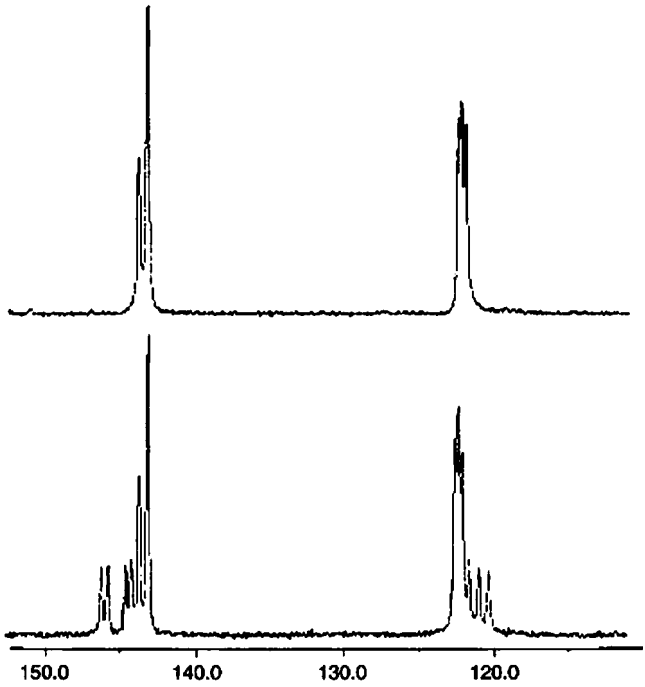

Fig. 2. Region of ^{13}C CPMAS of *cis*-verbenol containing signals from two olefinic carbons. Top spectrum shows existence of three lines (resonances at ~143 ppm are in a 2 : 1 ratio) for each of the olefinic carbons corresponding to three molecules per asymmetric unit, as was confirmed by the X-ray structure. Bottom shows a mixture of two polymorphs; the lower intensity lines are believed to be from an uncharacterized polymorphic form with four molecules per asymmetric unit. (Reproduced with permission from ref. 5.)

structures of the same chemical substance under the same conditions. Other definitions are more precise, requiring distinct properties and/or the same phase, or more general, allowing for amorphous states and solvates. The study of polymorphs has exploded, in large part due to their importance for the pharmaceutical industry,[23–25] as different polymorphs of a given compound can have different physical properties. In addition, patent rights which can play an important role in the stability, formulation, and commercialization of drugs are tied to a given polymorph. Many techniques have been used to study polymorphs, including microscopy, SSNMR, infrared, Raman, ultraviolet and fluorescence spectroscopies, thermal techniques, and of course X-ray crystallography. SSNMR has emerged as one of the most powerful tool in the characterization of polymporphs and is often used in conjunction with diffraction methods. In particular, the differences in the chemical shifts between polymorphs can be related to differences in structure, conformation, and/or intermolecular interactions. The literature of the study of polymorphs with SSNMR has rapidly increased since the 1990s. A typical example of the effect of polymorphism on the ^{13}C SSNMR spectra is given in Fig. 3.

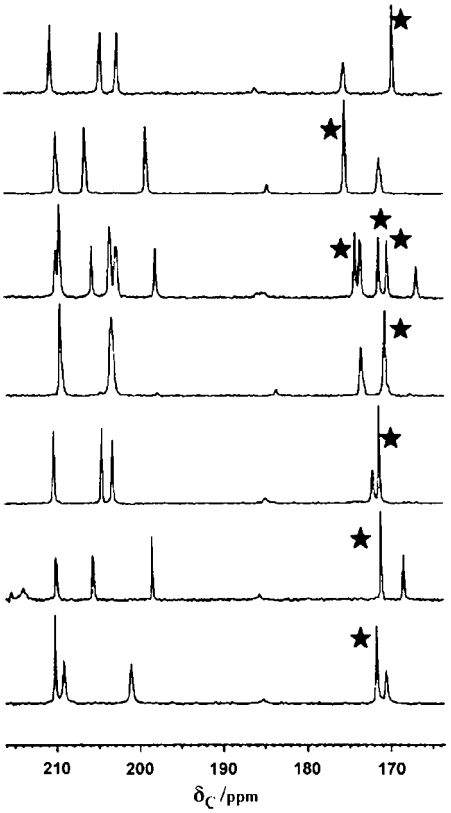

Fig. 3. High chemical shift region of the ^{13}C CP/MAS spectra of various polymorphic forms of cortisone acetate. Top to bottom: Forms I, II, III, IV_{aq}, IV_{et}, IV_{ac}, and V_{aq}. The stars indicated the signals from the same ester carbonyl carbon (C22) in each form. (Reproduced with permission from ref. 1.)

2.5. Multiple solid-state phases

Structural changes between different crystalline phases of a substance, i.e., different structures that exist under different temperature and/or pressure conditions, can also lead to changes in the chemical shift of a given nuclei. In many cases the phase transition is due to the loss of water leading to a transformation between a hydrate and anhydrous form of a substance. As in polymorphism, any number of spectroscopic and analytical techniques have been used to gain insight into the structural changes between solid-state phases, including SSNMR. However, there are typically limitations on the temperature and/or pressures at which the NMR experiments can be performed, thereby limiting the phases that can be studied. An example of changes that can be observed in the MAS spectra is given in Fig. 4.

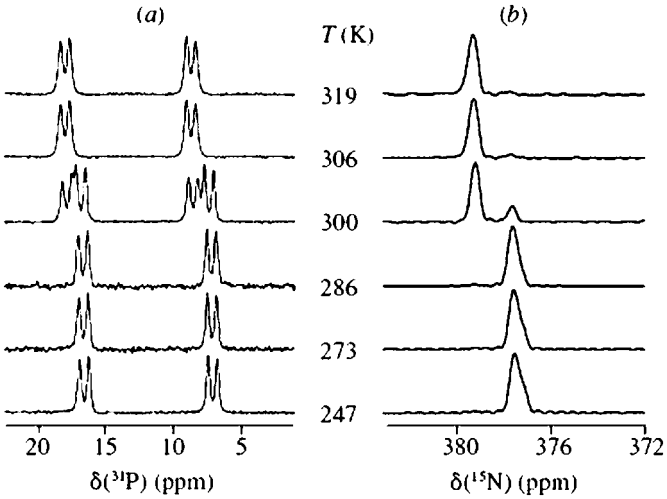

Fig. 4. ^{31}P and ^{15}N MAS spectra of $AgNO_3 \cdot PPh_3$ as a function of temperature, with the phase transition at 300 K. The splitting in the ^{31}P spectra is due to J coupling between the ^{31}P and the ^{107}Ag. (Reproduced with permission from ref. 26.)

2.6. Electrostatic effects

Electrostatic intermolecular effects can occur whenever there is a nonspherical distribution of charges in the environment surrounding a molecule, whether it is in a traditional ionic salt or in a substance that has polar bonds. The largest electrostatic effects are the Coulombic forces between unlike charged ions in ionic compounds. The effect of having neighboring charged species surrounding a molecular or atomic entity of interest, as is typically in ionic compounds, is large. In pure ionic compounds, the effect of this interaction cannot be theoretically reproduced by considering an isolated pair of ions as a given ion of interest is associated with more than one ion of the opposite charge. This makes these systems difficult to treat theoretically as any truncation in terms of nearest neighbors leads to a highly charged cluster. Electrostatic interactions also exist between compounds that do not have a net charge. Examples would be the zwitterionic form of amino acids as well as any compound containing a polar bond such as that in a carbonyl group. In this case a central molecule along with any molecules which interact with this central molecule should be used to include the intermolecular effects in a calculation, although this is not the only option. These electrostatic interactions produce significant polarization of the central molecule's electronic density that modify the strength of the induced magnetic fields when the molecule in placed in an external magnetic field. The specific mechanisms on how these affect the shielding will be further discussed in the next section where all methods of including intermolecular effects in calculations will be treated.

2.7. Hydrogen bonding

HB[27] is a phenomenon that occurs in a variety of chemical systems. A hydrogen bond is defined in the most general sense as a donor–acceptor interaction, either intramolecular or intermolecular, involving a hydrogen atom. These bonds are formed when a hydrogen atom that is bonded to an electronegative atom A, leaving the hydrogen atom with an electron deficit, is in a position to interact with a hydrogen acceptor atom B, which has the ability to provide electrons to form the hydrogen bond interaction. HB interactions encompass a wide range: from the interaction between the hydrogen atom and the acceptor atom being very strong, essentially a covalent interaction, to it being very weak, on the order of van der Waals forces. The majority of cases, known as moderate hydrogen bonds, fall between these two extremes; in these cases the interaction between the hydrogen and the acceptor atom is mostly electrostatic in nature. As will be discussed further in the next section, the strength of the hydrogen bond is very important in determining the best approach to use in calculations of shielding including these interactions. Hydrogen bonds strongly affect the NMR spectra in solids in a number of ways.[28] Intramolecular hydrogen bonds can be strengthened or weakened in the solid state relative to solution state structures, leading to conformation changes and/or significant changes of the molecular electron density. Furthermore, solid-state packing may lead to the formation of intermolecular hydrogen bonds that also may change molecular conformations and/or electron densities. All of these changes have significant effects on the NMR chemical shifts and quadrupolar constants, mainly in ^{17}O and ^{1}H, which make HB one of the most studied and most common origin of the intermolecular solid-state shielding effects.

2.8. Magnetic effects

The last intermolecular effect that must be introduced is the ring current or molecular magnetic susceptibility effect that can be observed in compounds with aromatic moieties. In aromatic compounds there exists highly anisotropic magnetic susceptibility due to the fact that large secondary magnetic fields are induced from the interaction of the delocalized electrons of the aromatic π system with the external magnetic field necessary for the NMR experiment. The magnetic field generated by these electrons is very directional with its largest strength directly above and below the π system. If any atoms are located in this area, the chemical shifts of those nuclei are impacted by these induced magnetic fields. Therefore this effect is only observed when atoms are fixed in this region. This ring current effect has been used in solution NMR of peptides to discuss the structural implications of unusually low chemical shifts of select protons in the vicinity of aromatic rings in the side chains.[29] In the solid state this effect has recently been observed between molecules in both ^{1}H isotropic chemical shifts[30] and ^{13}C chemical shift principal values[31] when the crystal packing of aromatic hydrocarbons stacks the molecules so that they lie parallel to each other. The directional nature of this interaction also results in the isolation of the effect in one of the principal components.

3. THEORETICAL METHODS

As discussed in the previous section, there are numerous mechanisms that can explain the changes observed between the NMR chemical shifts measured in solution versus those determined in a solid phase. While the experimental measurements can provide unequivocal evidence of the existence of solid-state effects on chemical shifts, the experiments alone seldom can provide conclusive information on their chemical and/or structural origins. Theoretical and computational methods play a fundamental role in interpreting the experimental results and providing insight on the physical origin of the solid-state effects, as it is possible to complete calculations on a variety of models, each of which can selectively include different, plausible mechanisms responsible for the solid-state effect on the chemical shifts.

The theoretical methods available to take into account intermolecular interactions can be classified in mainly two categories, those that represent the intermolecular interactions by an electric or magnetic field that mimics the interactions generated by the rest of the molecules in the crystal and those that explicitly treat the neighboring molecules. Most of the methods in the first category can be classified as electrostatic; in these methods either a finite distribution of charges or multipoles are used to represent the electric field generated by the environment.[32–34] Recently it has been shown that it is possible to observe purely magnetic intermolecular effects;[31] in this case the use of Nuclear Independent Chemical Shieldings (NICS)[35–37] calculations have been used to take into account these effects.[38]

The other category of methods available treats the neighboring molecules explicitly in the quantum mechanical calculations of the chemical shielding. For a number of years the explicit representation was accomplished by including a finite number of neighboring molecules in the calculations; this approach is usually described as a ''cluster model''. The greatest disadvantage of the ''cluster model'' is that their computational costs increases rapidly with the number of neighboring molecules included in the calculations. To avoid this problem a number of combinations of cluster and electrostatic models have been used over the years; in these hybrid models the closest neighbors are explicitly represented and the more remote ones are replaced by an approximate field. In recent years several research groups have proposed and implemented in available computer codes full crystal models to calculate the chemical shielding with periodic boundary conditions (PBC).[39–58] A description of the most popular methods of each category is given in the following sections.

3.1. Field expansion models

Field expansion methods were proposed many years ago in the pioneering work of Buckingham and Raynes,[59] but only in recent years, with the advances in the calculation of shielding using quantum mechanical methods,[34,60] have they been applied without resorting to empirical parameterizations. Using the uniform procedure for differentiation of molecular wave functions[61] it is possible to calculate

the derivatives of the shielding with respect to the electric field, EFG, etc. If the crystal field can be represented by a multipolar expansion, then the dependence of the chemical shielding with the crystal field can be expanded in powers of the electric field and field gradient. The coefficients in this expansion are the derivatives of the shielding tensor with respect to the electric field and its gradient. This methodology has been used as a model to explain the ^{13}C and ^{17}O shielding in carbonmonoxyheme proteins,[32,62] the effects of electric field on the ^{13}C and ^{17}O chemical shifts of carbon monoxide bound to Fe^{2+},[63] and the non equivalence of the ^{19}F NMR resonances in similar bonding situation due to lattice effects.[64]

3.2. Magnetic field methods

As mentioned above, recent work has demonstrated that for certain packing arrangements in polycyclic aromatic compounds it is possible to observe purely magnetic intermolecular effects on the chemical shifts.[30,31,65,66] These effects can be calculated using NICS[36,37,67] calculations of the magnetic field induced by the aromatic rings currents. The relationship between NICS and the magnetic field induced by the electronic structure of aromatic compounds has been recently discussed by Merino *et al.*,[68] who demonstrated that at any given point in space the induced magnetic field, B^{ind}, i.e., the magnetic field generated by the electronic currents induced in the molecular electronic structure by the presence of an external magnetic field, is proportional to the external magnetic field. The calculated NICS at the position of interest is the proportionality constant between the external and the induced field. Therefore, the NICS calculated at the position of a nucleus in a neighboring molecule, using as the source the electronic distribution of the central molecule, gives the intermolecular shielding contribution due to the molecular susceptibility or ring currents of the central molecule. This approach provides an accurate method to calculate intermolecular ring current effects without using semi-classical approximations. While the work from Merino *et al.*[68] discussed the isotropic NICS, the extension of this mechanism to the tensor components of the chemical shielding is straightforward, as has been demonstrated by Facelli.[38]

3.3. Electrostatic charge models

Charge models, which describe the intermolecular effects by a discrete distribution of point charges, are very attractive because they are derived from a very simple idea: namely that the crystalline electrostatic potential can be represented by a finite distribution of point charges, bond dipoles, and/or distributed multipoles. The great advantage of the charge models is that the cost of a shielding calculation does not significantly increase when a finite charge distribution is added and that they can be easily implemented in most of the existing programs for shielding calculations. A variety of point charge methods have been used to successfully reproduce the observed solid-state effects on shielding.[3,33,34,69–75] These methods will be discussed

individually below. In all the electrostatic methods the shielding calculations are performed using standard techniques,[76] but with a finite number of point charges added to the model system. The principal difference between the various approaches reported in the literature is the way in which the charges representing the crystal field are selected.

Numerous methods are also available to calculate intermolecular effects on shielding using continuum models; the interested reader can consult the recent review by Bagno *et al.*[77] However, as these methods only take into account the average of the intermolecular interactions, they are not suitable for the treatment of solid-state effects, which commonly are highly anisotropic.

It should be mentioned that limitations to the charge models have also been presented. Strohmeier *et al.*[78] have shown that strong HB interactions cannot be fully treated by a charge model; in this case a hybrid between the charge model and a cluster representation should be used. The cluster chosen in this case explicitly treated the strong HB interaction, whereas other intermolecular interactions were treated by the charge array model.

3.3.1. *Charge field perturbation theory*

Oldfield *et al.* pioneered the used of the Charge-Field Perturbation (CFP) method to take into account electrostatic effects on the quantum chemical calculation of shielding.[34] In the early work using the CFP method, the shielding was calculated with the TEXAS program[79,80] using an array of point charges to represent the intermolecular effects. These charges, calculated by the Mullikan population analysis using the Gaussian program,[81] were placed at the position of the lattice where the neighboring atoms would have been located. This method was used to study the intermolecular effects of a HF molecule on the shielding of fluorobenzene.[33] Further uses of the CFP method are the study of secondary and tertiary structural effects on protein shielding[3] and the lattice effects on the ^{13}C shielding tensors of the zwitterionic forms of L-threonine and L-tyrosine[82] using point charges determined with the AMBER[83] program.

3.3.2. *Karplus QM/MM*

Cui and Karplus introduced the Quantum Mechanics/Molecular Mechanics (QM/MM)[84] approach in which they combined the use of the CHARMM[85,86] program to treat the MM part and the Gaussian program[81] for the QM calculation of the chemical shifts. The effect of the MM region on the QM calculation of the chemical shifts is taking into account by introducing the point charges from the CHARMM simulations into the QM calculations. The authors note that it is important to include in the QM calculation of the chemical shifts not only the direct effects of the MM, by using an electronic density calculated in the presence of the point charges, but also the indirect effect, by including the point changes in the Coupled Perturbation Hartree Fock (CPHF) or Coupled Perturbation Kohn Sham (CPKS) equations. As with most methods using point charges, this method is not able to accurately reproduce strong HB effects.

3.3.3. *GEODESIC and GRID methods*

In the charge models discussed above the electrostatic field of the lattice is represented by point charges located at the position of the atoms of the neighboring molecules in the lattice; these charges are calculated using a suitable population analysis method for a given quantum mechanical electronic density. In an attempt to better represent the electrostatic field generated by the lattice Ferraro *et al.*[70] applied the GEODESIC[87] and GRID[88] methods to the calculation of shielding. These methods still place the point charges at the position of the atoms of the neighboring molecules in the lattice. However, the charges are determined by a least square fit procedure to reproduce the electrostatic potential of each neighboring molecule instead of using a population analysis method to determine them. In both methods the electrostatic potential of the molecule is calculated using the electronic density from a quantum mechanical method. The GRID method uses a regular grid of field points just outside of the fused spheres of the van der Waals surface of the molecule; at these points the electrostatic field generated by the QM electron density and the point charges is compared. In the GEODESIC scheme the points are selected on tessellations of an icosahedron surrounding the molecule's van der Waals surface. In the shielding calculation point charges are located at the lattice position of the atoms for as many shells as desired. The results reported by Ferraro *et al.*[70] included the charges for all molecules up to 5–6 Å from the central one.

3.3.4. *SCREEP method*

The Surface Charge Representation of the Electrostatic Embedding Potential (SCREEP) method, introduced originally by Truong *et al.*[89] to study catalysis, has been applied to the calculation of shielding by Solis *et al.*[73] The SCREEP[73] model for shielding calculations considers a region of space, $\boldsymbol{C}$, in which the electrostatic potential representing the lattice is produced by a charge distribution of the electronic density, $\rho(\mathbf{r})$, lying entirely outside $\boldsymbol{C}$. In the SCREEP model, $\boldsymbol{C}$ is the region occupied by the cluster of atoms treated by quantum mechanical methods and $\rho(\mathbf{r})$ is an appropriate charge density representing the crystalline environment outside $\boldsymbol{C}$. Using the Green's theorem[90] it is possible to replace the infinite charge distribution of the lattice outside $\boldsymbol{C}$, $\rho(\mathbf{r})$, by a surface charge density, $\sigma(\mathbf{r})$, over the boundary closed surface, $\mathbf{S}$, of the volume $\boldsymbol{C}$, such that the electronic potential generated by both distributions is the same inside the region $\boldsymbol{C}$:

$$V_{el} - \oint_S \frac{\sigma(r')}{|r - r'|} d^2r' = 0. \tag{1}$$

In the numerical implementation of the SCREEP method the surface $\mathbf{S}$ is divided into M elements of area, $\mathbf{S}_j$, for which individual point charges are assigned according to:

$$q_j \approx \sigma(\mathbf{r}_j)\mathbf{S}_j. \tag{2}$$

The calculation of these SCREEP charges proceeds in three steps:

- ☐ Construction of a discrete surface **S** around the cluster.
- ☐ Calculation of Madelung potentials on test points, V_j, inside $\boldsymbol{C}$.
- ☐ Solve the linear equations.

$$V_j - A_{ij}q_j = 0 \tag{3}$$

with

$$A_{ij} = \begin{cases} 1/\left|\mathbf{r}_i - \mathbf{r}_j\right| & \text{for } i \neq j \\ 1.07(4\pi/S_j)^{1/2} & \text{for } i = j \end{cases}. \tag{4}$$

In the SCREEP implementation[72,73] the **S** surface is generated employing the gepol93 algorithm[91] and the Madelung potentials, V_j, are calculated with the Ewald summation technique, using the lattice parameters and space group of the crystal and atomic charges for the atoms generated quantum mechanically. These charges are obtained for the isolated molecule with the Gaussian suite of programs[81] using the Charges from Electrostatic Potentials (CHELP) method.[92] The number of surface charges required to represent the Madelung potential depends on the size of the crystal. To improve the accuracy of the SCREEP calculations, charges from the environment that are close to the quantum cluster and the surface $\boldsymbol{S}$ may be treated explicitly without approximation. In this case, the potential of these explicit charges is evaluated inside the cluster and subtracted from the potential $V(r)$ in Eq. (3). A cutoff radius R_{cut} ($R_{\text{cut}}R_a$ = radius of the atomic spheres ~2.5–3.0 Å) was selected such that all the lattice ions in the environment lying within R_{cut} to the closest atom of the cluster are attributed to the explicit region. For nonionic compounds it was verified that it was not necessary to perform any further refinement of these charges to secure the convergence of the SCREEP results. However, for ionic system these procedures were repeated in an iterative fashion, quantum mechanically recalculating the atomic charges of the molecule embedded in the SCREEP potential of the charges generated by the previous iteration. This procedure was repeated until the standard deviation of the charges was less than 0.002*e*, usually three to four iterations.

3.3.5. *Embedded ion method*

The Embedded Ion Method (EIM) has been shown to improve the agreement between experimental and calculated chemical shifts in a wide variety of systems, ranging from ionic systems such as potassium carbonates and thiocarbonates[93] to systems with HB[75,94,95] and neutral systems with intermolecular Coulombic interactions such as β-HMX.[96] The EIM[74] method for shielding calculations utilizes the Ewald summation as implemented in the program EWALD written by Klintenberg *et al.*[97,98] The original program was written to work on pure ionic compounds and therefore was only able to deal with full electron charges. To work with molecules and molecular ions the EWALD

code was modified to deal with partial atomic charges.[74] The EIM accounts for intermolecular interactions by using charge arrays to mimic the electrostatic crystal potential. The potential experienced by a molecule of interest in an infinite crystal lattice, the Madelung potential, is simulated by a finite set of charges which are generated by the EWALD program. This finite set of charges is divided into three regions. The first region, which includes the molecule of interest, contains a relatively small number of fixed charges, generally 50–200 depending on the size of the molecule, at the crystallographic location of the atoms in the molecules nearest to the molecule of interest. These charges are fixed to partial atomic charges that have been calculated for the molecular system. The second region, a spherical volume surrounding the first region, is a second set of additional fixed charges. The remainder of the charges surrounding the inner two regions constitutes the third region and both the charges and their positions are varied such that the potential throughout the first region reproduces the Madelung potential as computed by the Ewald summation method.[99] The accuracy of the solution is checked at a set of randomly chosen points within the first region, with an rms of 1 μV agreement between the calculated potentials and the Ewald summation potential being required. In addition, the program checks the size of the charges in zone three as the observation of unreasonably high negative or positive charges is an indication of problems in the fitting procedure. The accuracy of the results has been shown to improve with an increase in the number of charges included in regions two and three. The unit cell parameters and the fractional coordinates of all atoms in a unit cell must be provided as well as an initial estimate of the atomic charges on each atom of the system of interest. The user is required to specify the number of unit cells to reproduce in each direction, the number of points in each of the first two regions, and the number of randomly chosen points at which the potential produced by the finite charge array will be compared with the potential calculated by the Ewald summation method.

The procedure of the calculations established by Stueber *et al.*[54] is to first obtain the partial atomic charges from a calculation of an isolated molecule or ion. The method chosen to calculate these partial charges is the Natural Bond Orbital (NBO) as implemented in the Gaussian suite of programs.[81] These charges are used in the EWALD program to calculate an initial charge array in which to embed the molecule of interest. The calculation of new NBO charges is then completed on the molecule or ion in this charge array. Using this second set of NBO charges, EWALD is used to calculate a second charge array that is then used to calculate a third set of NBO charges. This process is repeated until the NBO charges show no change larger than $0.001e$. At this point it was determined that a ''consistent'' set of charges had been reached and the chemical shielding is then also calculated. It generally takes three to five steps for this level of charge consistency to be attained. A recent study has shown that the EIM results are of similar quality to those obtained by the SCREEP method.[100]

3.4. Cluster models

Cluster models[101] are the most popular method used to treat solid-state effects on chemical shielding because they do not require any additional computational tools. Any quantum chemical program capable of performing a shielding calculation [60,76,102–104] can be used. The issues associated with the cluster methods are fundamentally related to the selection of a "representative" model cluster,[105] one that realistically represents the crystalline environment, while still being computationally treatable. In principle it can be argued that a large cluster of molecules, including several layers of neighbors, should be an adequate representation of the environment surrounding the central molecule. Unfortunately, computational limitations always severely constrain the number of molecules that can be treated quantum mechanically in the cluster model. This invariably leads to uncertainties in the results as it can be difficult to discriminate between the shortcomings of the model cluster used in the calculation and any uncertainties intrinsic to the method used in the shielding calculation. To reduce the computational cost of the cluster calculations many authors[106–108] have proposed the use of more dense basis sets for the central molecules and less complete ones for the molecules representing the environment.

To be meaningful any calculation using the cluster model should take into account the Basis Set Superposition Error (BSSE), as the calculation of solid-state effects are not given by the direct comparison of the results obtained for the isolated molecule and the one in the cluster, but by comparing the cluster calculation with a calculation of the central molecule when using all the basis functions used in the cluster calculation. This method to estimate the BSSE is often referred to as the counterpoise correction.[109]

3.5. ONIOM method

Karadakov and Morokuma introduced Our own N-layerd Integrated Molecular Orbital and Molecular Mechanics (ONIOM) hybrid method for the calculation of chemical shielding,[110] using a two layer model (ONIOM2(MP2-GIAO : HF-GIAO)). In the ONIOM approach the molecular system under consideration is divided in a series of layers which are treated with decreasing levels of theory when moving toward the outer layers and away from the region of interest. The level of treatment of each layer can include highly correlated methods such as MP2, HF, semi-empirical methods, and finally molecular mechanics. The same ONIOM approach was used by Rickard *et al.*[111] to study the chemical shifts of different conformers of β-D-glucopyranose. Finally Zheng *et al.*[112] used the ONIOM(MP2-GIAO : B3LYP-GIAO) method to calculate the carboxyl carbon shielding tensors in several amino acids in clusters representing at least one layer of first neighbors. While all the examples available on calculations of shielding using the ONIOM method can be classified as cluster calculation as they use quantum mechanical methods for all of the layers, it is possible also to use

ONIOM as an electrostatic approach if the outer layers are treated by molecular mechanics.

3.6. Tight-binding approach

The tight-binding (TB) MO-INDO/S sum-over-states theory[113] was used to study the interchain interactions on the ^{13}C shielding of several polymers. In principle the TB method, which takes into consideration the full periodicity of the crystal lattice, provides an exact description of all the intermolecular effects. However, very few calculations of shielding are performed using semi-empirical methods and this has been the only implementation of the TB approach for shielding calculations. The TB study of the interchain effects on ^{13}C shielding determined by calculations in seven different right- and left-handed alpha-poly(L-alanine) show qualitative agreement with the experiments. Due to the lack of a consistent literature it is difficult to assess the general applicability of the TB method to study intermolecular effects on shielding. Moreover, as with the full crystal methods discussed in the next section, the TB method includes all possible intermolecular interactions and does not provide any physical insight on the relative importance of different interaction mechanisms.

3.7. Full crystal models

In recent years two independent research groups have reported new theories that allow the calculation of shielding in systems with PBC. Sebastiani and Parrinello[39–44] implemented their method in the popular CPMD program.[114] Sebastiani proposed the use of localized Wannier orbitals and a periodic pseudoposition operator with a saw-tooth shape. This method can be used to calculate shielding in both isolated and full periodic systems. A similar theory was presented by Mauri *et al.*[50] in which the problems associated with the lack of definition of the position operator in periodic systems has been resolved by using a modulated external magnetic field; they calculate the shielding by numerical differentiation of the values calculated for two small, but not zero, wave vectors. This method, as well as the one from Sebastiani, has been implemented using pseudopotentials and therefore cannot take into consideration the contribution of the inner shells. This approximation can be problematic for non first row nuclei and in a subsequent paper[52] Pickard and Mauri introduced the Gauge Including Projector Augmented Wave (GIPAW) method that formally includes the contribution of the core electrons when using pseudopotentials. Numerous applications using this method have been presented.[45–58] A comprehensive comparison of both full crystal methods in a series of compounds for which both high quality NMR chemical shift tensor data and ND crystal structure data are available[16,17] is long overdue, but unfortunately the GIPAW method is only available through a very expensive license from a commercial vendor.

4. CASE STUDIES OF SOLID-STATE EFFECTS

In this section, we present a number of literature case studies measuring and interpreting the SSNMR effects on both chemical shifts and quadrupolar constants. As mentioned in the introduction, the examples presented are by no means a complete survey of the literature available on this topic; instead they were selected as representative case studies. In particular the cases chosen were ones in which there was an analysis or interpretation of the intermolecular effect in terms of the underlying intermolecular interactions and their physical origins. The examples are arranged by nuclei; consequently different aspects of several literature reports are discussed in multiple parts of the text as they contain information on more than one nuclei.

4.1. ^{13}C examples

The majority of SSNMR studies involving intermolecular effects have been on ^{13}C due to its widespread use for the characterization of organic substances and the relative ease to perform ^{13}C SSNMR spectroscopy using commonly available NMR spectrometers. In addition, ^{13}C measurements of chemical shifts tensors or principal components are much more common than in any other nuclei and present the most readily available source of data to demonstrate the high anisotropic character of intermolecular interactions. The effects studied in the literature and reported here include examples of all the different effects outlined in the first section of this review article.

4.1.1. *Intermolecular shielding due to magnetic susceptibility*

In a ^{13}C SSNMR study of 4,7-di-*t*-butylacenaphthene Ma *et al.*[31] observed that the experimental and theoretical tensor data from a calculation of an isolated single molecule lacked the expected level of agreement, with an RMS error of 7.0 ppm between the experimental and calculated chemical shift tensor principal values. The deviations were concentrated in the components perpendicular to the aromatic plane, with the largest effect being a 23 ppm difference in the δ_{11} component of the CH_2 carbon. A 23 ppm difference between experiment and theory for a tensor component is completely unexpected for a CH_2 carbon with a narrow tensor having a span of only 20–30 ppm and whose tensors have been shown previously to be calculated with high precision. It should also be noted that the difference between the solution and solid-state isotropic chemical shift for the CH_2 carbon is only 2 ppm; certainly this effect would have been easily overlooked in an analysis restricted to the chemical shift isotropic values. An even relatively larger solid-state effect was observed for the proton isotropic chemical shift of the hydrogen on this CH_2 group, with a 4.6 ppm difference measured between the isotropic chemical shift in the solid state (−0.9 ppm) and in solution (3.65 ppm). As discussed latter in the ^{1}H section of this review, this corresponds to nearly half of the typical ^{1}H chemical

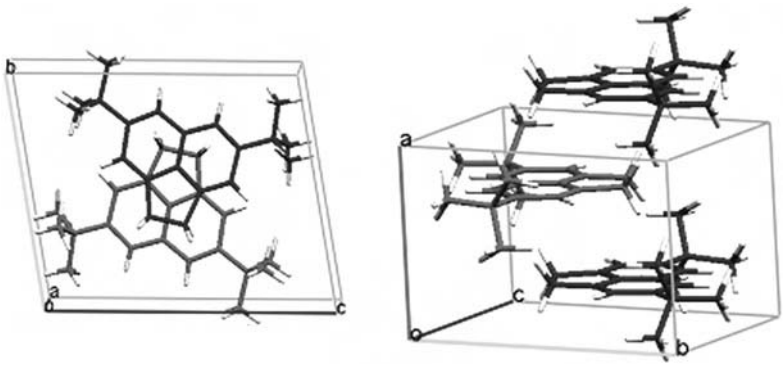

Fig. 5. Different views of the crystal structure of 4,7-di-*t*-butylacenaphthene showing how molecules stack. The distance between the planes of the molecules in the stack is 3.4 Å, with the hydrogen of the CH_2 group being 2.6 Å away from the plane of the neighboring molecule. (Reproduced with permission from ref. 31.)

shift range. A fragment of the crystal structure of 4,7-di-*t*-butylacenaphthene is shown in Fig. 5.

Theoretical efforts to account for the observed differences included calculations of the ^{13}C shielding using the EIM approach, cluster calculations, and the use of NICS calculations. Treatment with the EIM approach to include intermolecular effect did little to improve the agreement with the measured values, resulting in a RMS of 6.2 ppm and with a 22 ppm difference remaining between the calculated and experimental δ_{11} component in the CH_2 carbon. This is a clear indication that the discrepancy is not due to an electrostatic intermolecular interaction. A cluster calculation, including the molecules directly above and below the molecule of interest improved the overall agreement, leading to a overall RMS of 4.0 ppm as well as a much smaller 9 ppm discrepancy in the problematic δ_{22} component of the CH_2 carbon. There were also substantial improvements in other components that were perpendicular to the molecular plane, namely the δ_{33} components of the aromatic carbons near the CH_2 group. Finally, a NICS calculation at the position of the CH_2 carbon shows that the magnetic effect of the two first neighbor molecules accounts for a 14.5 ppm correction for the δ_{11} component. The fact that this intermolecular effect is additive, arising half from each of the first neighbors (top and bottom), and that it can be nearly completely modeled with the use of NICS calculations clearly confirms that it is an intermolecular magnetic susceptibility or ring current effect.

While this is the first study in which this type of effect has been reported in carbon tensor components (other studies on ^1H are outlined further below), it is an effect that can be observed whenever magnetic nuclei are positioned directly above or below an aromatic structure, with the strength of the effect being dependent only on the distance and the nature of the aromatic structure.[38] An examination of the crystal structures of aromatic compounds[115] indicates that as the aromatic molecules become larger and more disk-shaped, the π–π intermolecular interactions

begin to outweigh the C–H interactions, leading to a shift toward crystal structures with molecular arrangements that form parallel graphite-like planes, as observed in 4,7-di-*t*-butylacenaphthene. This indicates that as larger aromatic molecules became amenable to SSNMR studies the number of examples of these molecular susceptibly or ring current effects may increase.

4.1.2. *Loss of motional averaging*

There have been numerous studies in which conformational averaging due to molecular motion that is observed in solution NMR spectra is absent in the solid state. In other cases the averaging is still observed in the solid at room temperature, but is removed in low temperature studies.

One such case is a study of anisole,[18] with the spectra shown in Fig. 1. Solution and neat liquid room temperature spectra show only four aromatic resonances that can be assigned to the *ipso*, *ortho*, *meta*, and *para* carbons. However, by lowering the temperature to ~200 K the number of aromatic carbon resonances increases to six, with a 7 ppm difference between the two *ortho* carbons and 1.3 ppm between the *meta* carbons. The measurement of the tensor components of these carbons show that the differences in the isotropic chemical shift of the *ortho* carbons *cis* and *trans* to the methoxy carbon are concentrated in the δ_{11} (9 ppm) and δ_{33} (14 ppm) components.

A similar study on *p*-tolyl ether,[116] with the structure shown in Fig. 6, shows that the four ^{13}C resonances observed in a solution state measurement increase to eleven resolved resonances for the 14 magnetically nonequivalent carbons in the solid state when the molecular motion is stopped. With the help of the tensor components and quantum chemical calculations of the tensor several assignments could be made to individual carbons. Table 1 reports the comparison between solution and solid-state isotropic values along with tensor values that were obtained and the assignments

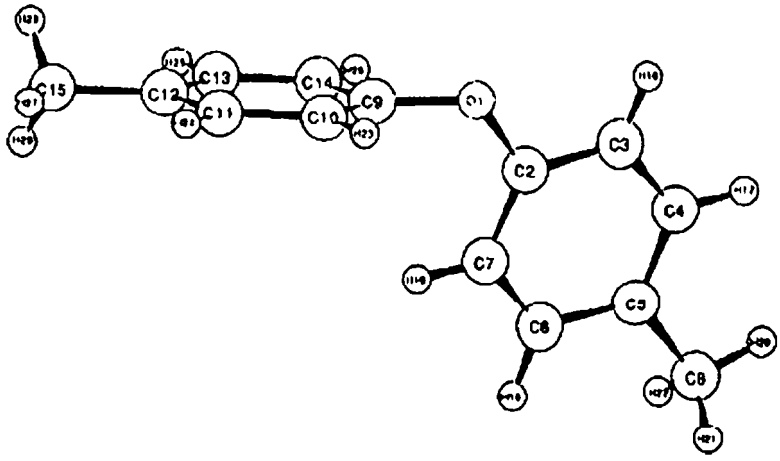

Fig. 6. Structure of *p*-tolyl ether.

Table 1. ^{13}C chemical shift data from *p*-tolyl ether

Carbon type	Assignment[a]	δ_{11}	δ_{22}	δ_{33}	δ_{iso}[b]	δ_{avg}[c]	δ_{liq}[d]	δ_{MAS}
C(O)	C_9	238.3	147.4	74.4	153.4	155.6	155.2	154.4
C(O)	C_2	238.6	160.7	74.4	157.9			159.1
$C(CH_3)$	C_5	228.3	152.9	14.2	131.8	132.7	132.1	131.9
$C(CH_3)$	C_{12}	232.7	160.2	7.6	133.5			134.3
CH_3		34.2	23.4	−0.4	19.1	20.8	20.6	18.5
CH_3		39.2	25.4	2.7	22.4			21.8
C_{meta}		226.5	143.1	23.8	131.1	131.4	129.9	130.8
C_{meta}		228.3	143.6	22.8	131.6			131.9
C_{ortho}	C_7	196.4	138.7	13.3	116.1	118.8	118.4	116.7
C_{ortho}		202.0	127.5	21.4	117.0			118.9
$C_{ortho}(2)$		204.4	140.5	18.1	121.0			121.7

Note: All values referenced to TMS.

[a]Assignment numbering taken from Fig. 6.

[b]The isotropic chemical shift taken as average of the three principal values.

[c]The weighted average of the isotropic chemical shifts of the same carbon type.

[d]The reader is referred to the original paper[116] for the reference for the solution chemical shifts.

that could be made. The NMR chemical shifts, especially the tensor components, were shown to be very sensitive to the dihedral angle between the two aromatic rings.

4.1.3. *Ionic materials*

An early study of the 2-propyl cation by Haw *et al.*[117,118] showed that the calculation of the ^{13}C chemical shift tensors measured for this cation in a solid matrix at low temperatures could not be satisfactorily reproduced by calculations on an isolated cation. Lacking a crystal structure of this ionic material, the best they could do was to test the effect of various counter ions along with various plausible spatial arrangements of these counter ions had on the calculated principal values. Their results showed that the addition of the counter ions had a large effect on the principal values, but they were unable to find an arrangement that gave a good match for the experimental data, most likely due to the lack of structural information.

The first rigorous treatment of intermolecular shielding effects in ionic compounds was a study on carbonate and thiocarbonate anions performed using the EIM method.[93] For the majority of these compounds crystal structures existed, allowing for the use of the EIM and avoiding any structural ambiguities in the crystal models used. The improvements gained in going from calculations on isolated anions to calculations that use EIM to treat the crystal environment are summarized in Fig. 7. The structures used in all cases have the heavy atoms locked at the X-ray diffraction positions while the hydrogen atom positions were optimized.

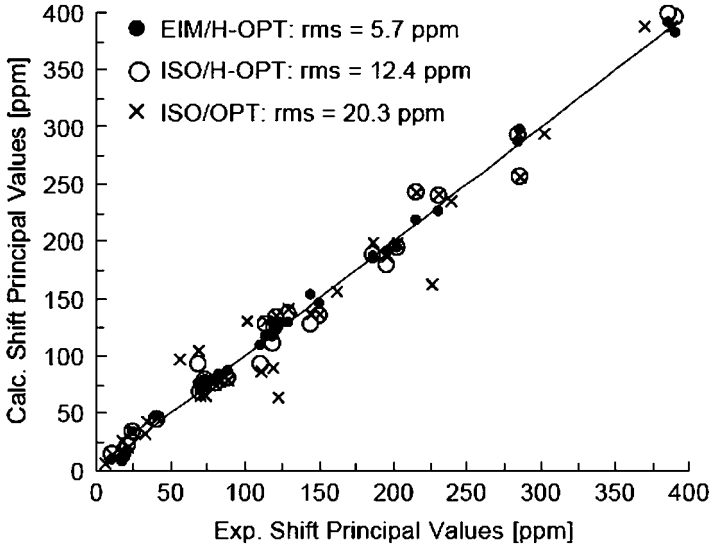

Fig. 7. Correlation between experimental and calculated chemical shift tensor principal values obtained for an isolated molecule with a fully optimized geometry (ISO/OPT), an isolated molecule with optimization of hydrogen atom positions only (ISO/H-OPT), and for an EIM calculation using this same H-OPT geometry (EIM/H-OPT) along with the corresponding RMS values. The solid line represents the linear fit in the EIM calculation. (Reproduced with permission from ref. 93.)

The improvement observed is such that the EIM results can be used to assign the orientation of the tensor components in the molecular frame, allowing further analysis of the results, a task not possible with the results of calculations on isolated anions.

4.1.4. *Multiple molecules per asymmetric unit*

Several studies have reported that modern SSNMR can resolve the ^{13}C resonances corresponding to nuclei in different molecules in the asymmetric unit. One such example is a study by Harper and Grant[5] on *cis*-verbenol (structure is shown in Fig. 8). This molecule has three molecules per asymmetric unit in its major polymorph, an observations first made on the basis of this NMR study and then confirmed with an X-ray analysis. As shown in Fig. 2, three resonances for the olefinic carbons are suggested by the splitting of the peaks in the spectrum. From a fitting of a FIREMAT dataset at least two distinct sets of tensor data were obtained for each of the ten carbons in this polymorphic form. An X-ray diffraction structure of this form[119] shows that the three molecules are very similar, with the largest variations in angles being less than 2° and bond lengths less than 0.013 Å. The crystal structure is dictated by HB, with the three molecules arranged in a helical chain about the short axis (*a*) of the unit cell and that the only major variation in

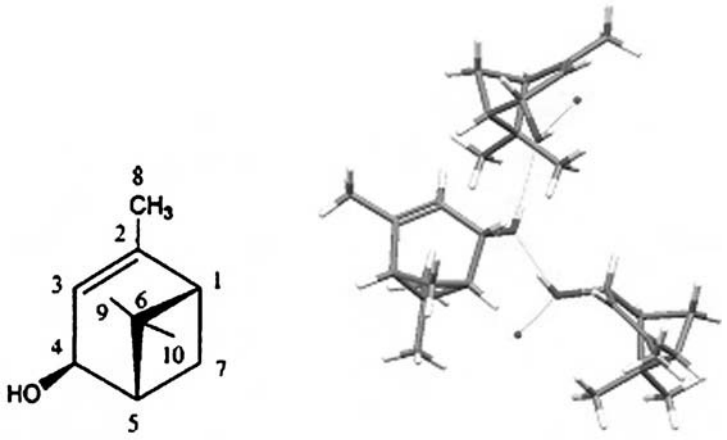

Fig. 8. Structure of *cis*-verbenol and asymmetric unit showing how the crystal structure is governed by the HB between the three molecules in the unit.

the structures was associated with the dihedral angle on the hydroxy hydrogen, with the dihedral angle describing the hydrogen position (H-O-C_4-C_3) determined to be 55, 69, and 74° in the three molecules of the asymmetric unit. Calculations showing the sensitivity of the tensor components to this dihedral angle were completed, and are summarized in Fig. 9 for the olefinic carbons C_2 and C_3. A ^{13}C MAS spectrum (Fig. 2) of this compound also shows the existence of a second polymorphic form that has never been isolated; the NMR indicates that this second form has four molecules per asymmetric unit. Principal values for several carbons of this second polymorph were extracted from a FIREMAT spectrum taken on the mixture of the two forms.

A second example of multiple molecules per asymmetric unit is parthenolide,[7] shown in Fig. 10. In this case there are two molecules per asymmetric unit and in the ^{13}C NMR spectrum there are 29 resolved resonances resolved for the 15 carbons.

In both of these cases very good correlation was observed between the tensor components from experiment and those from DFT calculations on a single molecule, with an RMS distance between the two sets of data found to be ~3 ppm. This seems to indicate that the small differences in conformation observed between the structures are the dominant factor in the differences in chemical shifts that are observed and that the actual intermolecular interactions play an indirect role only to the extent that they are the driving forces behind the formation and stabilization of the different structures.

4.1.5. *Studies of polymorphs*

The first example of polymorphism that will be discussed is that of two forms of dimethyl-3,6-dichloro-2,5-dihydroxyterephthalate.[120] The two known forms of this compound are commonly designated as the white and yellow forms based on their

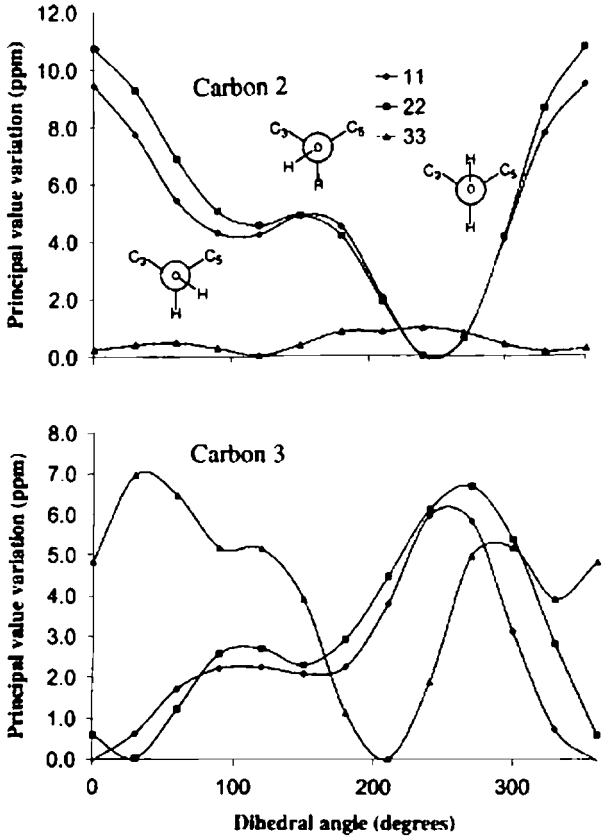

Fig. 9. Plots of the variation of the tensor components for the olefinic carbons C_2 and C_3 as a function of the H-O-C_4-C_3 dihedral angle. Geometries were relaxed at each point before the shielding calculations. (Reproduced with permission from ref. 5.)

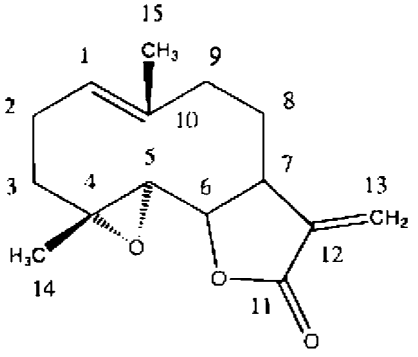

Fig. 10. Structure of parthenolide.

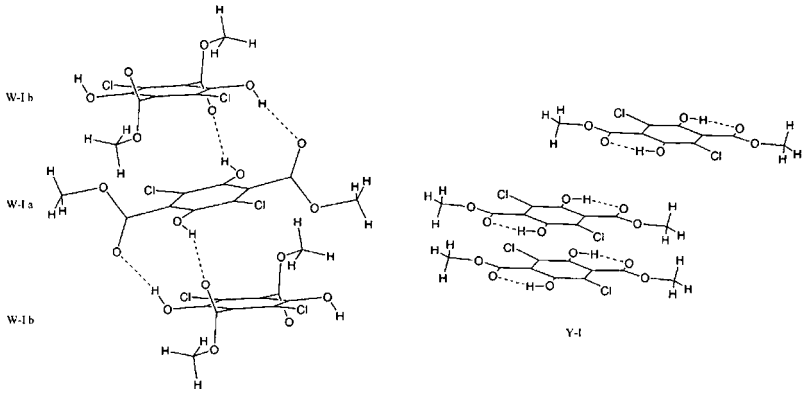

Fig. 11. Crystal packing and HB arrangement in the two polymorphs of dimethyl-3,6-dichloro-2,5-dihydroxyterephthalate. (Reproduced with permission from ref. 120.)

color; the white form has two molecules per asymmetric unit. A fragment of the crystal for these two polymorphs, showing the HB interactions is given in Fig. 11. Note that in the yellow form the hydrogen bonds are intramolecular, whereas in the white form they are intermolecular. The drastic difference in HB is due to the change in the dihedral angle between the planes of the ester group and the phenyl ring; in the yellow form this angle is 4° and in the two yellow form molecules it is 70 and 85°.

In this study, the principal values of the ^{13}C chemical shift tensors were measured from the fitting of FIREMAT data and calculations were completed at the B3LYP/D95** level on both a single molecule and a stack of three molecules, using the arrangements shown in Fig. 11 along with a third arrangement for the white form in which a *b* molecule was stacked between two *a* molecules. The overall agreement of these calculations is shown in Fig. 12.

As expected, the single molecule calculation for the yellow molecule, without any intermolecular HB, gave better agreement with experiment (RMS of 5.7 ppm) than those for the white-*a* or the white-*b* molecule (8.2 and 8.6 ppm, respectively), which have intermolecular HB. The white molecules, however, showed greater improvement with the addition of the neighboring molecules (RMS of 6.0 ppm for white-*a*, 5.9 ppm for white-*b*, and 4.5 ppm for yellow). A closer look at the individual shift components shows that the improvement was concentrated in the carbons most closely associated with the HB, specifically in the δ_{11} and δ_{22} components of the ester carbon and the δ_{22} component in the carbon with the hydroxyl group.

Smith *et al.*[121] reports a similar study on 5-methyl-2-[(2-nitrophenyl)amino]-3-thiophenecarbonitrile using the chemical shifts obtained from a 2D PASS experiment and chemical shifts calculated using DFT. This compound, shown in Fig. 13, has seven polymorphs for which their structures are known.[122] In this study measurements were made on three of them: the red, the orange, and the yellow forms

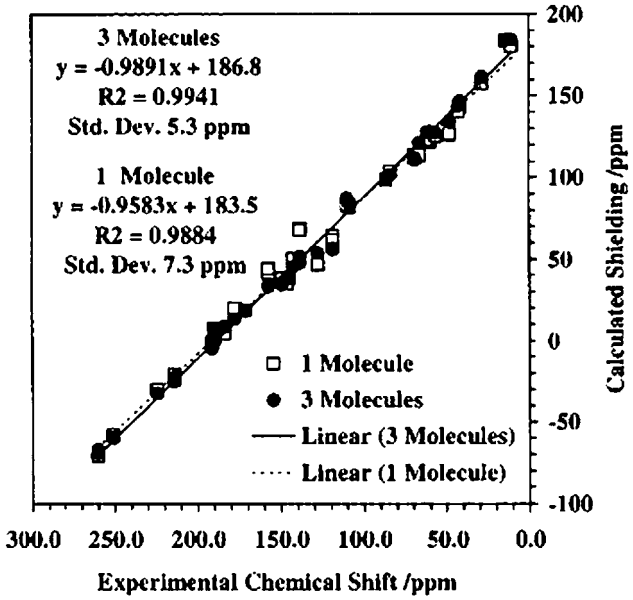

Fig. 12. Correlation between the calculated and experimental ^{13}C shift tensor components for the yellow, white-*a* and white-*b* molecules of dimethyl-3,6-dichloro-2,5-dihydroxyterephthalate. (Reproduced with permission from ref. 120.)

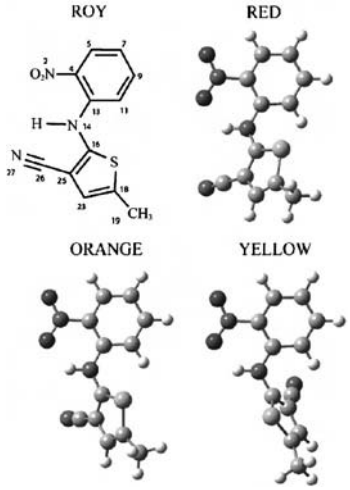

Fig. 13. Chemical structure of 5-methyl-2-[(2-nitrophenyl)amino]-3-thiophenecarbonitrile with numbering scheme used along with X-ray structures of the three polymorphs studied. (Reproduced with permission from ref. 121.)

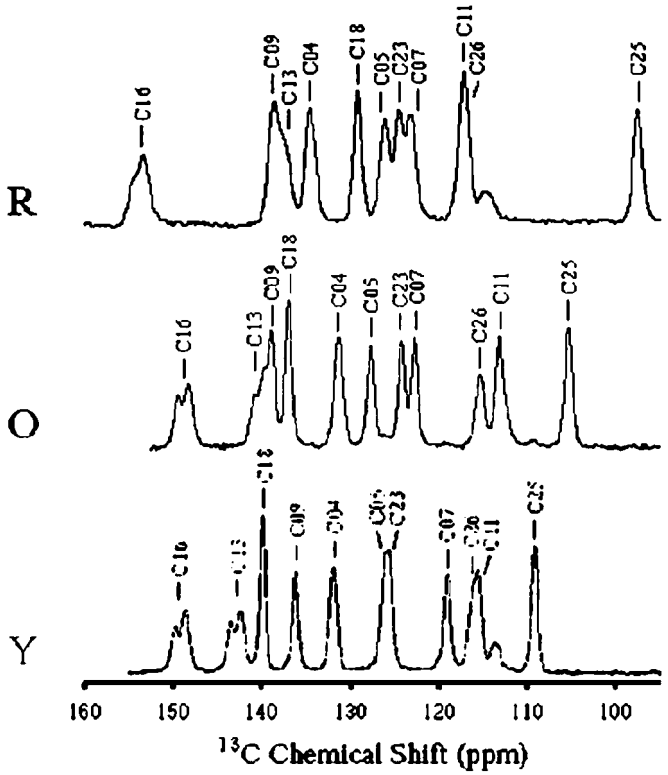

Fig. 14. ^{13}C CPMAS spectra of the ROY polymorphs. (Reproduced with permission from ref. 121.)

that are collectively referred to as ROY. These three polymorphs share a similar molecular structure with the only major difference being the angle between the planes of the two rings. The differences observed between the isotropic ^{13}C chemical shifts are shown in Fig. 14.

DFT calculations were performed only on an isolated molecule; the RMS between experiment and theory was 6.9 ppm for the ^{13}C chemical shift tensor components. This RMS is larger than typical, and is most likely an indication that intermolecular effects not accounted for in the calculations do play a role in the measured chemical shifts. Modeling of the dependence of the chemical shifts on the angle between the two rings, measured as the C_{11}-C_{13}-C_{16}-S_{17} dihedral angle was completed. A goodness of fit between calculated chemical shift components, both for ^{13}C and ^{15}N, done as a function of this angle with respect to the experimental results was completed; the best fit for the R form was at an angle of 41.0° (X-ray diffraction 43.6°), for the O form it was 58.0° (X-ray diffraction 50.1°), and for the Y form 91.9° (X-ray diffraction 91.8°).

There have been several different ^{13}C NMR studies of polymorphs using full crystal models; all of them report only isotropic chemical shift values[123–125] and in

all cases the agreement between the experimental and calculated isotropic chemical shifts is good. In the case of testosterone, the RMS agreement between theory and experiment for the two forms was 3.97 ppm.[125]

4.1.6. *Hydrogen bonding*

Whereas HB plays an indirect role in defining the structures of the crystals discussed in the above discussion of polymorphs and multiple molecules per asymmetry unit, in this section we present examples in which the HB interaction directly affects the ^{13}C shielding. The discussion deals with the effects of HB on the ^{13}C chemical shifts of the carbonyl, carboxyl, or carboxylic acid carbons which has been widely studied due to the role that they play in amino acid and peptide structures.

Before the widespread use of calculations of shielding, the trends in the ^{13}C chemical shift tensors of the carboxyl carbon in amino acids were discussed.[126] It was shown that while there was little difference between the isotropic chemical shifts of protonated and deprotonated carboxylic groups, there were large differences observed in the δ_{11} and δ_{22} components. In addition, the δ_{22} component could be correlated to the strength of the hydrogen bond formed by this carboxyl group, measured by the O-H separation. Early quantum chemical calculations showing similar trends were subsequently completed for a model system of acetic acid and methyl amine.[127] The results of these calculations show that the calculated tensor components reproduced this trend with the O-H distance (Fig. 15). In this paper, Facelli *et al.* go on to discuss how the O-H distance and therefore the trend in the components can be related to the difference between the two C-O bond lengths in the carboxylic group; at the short O-H distances you have a protonated group with two very different C-O bond lengths and in the other extreme of long O-H separations you have a structure where the two C-O distances are essentially the same. In the latter case the system is very similar to the π delocalization in aromatic carbons.

Other studies have theoretically treated the HB in amino acid systems by the CFP,[82] cluster,[128] EIM,[129] full crystal,[130] and ONIOM methods.[112] The set of amino acids used in these studies were different, as was the basis set used and the level of theory; therefore, a direct comparison of actual tensor components cannot be made nor can a direct comparison of the actual RMS be made. However, a general comparison of the improvement in the RMS of each of these methods can be made; this data is given in Table 2. The reader is directed to the individual papers for details of the calculations and a more complete analysis of the results, including that of the other carbons in the amino acids. In all cases there was substantial improvement of the calculated δ_{11} and δ_{22} components of the carbonyl carbon when the HB was treated in the calculations. It is also interesting to note that in the EIM calculation[129] the agreement between experiment and theory for the sp2 carbon data which includes the problematic carbonyl carbons is as good as that for the sp3 carbons; this is a good indication that the EIM effectively treats the HB intermolecular effect in these cases. The three methods using DFT (EIM, ONIOM, and full crystal) all produce results of comparable quality.

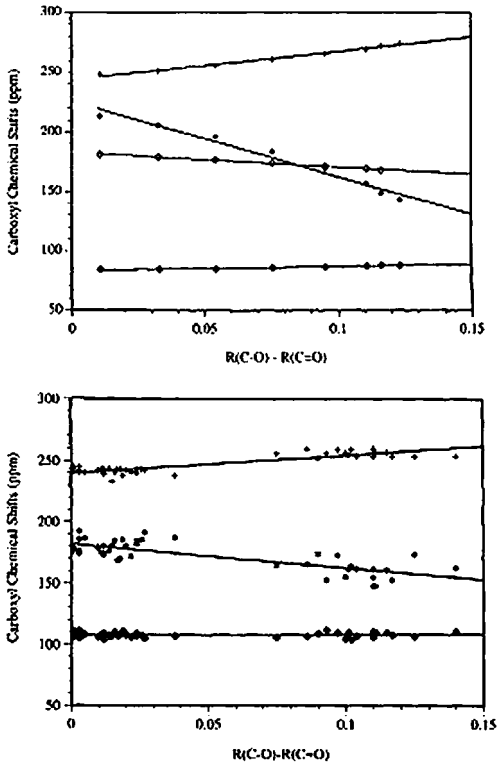

Fig. 15. Comparison of trends observed for the carbonyl carbons in calculations using acetic acid and methylamine at different separations (top) and experimentally in a set of carboxyl carbons from peptides and amino acids. (Reproduced with permission from ref. 127.)

Similar experimental trends in the tensor components were also observed for the carbonyl carbon in peptides, as shown in the plots in Fig. 16. However, very few calculations of shielding in peptides take intermolecular interactions into account, most likely due to the size of the system combined with the need for crystal structures for the noncluster methods. Early calculations done at the semi-empirical FPT-INDO method by the Ando group[131] using formamide molecules as the HB partner were able to model the general trends observed in the components as a function of the N···O separation.

More recently, a study of the ^{13}C isotropic chemical shifts and HB in a set of eight histidine containing dipeptides highlighted the need to include the nearby lattice into calculations.[132] In this study three models were used to calculate the ^{13}C isotropic chemical shifts; one of these was a supermolecule or cluster approach. While the single molecule calculation results had very poor agreement with experiment, the cluster approach had an RMS difference of 1.9 ppm. Finally, there has been one study using EIM in the peptide melanostatin (L-Pro-L-Leu-Gly amide).[133] The calculation was

Table 2. Comparison of the improvement in the agreement between theory and experiment for carbon chemical shifts of amino acids when intermolecular HB are included in the calculations

Method	Amino acids in dataset	Isolated molecule RMS (ppm)	RMS with intermolecular effects treated (ppm)
CFP[a]	L-Threonine L-Tyrosine	12.3	6.4
Cluster[b]	L-Alanine L-Serine DL-Serine α Glycine	35.5	19.6
EIM[c]	L-Alanine L-Asparagine · H_2O L-Histidine · HCl · H_2O α Glycine γ Glycine	13.3, 4.8, 17.8	4.1, 3.9, 3.8
ONIOM[b]	L-Alanine L-Serine α Glycine	35.5	5.9
Full crystal[a]	L-Alanine L-Tyrosine α Glycine	––[d]	4.8

[a]RMS of all carbons.
[b]RMS of only the carbonyl carbons.
[c]RMS of all carbons, sp3 only, sp2 only, respectively, with the D95** basis set.
[d]No comparison made to isolated molecule due to nature of calculation.

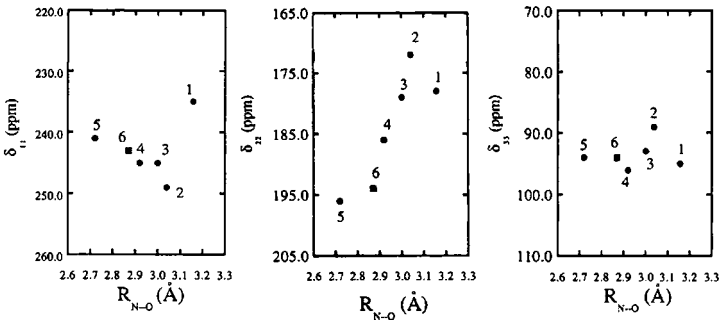

Fig. 16. Plots of the observed principal values of the carbonyl ^{13}C chemical shift tensors in peptides against the N···O hydrogen bond length in: (1) Ala-Pro-Gly · H_2O, (2) Ala-Ser, (3) Ala-Gly-Gly · H_2O, (4, 5) Ac-Ala-NHMe, and (6) $(Ala)_n$. (Reproduced with permission from ref. 131.)

done on the X-ray structure with optimized hydrogen atom positions. The RMS difference between the experimental and calculated ^{13}C shift components was improved from 6.47 ppm for the isolated molecule to 2.58 ppm in the EIM; as expected the majority of the improvement came in the carbonyl carbons involved in the HB.

4.2. $^{14}N/^{15}N$ examples

Many studies have shown that the nitrogen shieldings are very sensitive to their environment. This is not surprising because the high polarizability of the lone pair of electrons in nitrogen and the sensitivity of the nitrogen shielding to the electron density and energetics of this orbital. Nonetheless, the literature on nitrogen SSNMR is not as rich as the one for carbon, due to the great experimental difficulties presented by these nuclei.

4.2.1. *Study of phase transitions*

The five solid phases of NH_4NO_3[134] and the transitions between these phases were studied by a combination of ^{15}N MAS, with the spectra shown in Fig. 17, and static measurements of the nitrate nitrogen. Differences in all three tensor components were observed for the nitrate nitrogen in the different phases, with the lack of D_{3h} symmetry of this ion reflected in the non axially symmetric tensors. The difference between the two in-plane components (δ_{11} and δ_{22}) correlates with the differences in bond lengths of the unequal N-O bond lengths observed in the neutron diffraction data of the different phases, as shown in Table 3. In the case of the lowest temperature phase (*V*) the MAS clearly shows the presence of two inequivalent NO_3^- ions, as is indicated by the diffraction data. No calculations were performed in this study.

4.2.2. *Ionic compounds*

An exploration the effect of the change in the crystal environment on the NMR parameters of the ^{14}N, including the isotropic chemical shift (δ_{iso}) and the quadrupolar coupling constant (C_Q) and its associated asymmetry parameter (η_Q), of various ammonium and tetraalkylammonium salts was presented in a recent paper by Jakobsen *et al.*[135] The compounds studied included the following salts: CH_3NH_3Cl, $(NH_4)_2(COO)_2H_2O$, $(CH_3)_3(C_6H_5)NI$, $(CH_3)_3(C_6H_5CH_2)NCl$, $[(n\text{-}C_4H_9)_4N]_2Mo_2O_7$, $(NH_4)_2HPO_4$, and $NH_4H_2PO_4$, all of which have known crystal structures. While the variation in the isotropic chemical shift was relatively small, the quadrupolar parameters showed both a wide variety (C_Q varied from ~20 kHz to 1 MHz and the asymmetry parameter spanned nearly its entire range of 0–1). This great sensitivity to the crystalline environment allowed the authors to obtain two sets of parameters when there were multiple nitrogen sites in the asymmetric unit. No calculations were completed to analyze the variations observed.

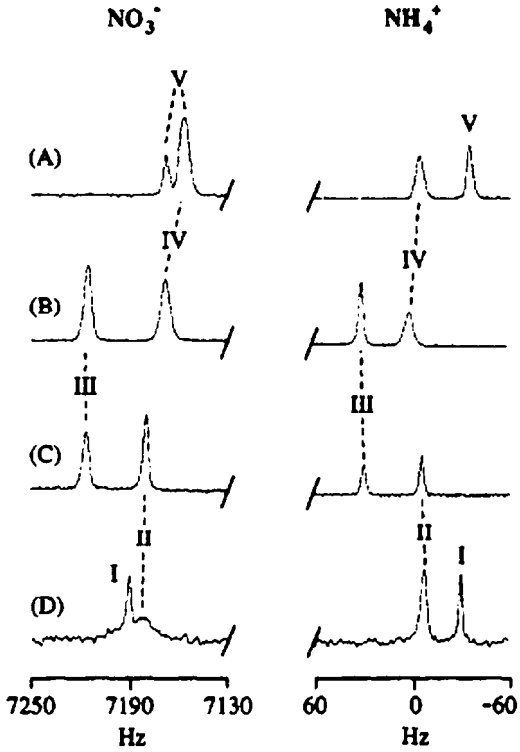

Fig. 17. CP/MAS spectra of NH_4NO_3 at each of the phase transition temperatures: (A) −40°C, (B) 36°C, (C) 83°C, and (D) 125°C. In the NO_3^- region of (A) the peak due to phase IV and one of the peaks due to phase V overlap. (Reproduced with permission from ref. 134.)

Table 3. Chemical shift data (ppm) and differences in the N-O bond lengths (Å) for the nitrate ion in the different phases of ammonium nitrate

Phase	δ_{MAS}	δ_{11}	δ_{22}	δ_{33}	$\Delta(\delta_{11}-\delta_{22})$	Δ(N-O)
V[a]	353.7, 353.1	442	414	204	28	0.032, 0.004
IV	353.4	441	410	210	31	0.046
III	355.8	432	423	211	9	0.003
II	354.1	434	417	219	17	0.027
I	354.5	354	354	354	0	0.0

[a]This phase has two molecules per asymmetric unit for which the nitrate resonances are resolved in the MAS, but for which only one set of tensor components were obtained in the static powder pattern.

4.2.3. *Tautomerism effects*

In nitrogen heterocycles, tautomerism via proton transfer often leads to averaging in solution just as molecular motion does in the anisole example presented earlier. There are a number of studies focused on the tautomeric process and on solid-state

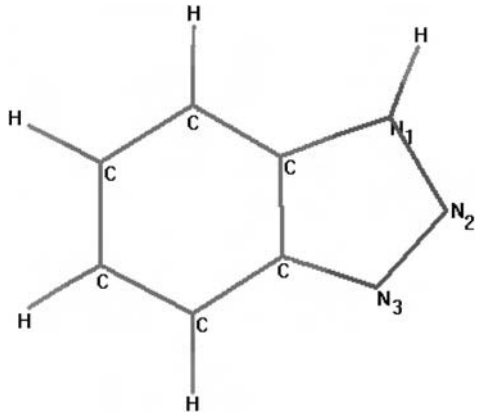

Fig. 18. Structure of benzotriazole.

Table 4. Comparison of solution and solid state ^{15}N chemical shifts of benzotriazole[a]

Solution				Solid state[b]	
	Acetone		Trifluoroacetic acid		
$N_{1,3}$	−102.0	$N_{1,3}$	−158.0	N_1	−157.6 (−157.4)
N_2	−10.3	N_2	−29.4	N_2	−11.8 (−9.4)
				N_3	−56.4 (−36.2)

[a]Chemical shifts in ppm relative to neat external nitromethane.
[b]Numbers in parenthesis are calculated chemical shifts using GIAO-CHF.

^{15}N chemical shifts of such systems as it relates to the form (e.g., protonation state) found in the solid state.[60,136,137] One such study by Weinch *et al.*[138] reports a comparison of the solution versus the solid state for a series of benzotriazole derivatives. The parent benzotriazole is shown in Fig. 18 and a comparison of the solution and solid-state chemical shifts for this molecule is in Table 4. This data clearly shows that in neutral solution the hydrogen is being exchanged between N_1 and N_3, whereas in the solid state it is found only on N_1. The data in trifluoroacetic acid reports the expected chemical shift when all of the nitrogens are protonated. The additional differences between the solution values and the average of the solid state can be attributed to weak intermolecular hydrogen bonds that can be seen from the X-ray diffraction structure.

4.2.4. *EIM treatment*

There have been several studies incorporating intermolecular effects using the EIM in the calculation of nitrogen NMR parameters. They include both the chemical shift tensor components and the quadrupolar coupling parameters. The first of

these studies was in a set of amino acids[129] that included L-asparagine monohydrate, L-histidine monohydrochloride monohydrate, γ glycine, α glycine, and L-alanine. Calculations were done on a single molecule, with the EIM, and for the L-histidine and L-asparagine with a combination EIM/cluster that explicitly treated the HB interactions by placing a cluster inside of the EIM charge array. It should be noted that the clusters used inside the EIM and the clusters used in the cluster model were not the same. In the cluster model truncation of the nearest neighbors is possible, whereas in the EIM this is not the case. Therefore, in the case of the cluster model ALL hydrogen bonds are included whereas in the case of the EIM/cluster calculations on L-histidine only the HB interactions of the C_α carbon sidechain were treated explicitly. The clusters used in the cluster model are shown in Fig. 19 and the results of all the calculations are displayed in Fig. 20.

In this study it was found that it was necessary to explicitly treat the strong HB in these compounds in order to get good agreement with experiment for the nitrogen shifts; this was not the case for the ^{13}C shielding in these same compounds where, as previously discussed, the EIM results are satisfactory. In this study the ^{14}N quadrupolar coupling constants were reported as the principal values (χ_{xx}, χ_{yy}, and χ_{zz}) of this tensor quantity; the results of their calculations are presented in Table 5. From Table 5 it is clear that the best results are obtained when neighboring molecules were explicitly treated in the cluster model or an EIM/cluster calculations (this group includes only $N^{\delta 2}$ of L-asparagine along with $N^{\delta 2}$ and $N^{\varepsilon 3}$ of L-histidine).

The above results using the cluster and EIM models for the calculation of the nitrogen shielding and quadrupolar parameters on amino acids can be compared with the same parameters calculated by Gervais *et al.*[130] on L-alanine and α glycine using full crystal methodology. A comparison of the two methods is given in Table 6. From these results it appears that both the cluster and the full crystal calculations reproduce both the chemical shifts and the experimental ^{14}N quadrupolar parameters, at least for these two compounds, better than either the single molecule or EIM calculations. This is an indication of the need to explicitly include strong HB interactions in the model being used.

4.2.5. *Hydrogen bonding*

Facelli *et al.*[139] showed that benzamide cluster calculations completed with models including HB drastically improved the agreement between experiment and theory. DFT calculations on an isolated molecule using a low temperature neutron diffraction structure had components that differed from the experiment by $-47, +19$, and -21 ppm for δ_{11}, δ_{22}, and δ_{33}, respectively. Using the neutron diffraction data to add the first neighbors of a benzamide molecule into the calculation reduced these differences to $-4, +10$, and $+4$ ppm. In these calculations the first neighbors were truncated by replacing the phenyl ring with a methyl group.

A similar study on the nucleic acid bases: adenine, cytosine, guanine, thymine, and uracil[140,141] also shows great sensitivity of the nitrogen tensor data to the inclusion of HB neighbors in the calculations. In several cases the more accurate calculations, those including HB, were a necessity in aiding in the assignment of the

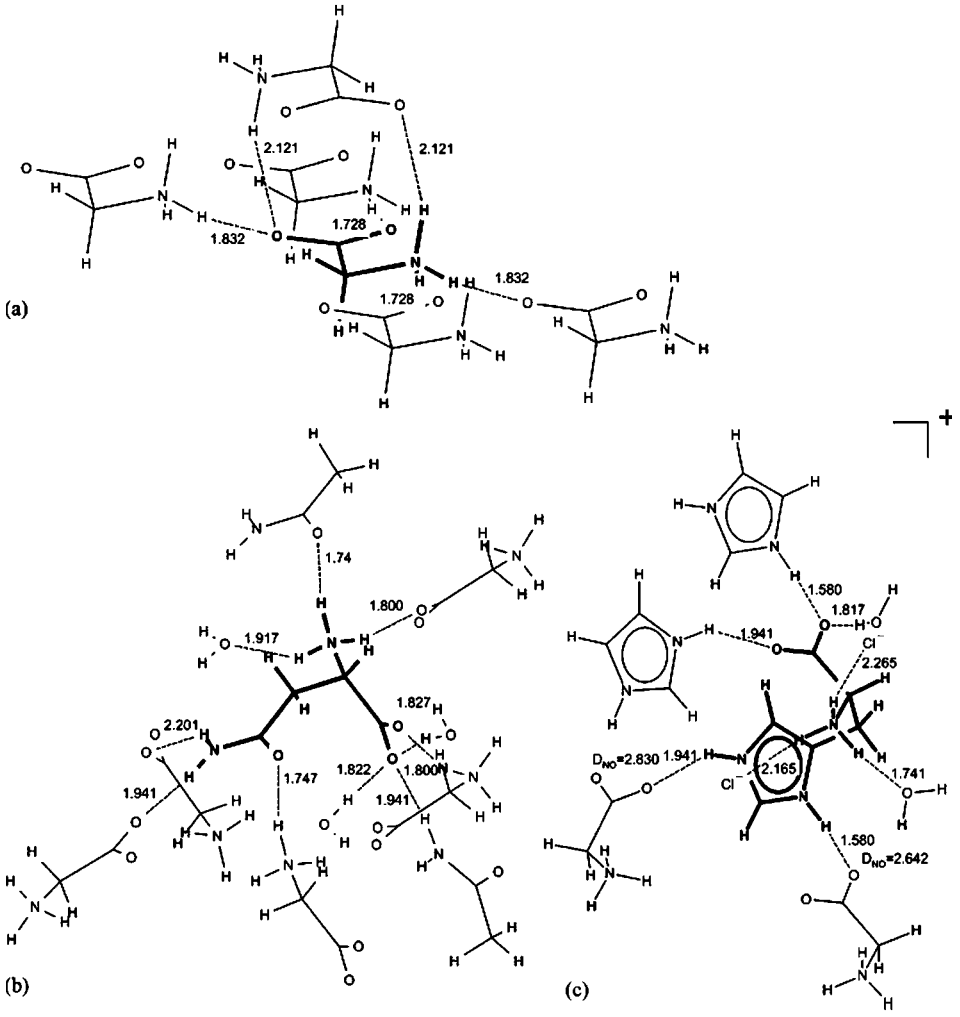

Fig. 19. Cluster used in the cluster calculations for (a) L-asparagine and (b) L-histidine. Hydrogen bonds are shown as dashed lines with distances given in Å. (Reproduced with permission from ref. 129.)

solid-state chemical shifts to specific nitrogens. Two models, both using molecular fragments of the nearest neighbors, were used to include the intermolecular interactions: model A in which the fragment's atoms, including the hydrogen atoms, were placed at the atomic positions of the X-ray diffraction structure, and model B in which the position of the hydrogen atoms were optimized before the chemical shift calculations. The fragments used in the models are shown in Fig. 21.

The RMS agreement between experiment and theory on the isolated molecules was 33.6 ppm; both models showed a substantial improvement, with the RMS of

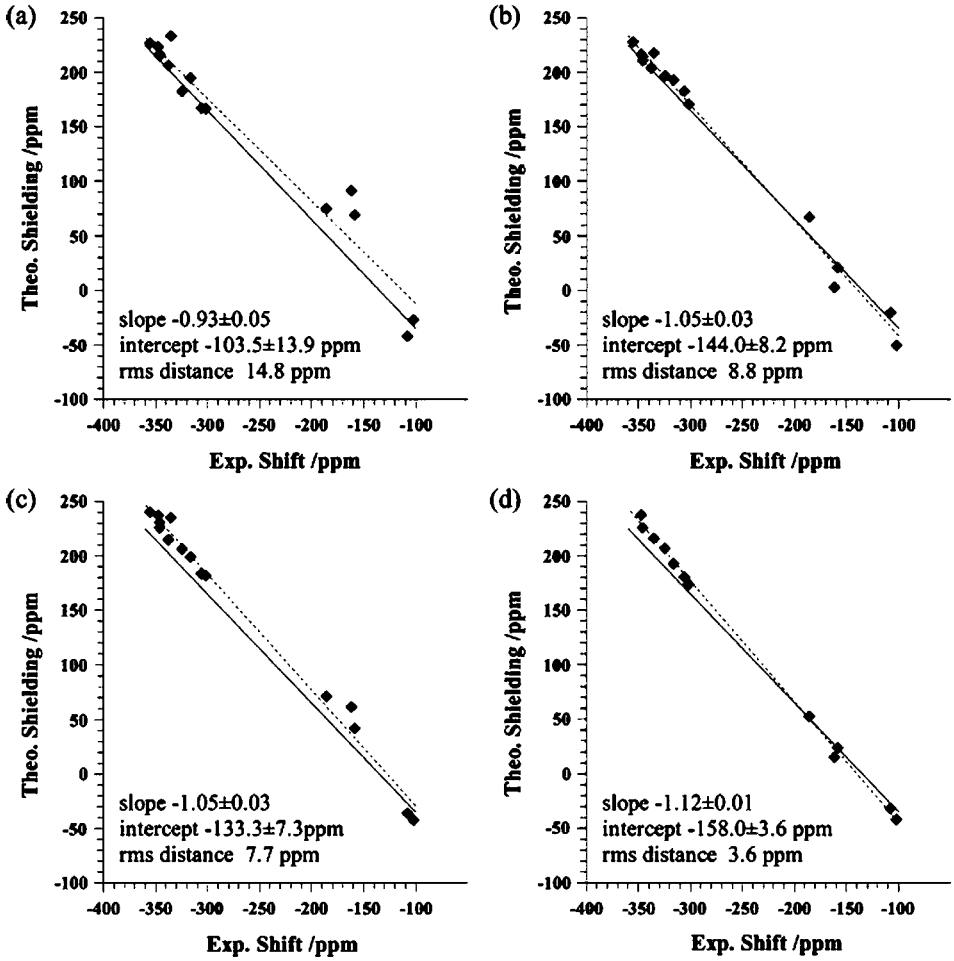

Fig. 20. Correlation between experimental ^{15}N tensor components and calculated shieldings for (a) isolated molecule, (b) cluster, (c) EIM, and (d) EIM/cluster. Solid lines indicate the expected correlations having a slope of −1 and an intercept of −135.8 ppm. All calculations done using B3LYP/D95**. (Reproduced with permission from ref. 129.)

model A calculated as 20.4 ppm and that of model B 16.6 ppm. Individual chemical shift components differed by as much as 54 ppm between calculations with and without intermolecular effects. It was found that there was only one nitrogen, N1 of adenine, which did not show any improvement in the calculations using the crystal model systems; this is not surprising as this is the only nitrogen having no HB interactions. The protonated nitrogens which act as proton donors, showed the largest effects in the δ_{22} component, the in-plane component that lies perpendicular to the N-H bond; this effect is always to a higher chemical shift, i.e., making the nucleus more deshielded. Smaller but still significant effects are observed in the

Table 5. Experimental and calculated QCC principal values (MHz)[a]

	Single molecule	Cluster	EIM	EIM/cluster	Experimental[b]
α Glycine					
N					
χ_{zz}	0.45	1.26	0.73		1.18
χ_{yy}	−0.35	−0.91	−0.48		−0.91
χ_{xx}	−0.10	−0.35	−0.25		−0.27
γ Glycine					
N					
χ_{zz}	0.51	0.96	0.66		1.24
χ_{yy}	−0.49	−0.63	−0.42		−0.80
χ_{xx}	−0.02	−0.33	−0.24		−0.44
L-Alanine					
N					
χ_{zz}	−0.57	1.08	0.66		1.21
χ_{yy}	0.48	−0.67	−0.44		−0.76
χ_{xx}	0.09	−0.41	−0.22		−0.45
L-Asparagine					
N					
χ_{zz}	0.46	1.16	0.77	0.77	1.15
χ_{yy}	−0.41	−0.94	−0.59	−0.53	−0.70
χ_{xx}	−0.05	−0.22	−0.18	−0.24	−0.45
$N^{\delta 2}$					
χ_{zz}	−4.71	−3.39	−3.61	−2.65	−2.68
χ_{yy}	2.46	2.24	2.32	1.72	1.78
χ_{xx}	2.25	1.16	1.28	0.93	0.90
L-Histidine					
N					
χ_{zz}	−0.45	1.69	0.95	0.93	1.15
χ_{yy}	0.35	−1.20	−0.71	−0.68	−0.69
χ_{xx}	0.09	−0.49	−0.24	−0.25	−0.47
$N^{\delta 1}$					
χ_{zz}	−2.57	1.92	−2.01	1.86	1.47
χ_{yy}	1.45	−1.40	1.55	−1.45	−0.93
χ_{xx}	1.12	−0.53	0.47	0.41	−0.54
$N^{\varepsilon 3}$					
χ_{zz}	−2.19	−2.21	−1.99	−1.82	−1.29
χ_{yy}	1.29	1.80	1.42	1.52	1.25
χ_{xx}	0.90	0.41	0.56	0.30	0.03

[a]The values are all from B3LYP/D95** calculations using NBO charges in the EIM; the original paper has results with other basis sets and with ChelpG charges used in the EIM.
[b]The reader is referred to original paper for references to the experimental data.

other two components. The nonprotonated nitrogens, which act as proton acceptors, have the δ_{11} component lying in the plane and perpendicular to the direction of the HB interaction; it is this component that shows the largest effect and the effect is to lower chemical shifts.

Table 6. Comparison of nitrogen NMR parameters in L-alanine and α glycine obtained by different methods

	Single molecule[a]	Cluster[a]	EIM[a]	Full crystal[b]	Experimental[a]
L-Alanine					
δ_{11}	−320.1	−327.9	−334.5	−329.3	
δ_{22}	−337.9	−340.3	−350.8	−340.5	
δ_{33}	−353.2	−349.3	−370.7	−350.4	
δ_{iso}	−337.1	−339.2	−352.0	−340.1	−337.1
χ_{zz}	−0.57	1.08	0.66	1.25	1.21
χ_{yy}	0.48	−0.67	−0.44	−0.79	−0.76
χ_{xx}	0.09	−0.41	−0.22	−0.46	−0.45
α Glycine					
δ_{11}	−341.5	−338.9	−350.0	−330.5	−337.6
δ_{22}	−351.8	−349.6	−366.1	−350.1	−346.0
δ_{33}	−361.9	−363.0	−375.2	−355.2	−355.4
δ_{iso}	−351.7	−350.5		−345.3	−346.3
χ_{zz}	0.45	1.26	0.73	1.28	1.18
χ_{yy}	−0.35	−0.91	−0.48	−0.98	−0.91
χ_{xx}	−0.10	−0.35	−0.25	−0.30	−0.27

[a]Results all with B3LYP/D95** from ref. 129.
[b]Results from ref. 130.

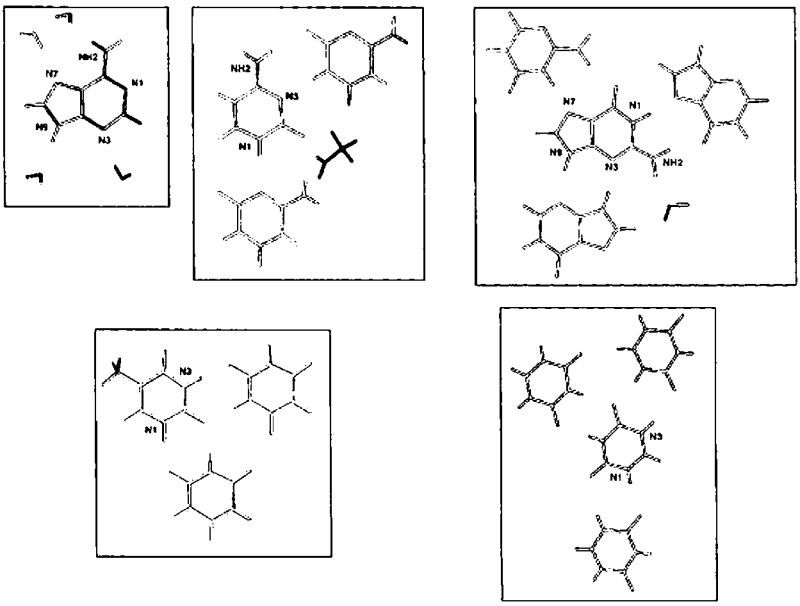

Fig. 21. Models used to simulate intermolecular interactions in: adenine (UL), cytosine (UC), guanine (UR), thymine (LL), and uracil (LR). (Reproduced with permission from ref. 140.)

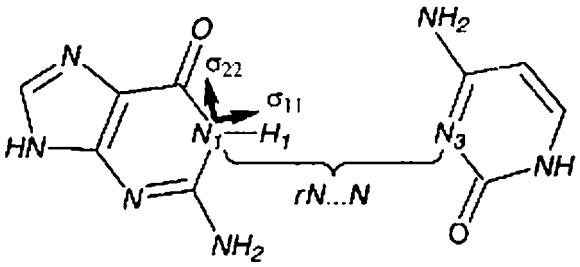

Fig. 22. Model of the guanine-cytosine (GC) base pair showing the definition of the N···N separation and the orientation of the N_1 chemical shielding tensor. The σ_{33} component is perpendicular to the plane of the page. (Reproduced with permission from ref. 142.)

Table 7. Changes in the nitrogen shielding tensor components of the imino nitrogen due to the formation of a hydrogen bonded base pair given as the difference between the shielding at the equilibrium N···N separation and the isolated base

Base pair	$\Delta\sigma_{11}$	$\Delta\sigma_{22}$	$\Delta\sigma_{33}$	$\Delta\sigma_{iso}$
AT	−12.9	−55.0	33.2	11.6
AU	−13.8	−55.4	33.0	12.1
GC	−10.6	−33.4	27.6	5.5

Czernek[142] completed a theoretical study of the changes in the ^{15}N tensors of the imino N (protonated) of the nucleic bases of cytosine and adenine, which act as HB donors with in Watson–Crick base pair, as a function of the length of the hydrogen bond. This length was measured by the N···N separation of the two nitrogens involved. An example of the guanine-cytosine (GC) base pair is given in Fig. 22; calculations were also completed on the adenine-thymine (AT) and the adenine-uracil (AU) base pairs. The changes at the equilibrium separation relative to the isolated molecule are shown in Table 7. The differences are in agreement with the effects of HB in the nucleic acid bases discussed above.

4.2.6. *EIM study of nucleosides*

Stueber and Grant[75] report both the ^{13}C and ^{15}N chemical shift tensors for the nucleosides adenosine, guanosine dihydrate, 2′-deoxythymidine, and cytosine, all of which demonstrate strong intermolecular HB. As with previous EIM studies, the ^{15}N tensor components show a significant improvement when the lattice effects are included; the RMS for structures with optimized hydrogen atom positions is improved from 24.3 to 12.6 ppm when the EIM charge array is added to the calculation.

This study also explores the sensitivity of the results to the hydrogen positions for adenosine, for which there is a neutron diffraction structure. The agreement

between the experimental and calculated ^{15}N chemical shift principal values shows an improvement when the neutron structure is used: for an isolated molecule the RMS is decreased to 15.3 ppm and for the EIM the RMS is 7.9 ppm. This improvement can be traced back to the more accurate determination of the location of the hydrogen atoms and is indicative of how sensitive the NMR shielding is to the hydrogen positions. A comparison of the X-H, for X = C, N, or O, bond lengths in this compound shows a difference of ~0.14 Å between those from the X-ray and neutron diffraction structures. The difference between the bond lengths from the neutron diffraction structure and those from the optimized structures in an isolated molecule are ~0.02 Å for bonds to N or O and 0.005 Å for bonds to C. For the case where the hydrogen positions are optimized within the EIM generated charge array the difference relative to the neutron diffraction distances for the O-H and N-H bond lengths decreases even more to ~0.01 Å.

4.2.7. *EIM study of β-HMX*

Finally, even in the absence of any strong electrostatic or bonding interactions, it has been shown that inclusion of the crystal environment can lead to an improvement in the calculated ^{15}N shift tensor components. This is the case in β-HMX, shown in Fig. 23, where a study of the crystal structure indicates the presence of two intermolecular Coulombic interactions.[143]

Clawson *et al.*[96] has completed a study of the ^{15}N chemical shift tensors in β-HMX, including calculations on a single molecule, a cluster containing the two significant Coulombic interactions, and two EIM calculations, one with a single molecule and one with the cluster. Using B3LYP/6-311G**, the RMS was 17 ppm on the isolated molecule, 11 ppm on the cluster, and 7 ppm for both of the EIM calculations. The improvement was largest in the in-plane components, with a large

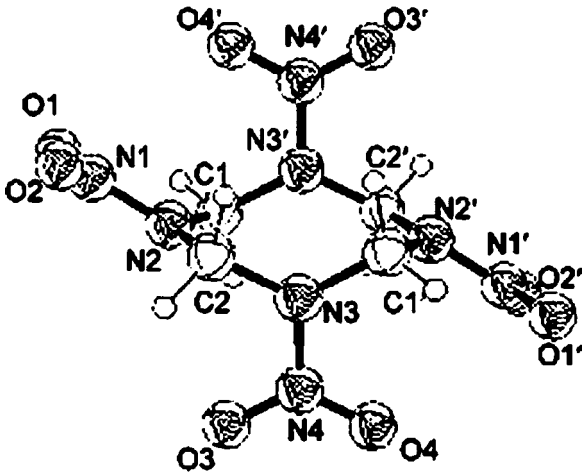

Fig. 23. Neutron diffraction structure of β-HMX. (Reproduced with permission from ref. 96.)

decrease in the chemical shift observed for the components that are perpendicular to the N-N bond for both nitrogens (the δ_{22} for the nitrate and the δ_{11} for the amine). Finally, the agreement between the EIM and cluster results provides further confirmation on the electrostatic nature of the intermolecular interactions in β-HMX.

4.3. ^{1}H examples

In recent years there have been significant advances in high resolution ^{1}H SSNMR which have made possible the study of the intermolecular interactions that affect the ^{1}H chemical shifts in greater detail. In general two main interactions have attracted most of the work in ^{1}H studies: the effects of the hydrogen bonds and the stacking effects due to intermolecular magnetic effects or also commonly named ring current effects. This review provides several examples of both types of effects.

4.3.1. *Hydrogen bonding*

The importance of HB on the proton chemical shifts was reported as early as 1979 by Rhim's study on single crystals of water.[144] The powder pattern spectrum and the single crystal spectrum for one particular orientation are given in Fig. 24, which shows clearly that there is only one ^{1}H chemical shift tensor in hexagonal ice and that the hydrogen bond interactions are responsible for its very large anisotropy, 28.5 ppm.

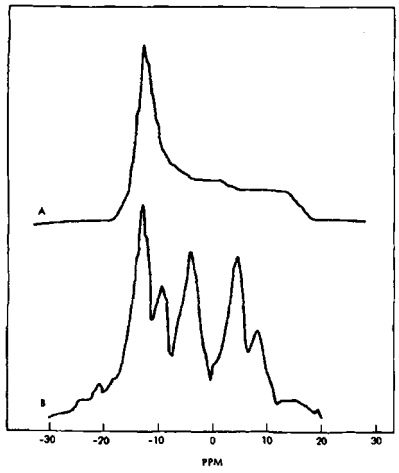

Fig. 24. (A) Anisotropic chemical shift spectrum of polycrystalline ice at liquid nitrogen temperature. (B) Anisotropic chemical shift pattern of a single crystal of hexagonal ice at certain crystal orientation at liquid nitrogen temperature. (Reproduced with permission from ref. 144.)

More recent computational studies in water,[101] using the cluster method, have demonstrated that modern computational calculations of water clusters are able to reproduce the experimental solid-state effects. The calculated anisotropy of the ^{1}H shielding tensor is 15.71 ppm for an isolated water molecule, 26.99 ppm in the dimer, 30.92 ppm in the trimer, and finally reaches a limit value of ~34.83 ppm for a cluster of 17 water molecules. The calculated values in these clusters agreed well with the experimental ones for ice that range from 28.5 to 34.2 ppm. It is noteworthy that the HB effect on the ^{1}H shielding tensor is highly anisotropic. While the shielding component along the O-H bond is almost constant, 41.36 ppm for the single molecule and 46.91 ppm for the 17 molecule cluster, the components perpendicular to the O-H bond move from 24.77 and 26.54 ppm in the isolated molecule to 11.97 and 12.19 ppm, respectively, in the 17 water molecule cluster.

Wu *et al.*[145] have studied the dependence of the ^{1}H shielding tensor components in a series of crystalline hydrates. The experimental results in Fig. 25 show the high sensitivity of the shielding components with the O···H hydrogen bond distances.

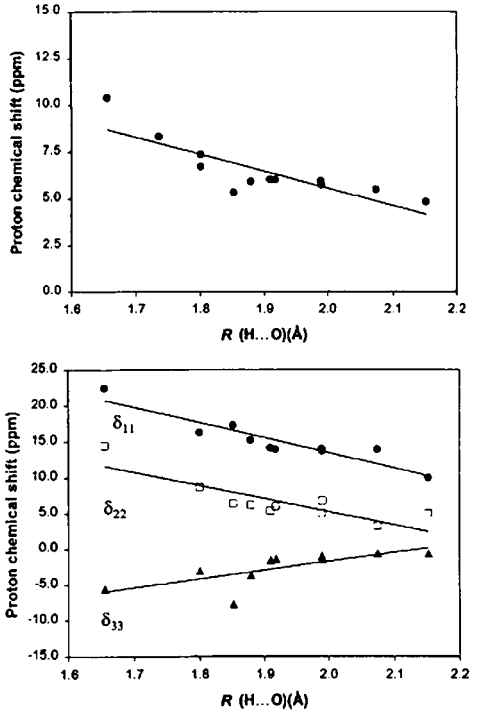

Fig. 25. Plot of the isotropic ^{1}H chemical shift (top) versus hydrogen bond length, the correlation coefficient is 0.8411. Individual shielding tensor components (bottom) versus hydrogen bond length for the flipping water molecules in hydrates. The correlation coefficients for δ_{11}, δ_{22}, and δ_{33} are 0.9256, 0.8392, and 0.7254, respectively. (Reproduced with permission from ref. 145.)

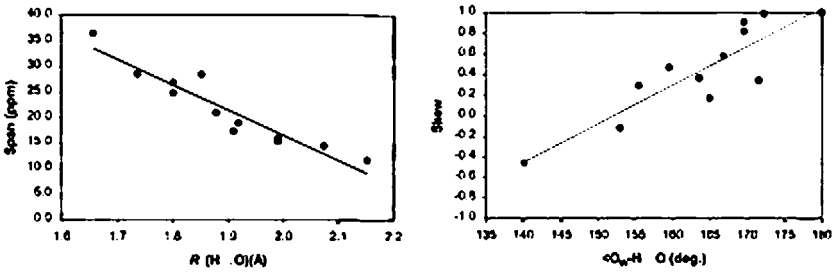

Fig. 26. Plot of span and skew of the chemical shift tensor versus hydrogen bond length for the stationary water molecules in hydrates. The correlation coefficients are 0.9469 and 0.9261 for the span and skew, respectively. (Reproduced with permission from ref. 145.)

The anisotropic character and structure dependence of the HB effects on the ^{1}H shielding are even more apparent for ^{1}H shielding tensor components in the molecular frame, which have been derived from the experimental components using a two site jump model. As depicted in Fig. 26, the span of the shielding tensor in water hydrates shows an excellent correlation with the length of the O···H hydrogen bond, while the skew of the tensor correlates well with O-H···O angle.

Harris *et al.*[146] presented a comparative study of the SSNMR in the white and yellow polymorphic forms of methylnitroacetaniline (MNA) using a combination of SSNMR and computations to determine the position of the hydrogen atoms in the crystal structures. These determinations are possible due to the high sensitivity of the ^{1}H chemical shifts to the crystal packing. While the previous examples show that the principal components of the shielding tensors are more sensitive that the isotropic values, it is apparent from Fig. 27 that even the easily measured isotropic MAS spectra is able to clearly differentiate between the two common polymorphs of MNA.

An extensive study of the hydrogen bond effects on bulk chemical shifts using first principle calculations with full PBC has been presented by Sebastiani *et al.*[147] The same computational approach, but using a very large periodic cell with only one molecule in the simulation cell produces reasonable estimates of the molecular shielding. While the comparison of these two calculations give a good estimate of the intermolecular effects on the shielding, the calculations using full PBC are not able to distinguish between the different types of intermolecular effects, as they are, in principle, exact calculations including all possible intra- and intermolecular interactions that the define the NMR shielding in the solid. Calculations were reported for L-alanine, L-tyrosine, L-histidine · HCl · H_2O, and L-adenine · HCl · H_2O using both X-ray diffraction and optimized geometries. All the calculations reported in this work used CPMD,[114] using the BLYP exchange correlation functional[148] with Goedecker-type of pseudopotentials[149] and with cutoffs ranging between 70 and 90 Ry. For the molecular calculations the supercells were selected such that the minimum distance between atoms in neighboring cells was 5 Å. The results of these studies are depicted in Figs. 28–30.

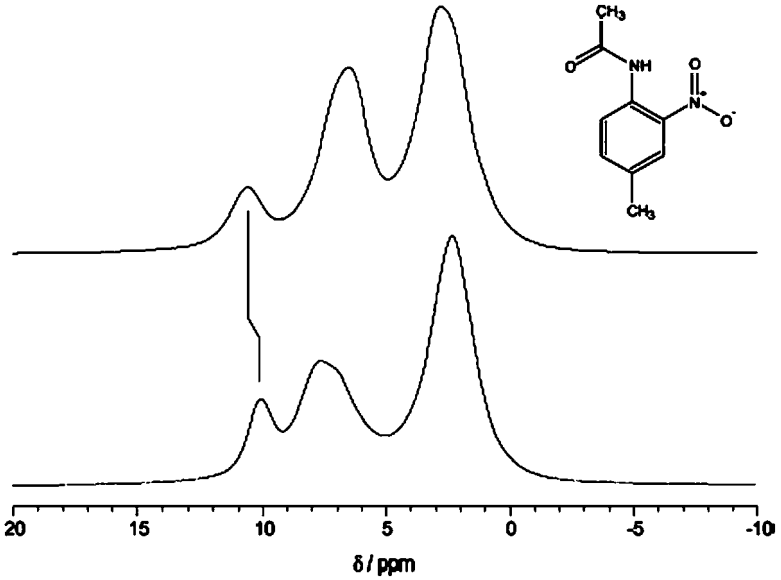

Fig. 27. Proton fast MAS SSNMR spectra of MNA; top: white form, bottom: yellow form. Upper right: molecular structure. (Reproduced with permission from ref. 146.)

4.3.2. *Molecular magnetic susceptibility effects*

Ring current effects[150] have been used to explain the chemical shifts of proton in polycyclic aromatic compounds for many years, but recently several groups have been able to measure these effects in solids using a combination of proton SSNMR and quantum chemical computations.[30,31,65,66,151]

As discussed above in the theory and ^{13}C sections, these effects are of magnetic origin and their magnitude is independent of the nuclei. While they are noticeable in the ^{13}C chemical shifts, they become extremely important for ^{1}H shielding as they can reach a significant fraction of the total spectral range. These large effects are depicted in the spectra of hexa-*n*-dodecyl-hexa-*peri*-hexabenzocoronene (HBC-C_{12}, Fig. 31) in Fig. 32.

Comparison of the liquid spectra (d) with the liquid crystal and solid phase spectra clearly show a significant shielding of the aromatic proton, with a shift from 8.2 ppm in the liquid to 6.2 ppm in the liquid crystal and solid phase. This remarkable shift of almost 20% the normal proton chemical shift scale has been attributed to ring current effects due to the stacking of the HBC-C_{12} molecules.

Quantum chemical calculations using different methods and models[30,65] provide a solid theoretical justification for the explanation of this intermolecular effect based on molecular magnetic susceptibility or ring current effects. Fig. 33 depicts the results from Ochsenfeld *et al.*[30] in a model system of two hexabenzocoronene molecules with varying inter-planar distances, which provide the quantitative basis

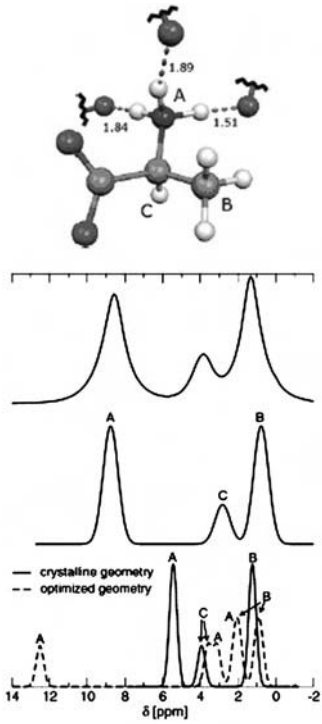

Fig. 28. Structure of L-alanine, where the NH···O hydrogen bond distances are in Å and the proton labels corresponds to the lines denoted in the simulated spectra for L-alanine in the condensed phase. The bottom spectrum corresponds to the spectrum of the isolated molecule with the crystal and optimized geometries, the middle to the computed spectrum using full periodic boundary conditions and the top is the experimental spectrum. In the computed spectra the CH_3 and NH_3 shifts have been averaged. (Reproduced with permission from ref. 147.)

for using the molecular susceptibility as the physical mechanism to explain the observed solid state.

4.4. ^{17}O examples

The observed and calculated intermolecular effects in ^{17}O chemical shifts are almost exclusively due to hydrogen bond interactions. A significant amount of experimental and theoretical work has been devoted to understanding the origins of these effects and to the development of empirical relationships between hydrogen bond structural parameters and ^{17}O shielding tensor components. As a consequence of the quadrupolar nature of the ^{17}O nuclei most studies of oxygen SSNMR provide additional information on the quadrupolar parameters, which are also affected by intermolecular interactions in general and by HB in most of the cases reported in the literature.

Gervais *et al.*[130] have reported the SSNMR of ^{17}O labeled amino acids. In this study the ^{17}O NMR parameters, chemical shifts, and quadrupolar constants were

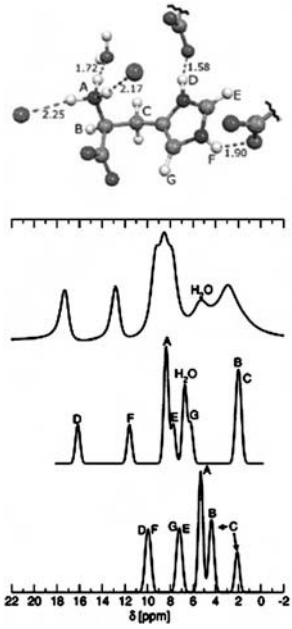

Fig. 29. Structure of L-histidine · HCl · H_2O, where the NH···O hydrogen bond distances are in Å and the proton labels corresponds to the lines denoted in the simulated spectra in the condensed phase. The bottom spectrum corresponds to the spectrum of the isolated molecule with the crystal and optimized geometries, the middle to the computed spectrum using full periodic boundary conditions and the top is the experimental spectrum. (Reproduced with permission from ref. 147.)

measured using several SSNMR techniques, MAS, DOR, and multiple quantum experiments, in order to resolve all of the nonequivalent resonances in the spectra. The calculations were performed using full PBC in the DFT approximation as implemented in the PARATEC code.[50] The calculated results show excellent agreement with the experimental values, as depicted in Table 8. However as only the calculations in the crystalline system have been reported it is not possible to quantitatively assess the importance of the intermolecular contributions to the ^{17}O shielding and quadrupolar constants.

Using the data in Table 8 and the experimental geometries of these amino acids it is possible to establish the relationships between the NMR parameters and characteristic bond lengths among the atoms involved in the HB interactions. These relationships are presented in Fig. 34 for the calculated principal components of the ^{17}O chemical shielding tensor. It is worth noting that the relative small dependence of the isotropic chemical shifts with the C═O···H-N bond length arrives from a significant cancellation between the larger effects on the principal components of the tensor.

In a similar study Yates *et al.*[56] have presented a similar relationship for a series of glutamic acid polymorphs. These correlations are presented in Fig. 35.

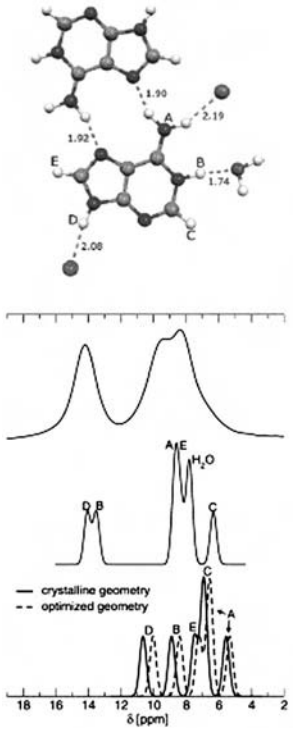

Fig. 30. Structure of L-adenine · HCl · H_2O, where the NH···O hydrogen bond distances are in Å and the proton labels corresponds to the lines denoted in the simulated spectra for L-adenine · HCl · H_2O in the condensed phase. The bottom spectrum corresponds to the spectrum of the isolated molecule with the crystal and optimized geometries, the middle to the computed spectrum using full periodic boundary conditions and the top is the experimental spectrum. (Reproduced with permission from ref. 147.)

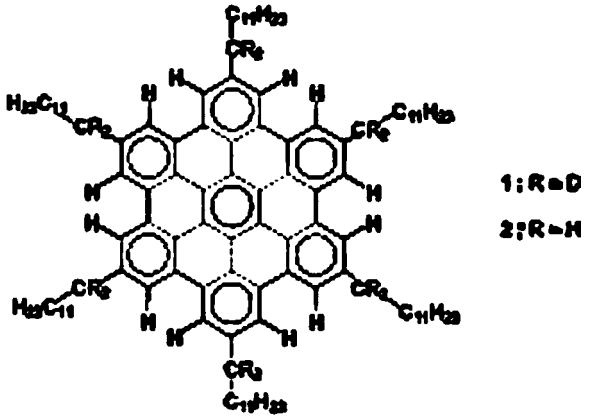

Fig. 31. Molecular schema of hexa-*n*-dodecyl-hexa-*peri*-hexabenzocoronene (HBC-C_{12}). (Reproduced with permission from ref. 151.)

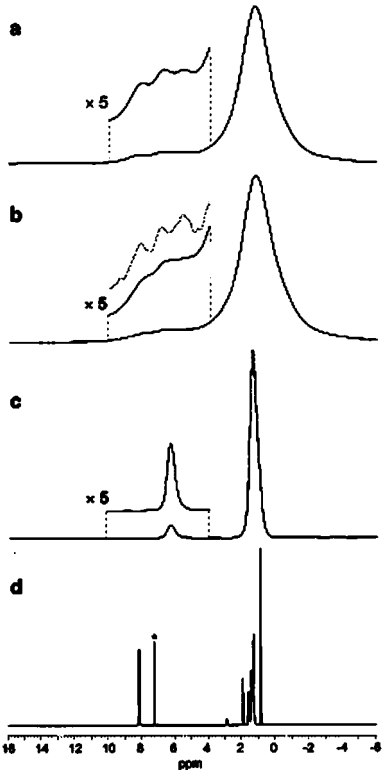

Fig. 32. One dimensional ^{1}H spectra of (a, c, d) α-deuterated and (b) fully protonated HBC-C_{12} (see schema in Fig. 31) in different physical states, namely: (a, b) crystalline phase at 333 K, (c) liquid crystal phase at 383 K, and (d) dissolved in deuterated chloroform. Spectra a–c were recorded under MAS at 35 kHz. The dashed line in spectrum (b) shows the enhanced resolution achieved by a data processing method. The asterisk in spectrum d indicates the signal due to residual $CHCl_3$. (Reproduced with permission from ref. 151.)

Wu *et al.*[152] have studied the influence of the N-H···O and C-H···O hydrogen bonds on the ^{17}O NMR tensors in crystalline uracil using the cluster model. These calculations were performed using the Gaussian suite of programs[81] with the B3LYP exchange correlation functional and with different basis sets. In all the calculations the positions of the hydrogen atoms were optimized prior to the NMR calculations. The cluster structures and atom numbering used in this study are depicted in Fig. 36.

From Figs. 37 and 38 the importance of including intermolecular interactions in the calculations of the ^{17}O NMR constants is apparent. The results clearly show that excellent agreement is achieved when the full cluster is included in the calculations. Unfortunately, this convergence is not monotonic and for several shielding components good agreement can also be observed for smaller clusters. As discussed earlier, this is a critical drawback of the cluster calculations, there are

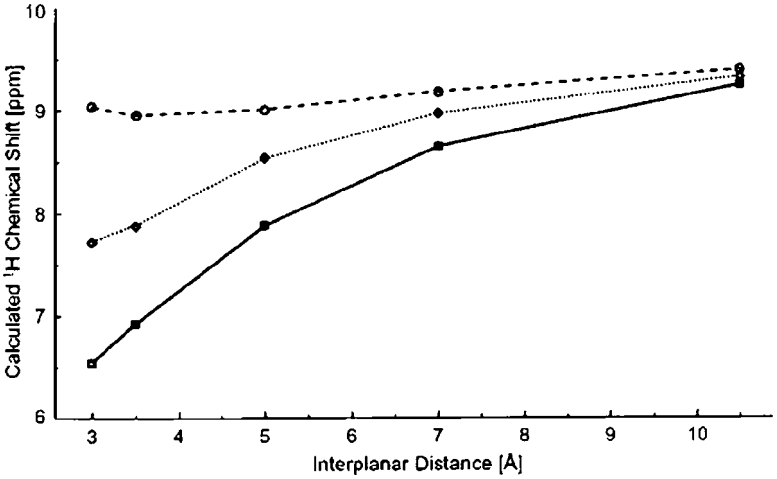

Fig. 33. Dependence of the calculated ^{1}H NMR shifts at the GIAO-HF/SVP level on the inter-plane distance for model structures. (Reproduced with permission from ref. 30.)

Table 8. Experimental and calculated ^{17}O isotropic chemical shift values, C_Q and η_Q parameters for several amino acids[130]

	Site	δ_{iso} (ppm)		C_Q (MHz)		η_Q	
		Exp.	Calc.	Exp.	Calc.	Exp.	Calc.
L-Alanine	O1	284.0	292.3	7.86	8.20	0.28	0.29
	O2	260.5	274.4	6.53	6.90	0.70	0.67
L-Alanine · HCl	O1	327.8	322.2	8.31	8.24	0.0	0.05
	O2	176.7	181.9	7.29	7.89	0.20	0.21
L-Valine · HCl	O1	351.0	338.7	8.40	8.67	0.03	0.04
	O2	181.0	181.3	7.35	7.68	0.21	0.24
Glycine · HCl	O1	333.0	331.2	8.40	8.62	0.0	0.00
	O2	178.0	181.3	7.60	7.77	0.25	0.25
L-Tyrosine · HCl	O1	327.0	319.3	8.22	8.47	0.0	0.01
	O2	183.0	185.7	7.35	7.46	0.19	0.20
	O3	83.0	90.5	8.56	8.60	0.65	0.8

no universal rules on how to build them and as shown here even agreement with the experimental values may be misleading in determining which neighboring molecules should be included in the calculations.

The results reported in urea[153] by the same research group further substantiates the findings in uracil. The urea results are depicted in Fig. 39, where the number of hydrogen bonds used in the *x*-axis represents the number of neighboring molecules

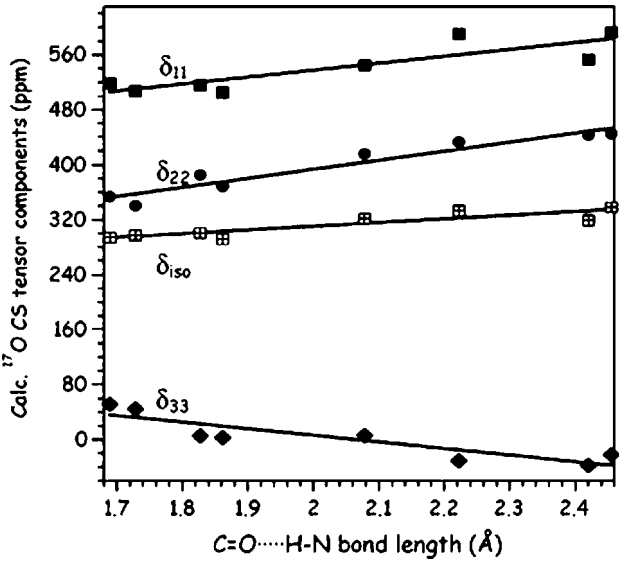

Fig. 34. Calculated ^{17}O chemical shielding principal components versus C═O···N-H hydrogen bond length for amino acids. (Reproduced with permission from ref. 130.)

included in the cluster calculations. In this case a monotonic convergence with the size of the cluster used in the calculations is observed.

Wu *et al.*[154] also studied in great detail the ^{17}O SSNMR of nucleic acid bases using site-specific enriched compounds. Extensive quantum mechanical calculations at the B3LYP/6-311 + + G(d,p) level were used to provide a better understanding of the intermolecular effects observed. To take into account these effects, the researchers used the cluster model based on the X-ray diffraction structures of these compounds with additional quantum chemical optimizations to determine the hydrogen positions. The cluster models used in the quantum mechanical calculation involved only the first neighbors linked to the central molecule by hydrogen bond interactions. From Fig. 40 the reader can get a sense of how important the solid-state effects are in these compounds. These results of this study[154] also confirm the well established observation that large changes in the chemical shielding principal values do not necessary imply large changes in their relative orientation in the molecular frame.

4.5. ^{31}P examples

The literature of solid-state effects on ^{31}P shielding is not as large as that of the previously discussed nuclei. Perhaps the fact that phosphorous does not form strong HB and that its electronic structure is less polarizable than nitrogen has

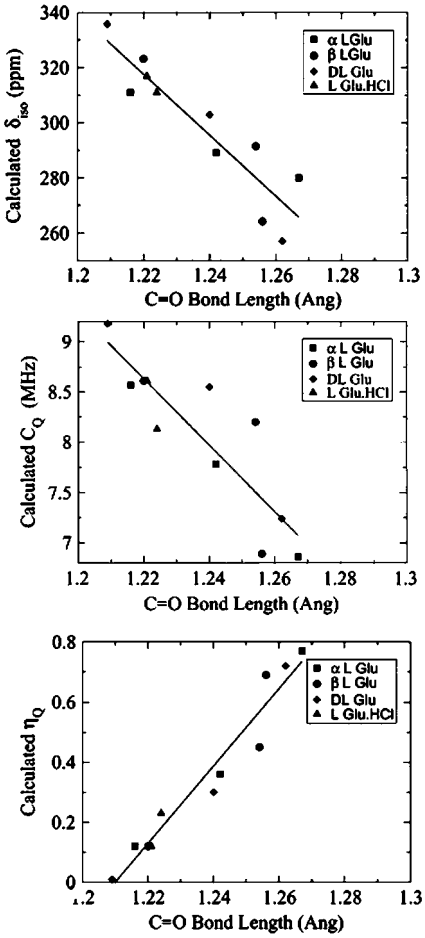

Fig. 35. Graphs (from top to bottom) of the calculated ^{17}O isotropic chemical shielding, the magnitude of the ^{17}O quadrupolar constant and the ^{17}O electric field tensor anisotropy as a function of the C═O bond length. (Reproduced with permission from ref. 56.)

limited the observation of the solid-state effects on the ^{31}P chemical shielding. Schneider *et al.*[71] used ^{31}P experimental chemical shift data in P_4S_3 to test the Crystal Potential Derived Point Charge (CPPCh) method to take into account the intermolecular effects. The results of this study would indicate that the solid-state effects on this compound are mostly indirect effects. The RMS between the experimental chemical shift principal values[155] and those calculated using the optimized molecular geometry (BLYP/6-31G**) is 58.5 ppm, but when using the experimental neutron diffraction geometry the RMS decreases to 28.9 ppm. The inclusion of the intermolecular interactions via the CPPCh charges does not improve the agreement with the experimental shielding values any further; in fact

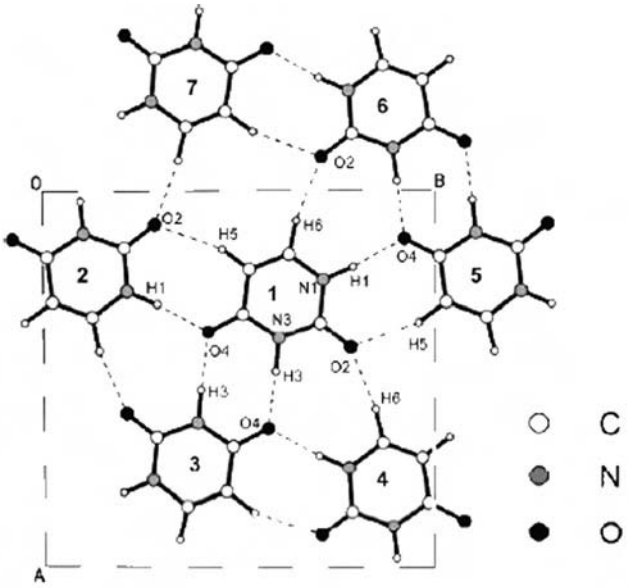

Fig. 36. Atomic numbering and hydrogen bonding network in crystalline uracil. (Reproduced with permission from ref. 152.)

the results using the CPPCh and Grid[70] methods show slightly higher RMS of 31.0 and 30.1 ppm, respectively.

The results in P_4S_3 appear not to be universal. The calculated ^{31}P chemical shifts in *O*-phosphoserine, *O*-phosphothreonine, and *O*-phosphotyrosine show significantly better agreement when a cluster model is used in the calculations.[156] This may be attributed to the existence of HB interactions in these compounds. These calculations were done using the B3LYP/6-311 + + G** level, for the isolated molecule, an electrostatic model and a cluster model. In all cases the calculations were based on the X-ray diffraction structures. The results in *O*-phosphoserine show that for this compound the point charge methods completely fail in reproducing the experimental data. As depicted in Fig. 41, this is not the case for the cluster model that shows a substantial improvement in the agreement between the calculated and experimental ^{31}P chemical shifts in the solid state.

The results reported in phosphonates and bisphosphonates are quite the opposite of the two previous cases.[157] As shown in Fig. 42 the shielding values calculated using charge lattice model introduced by Oldfield (CPF)[33] show a significant improved agreement with the experimental values, when compared with the results obtained for the isolated molecule.

Finally ^{31}P SSNMR spectroscopy has been used to illustrate the effect of sample grinding in SSNMR.[26] A sample of silver nitrate triphenylphosphine was subject to several grinding treatments; the MAS spectra depicted in Fig. 43 shows how

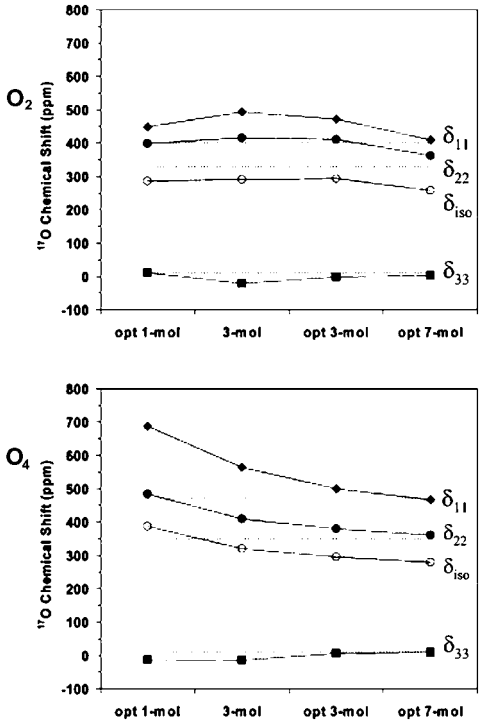

Fig. 37. Calculated (symbols) and experimental (dotted lines) ^{17}O chemical shielding tensors principal components for O_2 and O_4 (see Fig. 35) using different molecular models. All calculations are at the B3LYP/6-311 + + G(d,p) level. (Reproduced with permission from ref. 152.)

sensitive the spectra is to the grinding procedure used before taking the SSNMR spectra. It is remarkable that not only the line widths are significantly[158] affected by the grinding,[159] but also the position of the spectral lines. The grinding effect has been attributed to mechanically or thermally induced phase transitions in silver nitrate triphenylphosphine. Similar behaviors due to grinding and/or heating due to high speed spinning have been observed in poly(L-alanine).[159,160] These examples shows how sensitive SSNMR can be to the different packing arrangements possible in solids and promise its great value in providing a better understanding of polymorphic behaviors of crystalline materials.

4.6. ^{19}F examples

Limited studies have been reported on the solid-state effects on the shielding of ^{19}F; most are computational in nature. For example, Auguspurger and Dykstra[64] used

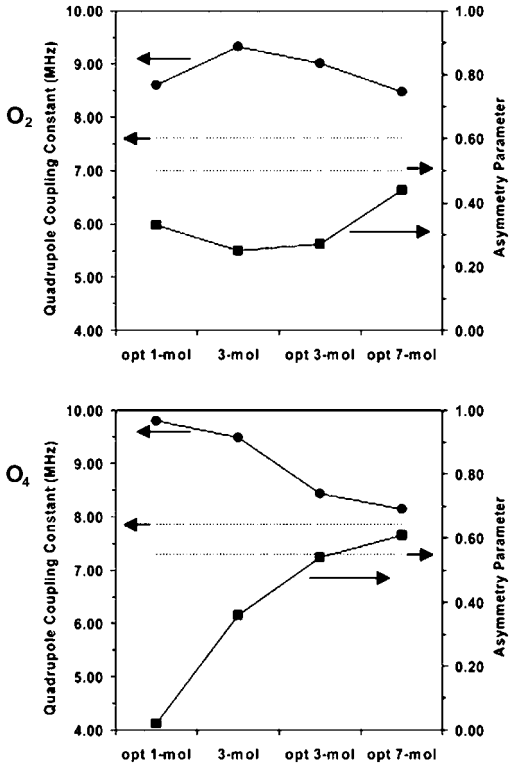

Fig. 38. Calculated (symbols) and experimental (dotted lines) ^{17}O quadrupole coupling constant and asymmetry parameter for O_2 and O_4 (see Fig. 35) using different molecular models. All calculations are at the B3LYP/6-311 + + G(d,p) level. (Reproduced with permission from ref. 152.)

the charge filed perturbation (CFP) approach[161] to provide a rational explanation for the different ^{19}F chemical shifts observed in equivalent bonding environments in proteins. They showed that nonequivalence effects associated with common nearby dipoles of small molecules can be as large as 20 ppm. de Dios and Oldfield[33] compared a point charge treatment with cluster calculations in a study of the ^{19}F chemical shielding in a series of clusters of fluorobenzene and $(HF)_x$. The results show an excellent correlation between the full cluster calculations, an additive cluster approach and the electrostatic treatment. This indicates that, at least in these systems, the intermolecular contributions to the ^{19}F shielding are additive and electrostatic in nature. This is the same conclusion that can be obtained from the study presented by Solis *et al.*[73] which shows that the intermolecular effects on the ^{19}F shielding in *o*-F-benzoic acid, *p*-F-benzoic acid, tetra-fluoro-1,4-benzoquinone, and 5-F-uracil calculated with the GRID and the SCREEP electrostatic approaches agree with those calculated using the cluster method. Finally, Body *et al.*[162]

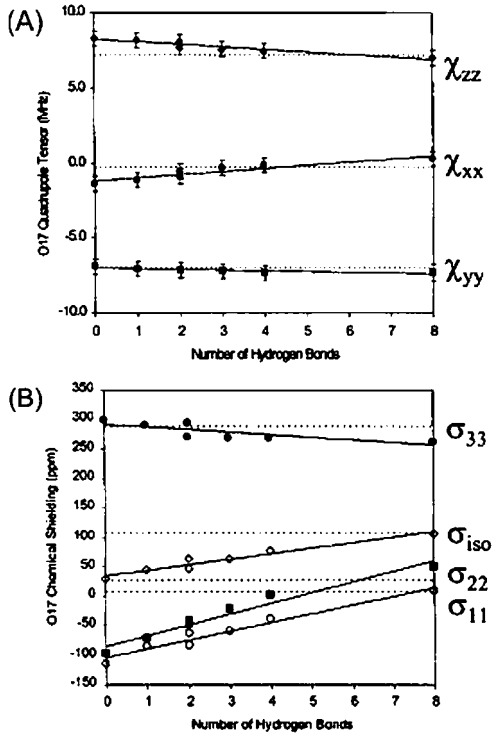

Fig. 39. (A) Calculated (B3LYP/6-311 + + G**) ^{17}O quadrupole coupling tensors in urea for different models with increasing number of hydrogen bonds. The error bars indicates the uncertainty arising from the Q calibration. (B) Calculated (B3LYP/6-311 + + G**) ^{17}O chemical shielding tensor principal values for different models with increasing number of hydrogen bonds. The dashed lines in both cases indicate the experimental values. (Reproduced with permission from ref. 153.)

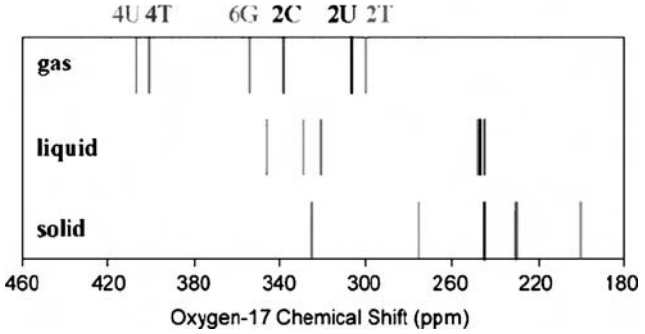

Fig. 40. The relationship between ^{17}O chemical shifts in gas, liquid and solid states. The gas-phase data are calculated results for single molecules fully optimized at the B3LYP/6-311G(d,p) level of theory. The liquid phase values are experimental data results in DMSO solutions and the solid-state values were determined by MAS. Chemical shifts are referenced to liquid H_2O. (Reproduced with permission from ref. 154.)

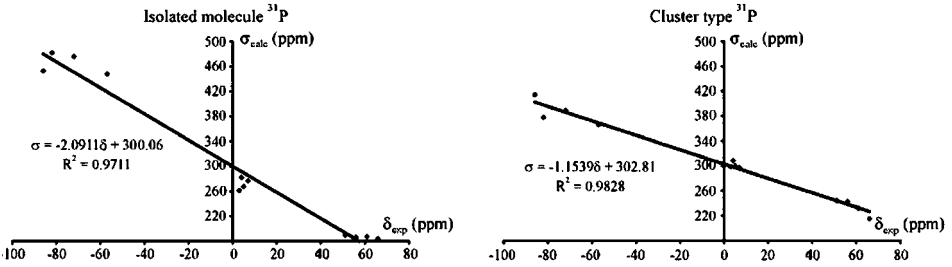

Fig. 41. Calculated shielding parameters versus experimental chemical shifts of the ^{31}P nuclei of *O*-phosphoserine, *O*-phosphothreonine, and *O*-phosphotyrosine (both conformers) as isolated molecules or as part of the hydrogen bonded cluster. (Reproduced with permission from ref. 156.)

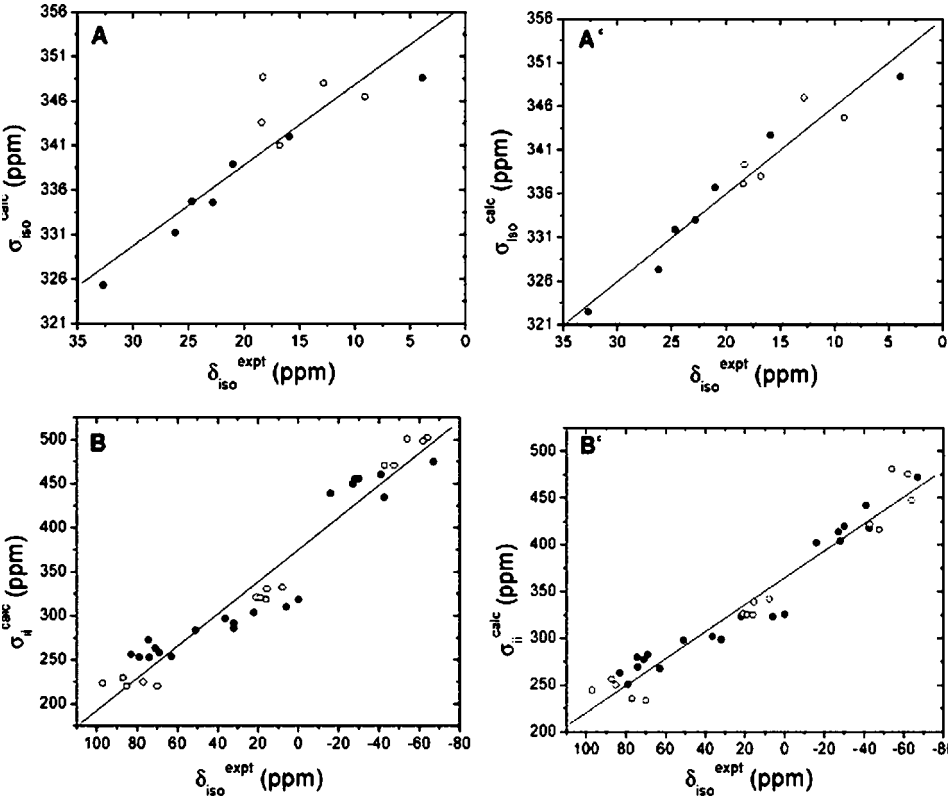

Fig. 42. Experimental versus computed ^{31}P shielding and chemical shifts, respectively for phosphonates and bisphosphonates. A and B correspond to the calculations using the isolated molecule model and A′ and B′ to the charge lattice model calculations. The solid and open circles denote the neutral and charges species respectively. (Reproduced with permission from ref. 157.)

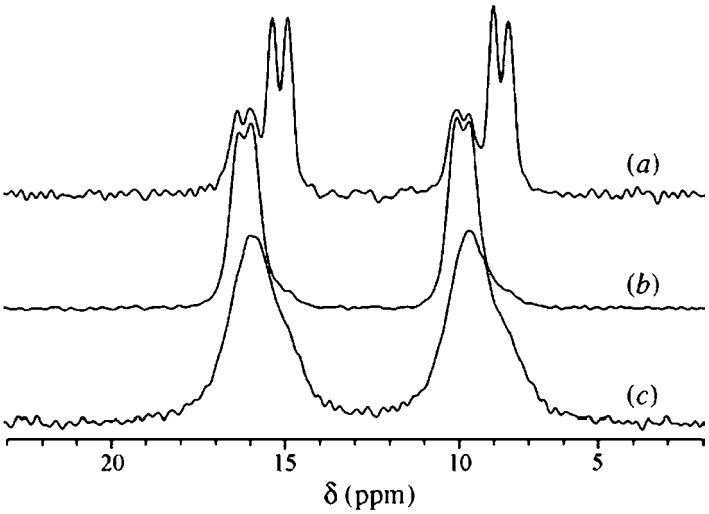

Fig. 43. Effect of sample grinding on the SSNMR ^{31}P spectra of $AgNO_3 \cdot PPh_3$. Trace (a) is obtained from a sample that was packed into a rotor without grinding; trace (b) is from a sample that was not subject to intense grinding; and trace (c) is obtained from a sample following intense grinding for 90 sec. All spectra were acquired at room temperature with CP at $\upsilon_{rot} = 3.0\,kHz$ and $B_0 = 4.70\,T$. (Reproduced with permission from ref. 26.)

demonstrated that in the case of inorganic fluorides it is necessary to use appropriate cluster models to reproduce ^{19}F chemical shielding using quantum chemical methods. As discussed in the theory section is quite difficult to decide on the composition of a representative cluster for ionic solids. The work of Body *et al.*[162] represents one of the first attempts to establish a systematic procedure to select cluster models for inorganic fluorides.

5. CONCLUDING REMARKS

This review presents a detailed description of the different physical mechanisms that lead to changes, with respect to the liquid state, in the observed chemical shifts measured by SSNMR. The review also presents a comprehensive discussion of the theoretical methods available to include intermolecular effects so that calculations reproduce the changes in the chemical shifts observed when going from the liquid to the solid state. The literature review clearly shows that the available methods are able to predict chemical shifts in solids with great accuracy, to the point that it is possible to use the chemical shifts to complement diffraction techniques for crystal and molecular structure elucidation. The review also presents selected examples of observations and calculations of solid-state effects on the shielding of several nuclei. The results of these case studies clearly establish the importance of considering

intermolecular effects when analyzing SSNMR. Also, the importance of studying, when possible, full shielding tensors or at least their principal values is highlighted in several of the examples that show the increase sensitivity to intermolecular effects of the tensor components relative to the isotropic values.

ACKNOWLEDGMENTS

Support from the National Science Foundation, The National Institutes of Health and the Office of Science of the Department of Energy, all of which have provided funding for the SSNMR program at Utah over the years, is acknowledged. Also acknowledged are discussions with the members of Professor David M. Grant's research group, which have greatly contributed to enhance our understanding of SSNMR.

REFERENCES

1. R. K. Harris, *Solid State Sci.*, 2004, **6**, 1025.
2. J. C. Facelli and D. M. Grant, *Nature*, 1993, **365**, 325.
3. A. C. de Dios, J. G. Pearson and E. Oldfield, *Science*, 1993, **260**, 1491.
4. J. K. Harper, J. C. Facelli, D. H. Barich, G. McGeorge, A. E. Mulgrew and D. M. Grant, *J. Am. Chem. Soc.*, 2002, **124**, 10589.
5. J. K. Harper and D. M. Grant, *J. Am. Chem. Soc.*, 2000, **122**, 3708.
6. J. K. Harper, G. McGeorge and D. M. Grant, *Magn. Reson. Chem.*, 1998, **36**, S135.
7. J. K. Harper, G. McGeorge and D. M. Grant, *J. Am. Chem. Soc.*, 1999, **121**, 6488.
8. J. K. Harper and D. M. Grant, *Cryst. Growth Design*, 2006, **6**, 2315.
9. C. A. Hunter, M. J. Packer and C. Zonta, *Prog. Nucl. Magn. Reson. Spectrosc.*, 2005, **47**, 27.
10. C. J. Jameson, D. N. Sears and A. C. de Dios, *J. Chem. Phys.*, 2003, **118**, 2575.
11. D. M. Grant, *Encyclopedia of Nuclear Magnetic Resonance*, Wiley, London, 1996, p.1298.
12. R. K. Harris, *Nuclear Magnetic Resonance Spectroscopy: A Physiochemical View*, Pitman, Toronto, 1983.
13. C. P. Slichter, *Principles of Magnetic Resonance*, Springer-Verlag, New York, 1992.
14. D. W. Alderman, G. McGeorge, J. Z. Hu, R. J. Pugmire and D. M. Grant, *Mol. Phys.*, 1998, **95**, 1113.
15. O. N. Antzutkin, S. C. Shekar and M. H. Levitt, *J. Magn. Reson. A*, 1995, **115**, 7.
16. T. H. Sefzik, D. Turco, R. J. Iuliucci and J. C. Facelli, *J. Phys. Chem. A*, 2005, **109**, 1180.
17. T. H. Sefzik, J. M. Fidler, R. J. Iuliucci and J. C. Facelli, *Magn. Reson. Chem.*, 2006, **44**, 390.
18. J. C. Facelli, A. M. Orendt, Y. J. Jiang, R. J. Pugmire and D. M. Grant, *J. Phys. Chem.*, 1996, **100**, 8268.
19. M. H. Sherwood, J. C. Facelli, D. W. Alderman and D. M. Grant, *J. Am. Chem. Soc.*, 1991, **113**, 750.
20. T. L. Threlfall, *Analyst*, 1995, **120**, 2435.
21. H. G. Brittain, *J. Pharm. Sci.*, 1997, **86**, 405.
22. R. K. Harris, *Analyst*, 2006, **131**, 351.
23. S. Byrn, R. R. Pfeiffer and J. G. Stowell, *Solid-State Chemistry of Drugs*, SSCI, Inc., West Lafayette, IN, 1999.
24. J. Smith, E. MacNamara, D. Raftery, T. Borchardt and S. Byrn, *J. Am. Chem. Soc.*, 1998, **120**, 11710.
25. P. A. Tishmack, D. E. Bugay and S. R. Byrn, *J Pharm. Sci.*, 2003, **92**, 441.

26. S. -W. Oh, G. M. Bernard, R. E. Wasylishen, R. McDonald and M. J. Ferguson, *Can. J. Chem.*, 2005, **83**, 1721.
27. G. A. Jeffrey, *An Introduction to Hydrogen Bonding*, Oxford University Press, New York, 1997.
28. E. Brunner and U. Sternberg, *Prog. Nucl. Magn. Reson. Spectrosc.*, 1998, **32**, 21.
29. D. A. Case, *Curr. Opin. Struct. Biol.*, 1998, **8**, 624.
30. C. Ochsenfeld, S. P. Brown, I. Schnell, J. Gauss and H. W. Spiess, *J. Am. Chem. Soc.*, 2001, **123**, 2597.
31. Z. Ma, M. D. Halling, M. S. Solum, J. K. Harper, A. M. Orendt, J. C. Facelli, R. J. Pugmire, D. M. Grant, A. W. Amick and L. T. Scott, *J. Phys. Chem. B*, 2007, **111**, 2020.
32. J. D. Augspurger, C. E. Dykstra, E. Oldfield, J. G. Pearson, *Intra- and Intermolecular Electrical Effects on Nuclear Magnetic Resonance, Nuclear Quadrupole Resonance and Infra-Red pectroscopic Parameters from Ab Initio Calculation and Experiment: From CO to Proteins*, J. A. Tossel, ed., NATO ASI series C, Vol. 386, Kluwer Academic Publisher, Boston, MA, 1993.
33. A. C. de Dios and E. Oldfield, *Chem. Phys. Lett.*, 1993, **205**, 108.
34. A. C. de Dios and E. Oldfield, *Solid State Nucl. Magn. Reson.*, 1996, **6**, 101.
35. H. Jiao, P. von Ragué Schleyer, B. R. Beno, K. N. Houk and R. Warmuth, *Angew. Chem. Int. Ed. Engl.*, 1998, **36**, 2761.
36. E. D. Jemmis, A. G. Subramanian, A. J. Kos and P. von Ragué Schleyer, *J. Am. Chem. Soc.*, 1997, **119**, 9504.
37. P. von Ragué Schleyer, C. Maerker, A. Dransfeld, H. Jiao and N. J. R. van Eikema Hommes, *J. Am. Chem. Soc.*, 1996, **118**, 6317.
38. J. C. Facelli, *Magn. Reson. Chem.*, 2006, **44**, 401.
39. D. Sebastiani, *Modern Phys. Lett. B*, 2003, **17**, 1301.
40. D. Sebastiani, *Chem. Phys. Chem.*, 2006, **7**, 164.
41. D. Sebastiani, G. Goward, I. Schnell and M. Parrinello, *Comput. Phys. Commun.*, 2002, **147**, 707.
42. D. Sebastiani, G. Goward, I. Schnell and H. W. Spiess, *J. Mol. Struct. (Theochem.)*, 2003, **625**, 283.
43. D. Sebastiani and M. Parrinello, *J. Phys. Chem. A*, 2001, **105**, 1951.
44. D. Sebastiani and U. Rothlisberger, *J. Phys. Chem. B*, 2004, **108**, 2807.
45. M. Benoit, M. Profeta, F. Mauri, C. J. Pickard and M. E. Tuckerman, *J. Phys. Chem. B*, 2005, **109**, 6052.
46. F. Buda, P. Giannozzi and F. Mauri, *J. Phys. Chem. B*, 2000, **104**, 9048.
47. C. Gervais, M. Profeta, F. Babonneau, C. J. Pickard and F. Mauri, *J. Phys. Chem. B*, 2004, **108**, 13249.
48. C. Gervais, M. Profeta, V. Lafond, C. Bonhomme, T. Azais, H. Mutin, C. J. Pickard, F. Mauri and F. Babonneau, *Magn. Reson. Chem.*, 2004, **42**, 445.
49. T. Gregor, F. Mauri and R. Car, *J. Chem. Phys.*, 1999, **111**, 1815.
50. F. Mauri, B. G. Pfrommer and S. G. Louie, *Phys. Rev. Lett.*, 1996, **77**, 5300.
51. B. G. Pfrommer, F. Mauri and S. G. Louie, *J. Am. Chem. Soc.*, 2000, **122**, 123.
52. C. J. Pickard and F. Mauri, *Phys. Rev. B*, 2001, **63**, 245101.
53. M. Profeta, M. Benoit, F. Mauri and C. J. Pickard, *J. Am. Chem. Soc.*, 2004, **126**, 12628.
54. S. Rossano, F. Mauri, C. J. Pickard and I. Farnan, *J. Phys. Chem. B*, 2005, **109**, 7245.
55. J. R. Yates, S. E. Dobbins, C. J. Pickard, F. Mauri, P. Y. Ghi and R. K. Harris, *Phys. Chem. Chem. Phys.*, 2005, **7**, 1402.
56. J. R. Yates, C. J. Pickard, M. C. Payne, R. Dupree, M. Profeta and F. Mauri, *J. Phys. Chem. A*, 2004, **108**, 6032.
57. J. R. Yates, T. N. Pham, C. J. Pickard, F. Mauri, A. M. Amado, A. M. Gilad and S. P. Brown, *J. Am Chem. Soc.*, 2005, **127**, 10216.
58. J. R. Yates, C. J. Pickard, M. C. Payne and F. Mauri, *J. Chem. Phys.*, 2003, **118**, 5746.
59. W. T. Raynes, A. D. Buckingham and H. J. Bernstein, *J. Chem. Phys.*, 1962, **36**, 3481.
60. J. C. Facelli, A. C. De Dios, eds., *Modeling NMR Chemical Shifts: Gaining Insights into Structure and Environment*, 2447, ACS Symposium Series, No 732, Washington DC, 1999.
61. J. D. Augspurger and C. E. Dykstra, *J. Phys. Chem.*, 1991, **95**, 9230.
62. J. D. Augspurger, C. E. Dykstra and E. Oldfield, *J. Am. Chem. Soc.*, 1991, **113**, 2447.

63. A. C. de Dios and E. M. Earle, *J. Phys. Chem. A*, 1997, **101**, 8132.
64. J. D. Augspurger and C. E. Dykstra, *J. Am. Chem. Soc.*, 1993, **115**, 12016.
65. C. Ochsenfeld, *Phys. Chem. Chem. Phys.*, 2000, **2**, 2153.
66. C. Ochsenfeld, F. Koziol, S. P. Brown, T. Schaller, U. P. Seelbach and F. -G. Klarner, *Solid State Nucl. Magn. Reson.*, 2002, **22**, 128.
67. H. Jiao and P. von Ragué Schleyer, *Angew. Chem. Int. Ed.*, 1996, **35**, 2383.
68. G. Merino, T. Heine and G. Seifert, *Chem. Eur. J.*, 2004, **10**, 4367.
69. H. -b. Le, J. G. Pearson, A. C. de Dios and E. Oldfield, *J. Am. Chem. Soc.*, 1995, **117**, 3800.
70. M. B. Ferraro, V. Repetto and J. C. Facelli, *Solid State Nucl. Magn. Reson.*, 1998, **10**, 185.
71. D. M. Schneider, M. C. Caputo, M. B. Ferraro and J. C. Facelli, *Int. J. Mol. Sci. [online computer file]*, 2000, **1**, 75.
72. D. Solis and M. B. Ferraro, *Theor. Chem. Acc.*, 2000, **104**, 323.
73. D. Solis, M. B. Ferraro and J. C. Facelli, *J. Mol. Struct.*, 2002, **602–603**, 159.
74. D. Stueber, F. N. Guenneau and D. M. Grant, *J. Chem. Phys.*, 2001, **114**, 9236.
75. D. Stueber and D. M. Grant, *J. Am. Chem. Soc.*, 2002, **124**, 10539.
76. J. C. Facelli, *Handbook of Modern NMR*, Kluwer Academic Publishers, London, 2007.
77. A. Bagno, F. Rastrelli and G. Saielli, *Prog. Nucl. Magn. Reson. Spectrosc.*, 2005, **47**, 41.
78. M. Strohmeier, D. Stueber and D. M. Grant, *J. Phys. Chem. A*, 2003, **107**, 7629.
79. P. Pulay and J. F. Hinton, *Encyclopedia of Nuclear Magnetic Resonance*, Wiley, London, 1996, p. 4334.
80. K. Wolinski, J. F. Hinton and P. Pulay, *J. Am. Chem. Soc.*, 1990, **112**, 8251.
81. M. J. Frisch, G. W. Trucks, H. B. Schlegel, *et. al., Gaussian 03*, Gaussian, Inc., Wallington, CT, 2003.
82. A. C. de Dios, D. D. Laws and E. Oldfield, *J. Am. Chem. Soc.*, 1994, **116**, 7784.
83. J. Wang, R. M. Wolf, J. W. Caldwell, P. A. Kollman and D. A. Case, *J. Comp. Chem.*, 2004, **25**, 1157.
84. Q. Cui and M. Karplus, *J. Phys. Chem. B*, 2000, **104**, 3721.
85. B. R. Brooks, R. E. Bruccoleri, B. D. Olafson, D. J. States, S. Swaminathan and M. Karplus, *J. Comp. Chem.*, 1983, **4**, 187.
86. A. D. MacKerell, B. Brooks, C. L. Brooks III, L. Nilsson, B. Roux, Y. Won and M. Karplus, *The Encyclopedia of Computational Chemistry*, Wiley, Chichester, 1998, p. 271.
87. M. A. Spackman, *J. Comp. Chem.*, 1996, **17**, 1.
88. J. G. Angyan and C. Chipot, *Int. J. Quantum Chem.*, 1994, **52**, 17.
89. E. V. Stefanovich and T. N. Truong, *J. Chem. Phys. B*, 1998, **102**, 3018.
90. J. D. Jackson, *Classical Electrodynamics*, 2nd ed., Wiley, New York, 1975.
91. J. L. Pascual-Ahuir and E. Silla, *J. Comp. Chem.*, 1990, **11**, 1047.
92. L. E. Chirlian and M. M. Francl, *J. Comp. Chem.*, 1987, **8**, 894.
93. D. Stueber, A. M. Orendt, J. C. Facelli, R. W. Parry and D. M. Grant, *Solid State Nucl. Magn. Reson.*, 2002, **22**, 29.
94. D. H. Barich, J. S. Clawson, D. Stueber, M. Strohmeier, R. J. Pugmire and D. M. Grant, *J. Phys. Chem. A*, 2002, **106**, 11375.
95. D. Stueber and D. M. Grant, *Solid State Nucl. Magn. Reson.*, 2002, **22**, 439.
96. J. S. Clawson, M. Strohmeier, D. Stueber, A. M. Orendt, D. H. Barich, B. Asay, M. A. Hiskey, R. J. Pugmire and D. M. Grant, *J. Phys. Chem. A*, 2002, **106**, 6352.
97. S. E. Derenzo, M. K. Klintenberg and M. J. Weber, *J. Chem. Phys.*, 2000, **112**, 2074.
98. M. Klintenberg, S. E. Derenzo and M. J. Weber, *Comput. Phys. Commun.*, 2000, **131**, 120.
99. P. Ewald, *Ann. Phys.*, 1921, **64**, 253.
100. N. di Fiori, A. M. Orendt, M. C. Caputo, M. B. Ferraro and J. C. Facelli, *Magn. Reson. Chem.*, 2004, **42**, S41.
101. J. F. Hinton, P. Guthrie, P. Pulay and K. Wolinski, *J. Am. Chem. Soc.*, 1992, **114**, 1604.
102. J. C. Facelli, *Encyclopedia of Nuclear Magnetic Resonance*, Wiley, London, 1996, p. 4299.
103. J. C. Facelli, *Encyclopedia of Nuclear Magnetic Resonance*, Wiley, London, 1996, p. 4327.
104. J. C. Facelli, *Concepts Magn. Reson.*, 2004, **20A**, 42.

105. A. M. Orendt, J. C. Facelli and D. M. Grant, *Chem. Phys. Lett.*, 1999, **302**, 499.
106. D. B. Chesnut, *Ann. Rep. NMR Spectrosc.*, 1994, **29**, 71.
107. D. B. Chesnut, *Reviews in Computational Chemistry*, vol. 8, VCH Publishers, New York, 1996, p. 245.
108. A. E. Tonelli, D. B. Chesnut and P. M. Gross, *Macromolecules*, 1996, **29**, 2537.
109. S. F. Boys and F. Bernardi, *Mol. Phys.*, 1970, **19**, 553.
110. P. B. Karadakov and K. Morokuma, *Chem. Phys. Lett.*, 2000, **317**, 589.
111. G. A. Rickard, P. B. Karadakov, G. A. Webb and K. Morokuma, *J. Phys. Chem. A*, 2003, **107**, 292.
112. A. Zheng, M. Yang, Y. Yue, C. Ye and F. Deng, *Chem. Phys. Lett.*, 2004, **399**, 172.
113. H. Kurosu and I. Ando, *J. Mol. Struct. (Theochem.)*, 1991, **77**, 231.
114. M. Parrinello and W. Andreoni, CPMD V3.9, http://www.cpmd.org/. Copyright IBM Corp 1990–2006, Copyright MPI fuer Festkoerperforschung Stuttgart, 1997–2001.
115. G. R. Desiraju and A. Gavezzotti, *J. Chem. Soc., Chem. Commun.*, 1989, 621.
116. J. C. Facelli, J. Z. Hu, A. M. Orendt, A. M. Arif, R. J. Pugmire and D. M. Grant, *J. Phys. Chem.*, 1994, **98**, 12186.
117. D. Farcasiu, D. Hancu and J. F. Haw, *J. Phys. Chem. A*, 1998, **102**, 2493.
118. J. B. Nicholas, T. Xu, D. H. Barich, P. D. Torres and J. F. Haw, *J. Am. Chem. Soc.*, 1996, **118**, 4202.
119. J. K. Harper, A. M. Arif and D. M. Grant, *Acta Cryst. C*, 2000, **56**, 451.
120. M. Strohmeier, A. M. Orendt, D. W. Alderman and D. M. Grant, *J. Am. Chem. Soc.*, 2001, **123**, 1713.
121. J. R. Smith, W. Xu and D. Raftery, *J. Phys. Chem. B*, 2006, **110**, 7766.
122. S. Chen, H. Xi and L. Yu, *J. Am. Chem. Soc.*, 2005, **127**, 17439.
123. R. K. Harris, P. Y. Ghi, R. B. Hammond, C. Y. Ma, K. J. Roberts, J. R. Yates and C. J. Pickard, *Magn. Reson. Chem.*, 2006, **44**, 325.
124. R. K. Harris, P. Y. Ghi, H. Puschmann, D. C. Applerly, U. J. Griesser, R. B. Hammond, C. Y. Ma, K. J. Roberts, G. J. Pearce, J. R. Yates and C. J. Pickard, *Org. Process Res. Dev.*, 2005, **9**, 902.
125. R. K. Harris, S. A. Joyce, C. J. Pickard, S. Cadars and L. Emsley, *Phys. Chem. Chem. Phys.*, 2006, **8**, 137.
126. Z. Gu, R. Zambrano and A. McDermott, *J. Am. Chem. Soc.*, 1994, **116**, 6368.
127. J. C. Facelli, Z. Gu and A. McDermott, *Mol. Phys.*, 1995, **86**, 865.
128. G. Zheng, L. Wang, J. Hu, X. Zhang, L. Shen, C. Ye and G. A. Webb, *Magn. Reson. Chem.*, 1997, **35**, 606.
129. M. Strohmeier, D. Stueber and D. M. Grant, *J. Phys. Chem. A*, 2003, **107**, 7629.
130. C. Gervais, R. Dupree, K. J. Pike, C. Bonhomme, M. Profeta, C. J. Pickard and F. Mauri, *J. Phys. Chem. A*, 2005, **109**, 6960.
131. N. Asakawa, S. Kuroki, H. Kurosu, I. Ando, A. Shoji and T. Ozaki, *J. Am. Chem. Soc.*, 1992, **114**, 3261.
132. F. Cheng, H. Sun, Y. Zhang, D. Mukkamala and E. Oldfield, *J. Am. Chem. Soc.*, 2005, **127**, 12544.
133. M. Strohmeier and D. M. Grant, *J. Am. Chem. Soc.*, 2004, **126**, 966.
134. K. L. Anderson-Altmann and D. M. Grant, *J. Phys. Chem.*, 1993, **97**, 11096.
135. H. J. Jakobsen, A. R. Hove, R. G. Hazell, H. Bildsoe and J. Skibsted, *Magn. Reson. Chem.*, 2006, **44**, 348.
136. F. Aguilar-Parrilla, F. Maennle, H. -H. Limbach, J. Elguero and N. Jagerovic, *Magn. Reson. Chem.*, 1994, **32**, 699.
137. R. M. Claramunt, D. Sanz, M. Perez-Torralba, E. Pinilla, M. R. Torres and J. Elguero, *Eur. J. Org. Chem.*, 2004, 4452.
138. J. W. Wiench, L. Stefaniak, A. Barszczewicz and G. A. Webb, *J. Mol. Struct.*, 1994, **327**, 321.
139. J. C. Facelli, R. J. Pugmire and D. M. Grant, *J. Am. Chem. Soc.*, 1996, **118**, 5488.
140. J. Z. Hu, J. C. Facelli, D. W. Alderman, R. J. Pugmire and D. M. Grant, *J. Am. Chem. Soc.*, 1998, **120**, 9863.
141. K. L. Anderson-Altmann, C. G. Phung, S. Mavromoustakos, Z. Zheng, J. C. Facelli, C. D. Poulter and D. M. Grant, *J. Phys. Chem.*, 1995, **99**, 10454.

142. J. Czernek, *J. Phys. Chem. A*, 2001, **105**, 1357.
143. T. B. Brill and C. O. Reese, *J. Phys. Chem.*, 1980, **84**, 1376.
144. W. K. Rhim, D. P. Burum and D. D. Elleman, *J. Chem. Phys.*, 1979, **71**, 3139.
145. G. Wu, C. J. Freure and E. Verdurand, *J. Am. Chem. Soc.*, 1998, **120**, 13187.
146. R. K. Harris, P. Y. Ghi, R. B. Hammond, C. -Y. Ma and K. J. Roberts, *Chem. Commun.*, 2003, 2834.
147. J. Schmidt, A. Hoffmann, H. W. Spiess and D. Sebastiani, *J. Phys. Chem. B*, 2006, **110**, 23204.
148. A. D. Becke, *J. Chem. Phys.*, 1993, **98**, 5648.
149. S. Goedecker, M. Teter and J. Hutter, *Phys. Rev. B*, 1996, **54**, 1703.
150. P. Lazzeretti, *Prog. Nucl. Magn. Reson. Spectrosc.*, 2000, **36**, 1.
151. S. P. Brown, I. Schnell, J. D. Brand, K. Müllen and H. W. Spiess, *J. Am. Chem. Soc.*, 1999, **121**, 6712.
152. R. Ida, M. De Clerk and G. Wu, *J. Phys. Chem. A*, 2006, **110**, 1065.
153. S. Dong, R. Ida and G. Wu, *J. Phys. Chem. A*, 2000, **104**, 11194.
154. G. Wu, S. Dong, R. Ida and N. Reen, *J. Am. Chem. Soc.*, 2002, **124**, 1768.
155. R. K. Harris, P. J. Wilkes, P. T. Wood and J. D. Woollins, *J. Chem. Soc., Dalton Trans.*, 1989, 809.
156. M. J. Potrzebowski, X. Assfeld, K. Ganicz, S. Olejniczak, A. Cartier, C. Gardiennet and P. Tekely, *J. Am. Chem. Soc.*, 2003, **125**, 4223.
157. Y. Zhang and E. Oldfield, *J. Phys. Chem. B*, 2004, **108**, 19533.
158. *http://www.physics.udel.edu/~szalewic/AROwks/Sugg_forSpeakers-rev2.htm*.
159. K. A. H. Wildman, D. -K. Lee and A. Ramamoorthy, *Biopolymers*, 2002, **64**, 246.
160. K. A. H. Wildman, E. E. Wilson, D. -K. Lee and A. Ramamoorthy, *Solid State Nucl. Magn. Reson.*, 2003, **24**, 94.
161. H. S. Gutowski, T. C. Germann, J. D. Augspurger and C. E. Dykstra, *J. Chem. Phys.*, 1992, **96**, 5808.
162. M. Body, G. Silly, C. Legein and J. -Y. Buzaré, *J. Phys. Chem. B*, 2005, **109**, 10270.

NMR Studies of Encapsulated Macromolecules

P.F. FLYNN, A.K. SIMORELLIS AND W.D. VAN HORN

Department of Chemistry, University of Utah, Salt Lake City, UT 84112, USA

Encapsulation of proteins with reverse micelles has recently been identified as an important new biological NMR application. Encapsulation involves transfer of a hydrated protein into the interior chamber formed within an inverted shell of surfactant (usually dioctyl sulfosuccinate), forming a particle that is dissolved in a low-viscosity solvent, most commonly a short chain alkane. Experimental evidence has demonstrated that macromolecules of significant size and complexity can be encapsulated, and that under appropriate conditions encapsulated molecules retain native structure and biological activity. The tumbling rate of an encapsulated protein is roughly proportional to the bulk viscosity of the solvent, and by selecting an appropriately low viscosity liquid the tumbling rate of an encapsulated molecule may be significantly over that that measured for the free protein in aqueous solution. Such samples may exhibit spectroscopic properties that are superior to those of the free molecules in aqueous solution, and encapsulation thus promises to provide an important enhancement to the resolution and sensitivity of solution NMR experiments.In addition to the benefits associated with increases in the rate

ANNUAL REPORTS ON NMR SPECTROSCOPY
VOLUME 62 ISSN 0066 4103
DOI 10.1016/S0066-4103(07)62004-3

of tumbling, encapsulation has also been shown to be an important biophysical technique that can be used to investigate the influence of environment on proteins. The function of proteins depends not only on the physiochemical attributes of the molecules themselves but also on the local environment in which the molecules are active. Reverse micelle based encapsulation is capable of producing novel environments that serve as a platform for studying the influence of confinement, hydration, ionic strength, and temperature in limits that are beyond the scope of other experimental approaches.

1. INTRODUCTION

Solution NMR spectroscopy plays an increasingly important role in the characterization of complex biopolymers. The remarkable pace of progress in the field continues to be advanced by a seemingly inexhaustible series of technological advances that focus on enhancement of the resolving power and sensitivity of the method. Solution NMR methods are currently routinely applied as a primary high resolution structure-determining approach for small through medium proteins and nucleic acid oligomers of up to ~30 kDa in size.[1,2] In addition to its demonstrated utility as a structural tool, analysis of NMR relaxation also provides the most effective approach for elucidating macromolecular dynamics across a wide range of relevant time scales with atomic (bond-vector) resolution. Finally, solution NMR is a highly effective platform for characterizing the structural and dynamic effects due to changes in temperature, solution conditions, and the binding of ligands.

This review focuses on the implementation of reverse micelle encapsulation as a complement to standard solution NMR and biophysical methods. The original motivation for application of the method was focused on addressing the fundamental problems that slow molecular tumbling has on the relaxation properties of nuclear spins. Therefore, a major component of this review is to recall the basic principles and achievements of the method. More recently, the natural compatibility of the reverse micelles with low temperature studies have led to a unique series of experiments that probe the influence of low temperature on the structure of water and the stability of encapsulated proteins. Finally, it has become apparent that multidimensional multinuclear NMR experiments and the tunable spatial confinement generated via encapsulation are a powerful combination for biophysical studies.

Encapsulation within reverse micelles involves transfer of a hydrated macromolecule of interest into the interior chamber formed within an inverted shell of surfactant (usually dioctyl sulfosuccinate), forming a *reverse micelle* particle that is dissolved in a low-viscosity solvent, most commonly a short-chain alkane (n-C_nH_{2n+2}). As discussed in Section 11, experimental evidence has demonstrated that macromolecules of significant size and complexity can be encapsulated and that under appropriate conditions encapsulated molecules retain native structure[3] and biological activity.[4–15] The tumbling rates of encapsulated macromolecules depend on the bulk viscosity of the solvent, and by selecting an appropriately low

viscosity liquid, the tumbling rate of an encapsulated molecule may be more rapid than that measured in aqueous solution. Such samples may exhibit spectroscopic properties that are superior to those of the free molecules in aqueous solution, and encapsulation thus promises to provide an important enhancement to NMR methods. In addition to the benefits associated with increases in the rate of tumbling, encapsulation has also been shown to be an important technique for investigating the influence of confinement and low temperature on complex macromolecules.

2. THE CHALLENGE OF COMPLEX BIOMACROMOLECULES

Every analytical method has natural constraints on its effectiveness, and for solution NMR, it is the very success of the approach that exposes the fundamental limitation. Improvements in the resolution and sensitivity of the method have quite naturally motivated its application to systems of increasing size and complexity, e.g., larger proteins. Such applications present three central challenges to solution NMR methodologies. First, as the size of the molecule under study increases, the number of resonances naturally increases, leading to spectral crowding. Spectral complexity can in principle be addressed by increasing the dimensionality of the experiments used to investigate the system of interest (2D, 3D, 4D, and even beyond); however, there are practical limits to the effectiveness of this strategy. Secondly, as the reorientational correlation time constant increases beyond 10 nsec the line width of NMR resonances becomes a limiting factor in the resolving power of the NMR experiment, independent of the considerations associated with spectral complexity. Finally, in addition to the limitations associated with spectral complexity and intrinsic resolution, increasing size of the molecule under investigation also compromises the ability to probe extensive coupled spin networks.

All modern multidimensional multinuclear NMR experiments rely on sensitivity enhancement of relatively insensitive nuclei (^{13}C and ^{15}N) with protons. Polarization transfer is commonly accomplished using an INEPT element,[16,17] the efficiency of which is intrinsically time-dependent (the INEPT contact time is equal to $1/2J_{HX}$). As a result of the shortened lifetime (T_2) of the coherent states, the efficiency of the polarization transfer is significantly reduced when applied to samples with effective molecular weights of ~30 kDa and larger. The dominant mechanism of NMR relaxation at moderate applied magnetic field strengths is the dipolar interaction, and thus deuteration (including random fractional deuteration and perdeuteration) may be successfully employed to improve relaxation characteristics through reduction of the dipolar interaction. The quantitative reduction is impressive here since the interaction is scaled by the ratio of the squares of the gyromagnetic ratios of the deuteron and proton. Deuteration allows high resolution two-dimensional (^{15}N-HSQC) and three-dimensional multinuclear spectra (HNCO, HNCACB, CBCA(CO)NH, etc.) to be recorded for moderate to large sized macromolecules.[18] Unfortunately, high levels of deuteration reduce or even eliminate the information available from the proton nuclear Overhauser enhancement (NOE) measurements, which are currently the fundamental source of structural

information available from solution NMR studies. Global structural restraints based on the comprehensive characterization of residual dipolar couplings (RDCs)[18–25] may eventually be developed into an effective complementary structural approach, but structural refinement that emphasizes ^{1}H-^{1}H NOEs remains the only established high resolution NMR-based structural approach.

Reduction in the rate of transverse relaxation can be accomplished spectroscopically using a technique named Transverse Relaxation-Optimized Spectroscopy (TROSY).[26] The TROSY method exploits the interference between dipolar and chemical-shift-anisotropy (CSA) relaxation mechanisms to reduce the net transverse relaxation rate, thus generating spectra with substantial improvement in resolution and sensitivity for correlations that involve nuclei with large CSA values (^{15}N and aromatic ^{13}C nuclei). Optimal application of TROSY requires access to very high magnetic field (>18 T), and fortunately access to this instrumentation continues to improve. Nevertheless, the relaxation properties of aliphatic ^{13}C nuclei present in all but the very largest particles will not be enhanced because they have a low CSA. Effective application of the method therefore generally requires deuteration, which as pointed out above, limits the measurement of the ^{1}H-^{1}H NOEs that are fundamental to the structure determining process. Therefore, although the TROSY-based approaches represent a significant advance, there remains a need for new methods aimed at enhancing the resolving power and sensitivity of NMR experiments.

3. THE RATE OF NMR RELAXATION DEPENDS ON THE MOLECULAR TUMBLING RATE

The rate of relaxation of excited nuclear spins depends on the rate of reorientational motion, e.g., tumbling, of the molecule containing those spins. This is distinct from electronic/optical spectroscopy, wherein the transition frequencies are much higher than those employed in NMR (10^{12}–10^{14} Hz as opposed to 10^{8} Hz). Relaxation due to spontaneous emission is efficient at higher frequency, but much less so at lower frequency, since that rate depends on the cube of the frequency. A defining feature of nuclear magnetic resonance relaxation is the explicit coupling between the rate of NMR relaxation (R_1, R_2) and molecular motion. NMR relaxation occurs as a result of the stimulated emission that arises as a result of the presence of fluctuating magnetic fields that can include both external effects (applied RF fields) and internal effects, which arise from the modulation of interactions due to molecular reorientation and/or the local motion of bond-vectors in the presence of the applied static magnetic field (B_0).

NMR relaxation may include contribution from a number of distinct mechanisms, including the dipolar interaction, chemical shift anisotropy, spin–rotation interactions, scalar coupling interactions, and electron–nuclear interactions. For biologically active macromolecules, the dominant mechanisms of relaxation are typically the dipolar and CSA interactions, and we focus the theoretical development here on these two key mechanisms.

The correlation time is the intrinsic constant of the time correlation function, $G(t)$. For random reorientational motion, the simple exponential form for the correlation function shown in Eq. (1) is generally assumed:

$$G(t) = Ce^{-t/\tau_c}, \tag{1}$$

wherein C is a constant that depends on the precise form of the longitudinal and transverse relaxation time constants and the NOE (see below). The correlation time, τ_c, of an isotropically reorienting spherical molecule may be related to the bulk solution viscosity through the Stokes–Einstein equation (Eq. (2)):

$$\tau_c = \frac{1}{6D_r} = \frac{\eta V_h}{k_B T}, \tag{2}$$

wherein D_r is the rotational diffusion constant for a sphere, η the viscosity, V_h the effective volume of the macromolecule, k_B the Boltzmann constant, and T the absolute temperature. Thus changes in temperature and viscosity lead to proportional changes in the rate constant for tumbling.

The rate constant for longitudinal relaxation, R_1, transverse relaxation, R_2, and the proton-nitrogen NOE all depend on reorientational motion, which is itself quantitatively expressed in terms of the frequency-domain representation of the correlation function. This spectral density function, $J(\omega)$, is obtained from the Fourier transformation of the time-domain correlation function, which is Lorentzian for the simple exponential form assumed above as demonstrated in Eq. (3):

$$J(\omega) = \frac{\tau_c}{1 + (\omega\tau_c)}, \tag{3}$$

wherein ω is the Larmor frequency of the spin (in $\text{rad} \cdot \text{sec}^{-1}$). It should be noted that the expression for the spectral density given above corresponds to the case in which there is no internal molecular motion – a more general form will be introduced below.

The rate constant for NMR relaxation depends on the spectral density function evaluated at several frequencies (Eq. (4)):

$$R_1 = \frac{1}{T_1} = N\left(\frac{\hbar^2\gamma_H^2\gamma_X^2}{4r_{XH}^6}\right)[4J(\omega_X) + J(\omega_H - \omega_X) + 6J(\omega_H + \omega_X)] + \frac{\omega_X^2\Delta\sigma^2}{3}J(\omega_X); \tag{4a}$$

$$\text{NOE} = 1 - \frac{\gamma_H}{\gamma_X}\left(\frac{\hbar^2\gamma_H^2\gamma_X^2}{4r_{XH}^6}\right)[J(\omega_H - \omega_X) - 6J(\omega_H + \omega_X)]NT_1; \tag{4b}$$

$$R_2 = \frac{1}{T_2} = \frac{\hbar^2\gamma_H^2\gamma_X^2}{8r_{HX}^6}[4J(0) + 3J(\omega_X) + J(\omega_H - \omega_X) + 3J(\omega_H) + 6J(\omega_H + \omega_X)] + \frac{\omega_X^2\Delta\sigma^2}{18}[4J(0) + 3J(\omega_X)] + R_{ex}. \tag{4c}$$

The H-subscripts in Eq. (4a–c) represent N numbers of H nuclei, γ_H and γ_X are the gyromagnetic ratios of ^1H and X-nuclei respectively, $\Delta\sigma$ is the chemical shift anisotropy of the X-nuclei, I the internuclear H–X distance, $\hbar$ is Planck's constant (reduced) and the X-subscripts usually refer to ^{13}C, ^{15}N, or ^{31}P nuclei. The dependence of transverse relaxation rate constant (R_2) on the reorientational correlation time may be evaluated by direct calculation, using an explicit form for the spectral density function. A popular expression for the spectral density function; the Lipari–Szabo Model-Free formalism (Eq. (5a, b)), is commonly employed for this purpose:[27,28]

$$J(\omega) = \frac{2}{5}\left(\frac{S^2\tau_c}{1+(\omega\tau_c)^2} + \frac{(1-S^2)\tau}{1+(\omega\tau)^2}\right); \tag{5a}$$

wherein

$$\frac{1}{\tau} = \frac{1}{\tau_c} + \frac{1}{\tau_e}. \tag{5b}$$

S^2 is an orientational (NMR) order parameter, and τ_e the correlation time for internal motion. In the limit of slow tumbling, the magnitude of the spectral density function inspected at various frequencies for an H–X pair may be ranked as shown in Eq. (6):

$$J(0) > J(\omega_X) \gg J(\omega_H - \omega_X) \approx J(\omega_H) \approx J(\omega_H + \omega_X). \tag{6}$$

In the limit of slow reorientational motion $J(0)$ becomes the dominate term in the overall rate of transverse NMR relaxation, and therefore R_2 is directly proportional to τ_c, as shown in Eq. (7a–c):

$$R_2 = \frac{\hbar^2\gamma_H^2\gamma_X^2}{8r_{HX}^6}[4J(0) + 3J(\omega_X) + J(\omega_H - \omega_X) + 3J(\omega_H) + 6J(\omega_H + \omega_X)]. \tag{7a}$$

$$R_2 \approx \frac{\hbar^2\gamma_H^2\gamma_X^2}{8r_{HX}^6}[4J(0)]. \tag{7b}$$

$$R_2 \propto J(0). \tag{7c}$$

The rotational correlation time of a spherical protein in water scales roughly with molecular weight over a substantial range, e.g., a spherical protein with molecular weight of 50 kDa and typical characteristics (partial specific volume ≈ 0.75 mL/g, $f/f_o \approx 1.2$) has a radius of ≈ 26 Å and tumbles in water ($\eta \approx 850\,\mu Pa \cdot sec^{-1}$ at 300 K) with a correlation time of ≈ 15 nsec. The viscosity of water is relatively sensitive to temperature, e.g., η_{water} varies from $\approx 1{,}000\,\mu Pa \cdot sec^{-1}$ at 293 K to $\approx 450\,\mu Pa \cdot sec^{-1}$ at 333 K, and this acute dependence may be exploited to reduce the rate of transverse relaxation in studies of thermostable macromolecules.[29]

Water is a relatively viscous fluid, whereas most solvents of relatively low polarity have intrinsically low relative viscosities. This class of liquids includes the

Table 1. Viscosity of short chain *n*-alkane liquids at 300 K

	Ethane	Propane	Butane	Pentane	Water
Viscosity (μPa · sec)	35	97	158	224	850
Liquefaction pressure (MPa)	4.7	1.05	0.40	0.10	–

Note: 1 MPa = 10 bar = 145 psi~10 atm; 1 μPa · sec = 10^{-3} centipoise.

short-chain *n*-alkanes (C_nH_{2n+2}), other solvents such as CO_2 and certain refrigerants whose intermolecular interactions are restricted to London forces. Such solvents have viscosities in the range necessary to impart greatly increased tumbling rates and correspondingly decreased rates of transverse relaxation (see Eqs. (2), (3), and (7a–c)). The viscosities of commonly available low viscosity liquids are listed in Table 1. Ethane, propane, and butane are gases at standard temperature and pressure but are liquefied by low pressures at room temperature to produce highly effective low viscosity solvent systems (note that the pressures required to liquefy butane, propane, and ethane are well below the pressures that can destabilize protein structure).

Water-soluble proteins fold so as to position most of the polar and charged residue on the surface of the molecule, with hydrophobic residues directed to the interior portion of the molecule. Transferring a water-soluble protein to an apolar environment will cause a reorganization of the protein structure to place hydrophobic residues in contact with the solvent and to minimize contact for polar and charged residues. Efforts to dissolve polypeptide or nucleic acids directly in low-polarity solvents will fail, leading to denaturation of the target macromolecule.

The challenge to expanding the applicability of reverse micelle-based encapsulation techniques is to make use of the very low viscosity alkane (or other) solvents while preserving native structure. Such technology involves encapsulation of a protein and several layers of aqueous buffer solution within a shell of surfactant that isolates the aqueous-protein component from the bulk hydrophobic environment. The protein-buffer-surfactant assembly thus forms an inverted or reverse micelle that is dissolved in a hydrophobic solvent such as liquid propane.

4. REVERSE MICELLES

Reverse micelles are spherical aggregates of amphipathic molecules that are organized with charged/polar headgroups oriented inward toward an aqueous nanoscale core and acyl chain moieties directed outward toward the bulk apolar solvent. A structural model of a reverse micelle particle is shown in Fig. 1. Historically, reverse micelles have a long record of applications in such diverse fields such as biocatalysis, bioseparations, cosmetics, nanoparticle synthesis, and oil recovery.[30–35] More recently, reverse micelles have been used in conjunction with NMR as a tool in structural biology and biophysical research. A number of polar and ionic surfactants spontaneously form reverse micelles in the presence of an

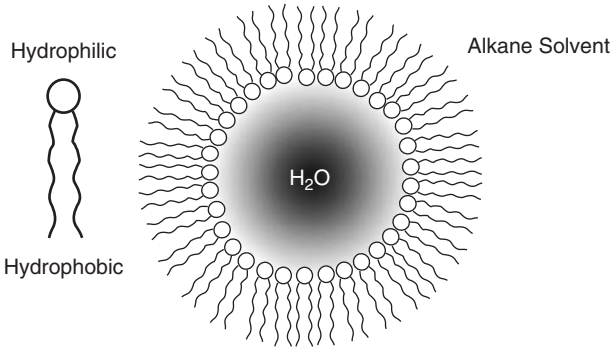

Fig. 1. Schematic model of the reverse micelle forming and resulting reverse micelle particle.

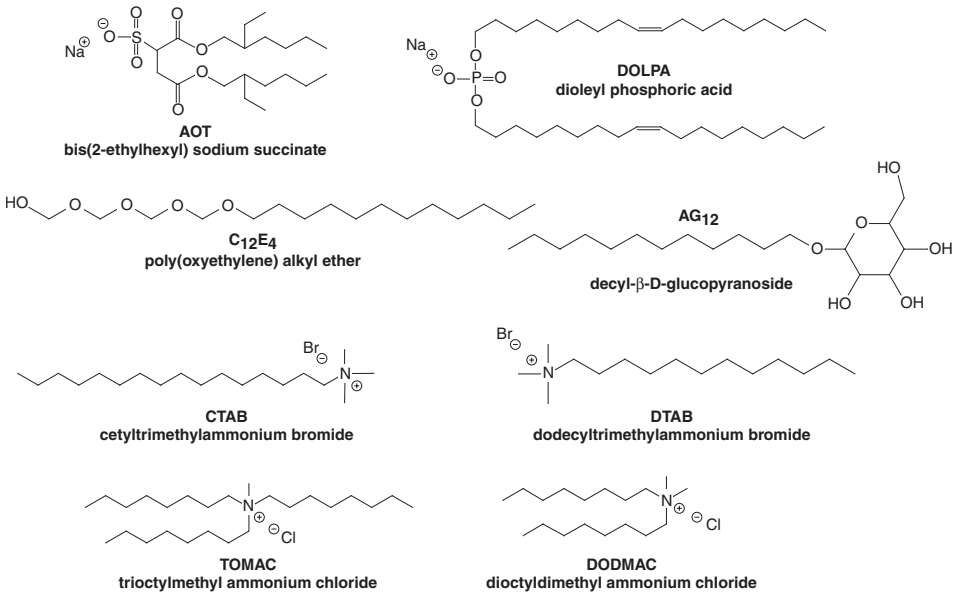

Fig. 2. Schematic diagrams of reverse micelle forming surfactants. All reverse micelle forming surfactants possess a characteristic wedge shape that promotes the characteristic keystone architecture.

apolar solvent and aqueous medium (Fig. 2). Dioctyl sulfosuccinate, AOT, is the most commonly used reverse micelle forming surfactant. The amphiphilic property of AOT is delicately balanced; AOT dissolves in nonpolar solvents at ambient and low temperatures and will solubilize water, while at elevated temperatures it will dissolve in water and solubilize apolar solvents.[36] The keystone shape of the AOT molecule is an important factor in formation of the reverse micelle particle, e.g., extending the arch-like shape in three-dimensions naturally produces the internal cavity that is occupied by the aqueous phase. Inverting the surfactant molecules in

a spherical assembly generates a unique charged/polar surface, the specific nature of which affects both the water holding capacity of the assembly as well as the distribution of counterions along the inner micellar surface.

According to the standard model of reverse micelle formation, nanoscale droplets of water promote the aggregation of the amphiphilic surfactant around a water core.[37,38] A fundamental physical parameter of reverse micelle particles is the water loading, w_0, which is defined as the molar ratio of water to surfactant. Water loading is under facile experimental control, and reverse micelles respond to changes in the amount of water used in their formulation with remarkable plasticity. The radius of the reverse micelle naturally increases as a function of w_0, and at sufficient values of w_0, the aqueous nanoemulsion is capable of solubilizing (coencapsulating) a variety of water-soluble substances, including complex dyes of widely varying size and chemical composition. Biomacromolecules, such as proteins and nucleic acid oligonucleotides, can also be encapsulated within the aqueous core, the former of which is the focus of this review.[39–41] The water pool will have properties similar to bulk water at w_0 above 40, although some reports assert that bulk-like behavior begins at a w_0 of 20.[41,42] The encapsulation/solubilization of water within the reverse micelle is proportional to the number of micelles in solution, and an increase of water or an increase of surfactant concentration will directly affect the number of reverse micelle particles in solution.[43] Another parameter that reflects the intrinsic plasticity of reverse micelles is the aggregation number, which is simply the number of surfactants that make up a single reverse micelle particle. In contrast to water loading, the aggregation number is indirectly controlled by tuning the surfactant and water concentrations. In the limit of low w_0, it has been estimated that the aggregation number of surfactant molecules in a reverse micelle will increase in a linear fashion as the amount of w_0 increases above lower limit values ($w_0 \sim 1.5$), and the limiting aggregation number of AOT in isooctane has been estimated at ~ 16.[37] At water loading values compatible with encapsulation of proteins, the accepted aggregation number falls in the broad range between 50 and 150, although there appears to be no direct quantitative experimental confirmation of this assumption.

The ability of reverse micelles to host a wide variety of molecules derives directly from the fact that the particles are capable of encapsulating an aqueous core formulated with widely varying compositions of salts, buffers, and pH. This tolerance to the variations in the core conditions allows the solution to be optimized for different types of guest molecules. Generally, the addition of salts to the water phase has been shown to decrease the amount of water uptake by the reverse micelle system.[43–48] With respect to protein uptake by reverse micelles, cations such as sodium and calcium are generally chosen to increase the size of the water pool, since the goal would be to confine the protein entirely in the water pool and minimize potential interactions between the protein and the interior surface of the reverse micelle.

A dynamic equilibrium exists between the water, solvent, and surfactant system, with reverse micelle particle colliding, coalescing, and then reemerging. Small amounts of solvent penetrate the surfactant up to the polar head groups, and water

will also interact with the hydrocarbon tails of the surfactant.[48] Increasing the salinity of the water pool will alter the curvature of the micelle, which in turn affects the amount of water solubilized. The salt interacts with the charge on the inner surface of the micelle, affecting the space available for fluctuation between the individual surfactant molecules by creating a more rigid and curved surface.[48,49]

Reverse micelle particles exhibit a size polydispersity that depends on a number of factors, but under typical conditions of median water loading and temperature, the polydispersity is low.[49–52] Theoretical and experimental methods aimed at evaluating polydispersity of AOT reverse micelle preparations conclude that the size distribution of reverse micelle populations is directly related to the particle size, with increasing particle size (water loading) leading to increases in polydispersity.[51] The overall amount of water solubilized by the particles in turn depends on parameters such as temperature, pressure, and ionic strength.

5. WATER IN REVERSE MICELLES

Water confined to reverse micelles has physical properties that are distinct from that of bulk water.[53] Virtually all of the data available on the physical properties of encapsulated water are derived from AOT-based systems, although the results are expected to be generally representative of all reverse micelles. A number of states of encapsulated water have been postulated, including the hydrogen bonded bulk-like state of water at standard temperature and pressure, a nonhydrogen-bonded or weakly hydrogen bonded state that can be induced by the introduction of a solute, e.g., a biopolymer, and in the limit of low hydration, water largely devoid of hydrogen bonding capacity due to solvation of the surfactant headgroups and dissolved salts.[53,54]

The proton chemical shift of water is a sensitive probe of water structure, that allows investigation of both dynamical states as well as the equilibrium condition of water.[54,55] Early work in the field established a fundamental relationship between the water content of the reverse micelle system and the chemical shift of the water proton resonance. This relationship was interpreted in terms of physical model, producing much of the intuitive framework that is under current common use. An essential feature of the model is that the chemical shift of the proton resonance of the encapsulated water depends on the water content. At low water loading values, most of the water molecules will be involved in solvating the surfactant and counterions, forming hydrogen bonds with oxygen molecules on the sulfonate and succinate groups, forming ion–dipole interactions with the anionic surfactant head group and counter ions or dipole–dipole interactions with the succinate group.[56] Estimates predict that at a water content below 1% (v/v% H_2O/solvent) all of the water molecules participate directly in solvation.[55] As more water is added to the system, water begins to form a bulk-like pool in which hydrogen bonding between the free water molecules occurs. The water exchanges between the two sites, the pool and the surfactant head groups, with a rate constant of $\sim 10^{-4}\,\mathrm{sec}^{-1}$.[55] Optimization of hydrogen-bonding between the water molecules leads to deshielding of

the proton, which moves the ^{1}H water resonance to lower frequency until finally the water exhibits the chemical shift of bulk water in the limit of large w_0.[57]

More recently, NMR and IR spectroscopy have been used in combination to visualize multiple types of water in AOT reverse micelles: free water in the pool, anion bound water (water bound to the carbonyl and sulfonate groups), bulk-like water, and cation bound water.[58] Free water is that which is dispersed through either the solvent layer or between the surfactant monomers and is described as out-of-core since it is not easily measurable. Solution NMR experiments showed a single resonance, which indicates relatively rapid exchange between the above mentioned water types on the NMR time scale. The resonance exhibited an upfield change in chemical shift (δ) as w_0 decreased, as expected based on previous studies.[55,57] Shifts in hydroxyl stretching frequencies to higher values correspond to greater hydrogen-bond strength and a higher electron density over the O–H bond, which is consistent with the qualitative change in the NMR chemical shift, e.g., the resonance moves upfield. The observed chemical shifts measured under a wide variety of conditions were fit to Eq. (8):

$$\delta = X_b\delta_b + X_c\delta_c + X_d\delta_d, \tag{8}$$

where in the b-subscript corresponds to anion bound water, the c-subscript to bulk water, the d-subscript to cation-bound water, and X_x and δ_x the molar fraction and chemical shift of the individual components. The results indicate that the anion-bound water resonance has a chemical shift of ~2.8 ppm, the cation-bound water has a chemical shift of ~6.1 ppm, and the shift of the bulk water resonance is ~5.7 ppm. At lower water loading values, most of the water is involved in solvating the negatively charged surfactant and the corresponding negatively charged environment draws electron density away from the water protons, causing the subsequent deshielding and a higher NMR resonance frequency.

6. THERMODYNAMICS OF REVERSE MICELLE PARTICLE FORMATION

Current theory suggests that the water uptake by reverse micelles is an entropy driven process.[59] According to the standard model, water molecules added to an AOT/*n*-pentane reverse micelle system initially cluster together, followed by surfactant monomers forming around the clusters creating a stable nanodispersion.[60] The clustering phenomenon is composed of a disruption of the pentane molecules ordered around the water molecules, which is an endothermic process, followed by an association of water molecules within the surfactant water pool, which is an exothermic process.[61] In addition to relatively free water molecules (at sufficiently high w_0) within the pool, there are additional water molecules which are bound to either the surfactant or the counter-ions, and there is a continuous equilibrium between the two species.[39,62,63] Once the system has reached thermodynamic equilibrium, it is stable and the nanodispersion can remain intact for

several months at room temperature. Calorimetric studies have been used to measure the enthalpy changes as a function of increasing AOT concentration,[59–61] and results indicated that as the concentration of AOT increases, the molar enthalpies of the bound water decrease. Positive values of the enthalpy change for bound water can be related to the disruption of the hydrogen-bonding networks that the water forms when in the pentane solution, and as the micellar structure expands and water is ordered around the head group charges.[59] Reverse micelle formation is a complicated solvation process. Although only enthalpy changes have been monitored, it is generally accepted that the positive ΔH values thus indicate that a corresponding change in entropy must be responsible for driving the system to spontaneously take up water. The water within the reverse micelles, although confined and ordered near solvent head group, is entropically favored over water in the apolar solvent phase.

7. PROTEINS ENCAPSULATED BY REVERSE MICELLES

There are currently dozens of literature citations describing studies of encapsulated proteins.[7,40,64–66] A schematic model of an encapsulated protein is shown in Fig. 3. The issue is not whether proteins can be encapsulated, but how the buffer conditions and surfactant selection can be manipulated to optimize encapsulation. Under optimized conditions, properly encapsulated proteins should exhibit native structure (as assayed spectroscopically). The encapsulated structure of human ubiquitin was solved using multidimensional multinuclear NMR methods and shown to be natively folded.[67] Similarly, the fast time scale dynamics of ubiquitin was investigated using NMR relaxation experiments and were shown to be very similar in the encapsulated and free solution forms (see Section 17).[35] Enzymatic activity has also been monitored in the encapsulated state. Native like enzymatic

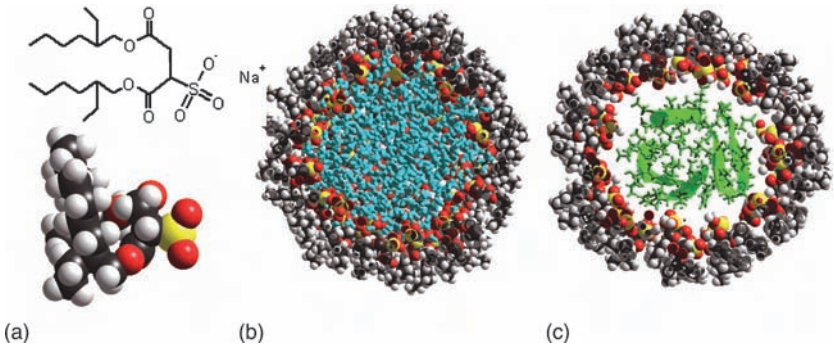

Fig. 3. Model diagrams of AOT reverse micelle and protein encapsulation. (a) AOT surfactant in both line and space-filling structure. (b) Water-filled reverse micelle with the near face cut-away to show the interior. (c) Encapsulated ubiquitin within an AOT reverse micelle. Note that the near and far face of the reverse micelle has been cut-away and the water removed to facilitate visual perspective of protein encapsulation.

activity strongly suggests the presence of native structure. Proteins such as α-chymotrypsin and malic dehydrogenase have been shown to be enzymatically active, and the activity is highly dependent on parameters such as water loading, temperature, and pressure.[68,69] It thus becomes apparent that reverse micelles are excellent hosts for a wide range of target proteins and that when properly optimized, encapsulation preserves native-like structure, activity, and dynamics of the hosted proteins.

AOT reverse micelles have been shown to be effective for encapsulation of the largest number of proteins, and examples included proteins which have a hydrophobic, basic, or acidic outer surfaces. A representative but highly abbreviated list includes lysozyme, ribonuclease A, trypsin, α-chymotrypsin, malic dehydrogenase, pepsin, HIV-1 reverse transcriptase, and bovine serum albumin.[70–77] AOT reverse micelles have also successfully solubilized DNA and RNA (ribosomes).[78–80] In spite of its demonstrated utility, a few proteins, notably highly basic proteins such as horse heart cytochrome *c*, appear to be incompatible with encapsulation within AOT reverse micelles. Several groups have advanced the idea of adjusting the surfactant composition to optimize encapsulation efficiency to produce NMR spectra that indicate the presence of a unique native-like protein fold – a concept that seems to have been appreciated by early researchers in the field.[70] In this regard, other surfactants such as CTAB, with and without nonionic cosurfactant components such as 1-hexanol have also proven to be very useful.[81,82] Recent efforts focusing on mixtures of $E_{12}C_4$ and AOT (and DTAB in one important example) and on mixtures of AOT and 1-hexanol have also yielded promising results.[83–86]

8. ENCAPSULATION PROTOCOLS

Reverse micelles may be suitably formulated in apolar solvents having a wide variety of physical properties. Much of the early work in the field was carried out using isooctane, which has a bulk viscosity of $\sim 500\,\mu Pa \cdot sec^{-1}$ and a boiling temperature of 60°C. More recently *n*-pentane has proved to be a useful solvent, largely owing to the fact that its relatively low viscosity provides a better platform for survey studies, and its relatively low boiling point, 37.5°C, provides a better predictor for the stability that will be encountered with more volatile solvents. Straight chain alkane solvents containing fewer than five carbon atoms have boiling temperature below normal laboratory temperature. The relatively low viscosities of these liquids, which for liquid *n*-butane, propane, and ethane at room temperature are 200, 158, 97, and $35\,\mu Pa \cdot sec^{-1}$, all compare favorably with water, which has a bulk viscosity of $\sim 1000\,\mu Pa \cdot sec^{-1}$. Practical requirements demand that the solvent is maintained in the liquid phase, and the minimum liquefaction pressures of *n*-butane, propane, and ethane are 4, 10.5, and 47 bar respectively at room temperature. The pressures required to maintain these solvents in there liquid phase is well below the pressure required to denature stable proteins, which falls in the range of 3–6 kbar.

Preparation of reverse micelles using the more volatile solvents is conducted in three major steps. In the first step the surfactant is mixed with the liquefied solvent, and in the second step the solution is transferred into a dedicated NMR cell that has been preloaded with a concentrated solution of the molecule of interest (the cell is pre-pressurized to within 10–50% of the final target pressure to minimize pressure drop during solution transfer). Finally, the two phases are mixed under vigorous agitation, which generates the stable nanodispersion. The NMR cell is then disconnected from the mixing chamber by closing an in-line ball-valve (Upchurch Scientific Inc.) and delivering the cell to the NMR instrument.[87]

The prototypical design of the of the high-pressure mixing chamber was fabricated from 318 stainless steel with small round or rectangular quartz view ports.[88–90] Although this design provides the greatest operational range, the relatively low pressures required to liquefy the straight-chain alkanes can, on the other hand, be readily accommodated using mixing cells made from polycarbonate or other plastics. A number of high-pressure NMR tube designs have been developed that accommodate the relatively modest pressure bearing requirements of these apolar liquids. Materials have included both ceramics[91] and plastics,[92] all of which provide excess pressure holding capacity relative to the target liquefaction pressures. Ancillary PEEK tubing and high-pressure valves were obtained from Alltech Associates Inc. (http://www.alltechweb.com/) and Upchurch Scientific Inc. (http://www.upchurch.com/). Deuterium lock was achieved using 5% D_2O for the aqueous samples and either 20% d_{15}-*n*-pentane in *n*-alkane or sealed capillary tubes containing 99.96% D_2O for encapsulated samples dissolved in nonpolar solvents.

9. SOLVENT SUPPRESSION

The relative concentration of solvent and surfactant both greatly exceed that of the encapsulated solute molecules. For example, the concentration of the neat *n*-pentane is ~8.7 M ($\rho = 0.626\,g \cdot mol^{-1}$), the surfactant concentration will be in the range of 100 mM, and the encapsulated protein concentration will be in 100–300 μM range. There are three major proton resonances in *n*-pentane, corresponding to the equivalent methyl groups (six protons), the equivalent methylene groups (four protons) and the unique methylene pair in the center of the molecule (two protons). The relative concentration of methyl protons in neat *n*-pentane will thus be greater than 50 M, which given an average concentration of encapsulated protein of ~0.25 mM, places the dynamic range between the solvent and protein resonances at greater than 200,000 : 1. As has been used for many years to reduce the dynamics range in aqueous samples, deuterated solvents, e.g., *n*-C_5D_{12}, represent a significant aid to solvent suppression.[3] Unfortunately, commercially available deuterated *n*-alkane solvents have deuterium enrichment levels that are generally less than 98%, which still leads to a dynamic range challenge of greater than 4,000 : 1. For alkane solvents, effective suppression of the solvent resonances may be accomplished using a WET (Water suppression Enhanced through T_1 effects) pulse sequence.[93–95] The WET sequence consists of a series of alternating long,

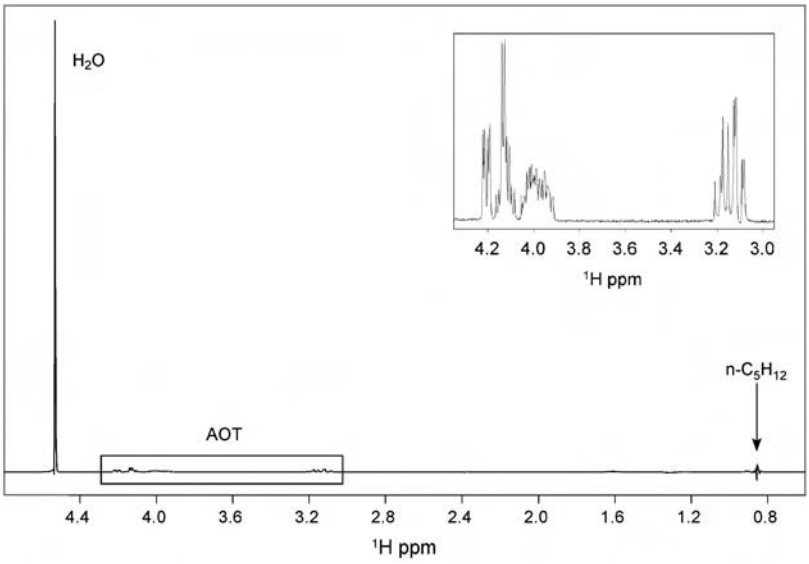

Fig. 4. One-dimensional ^{1}H spectrum of a sample of 75 mM AOT, w_0 of 30, in *n*-pentane recorded using the WET PFG DSTE pulse sequence (this particular spectrum was recorded with a PFG strength of $\sim$7.5 G cm^{-1}). The data were recorded at 20°C with a spectral width of 4,000 Hz into 8,192 complex points.

low-power frequency-selective RF-pulses and field-gradient pulses that provide superior suppression of solvent resonances. Frequency specificity is accomplished using tailored excitation[93–95] and a combination of individual waveforms to produce simultaneous RF excitation at multiple frequencies. A representative example of the suppression possible is demonstrated in Fig. 4.

10. HYDRODYNAMIC BEHAVIOR OF AOT REVERSE MICELLE ASSEMBLIES

The physical factor that places the greatest limits on the acquisition of high-resolution solution NMR spectra of macromolecules in aqueous solution is quite clearly the relatively high viscosity of bulk water ($\eta_{H_2O}\sim$1000 μPa sec^{-1}). As an alternative to the spectroscopic and isotope-enrichment based approaches outlined above, encapsulation of the molecules of interest within a shell of reverse-micelle forming surfactant and low viscosity solvents, has been suggested as an important alternative.[96,97] Apolar solvents all have viscosities that are low relative to that of water at room temperature (Table 1). If larger proteins can be transported into such low viscosity solvents, substantial improvements in the spectroscopic properties of these molecules may be achieved.[98]

Maintenance of native-like physical properties requires that water-soluble macromolecules be encapsulated in a hydrated, near native condition within a shell of

reverse-micelle forming surfactant. Encapsulation of macromolecules dissolved in low-viscosity solvents has been shown to increase the effective rates of both rotational diffusion and translational diffusion.[3,97,99,100] For example, the encapsulation of the 56 kDa dimeric protein triose phosphate isomerase (TIM) was shown to produce NMR spectra that unambiguously confirm that encapsulation can lead to a significant increase in the resolution of solution NMR spectra.[100] As of this writing, TIM remains the largest encapsulated protein studied by high resolution spectroscopic methods (see Section 11 for details).

Measurement of translational diffusion is arguably the most convenient method for characterizing effective particle radii across a wide molecular weight range. The pulsed-gradient stimulated-echo method (PGSE) provides a highly accurate and relatively straightforward approach to such measurements.[101] For larger molecules, including proteins encapsulated in reverse micelle aggregates, which naturally have shorter T_2 values, translational diffusion coefficients (D_t) are more effectively measured using a longitudinal encode-decode (LED) experiment that minimizes the influence of rapid transverse relaxation.[102,103] This is accomplished by storing magnetization along the z-axis during the diffusion interval. Intense solvent lines arising from the ^{1}H solvent resonances (e.g., n-C_nH_{2n+2}) are effectively suppressed using a WET pulse sequence as described in the previous section.

A fundamental assumption of the experimental design of all of the PFG diffusion experiments is that molecular motion is random. Convection currents, or any sort of net flow generally, produce additional dephasing of the isochromats that interferes with diffusion measurements by leading to unpredictable loss of signal intensity. In the context of solution NMR studies the nonrandom motion will be entirely due to convection. The occurrence of convection can display a sharp temperature dependence, reminiscent of a phase change. The temperature at which onset of convection is established in a fluid confined within an infinitely long cylinder may be expressed using a dimensionless parameter, γ, defined in Eq. (9a, b):

$$\gamma = \left(\frac{g\alpha}{\nu\kappa}\right) r^4 T' \tag{9a}$$

$$T' = \frac{\Delta T}{d} \tag{9b}$$

in which g is the acceleration due to gravity, α the coefficient of thermal volume expansion, ν the kinematic viscosity (η/ρ), κ the thermal diffusivity; which is equal to $k/\rho c_p$, where k is the thermal conductivity, c_p the heat capacity at constant pressure, r the inner radius of the cylinder (tube), and $T'(\Delta T/d)$ the temperature change across the height of the sample, d $\gg$ r.[104,105] The limiting of γ (γ_c), is equal to 67.4 for the case of a perfectly insulating wall and 215.8 [105] for the case of a perfectly conducting wall.[104] Convection occurs when γ exceeds the critical value, γ_c, and a corresponding critical temperature, T'_c, may also be defined, above which, convection is predicted to occur, as indicated in Eq. (10):

$$T'_c = \frac{\Delta T}{d} \propto \left(\frac{\nu\kappa}{g\alpha}\right)\left(\frac{\gamma}{r^4}\right). \tag{10}$$

For a sample of neat benzene at 20°C in a glass NMR tube (assuming a thermally conducting wall) with an inner radius of 4.5 mm, convection is predicted to be present if the temperature gradient exceeds $3.5\,\mathrm{K}\cdot\mathrm{m}^{-1}$.[105] Given the typical solution NMR sample, this suggests that convection can arise within the sample described above if the temperature gradient over the sample length is greater than ~0.2 K.

Consideration of Eq. (10) reveals that the onset of convection is directly proportional to the kinematic viscosity, and will thus be predicted to be more easily established in solutions of lower bulk viscosity. The kinematic viscosities of water and *n*-pentane are 1 and ~0.36 St respectively, which explains why convection is commonly observed in reverse micelle preparations, but is infrequently observed in aqueous solutions. A confirmation of the effects of convection are demonstrated in the results of PFG LED diffusion experiment[106] applied to a AOT reverse micelle sample dissolved in *n*-pentane. The resonance intensity is plotted as a function of the strength of the applied gradient pulse as shown in Fig. 5, and the data exhibit the classic signature of convection artifacts.

In the limit of highly regular convective flow, it has been shown that the effects of convection may be eliminated by adding two complementary experiments together.[107] In one experiment magnetization during the diffusion interval is stored

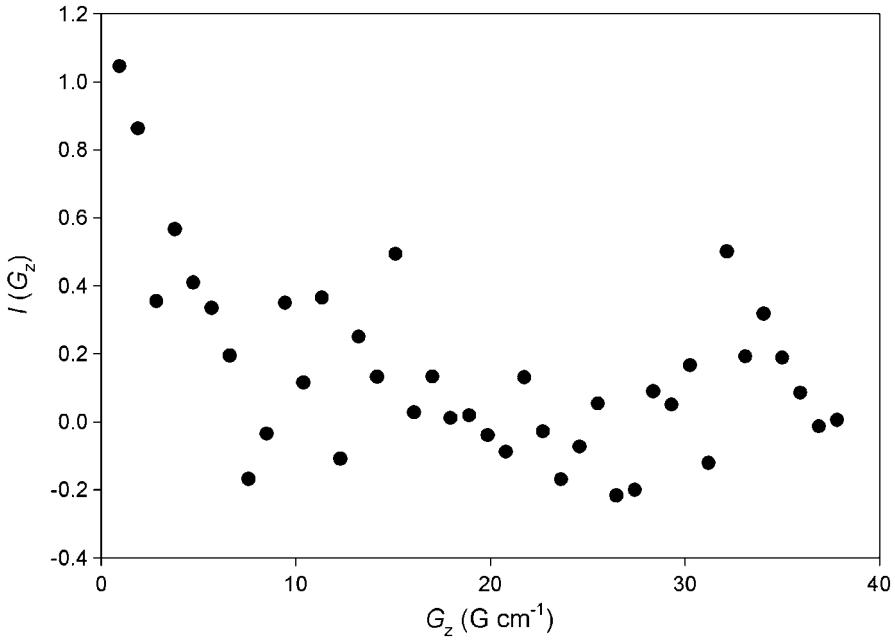

Fig. 5. Plot of resonance intensity, $I(G_z)$, versus applied gradient field strength for data recorded using a conventional, uncompensated, longitudinal-encode-decode, WET PFG STE LED pulse sequence. The sample was 75 mM AOT in *n*-pentane with a w_0 of 30. The data were recorded at 30°C with a spectral width of 4,000 Hz into 8,192 complex points. The diffusion interval was 100 msec and the length of the gradient employed to prepare and refocus the z-coil was 3 msec.

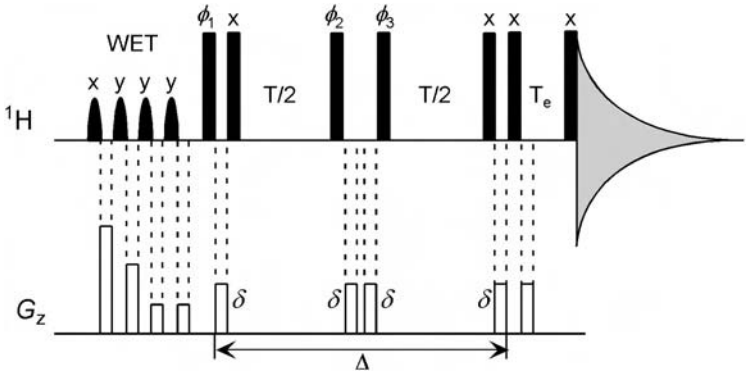

Fig. 6. WET PFG DSTE pulse sequence. The WET component of the sequence is discussed in detail in the text. All remaining RF pulses were 90° ($\pi/2$), with phases designated directly above each pulse. Pulses labeled with an explicit phase were not cycled; the remaining pulses were cycled according to the following schedule: ϕ_1: x, y, $-x$, $-y$; ϕ_2: $-x$, $-y$; ϕ_3: 4($-x$), 4(x). The receiver was cycled according to the following schedule: ϕ_{rec}: x, x, 4($-x$), x, x. The length of the gradient pulses (labeled δ in the figure) was 3 msec and the gradient pulse applied during the interval labeled T_e was 0.5 msec.

along the $+z$-axis, whereas in a second experiment, magnetization is stored along the $-z$-axis. The contributions of the convective flow should thus compensate one another, effectively negating the effects of convection. The experiment developed based on this principle actually employs a pair of stimulated echoes, and cancels the influence of convection prior to acquisition of the FID. This important experimental scheme has been named the PFG double stimulated echo pulse sequence, PFG DSTE,[107] and a version of the pulse sequence modified the include multifrequency solvent suppression that is required with reverse micelle samples is shown in Fig. 6. The translational diffusion coefficient, D_t, is determined by fitting the resonance intensity to the Gaussian function defined in Eq. (11a, b):

$$I(G_z) = I_0 \exp[-(\gamma\delta G_z)^2(\Delta)D_t] \tag{11a}$$

$$\Delta = T + \frac{4\delta}{3 + 2\tau} \tag{11b}$$

wherein $I(G_z)$ is gradient-dependent intensity, I_0 the initial intensity, G_z the strength of the applied field gradient pulse (which is arrayed in this experiment), γ the gyromagnetic ratio, δ the duration of the gradient pulse, and T the primary diffusion delay, which together with the length of the gradient pulses and associated delays, τ, determines the total diffusion interval.[107] Note that although Eq. (11a, b) applies to all experiments of the LED class, the specific interpretation of the time delay is dedicated to specific implementations of the scheme.

In contrast to the results shown in Fig. 5, the influence of convective flow is completely compensated by the DSTE experiment, and the intensity profile shown in Fig. 7 is devoid of any hint of the distortions observed in the uncompensated

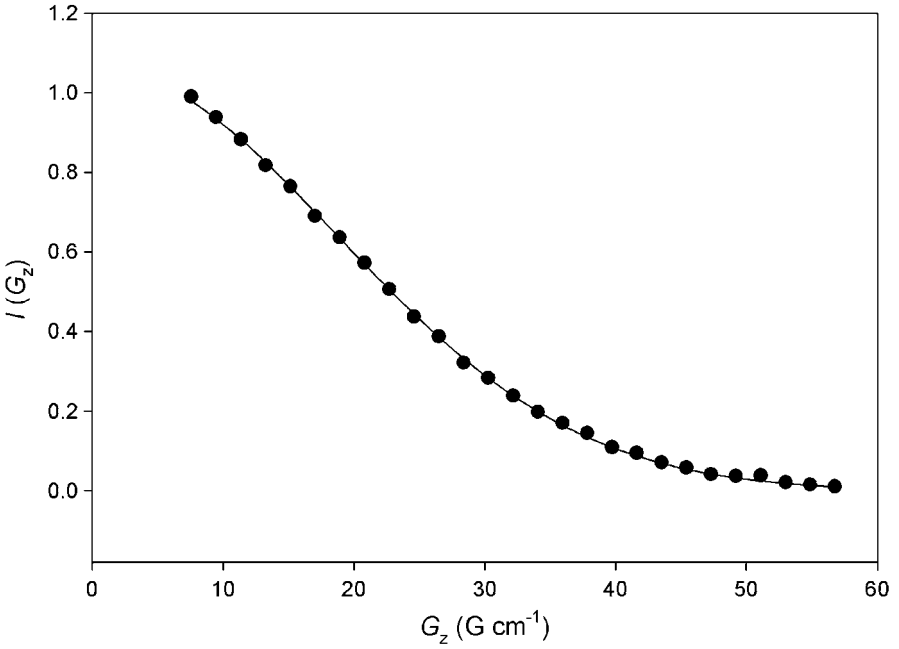

Fig. 7. Plot of resonance intensity, $I(G_z)$ versus applied gradient field strength for data recorded using the WET DSTE LED pulse sequence. Note the regular decrease in intensities relative to those generated using the uncompensated experiment (see Fig. 5).

experiment. Moreover and more importantly the fitted value of the diffusion coefficient, $2.1 \times 10^{-6}\,\mathrm{cm}^2 \cdot \mathrm{sec}^{-1}$, is in agreement with the predicted results.

11. PRACTICAL APPLICATION OF REVERSE MICELLE ENCAPSULATION TO LARGER POLYPEPTIDES

As a demonstration of the effectiveness of encapsulation strategy, a series of ^{15}N-HSQC spectra were recorded for the 56 kDa TIM homodimer and shown in Fig. 8 under a variety of conditions.[87] An HSQC spectrum recorded in water serves as a reference for the encapsulated experiments. The line widths of resonances present in the spectrum of the aqueous sample are those expected for a 56 kDa protein and serve as a reference for spectra recorded for the encapsulated samples. The line widths of resonances in the spectrum of encapsulated TIM dissolved in *n*-pentane are significantly broader than those present in the spectrum of the aqueous sample and are a result of the anticipated increase in the particle radius due to the surfactant, ~12 Å. The viscosity of *n*-pentane is too low to generate a net increase in the tumbling rate of the protein compared with that observed for that of the free protein in water (volume penalty of the surfactant shell). On the other hand, propane has a viscosity ~11% that of water, which is sufficiently low to overcome the

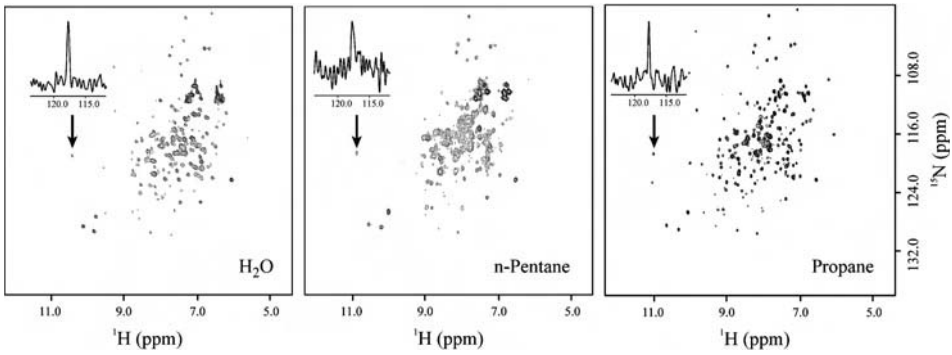

Fig. 8. Series of ^{15}N-HSQC spectra of triose phosphate isomerase (TIM). Left: TIM in free aqueous solution. Center: Encapsulated TIM in AOT reverse micelles in *n*-pentane. Right: TIM encapsulated in AOT reverse micelles in *n*-propane. The insets represent 1D ^{1}H cross-sections through specified resonance. All spectra were recorded at 750 MHz (^{1}H) at 20°C.

volume penalty, and this data exhibits the anticipated enhanced resolution and sensitivity relative to the data acquired in aqueous solution. The spectra shown confirm that encapsulation within an appropriately low solvent can be used to decrease the rate of transverse relaxation (and increase the rate of longitudinal relaxation) leading to a substantial enhancement in resolution and sensitivity.

12. MULTINUCLEAR RESONANCE ASSIGNMENTS OF ENCAPSULATED PROTEINS

Chemical shifts are extremely sensitive to changes in the electronic environment surrounding nuclei, which may be used to monitor the conformation of encapsulated macromolecules. Chemical shifts of encapsulated molecules may be conveniently referenced to internal sodium 3-trimethylsilyl)-1-propanesulfonate (DSS). DSS is readily incorporated into the buffer employed in the hydration of the encapsulated solute and serves as a direct chemical shift reference for ^{1}H resonances. As usual, it will be necessary to engage the ^{2}H lock system to accurately resolve chemical shift measurements, and moderate concentrations of deuterated solvent (C_5D_{12} at 5–20%) serves this function well. The ^{13}C and ^{15}N chemical shifts may be referenced indirectly using the zero-point frequency ratios: the ratios for ^{13}C and ^{15}N nuclei are 0.251449530 and 0.101329118 respectively.[108–111] The magnetic susceptibility difference between water and *n*-pentane leads to a difference in the measured chemical shift of DSS of −0.7 ppm.[112]

To provide a basis for quantitative analysis of chemical shift changes associated with encapsulation, complete multinuclear resonance assignments for encapsulated ubiquitin have been determined.[113,114] Backbone chemical shifts (amide ^{1}H and ^{15}N, C^{α} and C′) for ubiquitin in water were first determined for the specific buffer conditions used in encapsulation (50 mM sodium d_3-acetate buffer, pH 5.0, 250 mM NaCl, and 0.5 mM DSS) based on the previously published assignments.[115]

Equivalent shifts for resonances for encapsulated ubiquitin were compared with those for ubiquitin in free aqueous solution, and agreement between chemical shifts for ubiquitin in the aqueous and encapsulated states was generally found to be very good, although significant shifts were found in specific regions. Encapsulated ubiquitin residues 7–9, 45–49, and 71–75 were found to have significant chemical shift deviations from those of the protein free in solution. It is notable that the regions of ubiquitin for which the largest differences between aqueous and encapsulated states exist correspond to residues that lie on the surface of one face of the protein on which three of four positively charged arginine residues are also located. The chemical shift deviations may thus be the result of electrostatic interaction of the positive charge of this region of protein with the negatively charged anterior surface (head group) formed by the AOT surfactant. Recent studies of encapsulated ubiquitin studied at low temperatures suggest that this surface of the protein interacts with the interior surface of the AOT reverse micelle under conditions of low w_0.[34] Future studies will undoubtedly shed additional light on this important phenomenon.

13. STRUCTURAL STUDIES OF ENCAPSULATED MACROMOLECULES

Currently the only example of a high-resolution structure of an encapsulated macromolecule[114] is that of human ubiquitin. The structure was solved at Angstrom-level resolution using standard solution NMR-based methods. The primary source of structural information in this study was composed interproton distance restraints derived from interproton NOEs that were measured using ^{15}N-resolved and ^{13}C-resolved NOESY spectra. In a preliminary survey, secondary structure elements present in the encapsulated protein were judged to be very similar to those found in the aqueous state based on qualitative inspection of the interproton NOE patterns. The NOE restraints were supplemented by 63 experimental torsional angle restraints derived from quantitative HNHA J correlation measurements, and 23 H-bond restraints that were predicted based on direct observation of substructures present in the trial structures inspected at intermediate stages of refinement.

NMR-based structures are typically evaluated according to two metrics, which are self-consistency (reflecting completeness of the structural restraints), and absolute accuracy (reflecting agreement with the source structure). The refined family of ubiquitin structures, depicted using line diagrams in Fig. 9, had an average RMSD of 0.26 ± 0.05 Å for backbone atoms and 0.77 ± 0.04 Å for heavy atoms to the mean structure for residues 2–70. A detailed inspection of the structural statistics reveals that residues 9, 10, 35, 36, 52, and 53 have slightly higher local RMSD values compared with other regions of the molecule. These residues exhibit significant chemical shift variations in spectra recorded for the aqueous and encapsulated states, and are also the residues for which the lowest number of NOE restraints were generated. To investigate whether structural differences between the encapsulated form of ubiquitin and solution and/or crystalline forms, the family of

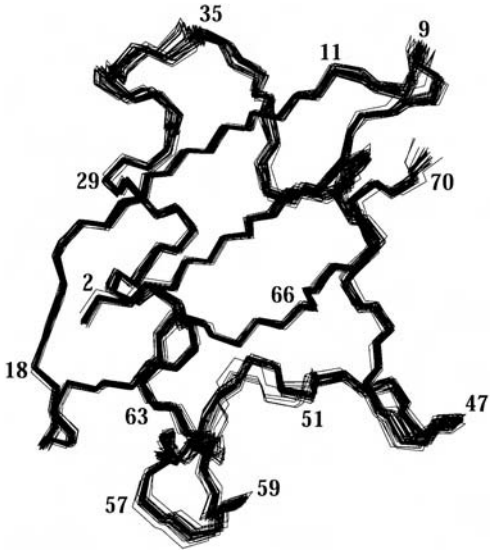

Fig. 9. Vector diagram of the family of structures determined for encapsulated ubiquitin. Backbone atoms only are shown to emphasize agreement of the family, and to identify regions in which structural variations are present.

structures of encapsulated ubiquitin were compared with both the crystal structure[116] and to the NMR-based structure determined in solution.[117] The superposition of the structures derived from crystallographic studies, a previous very high resolution NMR structural study, and the NMR-based structure of the encapsulated protein is shown in Fig. 10. This comparative structural analysis identifies small variations in the structure of encapsulated ubiquitin in the regions between residues 8 and 10, residues 32 and 34, and near residue 62.

Very recently, RDCs for a number of encapsulated proteins have been measured for encapsulated proteins.[118] RDCs have previously been shown to be an important complement to other NMR restraints (interproton NOEs and scalar couplings).[119–124] The result suggests that reverse micelle particles possess sufficient magnetic anisotropy to impart an observable RDC contribution to the direct N–H *J*-couplings. This is an important new result and may provide additional structural restraints for efforts focused on the structural characterization of encapsulated proteins. There are two central challenges to the general application of RDCs derived from encapsulation studies to proteins structure determination efforts. First, both high resolution NMR spectra and optical data recorded for the free and encapsulated forms of several proteins suggests that the encapsulation may alter the structure of the protein.[81,82,125–127] Secondly and perhaps more importantly, it has been shown that the order parameter for fast local backbone motion for proteins can be altered upon encapsulation.[35] Accurate interpretation of the RDCs will thus require comprehensive characterization of any changes in backbone motion that occur upon encapsulation.

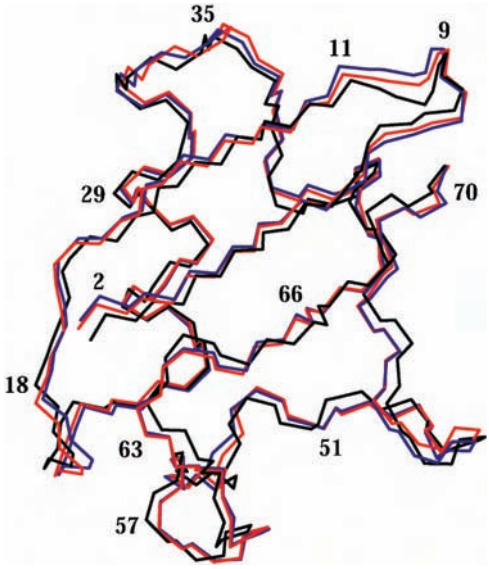

Fig. 10. Vector diagrams of superposed structures of ubiquitin. The crystalline structure is rendered in blue, solution structure in red, and reverse micelle encapsulated structure is black. Backbone atoms of residues 2 through 70 of the crystalline, lowest-energy free solution and reverse micelle structures were superimposed. The C-terminal residues are known to exhibit conformational heterogeneity and were not included.

14. LOW TEMPERATURE NMR STUDIES OF ENCAPSULATED WATER

Relatively few investigations of reverse micelles have previously been conducted at lower temperatures.[128–130] Nevertheless, low temperature encapsulation studies have been performed at temperatures as low as $-100^{\circ}C$, which supports access to liquid water cooled below the freezing point of pure water under standard laboratory conditions, a supercooled state.[130]

Solution NMR methods can also be used characterize the dynamics of encapsulated water at subzero temperatures.[131] Reverse micelles were monitored at temperatures between 20 and $-30^{\circ}C$ at varying solution ionic strengths using ^{1}H 1D solution NMR.[47] At temperatures well below zero, reverse micelles spontaneously expel water from the water pool and this water will subsequently freeze and form a solid mass at the bottom of the NMR tube. The expelled water is pure, as judged by measurement of the collected water conductivity, and is also free surfactant, and water shedding thus has potential application in the areas of water purification. The rate of temperature induced water shedding can vary substantially, depending on the ionic strength and temperature of the encapsulated solution. As previously observed, there is a corresponding upfield shift as w_0 decreases, signifying an increase in the population of bound water.

Reverse micelles prepared using solutions of relatively high ionic strength, e.g., a sample composed of 50 mM sodium acetate, pH 5.0, and 1 M NaCl, will produce the most stable low temperature nanodispersions. Reverse micelles composed of buffers of relatively low ionic strengths exhibited the most rapid loss of water, and in the limit of low ionic strength, e.g., ddH_2O, most of the encapsulated water is shed within the first 5 min of the experiment. For the high ionic strength sample mentioned above, the interval for the w_0 to be reduced to half the initial w_0 was approximately 40 min at $-30^{\circ}C$.

The ionic strength of the water pool will affect the w_0 of a sample, and thus in turn the radius of the reverse micelle particle. For example, a sample containing ddH_2O at $20^{\circ}C$ had the largest initial w_0 but the smallest water loading at $-30^{\circ}C$. Conversely, at room temperature increasing ionic strength steadily decreases the amount of buffer/water the reverse micelle solution can uptake and thus the system becomes saturated at smaller and smaller w_0, an effect which has been previously assumed.[45] However, unlike the ddH_2O sample, the sample with the highest ionic strength retained the highest w_0 at $-30^{\circ}C$. The size of AOT reverse micelles has been consistently shown to depend on water loading in a reliable manner.[56,70,132] As the ionic strength of the encapsulated solution is increased, reverse micelles shed water at slower rates and retain higher final w_0 values. Thus, experiments conducted with probe molecules, biopolymers, or substrates involved in chemical reactions at subzero temperatures should be conducted in buffers of relatively high ionic strength in order to avoid the deleterious effects of water shedding and any interactions of the molecule of choice with the surfactant layer.

In addition to water shedding, complex behavior of the ^1H water resonance is manifest in data recorded at higher ionic strength and low temperature. Spectra recorded for samples at multiple ionic strengths monitor changes in the chemical shift of the water resonance toward higher field, and also the dynamic appearance of multiple water resonances. The spectra shown in Fig. 11 demonstrate multiple water populations that exist simultaneously. These multiple water resonances vary both in intensity and chemical shift, and also include fine structure, which reflects the presence of multiple populations of water that evolve during the course of the 90 min water shedding experiment, all of which are shown in Fig. 12. Until recently, the bound water population was seen as a time averaged population. Studies of the time dependent composition of encapsulated water exposes the presence of multiple forms of water that coexist for long periods of time. Ongoing studies of this remarkable phenomenon should shed additional light on the subject.

15. THERMODYNAMICS OF WATER SHEDDING – A CONCISE ANALYSIS

At subzero temperatures, reverse micelles will spontaneously shed water from the core.[133] There is no published thermodynamic examination of water shedding, but it is reasonable to assume that the phenomenon is due to entropic destabilization of the encapsulated water, leading to spontaneous expulsion. At subzero temperatures,

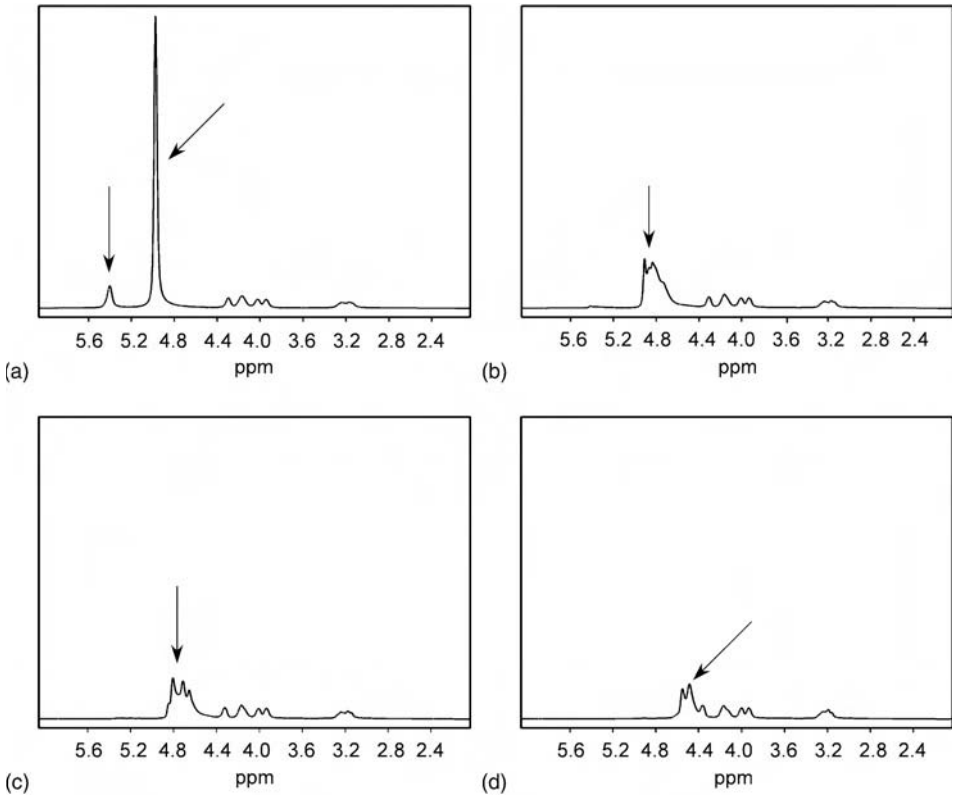

Fig. 11. Time dependent intensity and chemical shifts of multiple ^{1}H water resonances at $-30^{\circ}C$. Arrows indicate either a single water resonance or an area with multiple water resonances. Note the time dependent development of multiple water resonances. The sample was composed of 50 mM NaOAc, pH 5.0, 0.5 M NaCl. Selected spectra recorded at (a) 1 min, (b) 15 min, (c) 30 min, and (d) 40 min. Arrows in (a) indicate two separate resonances, (b) and (c) arrows indicate a triplet, and (d) a doublet. The small downfield peak in (a) represents water solubilized in pentane at $-30^{\circ}C$.

the hydrophobic effect becomes weaker, effectively scaling the energy barriers that previously favored the maintenance of water within the reverse micelles. Again, given that encapsulation is a spontaneous process, the positive change in enthalpy must necessarily be compensated by a net positive change in the system entropy ($-T\Delta S$).[59–61] Thus, as the temperature of the system is lowered, the encapsulated water becomes more ordered, which results in a weakening of the hydrophobic effect. Under these conditions, water molecules can more readily partition into the organic phase. Increasing the ionic strength of the buffer system causes more water molecules to be retained with the reverse micelle core to hydrate the salt and thus reduces the amount of water shed from the reverse micelles into the organic phase. Thus, the ionic strength dependence of water shedding behavior changes the

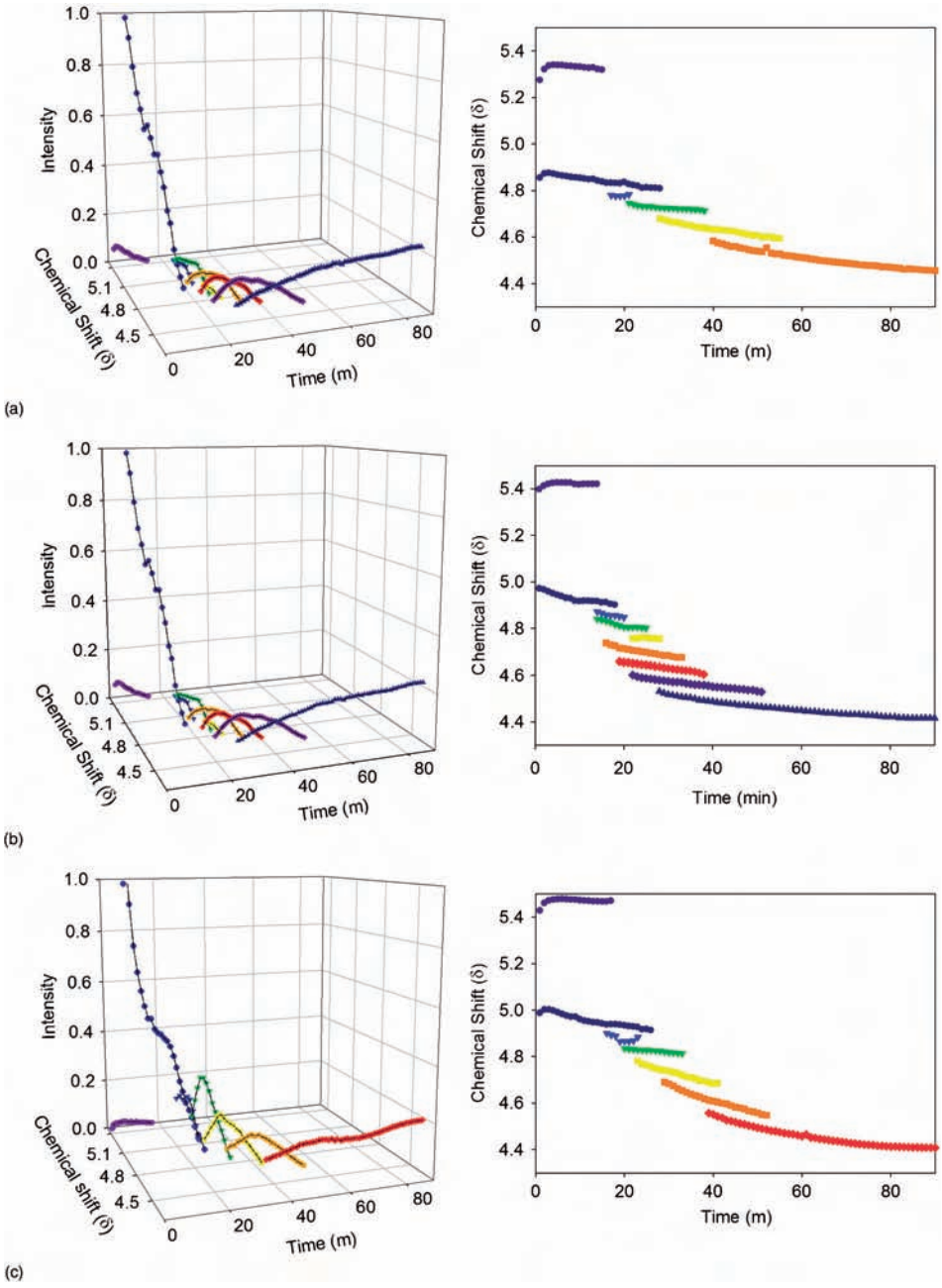

Fig. 12. Water resonance intensity and chemical shift versus time at low temperature. The plots demonstrate changes the presence of multiple populations of water that coexist for several minutes (macroscopic timescale). Plots labeled a, b, and c are 1 M, 500 mM, and 250 mM NaCl at −30°C respectively. Plots labeled d and e are 500 and 250 mM NaCl at −20°C respectively.

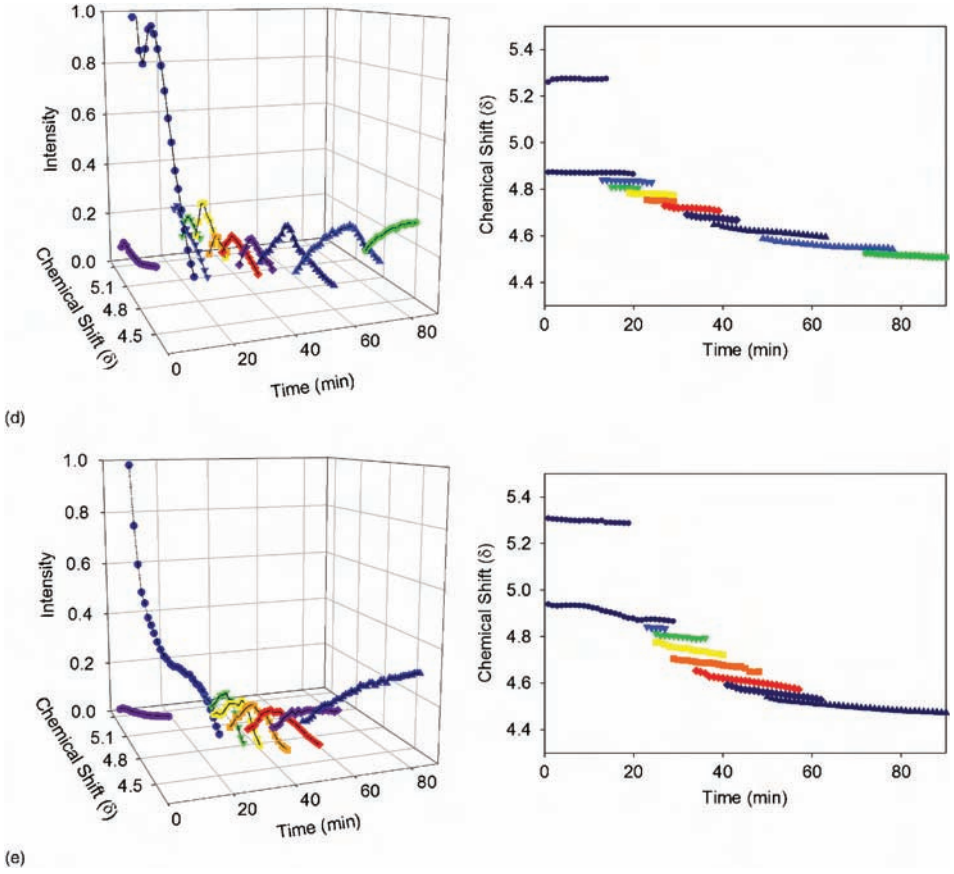

Fig. 12. Continued

thermodynamics of the system in such a manner as to provide increased water holding capacity at low temperatures.

16. LOW TEMPERATURE STUDIES OF ENCAPSULATED PROTEINS

Cold denaturation is the process of low temperature protein unfolding, which arises due the relatively large positive value for the change of the heat capacity of unfolding ($\Delta C_p \sim 12\,\mathrm{cal}\cdot\mathrm{mol}^{-1}\cdot\mathrm{res}^{-1}\cdot\mathrm{K}^{-1}$). This condition in turn causes the free energy of protein unfolding (ΔG_{D-N}) between native and denatured to have a convex dependence on temperature that is revealed quantitatively in Eq. (12)[134,135], and qualitatively in Fig. 13:

$$\Delta G_{D-N(T_2)} = \Delta H_{D-N(T_1)} + \Delta C_p(T_2 - T_1) - T_2\left(\Delta S_{D-N(T_1)} + \Delta C_p \ln\left(\frac{T_2}{T_1}\right)\right). \quad (12)$$

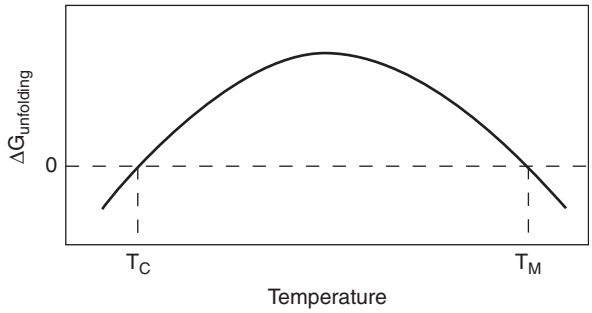

Fig. 13. Qualitative plot of the Gibbs free energy change of unfolding as a function of temperature. Note the convex temperature dependence of the ΔG curve.

The maximum value of ΔG_{D-N} for most proteins occurs near room temperature, and since proteins generally have large heat capacities of unfolding (ΔC_p), protein destabilization occurs as the temperature varies from room temperature in either direction.[136] The cold denaturation temperature of most proteins is predicted to occur well below the freezing point of water, which presents a significant limitation to the investigation of this phenomenon. The decreased stability of proteins at low temperature is usually attributed to increased solubility of hydrophobic residues in aqueous solutions, that is the stabilizing influence of the hydrophobic effect is reduced.[134,135]

Low temperature unfolding is generally accepted to be a two-state unfolding process analogous to thermal melting.[137–139] Recently however, experimental NMR data and theoretical results derived from studies of encapsulated ubiquitin have led some to the conclusion that low temperature unfolding may occur through an ensemble of intermediates involving local cooperative folding.[140,141] The interpretation of the NMR data is based on observation that the intensity of some resonances in ^{15}N-HSQC and ^{13}C-HSQC spectra exhibits a hypersensitivity to low temperature. A remarkable feature of the intensity loss is that it appears to represent a net loss of signal intensity, which is quite unlike that observed with high temperature protein unfolding. In the heat denatured case, protein resonances typically display a general decrease in resonance line width consistent with an increase in the transverse relaxation time constant, and a concomitant change in the chemical shift of resonances toward their random coil values. Wand and coworkers propose that: (1) the protein conformations that are populated as a result of cold denaturation are distinct in some way from those that occur in the heat denatured case; and (2) these states either exchange at a rate that leads to maximal exchange broadening or that a plethora of nonexchanging states is generated. Given the geometric constraints imposed by the interior volume of the reverse micelle, it is difficult to imagine that extended conformations are compatible with encapsulation. The question arises then however, as to whether the thermodynamics of the system are perturbed by encapsulation. The idea that the many denatured states do not exchange rapidly, as they do in the heat denatured state, is much more

controversial. Curiously, the resonances that loose intensity are located on the surface of ubiquitin that has previously been shown to bind a number of protein targets.[142–148]

Subsequent investigations of the low temperature reverse micelle-ubiquitin phenomenon included a comprehensive examination of the salt dependence of the low temperature driven unfolding. First, it was noted that the ^{15}N HSQC spectrum of ubiquitin was not altered by additional NaCl at 20°C. It was also noted that at each of the salt concentrations probed (no salt, 0.25, 1.0, and 1.5 M NaCl) the low temperature effects were completely reversible. Interestingly, the apparent amount of unfolding seemed highly dependent on the ionic strength of the reverse micelle aqueous core as shown in Fig. 14. Given what had been determined previously about the physical effects of ionic strength on reverse micelles, coupled with the fact that water is lost from the particles at low temperature, gives rise to the alternative hypothesis that what had been attributed to globally noncooperative unfolding was instead due to interactions between the interior surface of the reverse micelle and the exterior surface of the encapsulated protein (ubiquitin). Mapping the resonances from the ^{15}N HSQC data that had little or no perturbation in their chemical shifts provided direct support of this hypothesis. Under low ionic strength conditions, observations were consistent with either globally noncooperative unfolding or reverse micelle–protein binding interactions. However, under high ionic strength conditions loss of resonance intensity is found to be consistent with a globally cooperative unfolding process.

The apparent local unfolding can be understood by simply observing that at low ionic strength and temperature the encapsulated space within the reverse micelle becomes smaller due to water shedding. This in turn brings the protein surface close to the charged sulfonyl head groups present along the interior surface of the AOT reverse micelle (Fig. 15), and this proximity leads to an apparently local loss of protein structure. However, at elevated ionic strength and low temperatures the water loading and hence the internal radius of the particle is much greater (Table 2), and under such conditions the apparent local unfolding is not observed. Instead, under these conditions the behavior is consistent with a global two-state unfolding process (Fig. 16).

A recently published solution NMR study provides important additional details regarding the low temperature folding process.[149] It was found that with the assistance of high pressure (2 kbar) ubiquitin unfolding was complete near −21°C; whereas, without the use of destabilizing pressure ubiquitin is predicted to denature near −40°C.[150] A key result from this study is reproduced here in Fig. 17, which charts the loss of resonance intensities present in the low temperature ^{15}N-HSQC spectra. The salient feature of these data is that the decrease in resonance intensity as a function of temperature is globally consistent. Three resonance intensities display a relative hypersensitivity to temperature, however these small effects are completely at odds with the more dramatic apparent local unfolding phenomenon observed for the encapsulated protein at low ionic strength. Overall then, results from both encapsulation studies (under high ionic strength conditions) and free solution studies are consistent with a globally cooperative low temperature

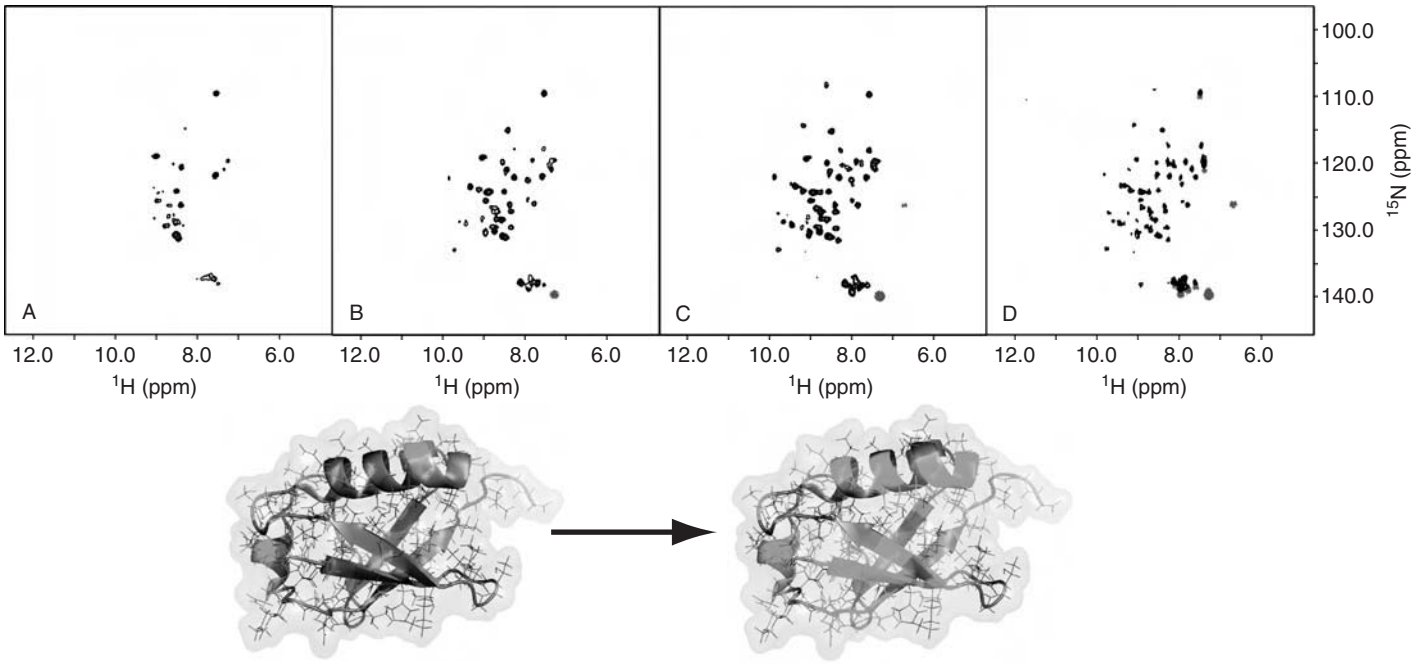

Fig. 14. The effects of low temperature are compensated by high ionic strength. All spectra are HSQC experiments at −30°C of ^{15}N labeled ubiquitin in 100 mM AOT, 50 mM NaOAc, pH 5.0. The ionic strength is varied, A, B, C, and D have no salt (e.g. neat water), 0.25, 1.0, and 1.5 M NaCl respectively. Note that all spectra are recorded and processed identically. Observed amide proton and nitrogen correlations from spectra A and D have been mapped on a structural model of ubiquitin and can be found in ref. 47.

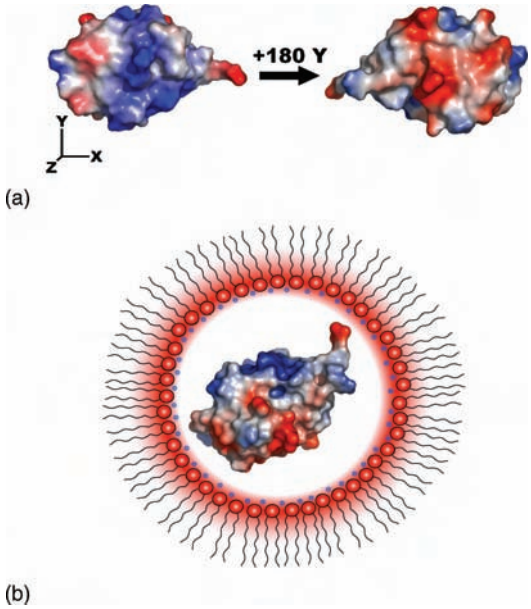

Fig. 15. (a) Electrostatic surface of ubiquitin. As ubiquitin is rotated 180° along the *y*-axis the general electrostatic surface potential changes sign. The blue is electropositive and the red is electronegative. Near the bottom of the electropositive half of ubiquitin (as shown) is the I44 surface. Under low ionic strength conditions ^{15}N HSQC resonances corresponding to the electropositive half of the protein are not detected. However, under high ionic strength conditions resonances from all portions of ubiquitin are detected (although many resonances disappear or shift). (b) A schematic representation showing essential electrostatic surfaces of the reverse micelle and the protein. The blue spheres correspond to positively charged sodium counter ions which are relatively small and mobile. The basic portion of the protein (blue) undergoes conformational exchange driven by an electrostatic interaction with the anterior surface of the reverse micelle (generally red). Reverse micelle and ubiquitin not drawn to accurate relative scale.

Table 2. Water loading capacity as a function of ionic strength[a]

Ionic strength	w_0 at +20°C	w_0 at −30°C	Δw_0
H_2O	37.6	7.0	30.6
0.25 M NaCl	26.9	9.7	17.2
1.0 M NaCl	27.0	13.9	13.1
1.5 M NaCl	18.9	16.0	2.9

[a]Two trends appear as the ionic strength of the sample is increased. First, at room or meso-temperatures, and in the limit of low ionic strength buffers, the water loading of a reverse micelle sample is maximal. The second trend is that water loading capacity at low temperatures increases as ionic strength is increased (these two trends are shown in the second and third columns). The fourth column is the difference between water loadings (Δw_0) at +20°C and −30°C.

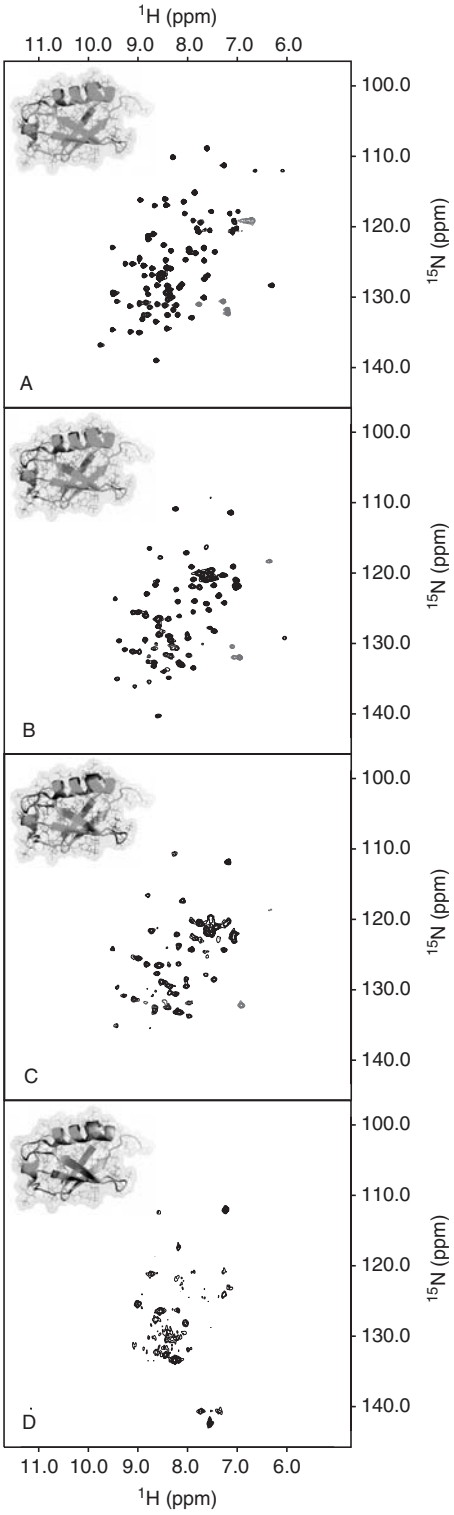
^{1}H (ppm)
11.0 10.0 9.0 8.0 7.0 6.0
100.0
110.0
120.0
130.0
140.0
^{15}N (ppm)
A
B
C
D

unfolding mechanism.[137–139] Finally, it must be acknowledged that although ubiquitin is an intrinsically interesting protein, it is remarkable for its thermodynamic stability. Future studies will undoubtedly include study targets with a range of stabilities, and the utility of encapsulation as a method for examining cold denaturation is best reviewed at a future date when additional results are available.

17. EFFECT OF REVERSE MICELLE ENCAPSULATION ON MOTIONAL DYNAMICS IN POLYPEPTIDES

Analysis of ^{15}N NMR relaxation has emerged as one of the most accurate methods for measuring the rate constant for reorientational motion. The approach is also the single most effective approach for investigating the amplitude and time scale of backbone motion in polypeptides. The transverse relaxation of ^{15}N nuclei may be efficiently measured using a modified version of the ^{15}N-HSQC experiment.[151,152] This approach has been used as a means of probing the effects of bulk solvent viscosity on the rate of rotational diffusion for proteins encapsulated within reverse micelles.[90] Results confirm that the apolar solvent systems influence hydrodynamic behavior of the reverse micelles in a predictable manner – one which will support structural and dynamical studies of macromolecules in the encapsulated state.

The characterization of local molecular motion is an important component of modern biophysical studies of proteins. The central significance of these studies derives from the fundamental principle that function depends on transitions from states of lower energy to states of higher energy, and that such excursions are coupled to conformational fluctuations. The detailed analysis of NMR relaxation is an effective probe of internal dynamics that is capable of accurately identifying areas of protein rigidity and flexibility. Backbone dynamics in polypeptides are most commonly analyzed based on the Model-Free analysis of measured ^{15}N T_1, T_2, and NOE values.[153] For reference, amide ^{15}N T_1, T_2, and NOE values in proteins that tumble with a reorientational time constant of 10 nsec have values of ~800, ~80 and ~0.8 msec respectively. The motion of the backbone N–H bond vector within the simple Model-Free framework is characterized using three fitted parameters; the time-constant for global reorientation of the entire molecule (τ_c), a time-constant for relatively fast internal (local) motion (τ_e), and an order parameter which is related to the amplitude of the fluctuation (S^2). The most natural context for application of Model-Free analysis is one in which the time scales of internal molecular motion are rapid compared with the global tumbling correlation time, e.g., picoseconds versus nanoseconds, suggesting that no coupling between the local

Fig. 16. Modulation of reverse micelle–protein interactions by high ionic strength reveals low temperature two-state unfolding. Panels A–D show ^{15}N-HSQC spectra recorded at 500 MHz (^{1}H) and 100 mM AOT, 50 mM NaOAc, pH 5.0 and 1.5 M NaCl. From A to D spectra were recorded at +20, −20, −30, and −40°C. All spectra were recorded and processed under identical conditions – note that spectrum D is displayed at a topographical level ~50% closer to the noise floor than the other spectra. Observed amide correlations mapped onto a structural model of ubiquitin can be found in ref. 47.

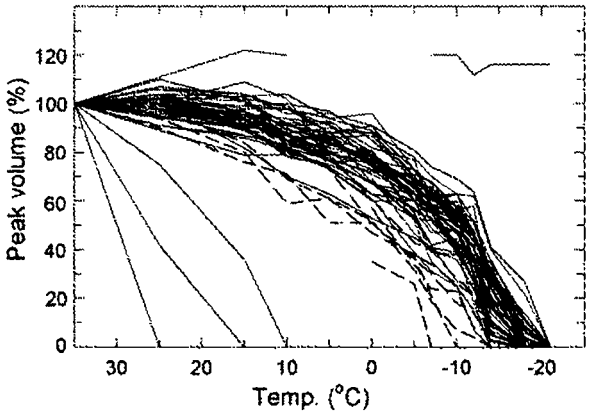

Fig. 17. Plot of the relative resonance peak volumes versus temperature for all observable 'native' resonances in the ^{15}N-HSQC spectrum of ubiquitin. Figure kindly provided by Drs. Kitahara and Akasaka.

and global motion exists. Although clearly an idealization, this perspective has proven to be extremely useful. A modified version of the Model-Free approach has been developed to support analysis of the effects of motion occurring on multiple fast time scales,[154] but were unnecessary for the current example. In addition to fast motion analysis, motion occurring on much longer time scales can also be probed using relaxation analysis. For example, chemical and conformational exchange events are defined as events that occur on the μsec–msec time scale. The presence of exchange can be revealed by a thorough examination of the T_1/T_2 ratio for all resolved amide groups within the molecule under study. This ratio is relatively insensitive to the influence of rapid local motion. Assuming that significant chemical and conformational exchange effects are confined to a limited number of residues within the protein (a reasonable assumption for stable, uniquely structured polypeptides), the average T_1/T_2 ratio will be dominated by the influence of the global correlation time, and will contain a minimal contribution from residues exhibiting exchange behavior, e.g., manifest in T_2. The approach involves statistical analysis of T_1/T_2 ratio for amide bond vectors, specifically, calculation of the average and standard deviation for all amide group that superficially appear to be free from conformational averaging effects (including low NOE values).[155] This selection process clearly scales the sensitivity of the method to lower exchange contributions. It should be noted that relaxation dispersion is a more sensitive method for determining the presence of exchange contributions to transverse relaxation as well as for quantifying the exchange rate.[156–159] However, such methods are relatively insensitive (even compared with standard T_1, T_2, and NOE experiments, which are themselves insensitive) and are thus precluded by the low concentration of protein obtained with encapsulation.

Recently, the fast local backbone dynamics for ubiquitin encapsulated within AOT reverse micelles was investigated using analysis of ^{15}N NMR relaxation

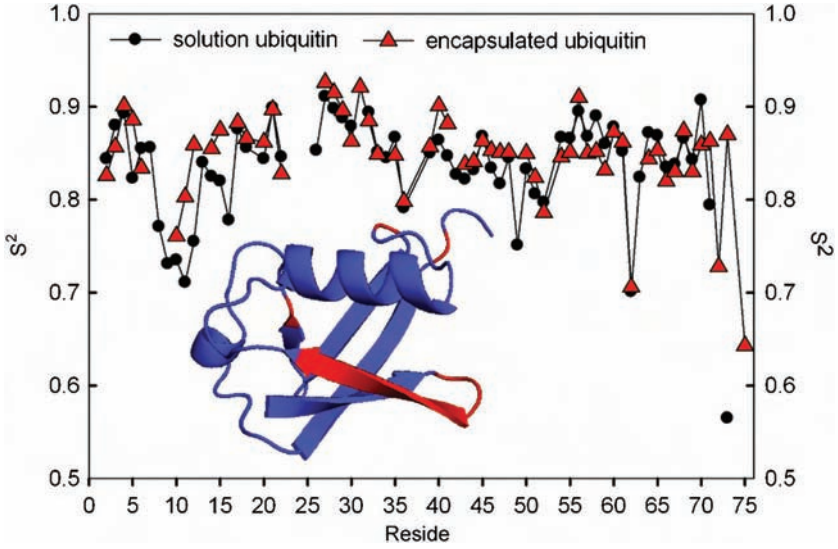

Fig. 18. Comparison of order parameters (S^2) for ubiquitin in free and encapsulated states. S^2 ranges from 0 to 1, indicating respectively, no restriction and complete restriction of N-H bond vector motion. Insert shows low solution S^2 values of ubiquitin colored in red.

conducted at both 50.68 and 60.78 MHz.[35] A plot of S^2 versus residue for encapsulated and free solution forms of ubiquitin is shown in Fig. 18, together with free solution ubiquitin S^2 values.[155] The trend of backbone dynamics for encapsulated ubiquitin follows that of solution ubiquitin, and in most regions encapsulated ubiquitin exhibits order parameters that are only slightly higher than those determined for the free protein. More significant differences in the order parameters for the free and encapsulated forms are found in the regions comprised of residues L8 through G16, which involves the loop between β-strands 1 and 2, as well as most of β-strand 2. In addition, residues Q40, Q41, L56, L71, R72, L73, and G75 exhibit significantly increased S^2 values in the encapsulated state relative to the solution state. Residues Q40 and Q41 lie at the beginning of β-sheet 3 and residue L56 lies at the beginning of the short 3_{10}-helix. Residues L71 through L73 compose the transition region between the end of terminal β-sheet 5 and the unstructured C-terminus (note that residues R72 and G75 were not characterized in the free solution study). Taken all together then, confinement thus appears to restrict the amplitude of fast backbone dynamics in regions that are naturally anticipated to possess relatively high structural flexibility.

The influence of encapsulation on the chemical and conformational exchange contribution to NMR relaxation was also investigated based on the previously described ^{15}N T_1/T_2 ratio analysis. Such studies conducted on the free solution form of ubiquitin indicate that residues E18, I23, N25, and I36 undergo significant conformational exchange on the μsec–msec time.[155] Residues 8–11, 62, and 73–76 exhibited low NOE values, which are indicative of motions occurring

on a time scale of 10^{-10}–10^{-9} sec. Rotating frame $R_{1\rho}$ measurements of the peptide amide groups of the solution form of ubiquitin have independently identified significant μsec–msec conformational exchange in residues I23, N25, T55, and V70.[157,160] Results for encapsulated ubiquitin indicate that residues T7, I23, N25, and K27 exhibit significant conformational exchange on the μsec–msec time scale using the same protocol employed in earlier studies of free solution ubiquitin.[155] Overall then, relaxation data recorded in the encapsulated state indicates that conformational exchange in ubiquitin is similar to that found for the free solution form.

The influence of confinement on the internal motions in polypeptides has also been investigated based on studies of proteins present in whole cells.[161,162] These important studies provide the most native-like environments for examining the influence on protein internal motions. As was found for encapsulation, it appears that backbone motion is restricted within the intracellular environment. Unfortunately, such studies present daunting technical challenges, from both molecular biology and NMR perspectives. Given that encapsulation studies are much more readily conducted, and have significantly higher precision that can currently be realized in the in-cell examples, it appears that a combination of in-cell and encapsulation studies should provide an enhanced approach to the examination of the influence of confinement on protein biophysics.

18. FUTURE STUDIES

Protein reverse micelle encapsulation continues to make important contributions to the elucidation of the most challenging issues in modern biophysics, and is emerging as an important tool to study such phenomena as macromolecular confinement and low temperature unfolding with atomic level resolution.

As the range of applications of encapsulation expands, discovery of additional surfactant molecules and formulation strategies will become increasingly important. To accomplish the goal of identifying new reverse micelle forming surfactants, a rational understanding of the tailoring process is necessary. The mechanism of encapsulation is not understood in atomic level detail, and current evidence strongly suggests that the interactions between the reverse micelle forming surfactants and the host molecule are complex. Detailed studies will be required to move the field from its current state, which is largely based on ad hoc assumptions, to a more rational enterprise that would support engineering approaches to surfactant formulation. Success in this effort will increase the importance and range of reverse micelle applications by incorporating more and more important target molecules, including larger proteins, proteins with complex chemical surfaces and perhaps most significantly, membrane proteins.

With respect to studies of conformational dynamics, future studies can be predicted to extend the approach outlined here to other proteins, especially systems in which there appears to be a coupling between internal motions and enzymatic activity as well as systems which exhibit conformational heterogeneity. In addition,

the influence of changes in reverse micelle composition, e.g., water-loading, surfactant type, etc., are prime candidates for dynamics studies.

Finally, reverse micelle promises to make an important impact on the final frontier in biophysics: membrane proteins. Although no published work has yet appeared. A number of studies have been conducted and the results should provide both important new insights into the nature of membrane structure and function and also provide novel suggestions for an entire new class of investigations.

ACKNOWLEDGMENTS

The authors thank Amy C. Spencer and Carla M. Flynn for critical reading of the manuscript.

REFERENCES

1. G. M. Clore and A. M. Gronenborn, *Nat. Struct. Biol.*, 1997, **4**, 849–853.
2. G. Wagner, *Nat. Struct. Biol.*, 1997, **4**, 841–844.
3. C. R. Babu, P. F. Flynn and A. J. Wand, *J. Biomol. NMR*, 2003, **25**, 313–323.
4. Y. Hayashi, M. M. R. Talukder, T. Takeyama, J. C. Wu, T. Kawanishi and N. Shimizu, *J. Chem. Technol. Biotechnol.*, 2003, **78**, 860–864.
5. Y. T. Hayashi, M. M. R. Talukder, J. Wu, T. Takeyama, T. Kawanishi and N. Simizu, *J. Chem. Technol. Biotechnol.*, 2001, **76**, 844–850.
6. M. Jimenez, J. Escribano, F. Gandia-Herrero, S. Chazarra, J. Cabanes, F. Garcia-Carmona and M. Perez-Gilabert, *Biotechnol. Prog.*, 2002, **18**, 635–640.
7. P. L. Luisi, F. Henniger, M. Joppich, A. Dossena and G. Casnati, *Biochem. Biophys. Res. Commun.*, 1977, **74**, 1384–1389.
8. F. C. Marhuenda-Egea, S. Piera-Velázquez, C. Chiquinquira and C. Eduardo, *J. Biotechnol.*, 2002, **93**, 159–164.
9. J. Michizoe, G. Masahiro and S. Furusaki, *J. Biosci. Bioeng.*, 2001, **92**, 67–71.
10. A. J. E. Pedro, P. S. Fevereiro, M. L. Serralheiro and M. R. Aires-Barros, *Biocatal. Biotransform.*, 2002, **20**, 129–135.
11. I. Shin, E. Wachtel, E. Roth, C. Bon, I. Silman and L. Weiner, *Protein Sci.*, 2002, **11**, 2022–2032.
12. M. M. R. Talukder, Y. Hayashi, T. Takeyama, M. M. Zamam, J. C. Wu, T. Kawanishi and N. Shimizu, *J. Mol. Catal. B Enzym.*, 2003, **22**, 203–209.
13. P. A. Viparelli, F. Alfani and M. Cantarella, *J. Mol. Catal. B: Enzym.*, 2001, **15**, 1–8.
14. P. Walde, Q. Peng, N. W. Fadnavis, E. Battistel and P. L. Luisi, *Eur. J. Biochem.*, 1988, **173**, 401–409.
15. J. C. Wu, Z. M. He, C. Y. Yao and K. T. Yu, *J. Chem. Technol. Biotechnol.*, 2001, **76**, 949–953.
16. G. A. Morris, *J. Am. Chem. Soc.*, 1980, **102**, 428–429.
17. G. A. Morris and R. Freeman, *J. Am. Chem. Soc.*, 1979, **101**, 760–762.
18. D. M. LeMaster, *Prog. NMR Spectrosc.*, 1994, **26**, 371–419.
19. M. R. Hansen, L. Mueller and A. Pardi, *Nat. Struct. Biol.*, 1998, **5**, 1065–1074.
20. M. R. Hansen, M. Rance and A. Pardi, *J. Am. Chem. Soc.*, 1998, **120**, 11210–11211.
21. H. C. Kung, K. Y. Wang, I. Golier and P. H. Bolton, *J. Magn. Reson. Ser. B*, 1995, **109**, 323–325.
22. M. L. Tillett, M. A. Horsfield, L. Y. Lian and T. J. Norwood, *J. Biomol. NMR*, 1999, **13**, 223–232.
23. N. Tjandra, S. Grzesiek and A. Bax, *J. Am. Chem. Soc.*, 1996, **118**, 6164–6274.
24. J. R. Tolman and J. H. Prestegard, *J. Magn. Reson. Ser. B*, 1996, **112**, 224–252.
25. J. R. Tolman and J. H. Prestegard, *J. Magn. Reson. Ser. B*, 1996, **112**, 269–274.

26. K. Pervushin, R. Riek, G. Wider and K. Wüthrich, *Proc. Natl. Acad. Sci. U.S.A.*, 1997, **94**, 12366–12371.
27. G. Lipari and A. Szabo, *J. Am. Chem. Soc.*, 1982, **104**, 4546–4559.
28. G. Lipari and A. Szabo, *J. Am. Chem. Soc.*, 1982, **104**, 4559–4570.
29. P. F. Flynn, A. Wendt and P. G. Gollnick, *Proteins*, 2002, **49**, 432–438.
30. A. J. Wand, C. R. Babu, P. F. Flynn and M. J. Milton, NMR spectroscopy of encapsulated proteins dissolved in low viscosity fluids, in: *Protein NMR for the Millennium*, L. J. Berliner ed., Kluwer Academic/Plenum Publishers, New York, 2003, pp. 121–160.
31. L. M. M. Nazário, J. P. S. G. Crespo, J. F. Holzwarth and T. A. Hatton, *Langmuir*, 2000, **16**, 5892–5899.
32. Y. L. Khmelnitsky, A. V. Kabanov, N. L. Klyachko, A. V. Levanshov and K. Martinek, in: *Structure and Reactivity in Reversed Micelles*, M. P. Pileni ed., Elsevier, New York, 1989, p. 230.
33. B. H. Robinson, A. N. Khen-Lodi and T. Tomey, Microparticle synthesis and characterization in reverse micelles, in: *Structure and Reactivity in Reversed Micelles*, M. P. Pileni ed., Elsevier, Amsterdam, 1989, p. 198.
34. W. D. Van Horn, A. K. Simorellis and P. F. Flynn, *J. Am. Chem. Soc.*, 2005, **127**, 13554–13560.
35. A. K. Simorellis and P. F. Flynn, *J. Am. Chem. Soc.*, 2006, **128**, 9580–9581.
36. H. Kunieda and K. Shinoda, *J. Colloid Interface Sci.*, 1979, **70**, 577–583.
37. M. Ueda and Z. A. Schelly, *Langmuir*, 1988, **4**, 653–655.
38. Z. -J. Yu, N. -F. Zhou and R. D. Neuman, *Langmuir*, 1992, **8**, 1885–1888.
39. R. E. Riter, E. P. Undiks and N. E. Levinger, *J. Am. Chem. Soc.*, 1998, **120**, 6062–6067.
40. P. L. Luisi and L. Magid, *J. CRC Crit. Rev. Biochem.*, 1986, **20**, 409–474.
41. N. V. Nucci and J. M. Vanderkooi, *J. Phys. Chem. B*, 2005, **109**, 18301–18309.
42. M. Ueda and Z. A. Schelly, *Langmuir*, 1987, **4**, 653–655.
43. E. Battistel and P. L. Luisi, *J. Colloid Interface Sci.*, 1989, **128**, 7–14.
44. S. G. Frank and G. Zografi, *J. Colloid Interface Sci.*, 1969, **29**, 27–35.
45. A. Kitahara and K. Kon-No, *J. Phys. Chem.*, 1966, **70**, 3395–3398.
46. E. B. Leodidis and T. A. Hatton, *Langmuir*, 1989, **5**, 741–753.
47. A. K. Simorellis, W. D. Van Horn and P. F. Flynn, *J. Am. Chem. Soc.*, 2006, **128**, 5082–5090.
48. M. J. Hou and D. O. Shah, *Langmuir*, 1987, **3**, 1086–1096.
49. S. A. Safran, *J. Chem. Phys.*, 1983, **78**, 2073–2076.
50. M. B. Mathews and E. Hirschhorn, *J. Colloid Interface Sci.*, 1953, **8**, 86–96.
51. M. Zulauf and H. F. Eicke, *J. Phys. Chem.*, 1979, **83**, 480–486.
52. M. J. Politi and H. Chaimovich, *J. Phys. Chem.*, 1986, **90**, 282–287.
53. E. Battistel and P. L. Luisi, *J. Phys. Chem.*, 1988, **92**, 6680–6685.
54. L. M. Grierasch, K. F. Thompson, J. E. Lacy and A. L. Rockwell, Peptide interaction with interfacial water, *Reverse Micelles*, Vol. 21–31, P. L. Luisi, B. E. Straub, eds., Plenum, New York, 1984.
55. M. Wong, J. K. Thomas and T. Nowak, *J. Am. Chem. Soc.*, 1977, **99**, 4730–4736.
56. R. E. Riter, D. M. Willard and N. E. Levinger, *J. Phys. Chem. B*, 1998, **102**, 2705–2714.
57. D. P. Eyman and R. S. Drago, *J. Am. Chem. Soc*, 1966, **88**, 1617–1620.
58. N. Zhou, Q. Li, J. Wu, J. Chen, S. Weng and G. Xu, *Langmuir*, 2001, **17**, 4505–4509.
59. A. D'Aprano, A. Lizzio and V. T. Liveri, *J. Phys. Chem.*, 1987, **91**, 4749–4751.
60. S. P. Moulik and P. K. Bhattacharya, *Langmuir*, 1992, **8**, 2135–2139.
61. S. P. Moulik and S. Ray, *Pure Appl. Chem.*, 1994, **66**, 521–525.
62. H. Z. Zhang and F. V. Bright, *J. Phys. Chem.*, 1991, **95**, 7900–7907.
63. D. S. Venables, K. Huang and C. A. Schmuttenmaer, *J. Phys. Chem. B*, 2001, **105**, 9132–9138.
64. P. L. Luisi, *Angew. Chem. Intl. Ed.*, 1985, **24**, 439.
65. P. L. Luisi and B. E. Straub, eds., *Reverse Micelles: Biological and Technological Structures in Apolar Media*, Plenum Press, New York, 1982.
66. L. J. Magid and C. A. Martin, *Reverse Micelles*, Plenum Press, New York, 1984.
67. C. R. Babu, P. F. Flynn and A. J. Wand, *J. Am. Chem. Soc.*, 2001, **123**, 2691–2692.
68. R. V. Rariy, N. Bec, J. L. Saldana, S. N. Nametkin, V. V. Mozhaev, N. L. Klyachko, A. V. Levashov and C. Balny, *FEBS Lett.*, 1995, **364**, 98–100.

69. N. L. Klyachko, P. A. Levashov, A. V. Levashov and C. Balny, *Biochem. Biophys. Res. Commun.*, 1999, **254**, 685–688.
70. M. E. Leser and P. L. Luisi, *Chimia*, 1990, **44**, 270–282.
71. E. Battistel, P. L. Luisi and G. Rinaldi, *J. Phys. Chem.*, 1988, **92**, 6680–6685.
72. D. Valdez, J. -Y. Huérou, M. Gindre, W. Urbach and M. Waks, *Biophys. J.*, 2001, **80**, 2751–2760.
73. R. V. Rariy, N. Bec, J. -L. Saldana, S. N. Nametkin, V. V. Mozhaev, N. L. Klyachko, A. V. Levashov and C. Balny, *FEBS Lett.*, 1995, **364**, 98–100.
74. N. L. Klyachko, P. A. Levashov, A. V. Levashov and C. Balny, *Biochem. Biophys. Res. Commun.*, 1999, **254**, 685–688.
75. P. Brochette, C. Petit and M. P. Pileni, *J. Phys. Chem.*, 1988, **92**, 3505–3511.
76. R. W. Gale, J. L. Fulton and R. D. Smith, *J. Am. Chem. Soc.*, 2001, **109**, 920–921.
77. R. O. Anarbaev, S. N. Khodyreva, A. L. Zakharenko, N. I. Rechkunova and O. I. Lavrik, *J. Mol. Catal.*, 2005, **33**, 29–34.
78. A. K. Shaw, R. Sarkar and S. K. Pal, *Chem. Phys. Lett.*, 2005, **408**, 366–370.
79. T. Maruyama, L. C. Park, T. Shinohara and M. Goto, *Biomacromolecules*, 2004, **5**, 49–53.
80. G. Palazzo and P. L. Luisi, *Biochem. Biophys. Res. Commun.*, 1992, **186**, 1546–1552.
81. E. P. Melo, R. P. Baptista and J. M. S. Cabral, *J. Mol. Catal. B Enzym.*, 2003, **22**, 299–306.
82. E. P. Melo, S. M. B. Costa, M. S. Joaquim, P. J. Cabral and S. B. Peterson, *Phys. Lipids*, 2003, **124**, 37–47.
83. E. P. Melo, S. M. B. Costa, M. S. Joaquim, P. J. Cabral and S. B. Peterson, *Phys. Lipids*, 2003, **124**, 37–47.
84. A. Shioi, M. Harada, H. Takahashi and M. Adashi, *Langmuir*, 1997, **13**, 609–613.
85. Z. Shi, R. W. Peterson and A. J. Wand, *Langmuir*, 2005, **21**, 10632–10637.
86. R. W. Peterson, M. S. Pomentum, Z. Shi and A. J. Wand, *Protein Sci.*, 2005, **14**, 2919–2921.
87. P. F. Flynn, M. J. Milton, C. R. Babu and A. J. Wand, *J. Biomol. NMR*, 2002, **23**, 311–316.
88. T. A. Betts and F. V. Bright, *Appl. Spectrosc.*, 1990, **44**, 1196.
89. M. R. Ehrhardt, P. F. Flynn and A. J. Wand, *J. Biomol. NMR*, 1999, **14**, 75–78.
90. A. J. Wand, M. R. Ehrhardt and P. F. Flynn, *Proc. Natl. Acad. Sci.*, 1998, **95**, 15299–15302.
91. R. W. Peterson, and A. J. Wand, *Rev. Sci. Instrum.*, 2005, **76**, 1–7.
92. P. F. Flynn, M. J. Milton, C. R. Babu and A. J. Wand, *J. Biomol. NMR*, 2002, **23**, 311–316.
93. R. J. Ogg, R. B. Kingsley and J. S. Taylor, *J. Magn. Reson. Ser. B*, 1994, **104**, 1.
94. S. L. Patt, *J. Magn. Reson.*, 1992, **96**, 94.
95. S. H. Smallcombe, S. C. Patt and P. A. Keifer, *J. Magn. Reson. A*, 1995, **177**, 295.
96. S. E. Gaemers, C. J. Elsevier and A. Bax, *Chem. Phys. Lett.*, 1999, **301**, 138.
97. A. J. Wand, M. R. Ehrhardt and P. F. Flynn, *Proc. Natl. Acad. Sci. U.S.A.*, 1998, **95**, 15303.
98. P. F. Flynn, *Prog. Nucl. Magn. Reson. Spectrosc.*, 2004, **45**, 31–51.
99. M. R. Ehrhardt, P. F. Flynn and A. J. Wand, *J. Biomol. NMR*, 1999, **14(75)**.
100. P. F. Flynn, M. J. Milton, C. R. Babu and A. J. Wand, *J. Biomol. NMR*, 2002, **23**, 311.
101. E. O. Stejskal and J. E. Tanner, *J. Chem. Phys.*, 1965, **42**, 288.
102. A. S. Altieri, D. P. Hinton and R. A. Byrd, *J. Am. Chem. Soc.*, 1995, **117**, 7566.
103. S. J. Gibbs and C. S. Johnson Jr., *J. Magn. Reson.*, 1991, **93**, 395.
104. L. D. Landau and E. M. Lifshiftz, *Fluids Dynamics*, 2nd ed., 1963, p. 217.
105. J. Lounila, K. Oikarinen, P. Ingman and J. Jokisaari, *J. Magn. Reson. Ser. A*, 1996, **118**, 50–54.
106. A. S. Altieri, D. P. Hinton and A. R. Byrd, *J. Am. Chem. Soc.*, 1995, **117**, 7566–7567.
107. A. Jerschow and N. Muller, *J. Magn. Reson.*, 1997, **125**, 372–375.
108. D. S. Wishart and B. D. Sykes, *J. Biomol. NMR*, 1994, **4**, 171–180.
109. D. S. Wishart, C. G. Bigam, A. Holm, R. S. Hodges and B. D. Sykes, *J. Biomol. NMR*, 1995, **5**, 67–81.
110. D. D. Laws, D. S. Wishart, R. H. Havlin, M. Westmeyer, B. D. Sykes and E. Oldfield, *J. Magn. Reson. B*, 1995, **108**, 274–275.
111. D. S. Wishart, C. G. Bigam, J. Yao, F. Abildgaard, H. J. Dyson, E. Oldfield, J. L. Markley and B. D. Sykes, *J. Biomol. NMR*, 1995, **6**, 135–140.
112. C. R. Babu, P. F. Flynn and A. J. Wand, *J. Biomol. NMR*, 2003, **25**, 313–323.
113. C. R. Babu, P. F. Flynn and A. J. Wand, *BMRB Entry 5387*, 2002.

114. C. R. Babu, P. F. Flynn and J. A. Wand, *J. Am. Chem. Soc.*, 2001, **123**, 2691–2692.
115. A. C. Wang, P. J. Lodi, J. Qin, G. Vuister, A. M. Groenborn and G. M. Clore, *J. Magn. Reson. Ser. B*, 1994, **105**, 196.
116. S. Vijay-Kumar, C. E. Bugg and W. J. Cook, *J. Mol. Biol.*, 1987, **194**, 531.
117. G. Cornilescu, J. L. Marquardt, M. Ottiger and A. Bax, *J. Am. Chem. Soc.*, 1998, **120**.
118. K. G. Valentine, M. S. Pometun, J. M. Kielec, R. E. Baigelman, J. K. Staub, K. L. Owens and A. J. Wand, *J. Am. Chem. Soc.*, 2006, **128**, 15930–15931.
119. A. Bax, G. Kontaxis and N. Tjandra, *Methods Enzymol.*, 2001, **339**, 127–174.
120. D. Fushman, R. Varadan, M. Assfalg and O. Walker, *Prog. Nucl. Magn. Reson. Spectrosc.*, 2004, **44**, 189–214.
121. R. S. Lipsitz and N. Tjandra, *Ann. Rev. Biophys. Biomol. Struct.*, 2004, **33**, 387–413.
122. J. H. Prestegard, H. M. Al-Hashimi and J. R. Tolman, *Q. Rev. Biophys.*, 2000, **33**, 371–424.
123. J. H. Prestegard, C. M. Bougault and A. I. Kishore, *Chem. Rev.*, 2004, **104**, 3519–3540.
124. J. R. Tolman, *Curr. Opin. Struct. Biol.*, 2001, **11**, 532–539.
125. B. G. Lefebvre, W. Liu, R. W. Peterson, K. G. Valentine and A. J. Wand, *J. Magn. Reson.*, 2005, **175**, 158–162.
126. R. W. Peterson, M. S. Pomentum, Z. Shi and A. J. Wand, *Protein Sci.*, 2005, **14**, 2919–2921.
127. Z. Shi, R. W. Peterson and A. J. Wand, *Langmuir*, 2005, **21**, 10632–10637.
128. P. Douzou, E. Keh and C. Balny, *Proc. Natl. Acad. Sci.*, 1979, **76**, 681–684.
129. M. Zulaf and H. F. Eicke, *J. Phys. Chem.*, 1979, **83**, 480–486.
130. C. A. Munson, G. A. Baker, S. N. Baker and F. V. Bright, *Langmuir*, 2004, **20**, 1551–1557.
131. A. K. Simorellis, W. D. Van Horn and P. F. Flynn, *J. Am. Chem. Soc*, 2006, **128**, 5082–5090.
132. N. E. Levinger, *Nature*, 2002, **298**, 1722–1723.
133. A. K. Simorellis, W. D. Van Horn and P. F. Flynn, *J. Am. Chem. Soc.*, 2006, **128**, 5082–5090.
134. A. Fersht, *Structure and Mechanism in Protein Science A Guide to Enzyme Catalysis and Protein Folding*, 2nd edn, W. H. Freeman and Company, 1999, pp. 511–512.
135. P. L. Privalov, *Crit. Rev. Biochem. Mol. Biol.*, 1990, **25**, 281–305.
136. G. Caldarelli and P. De Los Rios, *J. Biol. Phys.*, 2001, **27**, 229–241.
137. P. L. Privalov, Y. V. Griko and S. Y. Venyaminov, *J. Mol. Biol.*, 1986, **190**, 487–498.
138. B. Ibarra-Molero, G. I. Makhatadze and J. M. Sanchez-Ruiz, *Biochim. Biophys. Acta*, 1999, **1429**, 384–390.
139. P. L. Privalov and S. J. Gill, *Adv. Protein Chem.*, 1998, **39**, 191–234.
140. C. R. Babu, V. J. Hilser and A. J. Wand, *Nat. Struct. Mol. Biol.*, 2004, **11**, 352–357.
141. M. S. Pomentun, R. W. Peterson, C. R. Babu and A. J. Wand, *J. Am. Chem. Soc.*, 2006, **128**, 10652–10653.
142. S. L. Alam, J. Sun, M. Payne, B. D. Welch, B. K. Blake, D. R. Davis, H. H. Meyer, S. D. Emr and W. I. Sundquist, *EMBO J.*, 2004, **23**, 1411–1421.
143. R. Beal, Q. Deveraux, G. Xia, M. Rechsteiner and C. Pickart, *Proc. Natl. Acad. Sci. U.S.A.*, 1996, **93**, 861–866.
144. R. D. Fisher, B. Wang, S. L. Alam, D. S. Higginson, H. Robinson, W. I. Sundquist and C. P. Hill, *J. Biol. Chem.*, 2003, **278**, 28976–28984.
145. C. P. Ponting, *Biochem. J.*, 2000, **351**, 527–535.
146. R. Verma, N. R. Peters, M. D'Onofrio, G. P. Tochtrop, K. M. Sakamoto, R. Varadan, M. Zhang, P. Coffino, D. Fushman, R. J. Deshaies and R. W. King, *Science*, 2004, **306**, 117–120.
147. B. Wang, S. L. Alam, H. H. Meyer, M. Payne, T. L. Stemmler, D. R. Davis and W. I. Sundquist, *J. Biol. Chem.*, 2003, **278(22)**, 20225–20234.
148. Q. Wang, A. M. Goh, P. M. Howley and K. J. Walters, *Biochemistry*, 2003, **42**, 13529–13535.
149. R. Kitahara, A. Okuno, M. Kato, Y. Taniguchi, S. Yokoyama and K. Akasaka, *Magn. Reson. Chem.*, 2006, **44**, S108–S113.
150. G. W. Robinson and C. H. Cho, *Biophys. J.*, 1999, **77**, 3311–3318.
151. N. A. Farrow, D. R. Muhandiram, A. U. Singer, A. M. Pascal, C. M. Kay, G. Gish, S. E. Shoelson, T. Pawson, J. D. Forman-Kay and L. E. Kay, *Biochemistry*, 1999, **33**, 5984.
152. A. G. Palmer, N. J. Skelton, W. J. Chazin, P. E. Wright and M. Rance, *Mol. Phys.*, 1992, **75**, 699.

153. G. Lipari and A. Szabo, *J. Am. Chem. Soc.*, 1982, **104**, 4546–4559.
154. G. M. Clore, A. Szabo, A. Bax, L. E. Kay, P. C. Driscoll and A. M. Gronenborn, *J. Am. Chem. Soc.*, 1990, **112(12)**, 4989–4991.
155. N. Tjandra, S. F. Feller, R. W. Pastor and A. Bax, *J. Am. Chem. Soc.*, 1995, **117**, 12562–12566.
156. L. E. Kay, *J. Magn. Reson.*, 2005, **173(2)**, 193–207.
157. F. Massi, M. J. Grey and A. G. Palmer, *Protein Sci.*, 2005, **14**, 735–742.
158. A. G. I. Palmer, *Chem. Rev.*, 2004, **104(8)**, 3623–3640.
159. A. G. I. Palmer and F. Massi, *Chem. Rev.*, 2006, **106(5)**, 1700–1719.
160. T. J. Burch and A. L. Haas, *Biochemistry*, 1994, **33**, 7300–7308.
161. J. E. Bryant, J. T. J. Lecomte, A. L. Lee, G. B. Young and G. J. Pielak, *Biochemistry*, 2006, **45(33)**, 10085–10091.
162. P. Selenko, Z. Serber, B. Gadea, J. Ruderman and G. Wagner, *Proc. Natl. Acad. Sci.*, 2006, **103(32)**, 11904–11909.

This page intentionally left blank

Index